

ABSTRACT

MELILLO, MATTHEW JOSEPH. PDMS Network Structure-Property Relationships: Influence of Molecular Architecture on Mechanical and Wetting Properties. (Under the direction of Dr. Jan Genzer).

Poly(dimethylsiloxane) (PDMS) is one of the most common elastomers, with applications ranging from sealants and marine-antifouling coatings to medical devices and absorbents for water treatment. Fundamental understanding of how liquids spread on the surface of and absorb into and leach out of PDMS networks is of critical importance for the design and use in another application - microfluidic devices. The growing use of PDMS in microfluidic devices raises the concern that some researchers may use this material without fully understanding all of its advantages, drawbacks, and intricacies. The primary goal of this Ph.D. dissertation is to elucidate PDMS network molecular structure to macroscopic property relationships and to demonstrate how molecular architecture can alter dynamic mechanical and wetting characteristics.

We prepare PDMS materials by using vinyl/ tetrakis(dimethylsiloxy)silane (TDSS) and silanol/ tetraethylorthosilicate (TEOS) combinations of PDMS end-groups and crosslinkers as two model systems. Under constant curing conditions, we systematically study the effects of polymer molecular weight, loading of crosslinker, and end-group chemical functionality on the extent of gelation and the dynamic mechanical and water wetting properties of end-linked PDMS networks. The extent of the gelation reaction is determined using the Soxhlet extraction to quantify the amount of material that did and did not participate in the crosslinking reactions, termed the gel and sol fractions, respectively. We use the Miller-Macosko model in conjunction with the gel fraction and precise chemical composition (*i.e.*, stoichiometric ratio and molecular weight) to determine the fractions of elastic and pendant material, the molecular weight between chemical crosslinks, and the average effective functionality of the crosslinker molecule.

Based on dynamic mechanical testing, we find that the maximum storage moduli are achieved at optimal stoichiometric conditions in the vinyl/TDSS and commercial PDMS-based Sylgard 184 composite, but only keep improving with additional crosslinker in the silanol/TEOS systems due to *in situ* TEOS aggregation. We relate molecular network topology to mechanical properties using outputs from the Miller-Macosko model in the vinyl/TDSS

system. The elastic fraction and storage modulus correlate well, as do the pendant fraction and the loss tangent, demonstrating the importance of each fraction in bulk mechanical properties. By studying the dynamic behavior of water droplets wetting PDMS substrates, we observe non-linear wetting behaviors that are markedly different from linear behaviors seen on glassy polymer substrates. The non-linear behavior is only observed prior to extraction, while after extraction, both systems demonstrate behavior similar to glassy polymers. This reveals the dramatic role small amounts of uncrosslinked materials present in the sol fraction play in the surface wetting dynamics of PDMS materials. We further demonstrate the role of uncrosslinked material by adding silicone oils into otherwise fully crosslinked PDMS networks and study their wetting properties.

Through careful formulation and preparation of PDMS materials, compared to simply mixing two formulations present in Sylgard 184, one can apply polymer network models to glean useful information about network topology. The benefits of doing so outweigh the costs. We stress the importance of performing Soxhlet extraction to remove unreacted components from PDMS materials, even when using optimal stoichiometry. These mobile molecules that remain after crosslinking can alter significantly wetting behavior and readily leach into liquid environments. However, it is equally important to stress that Soxhlet extraction will not remove all unreacted material. Some will always remain in PDMS, which is often the practice in preparing microfluidic devices. While Sylgard 184 is very well suited for some applications, the results presented in this dissertation demonstrate to researchers that the material does have its limitations and that other options are available. These findings will aid in the design and implementation of reliable microfluidic devices and other PDMS-based materials that encounter liquid interfaces.

© Copyright 2017 Matthew Joseph Melillo

All Rights Reserved

PDMS Network Structure-Property Relationships: Influence of Molecular Architecture on
Mechanical and Wetting Properties

by
Matthew Joseph Melillo

A dissertation submitted to the Graduate Faculty of
North Carolina State University
in partial fulfillment of the
requirements for the degree of
Doctor of Philosophy

Chemical Engineering

Raleigh, North Carolina

2017

APPROVED BY:

Dr. Jan Genzer
Committee Chair

Dr. Kirill Efimenko

Dr. Michael Dickey

Dr. Karen Daniels

DEDICATION

I dedicate this dissertation to my parents, Robert and Nina Melillo, who have always supported me and believed in me. I would not have made it to this point without them. They have always encouraged me to pursue my passions, set ambitious goals, work hard and diligently, take pride in my work, take care of myself by getting enough food and sleep, and, most importantly, make time to have fun and relax with family and friends along the way. I am eternally grateful to them.

BIOGRAPHY

Matthew Melillo was born in Trenton, New Jersey to his parents, Robert and Nina Melillo. He was their second child, following his older sister, Jacqueline, and was followed by two younger sisters, Amanda and Gianna. He spent most of his childhood life living in Columbus, NJ and attended Northern Burlington Regional County High School in New Jersey. In school, he took a keen interest in science and math thanks to the excellent teachers there who made these subjects very interesting to him. He also became actively involved in long distancing running on the cross country and track teams.

Through his parents' encouragement, he pursued admittance to colleges and universities with strong engineering programs. As a result, he attended Lehigh University in Bethlehem, Pennsylvania and studied Chemical Engineering. Here he became involved in various environmental advocacy groups who worked on the national and local levels, helping to introduce improved recycling and composting systems at Lehigh. In the beginning of his senior year, he began doing research under the guidance of Dr. Jeetain Mittal. They used molecular dynamics simulations to study water flow through carbon nanotubes with the ultimate goal of creating advanced water purification membranes. It was Dr. Mittal who enlightened Matthew to the world of scientific research and recommended he consider North Carolina State University for Graduate School.

Matthew was admitted to North Carolina State University's Chemical and Biomolecular Engineering (CBE) Department, and after visiting and meeting professors, graduate students, and staff from the department, he knew he wanted to spend his time in graduate school there. After his first semester, he joined Dr. Jan Genzer's research group and began studying silicone elastomers for their potential application in water purification materials. This project turned into a fundamental study of the structure-property relationships in silicone elastomers. Throughout his time as a graduate student, he got involved in several extracurricular activities. He helped plan many Genzer Group Retreats and served as a Recruitment Captain for the (CBE) department to welcome and encourage potential new graduate students to pursue graduate studies there in the CBE department. Additionally, after serving as Secretary of the University Graduate Student Association (UGSA), he became

President for a year long term. In this role, he advocated for more funding on behalf of the ~ 9,000 graduate students at NC State to the university administration. He also organized and led meetings of the ~ 50 graduate student representatives from many academic departments who made up the regular UGSA membership.

In his spare time, he enjoys being outdoors camping, exploring national and state parks, running, road cycling, and capturing nature photography. He also spends time volunteering on political campaigns and keeping up with and teaching himself about numerous space, science, and technology topics through his avid consumption of articles and videos.

ACKNOWLEDGMENTS

I first wish to thank my advisor, Professor Jan Genzer, for so many reasons. I thank him for tirelessly writing grants to provide financial support for my work and the work of his other graduate students. I am very grateful to him for giving me ample opportunities to learn and develop professionally outside of the lab and the classroom. With his permission, I got to be the president of graduate student government, a recruitment captain, and a Preparing the Professoriate Fellow. Although those activities were not related to research, they have helped me grow into the person I am today. I sincerely thank Dr. Genzer for always being supportive and positive, even when research was not going well. His zeal for science has helped me to keep pushing to gain new knowledge and understanding while having fun along the way. I also wish to thank him for giving me opportunities to present my research three times at national APS conferences. Attendance is not cheap, but I am very grateful that he provided support for me to share our work with the community. Lastly, I thank Dr. Genzer immensely for providing his time and energy to give support and feedback in my last couple of months as a graduate student when I was writing this dissertation. He provided constructive feedback on data analysis and how to communicate findings in the forms of both words and imagery that have helped turn this document into its present form. I am tremendously grateful for his help, support, and encouragement throughout all my years as a graduate student.

Another person who helped greatly in achieving the work presented in this dissertation is my committee member, Professor Kirill Efimenko. I wish to thank him for teaching me much of what I know about siloxanes and introducing me to polymerization and crosslinking reactions when I first joined the group. I further thank Dr. Efimenko for keeping the lab running by providing chemicals and supplies, and helping us fix equipment when they inevitably break. Additionally, I thank Dr. Efimenko greatly for his contribution to writing grants with Dr. Genzer to provide financial support for our lab.

There are many former Genzer Group members who have made my experience at NC State University one I am truly happy to have had. Professor Julie Albert and Dr. Robin Mays taught me a lot about the synthesis and characterization of polysiloxanes shortly after joining the group. I also learned a great deal of small molecule organic chemistry from Dr. Erich Bain

during my first summer in the group. Casey Galvin shared his knowledge of polymer brushes with me through conversations and excellent research updates at group meetings. I want to thank Dr. Edwin Walker and Dr. Preeta Datta for being outstanding Safety Officers in the lab and helping all of us maintain a safe work environment. Additionally, I thank Dr. Edwin Walker greatly for his help in the early stages of the water wettability on PDMS project. I have had intriguing and helpful conversations with Dr. C. K. Pandiyarajan pertaining to polymer networks, crosslink density, and swelling. He has also taught the entire group through his outstanding research updates and presentations. I want to thank Dr. Rohan Patil for teaching me a lot about polymer brushes, but also for opening my eyes to the world of YouTube videos related to science, space, and technology. It has always been a pleasure discussing scientific topics with him.

I am grateful to be working with amazing colleagues in the Genzer Group. I thank Dr. Gilbert Castillo, Dr. Duncan Davis, Amber Hubbard, Jason Miles, Shreya Erramilli, Yeongun Ko, Steven Zboray, Russell Schmitz, and Yiliang Lin all for providing constructive criticism and a high degree of scrutiny to all presentations I have given. This has the cumulative effect helping me understand how people view presentations differently than I do and making necessary adjustments for giving better talks. I owe Dr. Gilbert Castillo additional gratitude for serving as the laboratory Safety Officer with me. I also want to thank the three undergraduate students who have worked with me. Zoe Klein helped prepare many of the silanol/TEOS PDMS samples and testing their mechanical properties. Marina Rodrigues da Costa helped prepare poly(vinylmethylsiloxane) (PVMS) materials filled with fumed silica particles. Victoria Fouchard helped make PDMS materials with bimodal chain length distributions.

I owe a special debt of gratitude to another committee member, Professor Michael Dickey. In addition to providing support and advice when Marina and I were working on the PVMS/Fumed Silica project, he was serving on the recruitment committee when I applied to become a graduate student at NC State. So, I thank him for granting me admittance and allowing me to pursue studies here. Further, I thank him for providing support as my committee member and for his feedback to this dissertation. I would not be here without the

guidance of my undergraduate research advisor, Dr. Jeetain Mittal. He introduced me to scientific research and was an outstanding advisor who let me, as an undergraduate researcher, develop my own experience and reach my own conclusions instead of just giving me busy work. Crucially, he recommended I investigate NC State for graduate school, since his friend from graduate school, Dr. Michael Dickey, was a professor there, and had been enjoying his job there. I further want to thank my friend, Dr. Jon Rosen, who realized before I did myself, that graduate school was a good fit for me and pushed me to apply. I also thank Professor Karen Daniels for agreeing near the end of my studies to become my committee member. Her valuable feedback to this dissertation is much appreciated.

I am very thankful for support from Dr. Beth Overman and Dr. Barbi Honeycutt, who provided advice and mentorship when I was President of the University Graduate Student Association. They helped me navigate brand new challenges pertaining to managing people and working in an exciting but demanding role I was not used to. Vice Chancellor and Dean, Dr. Mike Mullen is someone who inspires me because he truly cares about students and puts their best interests front and center. I also thank him for being extremely supportive of me in my role as President. As President, I had an excellent executive board and committee chairs to help make the UGSA achieve its goals that year. Those included Veronica Mbaneme, Chirag Gajjar, Yvonnte Matos, Katie Kennedy, Efrain Rivera Serrano, Barry Peddycord, Shannon Warchol, Keith Brannum, Haritha Malladi, Colin Funaro, Preston Countryman, Jacob Majikes, David Fiala, and Olivia Reeser. All of these individuals together helped make that year one of my most enjoyable.

Additionally, I am grateful to Professor Lisa Bullard for being my mentor as Preparing the Professoriate Fellow. She helped teach me how to teach and I greatly enjoyed working with her and undergraduate students that year. I also want to thank Sandra Bailey for helping me out on numerous occasions with paperwork and understanding course registration and student fees.

I am very thankful to the close friends I have made throughout high school, college, and graduate school who have provided me with support and laughs throughout my life. These include Zach Marshall, Dave Specca, Dave Cho, Laura DeBenedetto, Caleb Walton, Kyle

Schreiner, Veronica Adams, Joe Tilly, Deepti Srivastava, Dr. Gilbert Castillo, Shreya Erramilli, Dr. Martin Dufficy, Dr. Cody Addington, and Dr. Ryan Barton.

Lastly, I wish to sincerely thank my parents, Nina and Robert, my sisters, Jacqueline, Amanda, and Gianna, and my Aunt Mare and Uncle John. Their endless support, encouragement, and belief in me have helped me achieve my Ph.D. and create this dissertation. I am incredibly fortunate to have such strong support from my family and am very grateful to them.

TABLE OF CONTENTS

LIST OF TABLES	xv
LIST OF TABLES IN APPENDICES	xvi
LIST OF FIGURES	xvii
LIST OF FIGURES IN APPENDICES	xxx
CHAPTER 1: Introduction & Dissertation Scope.....	1
Introduction.....	1
What Makes PDMS Unique and Versatile?.....	1
Current Research Areas Using PDMS	3
Challenges Pertaining to PDMS-Based Materials	5
Scope of Dissertation	6
References.....	10
CHAPTER 2: Preparation Details for Making Silicones.....	14
Introduction.....	14
Background on Crosslinking & Gelation.....	16
Variables Affecting Gelation	17
PDMS Crosslinking Chemistry	20
Experimental Materials and Methods	24
Materials	24
Network Preparation	25
Kinetics	26
Gel and Sol Fraction Determination	27
Scanning Electron Microscopy	28

Results.....	29
Crosslinking Chemistry	29
Gel Fraction	31
Discussion.....	35
Stoichiometry.....	35
Reaction and Diffusion Limitations Necessitate Excess Crosslinker	36
Differences in Molecular Weight.....	37
End-Capping Chains vs. Aggregation.....	40
Conclusions.....	43
Acknowledgements.....	44
Chapter 2 Appendix	45
Catalysts and Crosslinkers	46
Size Exclusion Chromatography.....	46
References.....	48
CHAPTER 3: Molecular Insights Revealed from Applying the Miller-Macosko Model to the Vinyl/TDSS System.....	53
Introduction.....	53
In the Context of this Dissertation	53
Polymer Theories	53
Entanglements.....	55
Real Elastic Network Theory – Loop Defects	58
Miller–Macosko Model	60
Experimental Methods	64
Miller-Macosko Model Calculations	64

Materials	66
Network Preparation & Gel Fraction Determination.....	67
Results & Discussion	68
Reactivity Insights	69
Elastic and Pendant Fractions	72
Density of Elastically Effective Chains, ν	76
Molecular Weight between Elastically Effective Chemical Crosslinks	78
Entanglement Trapping Factor	86
Conclusions.....	88
Acknowledgements.....	90
References.....	91
CHAPTER 4: Mechanical Properties of Silicone Elastomers	94
Introduction.....	94
In the Context of this Dissertation	94
Mechanical Properties of Soft Materials.....	94
Theoretical Background.....	96
Previous Research on Dynamic Mechanical Properties of PDMS Networks.....	101
Experimental Materials and Methods	102
Materials	102
Methods.....	103
Results & Discussion	110
Model PDMS Systems	110
Sylgard 184 Dynamic Mechanical Properties.....	117

Comparison between Sylgard 184 and Model PDMS Systems.....	124
Network Topology Effects.....	129
Stress-Strain Properties of Sylgard 184	138
Conclusions.....	142
Acknowledgements.....	142
Chapter 4 Appendix	143
Sylgard 184 Data.....	144
Vinyl/TDSS Data	148
References.....	149
CHAPTER 5: Dynamic Water Wetting on PDMS Materials Due to Uncrosslinked Species	154
Introduction.....	154
In the Context of this Dissertation	154
Wetting.....	154
Surface Energy and Surface Tension.....	155
Contact Angle Measurements	159
Microfluidics.....	162
Chapter Goals.....	166
Experimental Materials and Methods	167
Materials	167
Methods.....	168
Results & Discussion	175
Droplet Parameters as a Function of Contact Time	175
Post-Extraction vs. Pre-Extraction Contact Angles	180

Initial and Final Values	183
Direct Comparison of Sylgard 184 with Model PDMS	191
PDMS-Water Interfacial Energy	197
Summary of Wetting & Stoichiometry Relationships	202
Wetting & Mechanical Properties	203
Silicone Oils Added to Sylgard 184 Networks	206
Conclusions	208
Acknowledgements	211
Chapter 5 Appendix	212
Low Molecular Weight Dimethylsiloxane Oligomers	213
Glassy Benchmark Materials	216
Model Vinyl/TDSS PDMS Data for All Molecular Weights	217
Pure Sylgard 184 Data	239
Silicone Oils Added to Sylgard 184 Networks Data	242
Matlab Image Analysis Code	250
References	266
CHAPTER 6: Summary & Outlook	272
Summary	272
Chapter 1	272
Chapter 2	272
Chapter 3	273
Chapter 4	274
Chapter 5	275

Conclusions.....	276
Outlook	277
Mechanical Properties.....	277
Wetting Dynamics	282
Functional Siloxane Polymers and Copolymers	284
References.....	287

LIST OF TABLES

Table 2.1 – PDMS Materials and Properties ^a Purchased from Gelest, Inc.	24
Table 2.2 – Composition of Sylgard 184 (Dow Corning) according to Safety Data Sheets ^{8,9}	25
Table 3.1 – Vinyl-Terminated PDMS Materials Purchased from Gelest, Inc.	67
Table 4.1 – Composition of Sylgard 184 (Dow Corning) according to Safety Data Sheets ^{36,37}	103
Table 5.1 – Silicone Oils Added to Sylgard 184 Networks	207

LIST OF TABLES IN APPENDICES

Table A2.1 – Catalysts and crosslinkers purchased and used in this research.....	46
Table A5.1 – Properties of low molecular weight (LMW) dimethylsiloxane oligomers. References for “C” denote cyclics and “L” denote linears.	215

LIST OF FIGURES

- Figure 1.1** – Adapted from Zheng and McCarthy.⁷ Molecular structures of PDMS (a) and poly(isobutylene) (PIB) (b) with accurate representations of bond lengths and angles as calculated using Pauling electronegativity values. Dimensions acquired from the literature.⁷⁻⁹ 2
- Figure 1.2** – Publications and patents awarded per year that mention “Sylgard 184” (red), “Sylgard 184 and Microfluidic” (blue), and “Sylgard 184 and Bio” (green) plotted as a function of year. Data acquired from Google Scholar on April 28, 2017..... 4
- Figure 1.3** – Reproduced from Delebecq and Ganachaud.²⁹ Non-perfect network topology in commercial silicone elastomers. 6
- Figure 1.4** – Scope of dissertation. Build PDMS materials from the “ground up” to understand their molecular network structure and relate that to macroscopic bulk and surface properties.⁷
- Figure 2.1** – Flow diagram depicting parameters to be considered with preparing silicone elastomers. The independent variables one can control in preparing PDMS networks are given on the left, with the green squares showing variables investigated in this dissertation. The red squares were held constant. The middle blue squares show what gelation phenomena the independent variables can influence. Those parameters then influence both the gelation equilibrium and kinetics, orange squares on the right. Finally, the resulting material properties, such as gel fraction, depend upon the gelation equilibrium and kinetics. 18
- Figure 2.2** – Simplified chemical mechanism of the Pt(II) catalyzed hydrosilylation crosslinking reaction. This example shows the formation of a tetrafunctional crosslink junction through the creation of new Si-C-C-Si covalent linkages. 21
- Figure 2.3** – Simplified chemical mechanism of the (1) hydrolysis reaction of tetraethoxysilane (TEOS) and (2) condensation reaction of silanol groups between TEOS and silanol-terminated PDMS, which creates new siloxane (Si-O-Si) bonds and liberates water. This example demonstrates the silanol/alkoxysilane crosslinking reactions for PDMS, forming a trifunctional crosslink junction. 23
- Figure 2.4** – Soxhlet Extraction instrumentation. Samples are separated by porous Teflon holders in the sample chamber, allowing toluene but not the PDMS sample to flow through. A heating mantle uses electrical resistive heating to increase the temperature of toluene and boiling chips in the round bottom flask. The toluene vapor (red arrows) travels within the external glass tube up and into the sample chamber where it is condensed from a water/ethylene glycol coolant mixture (green liquid). The condensed toluene liquid (blue arrows) fills the sample chamber until a critical liquid level is reached, causing the syphon to spill all of the liquid back into round bottom flask. The process is repeated, enabling a continuous rinse with fresh toluene. Coolant from a chiller (white arrows) enters the bottom of right condenser and

fills it, exits from the top, and then enters the bottom of the left condenser and fills it before being returned to the chiller. 28

Figure 2.5 – Schematic illustrations of the reactants and products used in each PDMS system studied in this dissertation. The Vinyl/TDSS system crosslinks through Pt(II)-catalyzed hydrosilylation, shown in a). The Silanol/TEOS system crosslinks through a Sn(II)-catalyzed two-step hydrolysis/condensation reaction to create PDMS networks, shown in b). The commercial Sylgard 184 material creates PDMS networks via hydrosilylation of chemicals in the Base and Curing Agent components. The gray spheres represent the filler particles present in both the Base and Curing Agent components of Sylgard 184. 30

Figure 2.6 – Schematic illustration of different stoichiometric ratios and “end-capping” in the Vinyl/TDSS system. Scenarios corresponding to stoichiometric ratios of $r = 0.5, 3,$ and 20 are depicted in a, b, and c, respectively. The left column represents networks before the extraction process while the right column demonstrates how the extraction process removes material not covalently attached to or permanently trapped in the network. PDMS chains are shown as green lines with cyan vinyl end groups and the TDSS crosslinkers are shown as navy blue “+” signs inside light blue circles. Reacted silicon-hydride groups are cyan lines inside the blue circle. The red “X” indicates the failure to form a fully crosslinked network due either insufficient or excess amounts of crosslinker. In c, “end-capped” chains that reacted with TDSS on both ends, but failed to react with the network are extracted, resulting in a degraded network. The size of PDMS chains relative to TDSS crosslinkers is not to scale, but the quantities of each are to scale with respect to r 32

Figure 2.7 – Schematic illustration of different stoichiometric ratios and TEOS aggregation in the Silanol/TEOS system. Scenarios corresponding to stoichiometric ratios, $r = 0.5, 3,$ and 20 are shown in a, b, and c, respectively. The left column portrays networks before the extraction process while the right column demonstrates how the extraction process removes material not covalently attached to or permanently trapped in the network. PDMS chains are shown as green lines with brown silanol end groups and the TEOS crosslinkers are shown as red “+” signs inside light red circles. Hydrolyzed and condensed TEOS groups are depicted as brown lines inside the red circle. The red “X” indicates the failure to form a fully crosslinked network. TEOS can react with itself in the presence of moisture and the Sn(II) catalyst, leading to aggregate formation, which is shown in c at a stoichiometric ratio of $r = 20$. This illustration is not meant to imply that the aggregates pack perfectly together. The size of PDMS chains relative to TEOS crosslinkers is not to scale, but the quantities of each are to scale with respect to r 33

Figure 2.8 – Gel Fraction, w_{gel} , plotted as a function of the stoichiometric ratio, r , prepared in the Vinyl/TDSS systems (a) and Silanol/TEOS systems (b). Molecular weights prior to crosslinking are shown as colors that change from violet to red with increasing molecular weight. Insets show zoomed in regions of low r -values. 34

Figure 2.9 – Gel fraction of Sylgard 184 samples as a function of the Curing Agent to Base (C/B) mass ratio. The top abscissa shows the B/C ratio, where B/C=10:1 is the recommended formula in the instructions for the Sylgard 184 kit. The bottom abscissa is the inverse of the top, <i>i.e.</i> , the C/B ratio, to demonstrate visual similarity to the model systems with increasing amounts of crosslinker from left to right.	34
Figure 2.10 – Mass fraction of polymer (filled symbols) and crosslinker (open symbols) for the vinyl/TDSS system (a) and the silanol/TEOS system (b) plotted as a function of the stoichiometric ratio.	38
Figure 2.11 – Gel fraction plotted as a function of mass fraction of crosslinker for the vinyl/TDSS systems (a) and the silanol/TEOS systems (b).....	39
Figure 2.12 – Scanning electron microscopy (SEM) images of cross-sections of Silanol/TEOS PDMS samples of $r = 1.5$ and $r = 40$ in a and b, respectively.	41
Figure 2.13 – Digital photographs demonstrating the macroscopic (mm length scale) topographical wrinkles at the air interface in certain Silanol/TEOS systems with high TEOS loading and low, 6 kDa molecular weights. Figures a and b correspond to $r = 12$ and c and d correspond to $r = 20$. The tick marks in a) are mm spacers.	42
Figure 3.1 – Adapted from Macosko and Benjamin. ¹⁷ Shear storage modulus, G' , plotted as a function of angular frequency, ω , for PDMS weight-average molecular weights of 9.9×10^6 , 2.1×10^6 , 0.95×10^6 , and 0.26×10^6 g/mol. The plateau modulus is extrapolated down to zero frequency from the plateau region in the high frequency portion of the graph.	56
Figure 3.2 – Adapted from Longin <i>et al.</i> ¹⁹ Zero-shear viscosity, η_0 , plotted as a function of weight-averaged molecular weight. Data was compiled by Longin <i>et al.</i> ¹⁹ and normalized for temperature differences.....	58
Figure 3.3 – Adapted from Zhong <i>et al.</i> ¹⁵ In a), loops of the first (1°), second (2°), and third (3°) order are depicted in columns from left to right for 3- and 4-functional crosslinkers on the top and bottom rows, respectively. Nomenclature of $n_{x,y}$ refers to x -order loop with y -functionality crosslinker. In b), elastic effectiveness, ϵ , of chains within loops is plotted as a function of the loop order, l , for 3- (blue) and 4- (red) functional crosslinkers.....	59
Figure 3.4 – Illustration of topological network parameters calculated from the Miller-Macosko model. Elastically effective chains are shown in green and pendant chains, as either dangling ends or loops, are shown in red. Trapped entanglements occur when all four ends of the two entangled chains are covalently bound to elastically effective crosslinkers. Temporary entanglements occur with dangling ends and can disentangle. Molecular weight between elastically effective chemical crosslinks, M_{CL} , is shown as the black line with arrows at both ends. Crosslinker sites that have reacted are depicted as cyan lines inside light blue circles. Unreacted crosslinker sites are shown as navy blue lines inside the light blue circles. Effective	

crosslinker functionality, f_{eff} , is given for each crosslinker. Unreacted polymer end-groups are depicted as cyan ellipses. 62

Figure 3.5 – Gel fraction as a function of stoichiometric ratio, r , for molecular weights ranging from 6 (violet) to 117 (red) kDa. 68

Figure 3.6 – Extent of reaction, p , plotted as a function of stoichiometric ratio, r , on a semi-log scale. The black stars are extents of reaction calculated from data reported by Patel *et al.*²⁸ In their study, only optimal stoichiometric ratios were reported, between values of $r = 1$ and $r = 2$, for a variety of molecular weights between 2.5 and 58 kDa..... 69

Figure 3.7 – Effective crosslinker functionality, f_{eff} , plotted as a function of stoichiometric ratio, r , and gel fraction, w_{gel} , in a and b, respectively. The stoichiometric ratio, r , increases in a clockwise fashion, depicted by the arrow in the bottom left corner of b. 70

Figure 3.8 – Gel fractions, w_{gel} , (filled symbols, solid lines), elastic fractions, w_{el} , (open symbols, dashed lines) and pendant fractions, w_{pen} , (open symbols with “+” sign, dotted lines) are plotted as a function of stoichiometric ratio, r , for molecular weights prior to crosslinking of 6 (violet), 17 (blue), 28 (cyan), 50 (green), 63 (orange), and 117 kDa (red) in a) through f), respectively. 73

Figure 3.9 – Elastic (top row) and pendant (bottom row) fractions shown as a function of stoichiometric ratio, r , (left column) and gel fraction, w_{gel} , (right column) in a) through d). The curved lines in b) and d) are only to guide the eye. 74

Figure 3.10 – Elastic, w_{el} , (filled symbols) and pendant, w_{pen} (open symbols) fractions plotted as a function of the gel fraction for all molecular weights. The $y = x$ line represents the sum of the elastic and pendant fractions to equal the gel fraction, according to Equation (3.11). The $y = x/2$ dashed line represents the line of symmetry for the elastic and pendant fractions. The gray solid lines are guides to the eye. 76

Figure 3.11 – Density of elastically effective chains, ν , (mol/m^3) plotted as a function of stoichiometric ratio, r , and gel fraction in a and b, respectively. The stoichiometric ratio, r , increases in a clockwise fashion, as depicted by the arrow in the bottom right corner of b... 77

Figure 3.12 – Density of elastically effective chains, ν , (mol/m^3) plotted as a function of effective functionality of the crosslinker molecule, f_{eff} , for various molecular weights of PDMS. The stoichiometric ratio, r , increases in a counter clockwise fashion, depicted by the arrow in the bottom right corner. The numerical labels indicate r_{opt} 78

Figure 3.13 – Chain Extension shown by the three blue chains that are connected by two 2-functional crosslinkers ($f_{eff} = 2$). This has the effect of extending the molecular weight between elastically effective chemical crosslinking junctions to $M_{CL,MM} = 3M_n$ 79

Figure 3.14 – Molecular weight between elastically effective chemical crosslinks, $M_{CL,MM}$, plotted as a function of stoichiometric ratio, r , and sol fraction, w_{sol} , in a) and b), respectively. $M_{CL,MM}$ normalized by number-averaged molecular weight, M_n , is plotted as a function of stoichiometric ratio, r , and sol fraction, w_{sol} , in c and d, respectively. Black arrows in b and d indicate increasing stoichiometric ratios in the counter clockwise direction. 80

Figure 3.15 – Molecular weight between elastically effective chemical crosslinks, $M_{CL,MM}$, plotted as a function of the effective crosslinker functionality, f_{eff} , and the density of elastic chains, ν in a and b, respectively. $M_{CL,MM}$ normalized by M_n is plotted against the same variables in c and d, respectively. The colored and black curves are guides to the eye in a and c. The black arrows in b and d indicate counter clockwise directionality for increasing stoichiometric ratios..... 83

Figure 3.16 – Elastic (top row) and pendant (bottom row) fractions plotted as a function of effective functionality (left column) and molecular weight between elastically effective chemical crosslinks (right column). The black arrows indicate the directionality for increasing stoichiometric ratios. The black arrows in a and d indicate counter-clockwise directionality for increasing stoichiometric ratios while clockwise directionality is shown in b and c..... 85

Figure 3.17 – Entanglement trapping factor, T_e , plotted as a function of stoichiometric ratio, r , in a and as a function of gel fraction, w_{gel} , in b. 87

Figure 3.18 – Entanglement trapping factor, T_e , plotted as a function of the elastic fraction w_{el} , in a and the pendant fraction, w_{pen} , in b The inset, c, shows the entanglement trapping factor as a function of pendant fraction normalized by elastic fraction. 88

Figure 4.1 – Adapted from Rus and Tolley.¹ The range of Young’s modulus values for a variety of biological (blue) and engineered (red) materials. The green region corresponds to silicone elastomers prepared and studied in this dissertation. 95

Figure 4.2 – Adapted from Macosko and Benjamin.¹⁸ Shear storage modulus, G' , plotted as a function of angular frequency, ω , for PDMS weight-average molecular weights of 9.9×10^6 , 2.1×10^6 , 0.95×10^6 , and 0.26×10^6 g/mol. The plateau modulus is extrapolated down to zero frequency from the plateau region in the high frequency portion of the graph. 98

Figure 4.3 – Adapted from the RSA-G2 Solids Analyzer Brochure from TA Instruments.⁴⁰ For elastic materials, when oscillatory stress is applied, the strain is perfectly in phase (*i.e.*, the phase angle, $\delta = 0^\circ$) as shown in the left plot in a. In purely viscous materials, the strain lags the stress by a phase angle of $\delta = 90^\circ$ (right, a). In b, polymers exhibit viscoelastic behavior, where the lag between stress and strain is somewhere in between the two ideal elastic and viscous cases. The complex modulus, E^* , is the vector sum of the storage modulus, E' , and loss modulus, E'' , which are related to the phase angle according to the equations in the figure. The phase angle, δ , is often reported as the loss tangent, $\tan(\delta)$, which is defined as the ratio of loss modulus to storage modulus, E''/E' 105

Figure 4.4 – Adapted from the RSA-G2 Solids Analyzer Brochure from TA Instruments.⁴⁰ Typical plot of storage and loss moduli, E' and E'' , respectively for a viscoelastic polymer as a function of frequency of applied strain. The inset demonstrates a constant strain amplitude applied at an increasing frequency with over the time of the experiment. The frequencies used in this dissertation were such that the rubbery plateau region of PDMS was investigated, which does not correspond to those in this example. 106

Figure 4.5 – ASTM-D412 Type D⁴¹ mold for performing tensile stress-strain experiments on silicone elastomers. Units are in mm. Depth of mold is ~1.5 mm..... 108

Figure 4.6 – Gel fraction plotted as a function of stoichiometric ratio, r , for the Vinyl/TDSS system (a) and the Silanol/TEOS system (b) for various molecular weights of PDMS prior to crosslinking. The insets show the region zoomed into low stoichiometric ratios. 111

Figure 4.7 – Dynamic mechanical properties at an angular frequency of 1 rad/s of model PDMS systems plotted as a function of stoichiometric ratios for constant molecular weight series. Mechanical properties at an angular frequency of $\omega = 1$ rad/s for all model PDMS samples prepared in this investigation are plotted as a function of the stoichiometric ratio, r . Plots a, b, and c show the storage modulus, loss modulus, and the loss tangent, respectively, for vinyl-terminated PDMS networks. Plots d, e, and f show the storage modulus, loss modulus, and the loss tangent, respectively, for silanol-terminated PDMS networks. 112

Figure 4.8 – Dynamic mechanical properties at an angular frequency of 1 rad/s of model PDMS systems plotted as a function of molecular weight for constant stoichiometric ratio series. Storage modulus is plotted in a and d, loss modulus is plotted in b and e and $\tan(\delta)$ is plotted in c and f as a function of molecular weight prior to crosslinking for the Vinyl/TDSS system in plots a, b, c and the Silanol/TEOS system in plots d, e, f for various stoichiometric ratios. The legends are the same for plots a, b, and c in the vinyl system and for plots d, e, and f in the silanol system. Samples were extracted prior to testing. 115

Figure 4.9 – Dynamic mechanical properties of Sylgard 184 commercial PDMS at an angular frequency of $\omega = 1$ rad/s. In a and b, the storage modulus (blue squares, left ordinates), loss modulus (red circles, left ordinates), and $\tan(\delta)$ (green triangles, right ordinates), prior to (filled symbols, solid lines) and after (open symbols, dashed lines) Soxhlet extraction are plotted as a function of the B/C ratio and sol fraction, respectively. The percent change in storage modulus (blue squares), loss modulus (red circles) and loss tangent (green diamonds) is plotted as a function of stoichiometric ratio in c and sol fraction in d. The inset, shows a zoomed in region of d. The percent change in mechanical properties is defined as the quantity of value post-extraction minus the value pre-extraction divided by the value pre-extraction. Thus, negative percent changes correspond to smaller values post-extraction. The data labels in d correspond to B/C ratios and align vertically with the data in b. 118

Figure 4.10 - Mechanical properties vs. angular frequency curves were fit with power-law functions according to $y = A\omega^b$, as shown in Figure A4.2 in the Appendix. The slopes of the

curves, b , are plotted for the storage (blue squares) and loss (red circles) moduli pre-extraction (filled symbols, solid lines) and post-extraction (open symbols, dashed lines) as a function of stoichiometric ratio and sol fraction in plots a and b, respectively. The legend is the same for a) and b). In plots c and d, the percent change in the slope as a result of extraction is plotted for storage (blue square) and loss (red circle) moduli as a function of B/C ratio and sol fraction, respectively. The legend is the same for plots c and d. Labels in plots b and d correspond to B/C values..... 123

Figure 4.11 – Plots of storage modulus, loss modulus, and $\text{Tan}(\delta)$ in plots a, b, and c, respectively, at an angular frequency of $\omega = 1$ rad/s for post-extraction samples as a function of sol fraction for all model networks and Sylgard 184 samples tested..... 125

Figure 4.12 – Comparison of all dynamic mechanical properties for samples all model PDMS and Sylgard 184 samples post-extraction. $\text{Tan}(\delta)$, is plotted against the storage modulus in a, and loss modulus in b. The loss modulus is plotted as a function of the storage modulus in c. Insets show digital photographs demonstrating the flexibility of Vinyl/TDSS systems of 117 kDa (top) and 6 kDa (bottom). SEM images of 18 kDa PDMS from the Silanol/TEOS system at stoichiometric ratios of $r = 40$ and $r = 1.5$ are shown in d and e, respectively. All mechanical data is taken at an angular frequency of $\omega = 1$ rad/s. Gray lines are to guide the eye according to all model PDMS (*i.e.*, particle-free samples)..... 127

Figure 4.13 – Molecular weight between effective crosslinks according to the affine model, M_{Aff} , plotted as a function of stoichiometric ratio for the Vinyl/TDSS system in plot a and the Silanol/TEOS system in plot b..... 130

Figure 4.14 – Plots a, b, and c show the storage modulus, loss modulus, and the loss tangent, respectively, as a function of the elastic fraction. Plots d, e, and f show the same properties, respectively, as a function of the pendant fraction. Dynamic mechanical properties are reported at an angular frequency of 1 rad/s for post extraction samples..... 131

Figure 4.15 – Plots a, b, and c show the storage modulus, loss modulus, and the loss tangent, respectively, as a function of effective crosslinker functionality. Plots d, e, and f show the same properties, respectively, as a function of entanglement trapping factor. Dynamic mechanical properties are reported at an angular frequency of 1 rad/s for post extraction samples. Black curve demonstrates direction of increasing stoichiometric ratio. 133

Figure 4.16 – Molecular weights between effective crosslinks as calculated from the affine model, M_{Aff} , and from the phantom model, M_{Ph} , are plotted as a function of the molecular weight between elastically effective chemical crosslinks according to the Miller-Macosko model, $M_{\text{CL,MM}}$, in plots a and c, respectively. The value from the Miller-Macosko model is normalized by the affine and phantom values in plots b and d, respectively, and plotted as a function of the stoichiometric ratio. All data shown is for the Vinyl/TDSS system after extraction..... 135

Figure 4.17 – Schematic illustrating the different values of molecular weight between crosslinks calculated from the affine, M_{Aff} , phantom, M_{Ph} , and Miller-Macosko, $M_{CL,MM}$, models. Chemical crosslink junctions are depicted as light blue circles with cyan lines. ... 136

Figure 4.18 – Stress-strain responses for pre-extraction Sylgard 184 samples. In a), the engineering stress-engineering strain curves for 4 different B/C ratios (5:1 in red, 10:1 in blue, 20:1 in green, and 38:1 in orange) at 3 trials each (solid, dashed, and dotted lines). In b) the data have been converted to true stress-true strain curves for the same samples. Insets c) and d) show the zoomed in regions of 10% strain, the slopes of which are used to determine Young’s modulus. A strain rate of 5 mm/min was used for all samples. 138

Figure 4.19 – Ultimate properties of Sylgard 184 samples. Ultimate stress (MPa) is shown on the left ordinate as blue circles and is plotted as a function of the Young’s modulus as determined from the slope in the small-strain (< 10%) region. Ultimate strain is given as red squares on the right ordinate and is also plotted as a function of Young’s modulus. Values of Young’s modulus, ultimate stress, and ultimate strain determined from the engineering stress-strain curves are given as filled symbols with connected by dotted lines. The same values determined from the true stress-strain curve are shown as open symbols with dashed lines. 140

Figure 4.20 – Comparison of Young’s modulus from stress-strain experiments and storage modulus from dynamic experiments. The Young’s modulus as determined from the engineering and true stress-strain curves are shown in orange pentagons and green diamonds, respectively. Stress-strain tests were performed at a strain rate of 5 mm/min. Dynamic storage modulus values are given at a frequency of $\omega = 1$ rad/s. All data were acquired on samples prior to Soxhlet extraction. Linear best fit curve equations are given for engineering and true data in orange and green, respectively. The equation for the linear best fit curve for Young’s modulus determined from engineering stress-strain is $y = 0.723x - 0.046$ (orange dashed line), and that for true stress-strain is $y = 0.806x - 0.051$ (green dashed line). 141

Figure 5.1 – a) A water droplet spreads out and fully wets a cleaned, polished silicon wafer. A defect or dust particle is present in the top-right where water does not fully spread. The bottom horizontal dimension of the wafer is about 1 inch. b) Water droplets beading up and minimally wetting a *colocasia* leaf, which is commonly referred to as an “elephant ear” plant. The leaves are about 3 feet in length and 1 foot in width. Digital photographs were taken by the author of this dissertation. 155

Figure 5.2 – Diagram depicting different forces acting on species in the bulk and near the surface.³ 156

Figure 5.3 – Various wetting states between a liquid droplet and a substrate. a) Depicts the ideal case with an atomically flat substrate. Surface roughness is depicted in b) where the droplet is in the Wenzel state. When the roughness aspect ratio is increased, the droplet enters

the Cassie-Baxter state, shown in c). This figure is reproduced from Genzer and Efimenko.¹¹
..... 160

Figure 5.4 – Reproduced from Cao and Dobrynin.¹⁸ Three different systems are depicted. In system a), a solid, rigid substrate is described well by Young’s law. For two immiscible liquids, as shown in b), Neumann’s triangle accurately describes the system. For a soft deformable substrate, such as a gel, the system is complex and the subject of on-going research.
..... 161

Figure 5.5 – Reproduced from Kim, J., Chaudhury, M., and Owen, M. J.⁵² Schematic illustration of the cross-sectional section of PDMS after exposed to surface treatment. 164

Figure 5.6 – Publications and patents awarded per year that mention “Sylgard 184” (red), “Sylgard 184 and Microfluidic” (blue), and “Sylgard 184 and Bio” (green) plotted as a function of year. Data acquired from Google Scholar on April 28, 2017..... 165

Figure 5.7 – Gel fraction as a function of stoichiometric ratio, r , for molecular weights ranging from 6 (violet) to 117 (red) kDa in the Vinyl/TDSS system plotted in a. Gel fraction is plotted against the curing agent/base ratio (bottom abscissa) and against the base/curing agent (B/C) ratio (top abscissa) for Sylgard 184 (b)..... 168

Figure 5.8 – Representative result of droplet image analysis performed with Matlab code. The raw data is a side-view image of the droplet on the surface with a small amount of droplet reflection visible on the surface below the droplet. The code returns the contact time (based on the file naming scheme used in saving images from the goniometer) between water and the substrate along with droplet parameters given in the top left of the image. The tick labels on the left and bottom axes in the image represent pixels. The green horizontal line on the needle is the scale factor of pixels to mm. The green dotted line is the boundary of the droplet as determined by a built-in Matlab function. The red line is the ellipse that has been fitted to the droplet boundary. Yellow “x” marks indicate the user-defined 3-phase contact points. The yellow dashed line connects the two 3-phase contact points and serves as the diameter of the interfacial circular area between water and the substrate. The blue lines indicate the lines tangent to the ellipse at the 3-phase contact points. The slope of the tangent lines is used to calculate the contact angle, θ , which is shown in yellow as the angle between the water-PDMS interface and the blue tangent lines. Full codes are given in the Appendix..... 171

Figure 5.9 – Schematic of a water droplet in the shape of an oblate spheroidal cap showing variables used in calculating droplet parameters. The two major radii that are parallel to the substrate are given by a while the minor radius that is perpendicular to the substrate is given by b . The distance between the substrate and the major diameter of the drop is given by y_d . The total drop height, h_d , is the sum of the minor radius, b , and y_d . The radius of the circular interfacial area between water and PDMS, referred to as the Base Area, A_b , is given by r . The interfacial area between water and air is referred to as the surface area, A_s 172

Figure 5.10 – The negative cosine of the contact angle, $-\cos(\theta)$ (left ordinates), and contact angle, θ (right ordinates) are plotted in the top row (a and b) as a function of contact time, t , between water droplet and PDMS substrate pre- (left) and post-extraction (right) for the 28 kDa Vinyl/TDSS system of various stoichiometric ratios, r . The base area, A_b is given in the bottom (c and d). 177

Figure 5.11 – The negative cosine of the contact angle, $-\cos(\theta)$ (left ordinates), and contact angle, θ (right ordinates) are plotted in the top row (a and b) as a function of contact time, t , between water droplet and PDMS substrate pre- (left) and post-extraction (right) for the Sylgard 184 system of various B/C ratios. The base area, A_b is given in the bottom (c and d). 178

Figure 5.12 – Post-extraction contact angle plotted as a function of pre-extraction contact angle for 6, 17, 28, 63, and 117 kDa model PDMS systems in a) through e), respectively. The diagonal solid black line represents $y = x$. Data to the left the $y = x$ line occur when post-extraction contact angle is greater than pre-extraction contact angle. The opposite occurs for data to the right of the $y = x$ line. Stoichiometric ratio values are given by different shapes according to the legend. The contact time at which each data point was acquired, both pre-extraction and post-extraction is categorized into 7 different colors according to the visible light spectrum. Short times correspond to violet symbols while long times correspond to red symbols. 181

Figure 5.13 – Post-extraction contact angle plotted as a function of pre-extraction contact angle for the Sylgard 184 system. The diagonal solid black dashed line represents $y = x$. Data to the left the $y = x$ line occur when post-extraction contact angle is greater than pre-extraction contact angle. The opposite occurs for data to the right of the $y = x$ line. In plot a), the colors are assigned to B/C ratios while in plot b), the colors change according to the contact time. In b), B/C ratios are given by different shapes according to the legend. The contact time at which each data point was acquired, both pre-extraction and post-extraction is categorized into 8 different colors according to the visible light spectrum. Short times correspond to violet symbols while long times correspond to red symbols. 182

Figure 5.14 – Initial (open symbols, dashed lines) and final (filled symbols, solid lines) water contact angles plotted as a function of stoichiometric ratio for the 6, 17, 28, 63, and 117 kDa model PDMS systems in plots a through e, respectively. Pre-extraction data are blue squares and post-extraction data are red circles. The gaps between initial and final values are shaded blue and red for pre-extraction and post-extraction data, respectively. 184

Figure 5.15 – Initial (open symbols, dashed lines) and final (filled symbols, lines) water contact angles plotted as a function of base/curing agent ratio for the Sylgard 184 system. Pre-extraction data are blue squares and post-extraction data are red circles. The gaps between initial and final values are shaded blue and red for pre-extraction and post-extraction, respectively. 185

Figure 5.16 – Absolute change (left ordinate, solid lines, filled symbols) and percent change (right ordinate, dashed lines, open symbols) in contact angle (top row) and base area (bottom row) plotted as a function of stoichiometric ratio (left column) and sol fraction (right column) for the 28 kDa model PDMS system. Pre-extraction data are blue squares and post-extraction data are red circles. Numerical labels correspond to stoichiometry ratios. 187

Figure 5.17 – The absolute change in $\cos(\theta)$ (left ordinates) and θ (right ordinates) with respect to contact time are given in plots a) and c). In plots b) and d), the absolute change (left ordinate, solid lines, filled symbols) and percent change (right ordinate, dashed lines, open symbols) in base area are depicted. All variables are plotted as a function of B/C ratio (left column) and sol fraction (right column) for the Sylgard 184 system. Pre-extraction data are blue squares and post-extraction data are red circles. Numerical labels in plots c) and d) correspond to B/C ratios..... 188

Figure 5.18 – Change in $-\cos(\theta)$ plotted as a function of change in base area in plot a) and change in volume in plot b) for the 28 kDa model PDMS system. Pre-extraction data are blue squares and post-extraction data are red circles. The numerical labels on the data points are the stoichiometric ratio values. 190

Figure 5.19 – Absolute change in contact angle plotted as a function of absolute change in base area in plot a) and absolute change in volume in plot b) for the Sylgard 184 system. Pre-extraction data are blue squares and post-extraction data are red circles. The numerical labels on the data points are the B/C values..... 190

Figure 5.20 – Change in water contact angle ($\theta_{\text{Initial}} - \theta_{\text{Final}}$) and change in base area ($A_{\text{b,Final}} - A_{\text{b,Initial}}$) plotted in the top and bottom rows, respectively, as a function of sol fraction. Left column shows pre-extraction data. Right column shows post-extraction data..... 192

Figure 5.21 – Change in $\cos(\theta)$ as a function of change in base area, with respect to contact time between the water droplet and substrate. Data for pre-extraction samples are given in plot a), and data for post-extraction samples are given in plot b). The straight lines in plot a) are linear best-fit lines. The black line has an equation of $y = 0.202x + 0.117$ with an $R^2 = 0.98$. This is a fit for Sylgard 184 data only. A fit for all model PDMS samples is given by the green line and has the form $y = 0.137x + .071$ with an $R^2 = 0.92$. The post-extraction data do not exhibit a linear trend. 193

Figure 5.22 – The value of $-\cos(\theta)$ is plotted as a function of the corresponding base area for each stoichiometric ratio at each time interval throughout the course of the experiment for 28 kDa model Vinyl/TDSS PDMS. In plot a), the symbol colors represent different B/C ratios. In plot b), the colors change according to contact time between the droplet and substrate. Plots a) and b) show pre-extracted data and plots c) and d) show post-extracted data. Zoomed in post-extraction data are given in Figure A5.14 in the Appendix..... 195

Figure 5.23 – The value of $-\cos(\theta)$ is plotted as a function of the corresponding base area for each B/C ratio at each time interval throughout the course of the experiment for Sylgard 184. In plot a), the symbol colors represent different B/C ratios. In plot b), the colors change according to contact time between the droplet and substrate. Plots a) and b) show pre-extracted data and plots c) and d) show post-extracted data. Zoomed in post-extraction data are given in Figure A5.27 in the Appendix. 196

Figure 5.24 – The quantity of base area multiplied by the negative $\cos(\theta)$ is plotted as a function of contact time between the drop and substrate for pre-extraction data and post-extraction data in plots a) and b), respectively for 28 kDa model PDMS samples of various stoichiometric ratios. Data are fit with a linear best-fit line whose slopes are given as a function of the stoichiometric ratio, r , in the inset 198

Figure 5.25 – The quantity of base area multiplied by the negative $\cos(\theta)$ is plotted as a function of contact time between the drop and substrate for pre-extraction data and post-extraction data in plots a) and b), respectively for Sylgard 184 samples of various B/C ratios. Data are fit with a linear best-fit line whose slopes are given as a function of B/C ratio in the inset. 198

Figure 5.26 – In plots a) and b), the post-extraction value of $-A_b\cos(\theta)$ is plotted as a function of the same value for pre-extraction samples. The colors in plot a) correspond to different stoichiometric ratios. The data are fitted with a linear best-fit line. In plot b), the colors corresponded to the amount of contact time. Generally, the amount of contact time between the water droplet and the substrate increases downward to the left. In plot c), the slope of the data sets in plot a) is given as a function of the stoichiometric ratio. In plot d), a measure of the deviation from the $y = x$, lines in plots a) and b) is given for samples made from each stoichiometric ratio. The equation for deviation from $y = x$ is given in plot d)..... 199

Figure 5.27 – In plots a) and b), the post-extraction value of $-A_b\cos(\theta)$ is plotted as a function of the same value for pre-extraction samples. The colors in plot a) correspond to different B/C ratios. The data are fitted with a linear best-fit line. In plot b), the colors corresponded to the amount of contact time. Generally, the amount of contact time between the water droplet and the substrate increases downward to the left. In plot c), the slope of the data sets in plot a) is given as a function of the B/C ratio. In plot d), a measure of the deviation from the $y = x$, lines in plots a) and b) is given for samples made from each B/C ratio. The equation for deviation from $y = x$ is given in plot d). 200

Figure 5.28 – Change in $\cos(\theta)$ for the pre-extracted (blue squares) and post-extracted (red circles) Sylgard 184 data with respect to contact time between water droplet and the substrate ($\cos(\theta_{\text{Initial}}) - \cos(\theta_{\text{Final}})$) is plotted as a function of the percent change in dynamic mechanical properties resulting from the extraction process. The percent change is defined as $(M_{\text{Post}} - M_{\text{Pre}})/M_{\text{Pre}}$, where M is a dynamic mechanical property evaluated at an angular frequency of $\omega = 1$ rad/s. Plot a) shows the change in storage modulus, E' , plot b) gives the change in the loss

modulus, E'' and plot c) gives the change in $\tan(\delta)$. The linear best-fit-line has the form $y = 0.07x + 0.125$ with an R^2 value of 0.85. Labels are B/C ratios..... 204

Figure 5.29 – Approximation of the wetting ridge height for pre-extraction (blue squares) and post-extraction (red circles) Sylgard 184 samples..... 206

Figure 5.30 – The water contact angle, θ (right ordinates), and $\cos(\theta)$ (left ordinates) are plotted as a function of contact time between the water droplet and the silicone oil-infused Sylgard 184 PDMS substrate for 2.5, 5, and 10% oils in plots a), b), and c), respectively. Pure Sylgard 184 samples at the B/C = 10 ratio with no additional silicone oils are shown as black stars. The D₄ oil is shown as red squares, the 1 kDa oil is shown as blue triangles, the 6 kDa oil is shown as green circles, and the 28 kDa oil is shown as orange diamonds. 208

Figure 5.31 – Schematic illustration depicting the dynamic wetting behavior of water on a PDMS substrate. The droplet starts at some initially high contact angle and small base area. Over time, the drop settles into an equilibrium with a lower contact angle and greater base area. Uncrosslinked polymers, oligomers, and crosslinkers present in PDMS materials prior to extraction can migrate to the water-interface and act like a surfactant, lowering the interfacial energy. After extraction, the system approaches equilibrium much more quickly, when most of the uncrosslinked material has been removed. 209

Figure 6.1 – Elastomers formed solely by chain extension through the combination of hydride- and vinyl-terminated PDMS with a Pt catalyst (a) and corresponding dynamic mechanical properties (b)..... 280

Figure 6.2 – Reproduced from Cai *et al.*¹⁸ Soft PDMS bottle-brush polymers yielding storage modulus values below the entanglement plateau..... 281

Figure 6.3 – Wetting ridge observed on same sample corresponding to mechanical properties given in Figure 6.1. A 6 μ L water droplet was placed on the substrate and allowed to equilibrate for \sim 8 min. Times in upper left correspond to time after droplet removal. It was then removed and the wetting ridge remained visible for up to 3.5 min after droplet removal. The needle in the background has an outer diameter of 0.72 mm. 283

Figure 6.4 – Scheme for endowing silanol-terminated PDMS with functional thiol side-chains at sporadic intervals along the linear chain through chain extension reactions. A primary permanently network could be formed by crosslinking with TEOS (red circles) and a secondary reversible network could be formed by disulfide bonds along the side-chains (blue S-S linkages)..... 285

Figure 6.5 – Thiol-functional (blue circles) and silanol functional (red circles) silica particles for both reversible and permanent covalent attachment to PDMS chains..... 286

LIST OF FIGURES IN APPENDICES

- Figure A2.1** – Molecular weight distributions of samples purchased from Gelest, Inc. using size exclusion chromatography. The data were generated from size exclusion chromatography measurements in tetrahydrofuran with mododisperse polystyrene and poly(methylmethacrylate) standards. 47
- Figure A4.1** – Storage (blue squares) and loss (red circles) moduli shown on the left ordinate and $\tan(\delta)$ (E''/E' , green diamonds) on the right ordinate all plotted as a function of angular frequency. This plot is a representative example of data gathered from dynamic mechanical analysis of PDMS samples. The moduli (E' , E'') are fit with a power law function, as shown in the legend. The exponent value, b , is the slope of the line (black lines) on this plot. 144
- Figure A4.2** – Raw dynamic mechanical data of Sylgard 184 shown for various B/C ratios pre-extraction (left) and post-extraction (right). Storage modulus a) and b), loss modulus c) and d), and loss tangent e) and f) are plotted as a function of angular frequency. 145
- Figure A4.3** – Post-extraction properties (ordinates) plotted as a function of the pre-extraction properties (abscissae) for storage modulus, loss modulus, and $\tan(\delta)$ in the left, middle, and right columns, respectively. The data are plotted on linear scales in the top row and log-log scales in the bottom row. The data are fit with a linear best-fit line whose equation and R^2 value are given in each plot. The black solid line represents no change in properties due to extraction and is thus $y = x$ 147
- Figure A4.4** – Storage modulus at an angular frequency of 1 rad/s plotted against the stoichiometric ratio for the Vinyl/TDSS system on a semi-log scale to visualize differences in maximum storage modulus. 148
- Figure A5.1** – Water contact angle, base area, volume, and surface area of water droplets on glassy polymer substrates are plotted as a function of contact time between the droplet and substrate in parts a), b), c), and d), respectively. All data are fit well with linear best-fit lines. 216
- Figure A5.2** – Water contact angle, θ (top), and base area, A_b (bottom), plotted as a function of contact time, t , between water droplet and PDMS substrate pre- (left) and post-extraction (right) for the model vinyl/hydride system of 6 kDa and various stoichiometric ratios. The symbols are data while the lines are fits using the hyperbolic tangent function..... 217
- Figure A5.3** – Droplet volume (top) and surface area (bottom) plotted as a function of contact time before (left) and after (right) extraction for the 6 kDa system..... 218
- Figure A5.4** – Absolute change (left ordinate, solid lines, filled symbols) and percent change (right ordinate, dashed lines, open symbols) in contact angle (top row) and base area (bottom row) plotted as a function of stoichiometric ratio (left column) and sol fraction (right column)

for the 6 kDa model PDMS system. Pre-extraction data are blue squares and post-extraction data are red circles. Numerical labels correspond to stoichiometry ratios. 219

Figure A5.5 – Absolute change in contact angle plotted as a function of absolute change in base area (a) and absolute change in volume (b) for the 6 kDa model PDMS system. Pre-extraction data are blue squares and post-extraction data are red circles. The numerical labels on the data points are the stoichiometric ratio values. 220

Figure A5.6 – Post-extraction contact angle plotted as a function of pre-extraction contact angle for 6 kDa model PDMS system for stoichiometric ratios of $r = 1, 1.5, 3, \text{ and } 4$ in a) through d), respectively. The diagonal solid black line represents $y = x$. Data to the left the $y = x$ line occur when post-extraction contact angle is greater than pre-extraction contact angle. The opposite occurs for data to the right of the $y = x$ line. Stoichiometric ratio values are given by different shapes according to the legend. The contact time at which each data point was acquired, both pre-extr. and post-extr. is categorized into 7 different colors according to the visible light spectrum. Short times correspond to violet symbols while long times correspond to red symbols. 220

Figure A5.7 – Water contact angle, θ (top), and base area, B (bottom), plotted as a function of contact time, t , between water droplet and PDMS substrate pre- (left) and post-extraction (right) for the model vinyl/hydride system of 17 kDa and various stoichiometric ratios. The symbols are data while the lines are fits using the hyperbolic tangent function..... 221

Figure A5.8 – Droplet volume (top) and surface area (bottom) plotted as a function of contact time before (left) and after (right) extraction for the 17 kDa system..... 222

Figure A5.9 – Absolute change (left ordinate, solid lines, filled symbols) and percent change (right ordinate, dashed lines, open symbols) in contact angle (top row) and base area (bottom row) plotted as a function of stoichiometric ratio (left column) and sol fraction (right column) for the 17 kDa model PDMS system. Pre-extraction data are blue squares and post-extraction data are red circles. Numerical labels correspond to stoichiometry ratios. 223

Figure A5.10 – Absolute change in contact angle plotted as a function of absolute change in base area (a) and absolute change in volume (b) for the 17 kDa model PDMS system. Pre-extraction data are blue squares and post-extraction data are red circles. The numerical labels on the data points are the stoichiometric ratio values. 224

Figure A5.11 – Post-extraction contact angle plotted as a function of pre-extraction contact angle for the 17 kDa model PDMS system for stoichiometric ratios of $r = 1.5, 3, 4, 6, \text{ and } 12$ in a) through e), respectively. The diagonal solid black line represents $y = x$. Data to the left the $y = x$ line occur when post-extraction contact angle is greater than pre-extraction contact angle. The opposite occurs for data to the right of the $y = x$ line. Stoichiometric ratio values are given by different shapes according to the legend. The contact time at which each data point was acquired, both pre-extr. and post-extr. is categorized into 7 different colors according

to the visible light spectrum. Short times correspond to violet symbols while long times correspond to red symbols. 225

Figure A5.12 – Droplet volume (top) and surface area (bottom) plotted as a function of contact time before (left) and after (right) extraction for the 28 kDa system..... 226

Figure A5.13 – Post-extraction contact angle plotted as a function of pre-extraction contact angle for the 28 kDa model PDMS system for stoichiometric ratios of $r = 1.5, 3, 4, 12, \text{ and } 20$ in a) through e), respectively. The diagonal solid black line represents $y = x$. Data to the left the $y = x$ line occur when post-extraction contact angle is greater than pre-extraction contact angle. The opposite occurs for data to the right of the $y = x$ line. Stoichiometric ratio values are given by different shapes according to the legend. The contact time at which each data point was acquired, both pre-extr. and post-extr. is categorized into 7 different colors according to the visible light spectrum. Short times correspond to violet symbols while long times correspond to red symbols. 227

Figure A5.14 – Zoomed in plots from Figure 5.22 provide a more clear picture of the post-extracted $-\cos(\theta)$ data as a function of base area..... 228

Figure A5.15 – Water contact angle, θ (top), and base area, B (bottom), plotted as a function of contact time, t , between water droplet and PDMS substrate pre- (left) and post-extraction (right) for the model vinyl/hydrate system of 63 kDa and various stoichiometric ratios. The symbols are data while the lines are fits using the hyperbolic tangent function..... 229

Figure A5.16 – Droplet volume (top) and surface area (bottom) plotted as a function of contact time before (left) and after (right) extraction for the 63 kDa system..... 230

Figure A5.17 – Absolute change (left ordinate, solid lines, filled symbols) and percent change (right ordinate, dashed lines, open symbols) in contact angle (top row) and base area (bottom row) plotted as a function of stoichiometric ratio (left column) and sol fraction (right column) for the 63 kDa model PDMS system. Pre-extraction data are blue squares and post-extraction data are red circles. Numerical labels correspond to stoichiometry ratios. 231

Figure A5.18 – Absolute change in contact angle plotted as a function of absolute change in base area (a) and absolute change in volume (b) for the 63 kDa model PDMS system. Pre-extraction data are blue squares and post-extraction data are red circles. The numerical labels on the data points are the stoichiometric ratio values. 232

Figure A5.19 – Post-extraction contact angle plotted as a function of pre-extraction contact angle for the 63 kDa model PDMS system for stoichiometric ratios of $r = 3, 4, 6, 12, \text{ and } 20$ in a) through e), respectively. The diagonal solid black line represents $y = x$. Data to the left the $y = x$ line occur when post-extraction contact angle is greater than pre-extraction contact angle. The opposite occurs for data to the right of the $y = x$ line. Stoichiometric ratio values are given by different shapes according to the legend. The contact time at which each data

point was acquired, both pre-extr. and post-extr. is categorized into 7 different colors according to the visible light spectrum. Short times correspond to violet symbols while long times correspond to red symbols. 233

Figure A5.20 – Water contact angle, θ (top), and base area, B (bottom), plotted as a function of contact time, t , between water droplet and PDMS substrate pre- (left) and post-extraction (right) for the model vinyl/hydrate system of 117 kDa and various stoichiometric ratios. The symbols are data while the lines are fits using the hyperbolic tangent function..... 234

Figure A5.21 – Droplet volume (top) and surface area (bottom) plotted as a function of contact time before (left) and after (right) extraction for the 117 kDa system..... 235

Figure A5.22 – Absolute change (left ordinate, solid lines, filled symbols) and percent change (right ordinate, dashed lines, open symbols) in contact angle (top row) and base area (bottom row) plotted as a function of stoichiometric ratio (left column) and sol fraction (right column) for the 117 kDa model PDMS system. Pre-extraction data are blue squares and post-extraction data are red circles. Numerical labels correspond to stoichiometry ratios. 236

Figure A5.23 – Absolute change in contact angle plotted as a function of absolute change in base area (a) and absolute change in volume (b) for the 117 kDa model PDMS system. Pre-extraction data are blue squares and post-extraction data are red circles. The numerical labels on the data points are the stoichiometric ratio values. 237

Figure A5.24 – Post-extraction contact angle plotted as a function of pre-extraction contact angle for the 117 kDa model PDMS system for stoichiometric ratios of $r = 3, 4, 6, 12, \text{ and } 20$ in a) through e), respectively. The diagonal solid black line represents $y = x$. Data to the left the $y = x$ line occur when post-extraction contact angle is greater than pre-extraction contact angle. The opposite occurs for data to the right of the $y = x$ line. Stoichiometric ratio values are given by different shapes according to the legend. The contact time at which each data point was acquired, both pre-extr. and post-extr. is categorized into 7 different colors according to the visible light spectrum. Short times correspond to violet symbols while long times correspond to red symbols. 238

Figure A5.25 – Droplet volume (top) and surface area (bottom) plotted as a function of contact time before (left) and after (right) extraction for the Sylgard 184 system..... 239

Figure A5.26 – Post-extraction contact angle plotted as a function of pre-extraction contact angle for the Sylgard system for Base/Curing Agent ratios of $B/C = 2, 5, 10, 15, 20, 27, 38, \text{ and } 48$ in a) through h), respectively. The diagonal solid black line represents $y = x$. Data to the left the $y = x$ line occur when post-extraction contact angle is greater than pre-extraction contact angle. The opposite occurs for data to the right of the $y = x$ line. Stoichiometric ratio values are given by different shapes according to the legend. The contact time at which each data point was acquired, both pre-extr. and post-extr. is categorized into 8 different colors

according to the visible light spectrum. Short times correspond to violet symbols while long times correspond to red symbols..... 240

Figure A5.27 – Zoomed in plots from Figure 5.23 provide a more clear picture of the post-extracted $-\cos(\theta)$ data as a function of base area..... 241

Figure A5.28 – Approximate height of the wetting ridge resulting from the vertical component of surface tension of the water droplet at the 3-phase contact line. 241

Figure A5.29 – Approximate wetting ridge height of Sylgard 184 samples at the final contact time for pre- and post-extracted samples in blue and red, respectively..... 242

Figure A5.30 – Water contact angle (left column) and base area (right column) plotted as a function of contact time between water droplet and the substrate. Substrates are B/C = 10 Sylgard 184 samples with various mass fractions of silicone oils of various molecular weights. Plots a) and e) are for the cyclic siloxane oligomer, D₄. Plots b) and f) show data for samples filled with a linear trimethyl-terminated PDMS silicone oil of molecular weight 1 kDa and viscosity of 10 cSt. Plots c) and g) show data for a 6 kDa and 100 cSt. silicone oil. Plots d) and h) show data for 28 kDa and 1000 cSt. silicone oil. 243

Figure A5.31 - Changes in interfacial energy between water droplet and silicone-oil-infused PDMS substrates as a function of contact time (left columns). The oil is a cyclic, D₄, with ~0.3 kDa and 2.3 cst. Various mass fractions of oils are shown. The interfacial energy terms are plotted as a function of base area in the right columns..... 244

Figure A5.32 - Changes in interfacial energy between water droplet and silicone-oil-infused PDMS substrates as a function of contact time (left columns). The oil is 1 kDa and 10 cst. Various mass fractions of oils are shown. The interfacial energy terms are plotted as a function of base area in the right columns. 245

Figure A5.33 – Changes in interfacial energy between water droplet and silicone-oil-infused PDMS substrates as a function of contact time (left columns). The oil is 6 kDa and 100 cst. Various mass fractions of oils are shown. The interfacial energy terms are plotted as a function of base area in the right columns. 246

Figure A5.34 – Changes in interfacial energy between water droplet and silicone-oil-infused PDMS substrates as a function of contact time (left columns). The oil is 28 kDa and 1000 cst. Various mass fractions of oils are shown. The interfacial energy terms are plotted as a function of base area in the right columns. 247

Figure A5.35 – Changes in interfacial energy between water droplet and silicone-oil-infused PDMS substrates as a function of contact time (left columns). The mass fraction of oil is constant at 2.5% and the oils change according to the legend. The interfacial energy terms are plotted as a function of base area in the right columns..... 248

Figure A5.36 – Changes in interfacial energy between water droplet and silicone-oil-infused PDMS substrates as a function of contact time (left columns). The mass fraction of oil is constant at 5% and the oils change according to the legend. The interfacial energy terms are plotted as a function of base area in the right columns..... 249

Figure A5.37 – Changes in interfacial energy between water droplet and silicone-oil-infused PDMS substrates as a function of contact time (left columns). The mass fraction of oil is constant at 10% and the oils change according to the legend. The interfacial energy terms are plotted as a function of base area in the right columns..... 250

CHAPTER 1: Introduction & Dissertation Scope

Introduction

Poly(dimethylsiloxane) (PDMS) is the most common polysiloxane and is frequently referred to as “silicone” oils, fluids, materials, additives, *etc.*, depending on the application. PDMS has found wide use in many industrial applications ranging from lubricants, hydraulic fluids, and electrical insulating materials to foam control agents in food, pulp and paper, textiles and cleaning supplies industries.^{1,2} It also performs well as sealants, caulking agents, and paint additives for water- and bio-repellant coatings.^{1,2} Additionally, in its crosslinked form, it serves as molds and elastomers and due to its bio-repellency, it performs well as medical devices.^{1,2} In 2015, 391,000 metric tons of silicone elastomers were produced, and that number is expected to grow to 558,000 metric tons in 2021.³ This is clearly an important industrial polymer.

What Makes PDMS Unique and Versatile?

For one polymer type to be used in such a broad array of applications is very impressive. The reason PDMS is so versatile is due to its chemical structure. Unlike many common polymers, PDMS contains both inorganic and organic chemical functionalities. The alternating Si-O-Si (siloxane) inorganic backbone of the polymer is inherently much more flexible than typical C-C (alkane) backbone polymers. This is due to the bonding geometries, which are depicted in Figure 1.1 where in a) PDMS is compared to its hydrocarbon-equivalent, polyisobutylene (PIB) in b). From this diagram, we observe several key findings. First, the bond angles associated with the siloxane backbone are much greater than the alkane bond angles. Additionally, the Si-O bond length is greater than that for C-C bonds and can fluctuate more. Not depicted but still important, the van der Waals radius of the O atom is smaller than that for a CH₂ group.⁴ Together, these properties combine to reduce steric hindrance and yield an incredibly flexible polymer. For these reasons, PDMS has one of the lowest glass transition temperatures of nearly any common polymer ranging from ~ -150°C for short oligomers to ~ -123°C for high molecular weight linear macromolecules.⁵ That being said, the melting

temperature of PDMS is -40°C , which effectively limits its operating range to temperatures greater than that.⁶ Usually copolymers using phenyl or fluorinated side groups are combined with PDMS to lower the melting temperature, but this has the effect of increasing the glass transition temperature.⁶

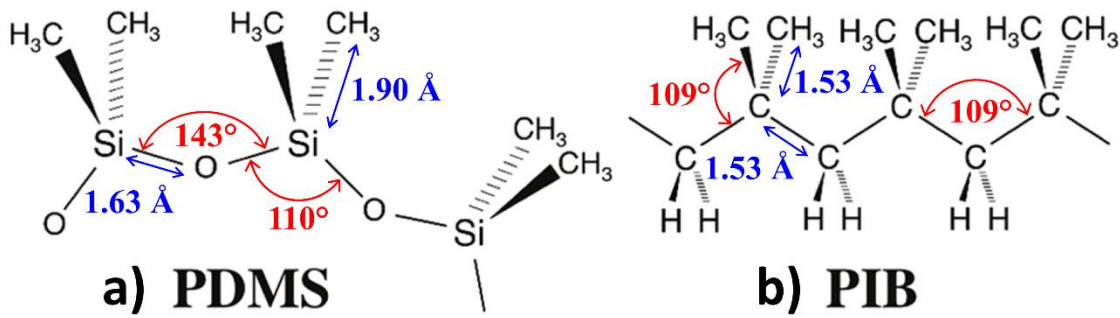


Figure 1.1 – Adapted from Zheng and McCarthy.⁷ Molecular structures of PDMS (a) and poly(isobutylene) (PIB) (b) with accurate representations of bond lengths and angles as calculated using Pauling electronegativity values. Dimensions acquired from the literature.⁷⁻⁹

The aforementioned properties of the PDMS molecule yield greater spacing between dimethyl functional groups on PDMS compared to PIB, which in combination of the attributes of the siloxane bond, results in those groups being able to rotate more freely. The rotational bond energy for the silicon atom in PDMS is only 3.3 kJ/mol while that for carbons in polyethylene is 13.8 kJ/mol.¹⁰ Thus, PDMS has a very low surface tension compared to other common polymers because the methyl groups can reorient to the interface quickly with a minimal energy barrier to rotation. Even when bulkier side-groups have been substituted for methyl groups, the siloxane backbone can still rotate fairly rapidly.^{11,12}

The flexibility of the siloxane backbone has endowed PDMS with the ability to remain elastomeric at cold temperatures due to the bond geometries. However, when operating at high temperatures, the bond energies are what play a key role in making PDMS so versatile. The Si-O bond is fairly polar due to the greater electronegativity differences between Si-O compared to C-C. This provides it with a bond energy greater than both C-C and C-O bond energies, reported as 445 kJ/mol vs. 346 kJ/mol and 358 kJ/mol, respectively.⁶ This provides

for the high thermal stability of PDMS, allowing it to withstand temperatures of 200°C continuously for an entire year without any significant changes in material properties.⁶ One key disadvantage to PDMS over conventional hydrocarbons is its susceptibility to hydrolytic degradation in environments where $\text{pH} < 2.5$ and $\text{pH} > 11.0$.⁶ Nevertheless, the unique combination of inorganic backbone with organic side chains has made PDMS an excellent material in a variety of industrial applications.

Current Research Areas Using PDMS

In addition to many industrial applications, PDMS has enjoyed growing use in numerous research communities as well. PDMS is the flexible material of choice for a variety of applications ranging from microfluidic devices¹³ to biomedical implants.¹⁴ Neural system implants in either the spinal cord or brain, for example, have the potential to help patients suffering from paralysis and/or dementia to regain control of their bodies and minds.^{14,15} In addition to creating synthetic links for the transmission of signals in artificial neural-like materials, flexible synthetic materials have the potential to serve as artificial muscles and actuators in the field of tissue engineering.^{16,17} Artificial muscles can help patients recover from injuries or illnesses, but can also be employed to enhance human performance. Instead of implanting artificial muscles in a body, other research has focused on applying the same principles to the advancement of soft robotics^{18,19} for an entirely new paradigm in what we traditionally conceive of as robots. To make all of the preceding applications possible, materials must be soft and flexible, but also, vitally, electronically conductive for sending and receiving signals. Consequently, research in the area of flexible electronics is also rapidly expanding.^{20,21} PDMS is a promising candidate material in all of these applications.

Pertaining to microfluidics, in the past ~20 years, interdisciplinary research has taken off between the fields of materials science and biology wherein PDMS is used as the material to make microfluidic devices^{22,23} for studying biological phenomena. Micron-sized features are very relevant in the field of biology and can be created using soft lithographic techniques with PDMS.²⁴ Additionally, PDMS in its macromolecular form, *i.e.*, high molecular weight

linear chains, have been found to be biocompatible,^{15,25} with biomedical implants being stable *in vivo* for up to 25 years.²⁶

The formulations for making such a wide array of PDMS materials vary based on the application. Sometimes the formulations are purely chemical-based, and include only polymers and crosslinkers to create super soft materials.²⁷ In other instances, filler particles are incorporated to make composite materials that achieve desired properties such as enhanced mechanical strength or electrical conductivity.²⁸ Many commercial silicones incorporate nanosized filler particles^{29,30} and one of the most commonly used commercial silicones in research settings is Sylgard 184 manufactured by Dow Corning. In microchannel fabrication in particular, quite frequently Sylgard 184 is used rather than pure PDMS due to its commercial availability and to its favorable mechanical properties that readily allow for the creation of micro-scale surface features. The trends in the growing use of Sylgard 184 in both the microfluidic and biological fields are presented in Figure 1.2. Note that the two fields are not mutually exclusive.

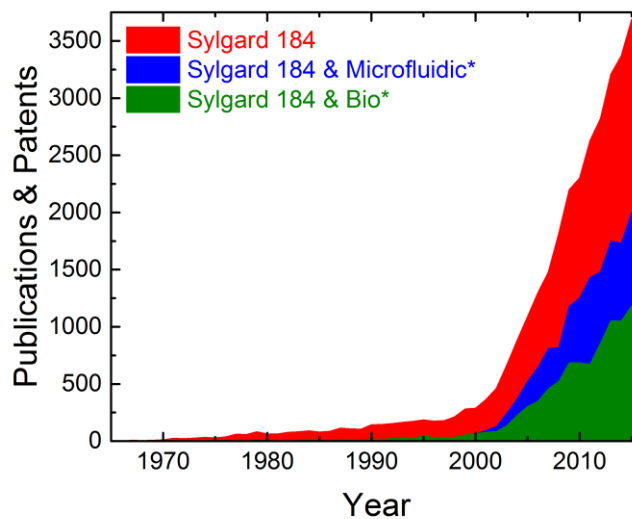


Figure 1.2 – Publications and patents awarded per year that mention “Sylgard 184” (red), “Sylgard 184 and Microfluidic” (blue), and “Sylgard 184 and Bio” (green) plotted as a function of year. Data acquired from Google Scholar on April 28, 2017.

The use of Sylgard 184 is widespread and has enabled numerous advances. It has been used in anti-biofouling coatings^{31,32} and has been the material of choice in a variety of cell and protein adhesion and mobility studies.³³⁻³⁷ Its commercial availability and well characterized mechanical properties^{33,38-42} have made it readily accessible to researchers both in and out of the polymer science community.

Challenges Pertaining to PDMS-Based Materials

In the previous two sections, we listed numerous attributes about PDMS and PDMS-based materials that have led to their wide adoption in many different applications. Now we present several challenges that arise when using this material in specific applications. As hinted at above, when using commercial materials, one does not know the precise chemical composition of the material and it is not guaranteed that the silicone elastomer purchased is purely PDMS. In fact, it is unlikely to be only PDMS, at least based on one of the most common commercial silicone elastomers, Sylgard 184.

Commercial silicone elastomers are often not purely mixtures of polymer, crosslinker, and catalyst. They may contain broad ranges of material composition and exhibit highly irregular network topological structures. Delebecq and Ganachaud^{29,30} investigated the chemical and topological properties of several commercial elastomers and found many differences among each commercial material. The network topology in these commercial materials can be generalized to that shown in Figure 1.3 where crosslinkers are depicted as spheres.

In commercial materials, there can be topological imperfections such as dangling ends and loops as well as non-uniform molecular weights between crosslinks, M_c . However, since the chemical composition of commercial silicone elastomers is proprietary, researchers working with these types of materials would not necessarily know the network topology. Nor could they figure it out to high precision by applying theories and models because most theories rely on stoichiometric or molecular property inputs that are unknown in commercial materials. We believe the consequence of this lack of knowledge of the underlying

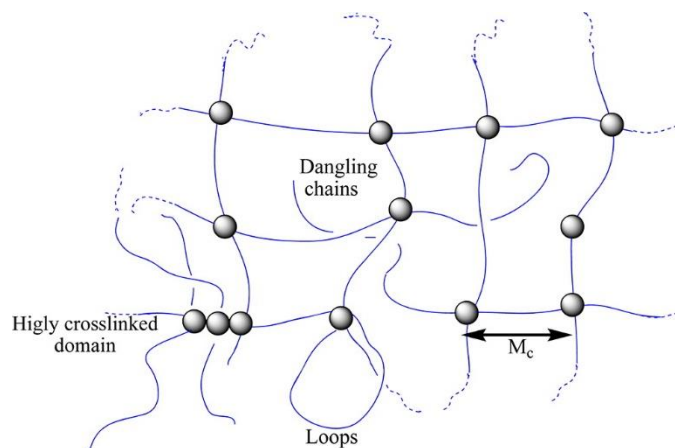


Figure 1.3 – Reproduced from Delebecq and Ganachaud.²⁹ Non-perfect network topology in commercial silicone elastomers.

Additionally, as more research involves proteins and cells in microfluidic devices, the surface properties of PDMS become of paramount interest. A major question that must be answered is whether or not the substrate used in such experiments is static or dynamic, *i.e.*, whether or not the substrate is influencing the experiment in any way. In such confined volumes, the cells may be sensitive to any impurities that could be leaching out of the underlying PDMS substrate, particularly small PDMS precursors such as cyclic and linear oligomers.⁴³ Another challenge is that PDMS may absorb hydrophobic molecules, such as hormones and drugs, that are introduced to the cell media, which may skew the dosages and thus, the cell responses.²⁵ We are not the only scientists to point out these challenges to commercial PDMS materials.⁴⁴ The leaching of siloxane oligomers has been examined previously^{45,46} using micro-contact printing to study the amount and type of leached siloxanes when brought in contact to another substrate.

Scope of Dissertation

While Sylgard 184 has received much attention in the last two decades, we would be remiss to argue that model PDMS materials, *i.e.*, not commercial kits, have not been studied in detail. On the contrary, there is a rich literature of various model PDMS systems prepared with precise chemical stoichiometry for specific applications. A thorough review of such

materials was provided by Larsen, Sommer-Larsen, and Hassager in 2004.⁴⁷ However, to the best of our knowledge, a systematic investigation that directly compares the dynamic mechanical and dynamic surface wetting properties of Sylgard 184 and model PDMS systems made from various molecular weights and amounts and types of crosslinker, has not yet been performed. This dissertation seeks to fill this void.

The primary goal of this dissertation is to elucidate PDMS network molecular structure to macroscopic property relationships, as depicted in Figure 1.4. Herein, we design PDMS materials from the “ground up” to ensure knowledge of the precise chemical composition and relate that to macroscopic properties. Overall, we address several key questions related to the use of PDMS-based materials in many applications. We determine how and to what extent the molecular network architecture and chemical composition of PDMS materials influence both bulk and surface material properties of silicone elastomers. We also reveal the vital importance of the Soxhlet extraction technique, which removes the mobile material that did not participate in the crosslinking reaction, on the mechanical and surface properties of PDMS materials. Further, the influence of filler particles and diluents on mechanical and surface properties are demonstrated

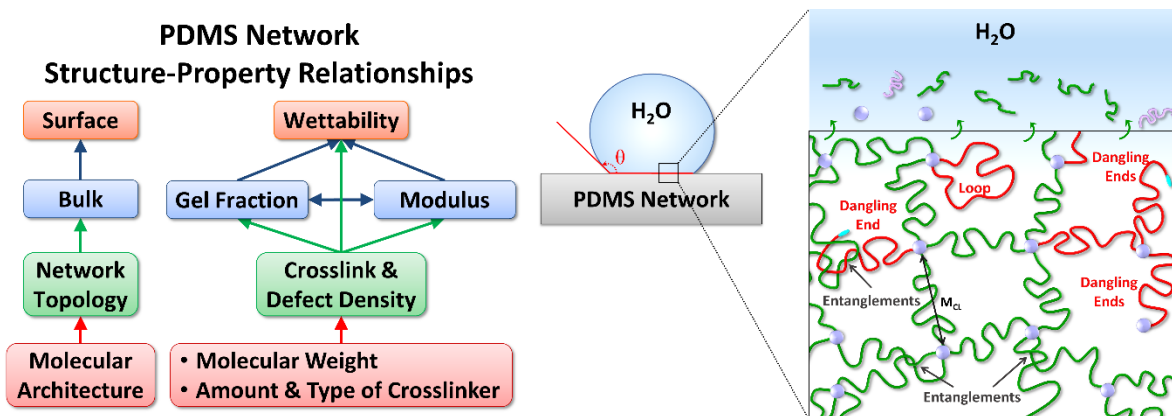


Figure 1.4 – Scope of dissertation. Build PDMS materials from the “ground up” to understand their molecular network structure and relate that to macroscopic bulk and surface properties.

To accomplish these tasks, we begin in chapter 2 of this dissertation by comparing and contrasting two different model PDMS materials prepared with precise chemical compositions

of varying molecular weights and crosslinkers to the commercial product, Sylgard 184, prepared with various formulations. We use the vinyl/TDSS and silanol/TEOS combinations of PDMS end-groups and crosslinkers as our two model systems to study. Comparison of model and commercial systems permits us to elucidate the strong influence filler particles have on material properties. We do not add any filler particles, to our systems, but some will be formed during crosslinking (*vide infra*). In chapter 2, the preparation details for making these silicone elastomers are provided. Then, we perform an analysis of the extent of the gelation reaction by using the Soxhlet extraction technique to quantify the amount of material that did and did not participate in the crosslinking reactions, termed the gel and sol fractions, respectively. Prior to extraction, the sol fraction remains in the network and exists as a mobile, uncrosslinked material that plays a role in the mechanical and surface wetting properties.

In chapter 3, we use the knowledge of precise chemical composition and the extent of the gelation reactions as inputs to a polymer network theory called the Miller-Macosko model.^{48,49} This powerful model, which has been verified experimentally,⁵⁰ provides a plethora of information pertaining to the network topology, such as the fractions of elastic and pendant material, the molecular weight between chemical crosslinks, and the average effective functionality of the crosslinker molecule, which may not have fully reacted. The derivations of the model and the final equations used to determine such parameters are not trivial, but taking the time to understand them and apply them is worth the effort based on the vast topological network knowledge gained.

The findings from the Miller-Macosko model related to network topology have ramifications specifically on the dynamic mechanical properties of silicone elastomers. Hence, in chapter 4, we investigate those properties. We perform dynamic mechanical analyses on both vinyl and silanol model systems as well as Sylgard 184 to elucidate both the viscous and elastic responses of these materials. Then, the output of the topological network parameters from the Miller-Macosko model is compared to the dynamic mechanical properties in the vinyl system. This analysis elucidates how and why materials act the way they do under macroscopic deformations. Their behavior is related back down to molecular level topology. We also demonstrate the importance of the Soxhlet extraction technique in this chapter by comparing

the mechanical properties of Sylgard 184 before and after extraction. Additionally, we perform classical stress-strain experiments on Sylgard 184 samples of different formulations to elucidate how the extent of crosslinking changes the material's ultimate performance.

Lastly, in chapter 5, we investigate the dynamic behavior of water droplets wetting PDMS substrates. We observe non-linear wetting behaviors that are markedly different from linear behaviors seen on glassy polymer substrates. The dynamic wetting behavior on model vinyl PDMS is compared to Sylgard 184 on samples both before and after the extraction process. The non-linear behavior is only observed prior to extraction, while after extraction, both systems demonstrate behavior similar to glassy polymers. This reveals the dramatic role small amounts of uncrosslinked materials play in the surface wetting dynamics of PDMS materials. We demonstrate the dynamic nature of the interfacial energy between water and PDMS further by taking the product of the interfacial area and the negative cosine of the contact angle, which elucidates the changes in interfacial energy with respect to the probing liquid, water. After that, we briefly compare the wetting behavior to mechanical properties for Sylgard 184 materials. Lastly, we reveal the ability to tune the dynamic wetting behavior by incorporating extra inert silicone oils into otherwise fully crosslinked materials, thereby controlling both the amount and type of material that is present in the sol fraction. These mobile excess silicone oils can migrate to the water-PDMS interface, but their ability to change the interfacial energy is related to their molecular weight.

Overall, we hope to demonstrate that through careful preparation of PDMS materials, compared to simply mixing two formulations present in commercial Sylgard 184, one can apply polymer network models to glean useful information about network topology, and that the benefits of doing so outweigh the costs. While Sylgard 184 is very well suited for some applications, we believe the results presented in this dissertation will demonstrate to researchers that the material does have its limitations and that other options are available.

References

1. Moretto, H.-H., Schulze, M. & Wagner, G. in *Ullmann's Encyclopedia of Industrial Chemistry* **33**, 9–12 (Wiley-VCH Verlag GmbH & Co. KGaA, 2000).
2. Andriot, M., Chao, S. H., Colas, A., Cray, S. & Buyl, F. *Silicones in Industrial Applications*. **84**, (2009).
3. *The Future of Silicone Elastomers to 2021*. **44**, (2015).
4. Mark, J. E. & Flory, P. J. Configuration of the Poly-(dimethylsiloxane) Chain. I. The Temperature Coefficient of the Unperturbed Extension. *J. Am. Chem. Soc.* **86**, 138–141 (1964).
5. Clarson, S. J., Dodgson, K. & Semlyen, J. A. Studies of cyclic and linear poly(dimethylsiloxanes): 19. Glass transition temperatures and crystallization behaviour. *Polymer* **26**, 930–934 (1985).
6. Kim, J., Chaudhury, M. K. & Owen, M. J. Hydrophobicity loss and recovery of silicone HV insulation. *IEEE Trans. Dielectr. Electr. Insul.* **6**, 695–702 (1999).
7. Zheng, P. & McCarthy, T. J. Rediscovering silicones: molecularly smooth, low surface energy, unfilled, UV/vis-transparent, extremely cross-linked, thermally stable, hard, elastic PDMS. *Langmuir* **26**, 18585–90 (2010).
8. Crowe, J. A., Efimenko, K. & Genzer, J. in *Science and Technology of Silicones and Silicone-Modified Materials* 400 (American Chemical Society, 2007).
9. Flory, P. J., Crescenzi, V. & Mark, J. E. Configuration of the Poly-(dimethylsiloxane) Chain. III. Correlation of Theory and Experiment. *J. Am. Chem. Soc.* **86**, 146–152 (1964).
10. Colas, A. & Curtis, J. in *Biomaterials Science: An Introduction to Materials in Medicine* (eds. Ratner, B., Fredrick, A. H. & Lemons, J.) (Elsevier, Inc., 1996). doi:10.1016/B978-0-08-087780-8.00025-5
11. Crowe, J. A. & Genzer, J. Creating responsive surfaces with tailored wettability switching kinetics and reconstruction reversibility. *J. Am. Chem. Soc.* **127**, 17610–1 (2005).
12. Crowe-Willoughby, J. A. & Genzer, J. Formation and Properties of Responsive Siloxane-Based Polymeric Surfaces with Tunable Surface Reconstruction Kinetics. *Adv. Funct. Mater.* **19**, 460–469 (2009).
13. Araci, I. E. & Brisk, P. Recent developments in microfluidic large scale integration. *Curr. Opin. Biotechnol.* **25**, 60–68 (2014).
14. Fekete, Z. & Pongrácz, A. Multifunctional soft implants to monitor and control neural activity in the central and peripheral nervous system: A review. *Sensors Actuators B Chem.* **243**, 1214–1223 (2017).
15. Hassler, C., Boretius, T. & Stieglitz, T. Polymers for neural implants. *J. Polym. Sci. Part*

- B Polym. Phys.* **49**, 18–33 (2011).
16. Carpi, F., Kornbluh, R., Sommer-Larsen, P. & Alici, G. Electroactive polymer actuators as artificial muscles: are they ready for bioinspired applications? *Bioinspir. Biomim.* **6**, 45006 (2011).
 17. Romasanta, L. J., Lopez-Manchado, M. A. & Verdejo, R. Increasing the performance of dielectric elastomer actuators: A review from the materials perspective. *Prog. Polym. Sci.* **51**, 188–211 (2015).
 18. Gossweiler, G. R. *et al.* Mechanochemically Active Soft Robots. *ACS Appl. Mater. Interfaces* **7**, 22431–22435 (2015).
 19. Rus, D. & Tolley, M. T. Design, fabrication and control of soft robots. *Nature* **521**, 467–475 (2015).
 20. Rogers, J. A., Someya, T. & Huang, Y. Materials and Mechanics for Stretchable Electronics. *Science (80-.)*. **327**, 1603–1607 (2010).
 21. Khan, S., Lorenzelli, L. & Dahiya, R. S. Technologies for printing sensors and electronics over large flexible substrates: A review. *IEEE Sens. J.* **15**, 3164–3185 (2015).
 22. Whitesides, G. M., Ostuni, E., Takayama, S., Jiang, X. & Ingber, D. E. Soft Lithography in Biology and Biochemistry. *Annu. Rev. Biomed. Eng.* **3**, 335–373 (2001).
 23. Sia, S. K. & Whitesides, G. M. Microfluidic devices fabricated in Poly(dimethylsiloxane) for biological studies. *Electrophoresis* **24**, 3563–3576 (2003).
 24. Xia, Y. & Whitesides, G. M. SOFT LITHOGRAPHY. *Annu. Rev. Mater. Sci.* **28**, 153–184 (1998).
 25. Halldorsson, S., Lucumi, E., Gómez-Sjöberg, R. & Fleming, R. M. T. Advantages and challenges of microfluidic cell culture in polydimethylsiloxane devices. *Biosens. Bioelectron.* **63**, 218–231 (2015).
 26. Brindley, G. S. The first 500 sacral anterior root stimulators: implant failures and their repair. *Paraplegia* **33**, 5–9 (1995).
 27. Daniel, W. F. M. *et al.* Solvent-free, supersoft and superelastic bottlebrush melts and networks. *Nat. Mater.* 1–8 (2015). doi:10.1038/nmat4508
 28. Paul, D. R. & Mark, J. E. Fillers for polysiloxane (‘silicone’) elastomers. *Prog. Polym. Sci.* **35**, 893–901 (2010).
 29. Delebecq, E. & Ganachaud, F. Looking over Liquid Silicone Rubbers: (1) Network Topology vs Chemical Formulations. *ACS Appl. Mater. Interfaces* **4**, 3340–3352 (2012).
 30. Delebecq, E., Hermeline, N., Flers, A. & Ganachaud, F. Looking over Liquid Silicone Rubbers: (2) Mechanical Properties vs Network Topology. *ACS Appl. Mater. Interfaces* **4**, 3353–3363 (2012).
 31. Shivapooja, P. *et al.* Bioinspired Surfaces with Dynamic Topography for Active Control

- of Biofouling. *Adv. Mater.* **25**, 1430–1434 (2013).
32. Zhang, H. & Chiao, M. Anti-fouling coatings of poly(dimethylsiloxane) devices for biological and biomedical applications. *J. Med. Biol. Eng.* **35**, 143–155 (2015).
 33. Brown, X. Q., Ookawa, K. & Wong, J. Y. Evaluation of polydimethylsiloxane scaffolds with physiologically-relevant elastic moduli: interplay of substrate mechanics and surface chemistry effects on vascular smooth muscle cell response. *Biomaterials* **26**, 3123–9 (2005).
 34. Li, J., Han, D. & Zhao, Y.-P. Kinetic behaviour of the cells touching substrate: the interfacial stiffness guides cell spreading. *Sci. Rep.* **4**, 3910 (2015).
 35. Evans, N. *et al.* Substrate stiffness affects early differentiation events in embryonic stem cells. *Eur. Cells Mater.* **18**, 1–14 (2009).
 36. Fuard, D., Tzvetkova-Chevolleau, T., Decossas, S., Tracqui, P. & Schiavone, P. Optimization of poly-di-methyl-siloxane (PDMS) substrates for studying cellular adhesion and motility. *Microelectron. Eng.* **85**, 1289–1293 (2008).
 37. Völcker, N., Klee, D., Höcker, H. & Langefeld, S. Functionalization of silicone rubber for the covalent immobilization of fibronectin. *J. Mater. Sci. Mater. Med.* **12**, 111–119 (2001).
 38. Johnston, I. D., McCluskey, D. K., Tan, C. K. L. & Tracey, M. C. Mechanical characterization of bulk Sylgard 184 for microfluidics and microengineering. *J. Micromechanics Microengineering* **24**, 35017 (2014).
 39. Schneider, F., Draheim, J., Kamberger, R. & Wallrabe, U. Process and material properties of polydimethylsiloxane (PDMS) for Optical MEMS. *Sensors Actuators, A Phys.* **151**, 95–99 (2009).
 40. Schneider, F., Fellner, T., Wilde, J. & Wallrabe, U. Mechanical properties of silicones for MEMS. *J. Micromechanics Microengineering* **18**, 65008 (2008).
 41. Gutierrez, E. & Groisman, A. Measurements of elastic moduli of silicone gel substrates with a microfluidic device. *PLoS One* **6**, e25534 (2011).
 42. Rubino, E. & Ioppolo, T. Young's modulus and loss tangent measurement of polydimethylsiloxane using an optical lever. *J. Polym. Sci. Part B Polym. Phys.* **54**, 747–751 (2016).
 43. Regehr, K. J. *et al.* Biological implications of polydimethylsiloxane-based microfluidic cell culture. *Lab Chip* **9**, 2132 (2009).
 44. RAJENDRANI MUKHOPADHYAY. When PDMS isn't the best. *Anal. Chem.* 1–5 (2007). doi:10.1007/s13398-014-0173-7.2
 45. Thibault, C., Séverac, C., Mingotaud, A. F., Vieu, C. & Mauzac, M. Poly(dimethylsiloxane) contamination in microcontact printing and its influence on patterning oligonucleotides. *Langmuir* **23**, 10706–10714 (2007).
 46. Yang, L. *et al.* Effect of surface free energy on PDMS transfer in microcontact printing

and its application to ToF-SIMS to probe surface energies. *Langmuir* **25**, 5674–5683 (2009).

47. Larsen, A. L., Sommer-Larsen, P. & Hassager, O. Some experimental results for the end-linked polydimethylsiloxane network system. *E-Polymers* 1–18 (2004).
48. Macosko, C. W. & Miller, D. R. A New Derivation of Average Molecular Weights of Nonlinear Polymers. *Macromolecules* **9**, 199–206 (1976).
49. Miller, D. R. & Macosko, C. W. A New Derivation of Post Gel Properties of Network Polymers. *Macromolecules* **9**, 206–211 (1976).
50. Chassé, W., Lang, M., Sommer, J.-U. & Saalwächter, K. Cross-Link Density Estimation of PDMS Networks with Precise Consideration of Networks Defects. *Macromolecules* **45**, 899–912 (2011).

CHAPTER 2: Preparation Details for Making Silicones

Introduction

PDMS is the polymeric material of choice for a variety of applications ranging from microfluidic devices¹ to biomedical implants² to soft robots.³ The formulations for making such materials vary based on the application. Sometimes the formulations are purely chemical-based, and include only polymers and crosslinkers to create super soft materials.⁴ In other instances, filler particles are incorporated to make composite materials that achieve desired properties such as enhanced mechanical strength or electrical conductivity.⁵ Many commercial silicones incorporate nanosized filler particles^{6,7} and one of the most common commercial silicones used is Sylgard 184 manufactured by Dow Corning. Sylgard 184 comes as a two-component kit, a base (B) and a curing agent (C) and the manufacturer recommends using a 10:1 base to curing agent mass ratio (B/C ratio) for optimal performance. According to the Safety Data Sheet, this product contains up to 50% chemically treated fumed silica particles.^{8,9} The addition of particles increases the strength and extensibility of the material. Additionally, this material has extremely high fidelity with respect to reproducing 3D micro-scale topographies from a master mold,^{10,11} which makes it ideal for fabricating microfluidic devices.¹²⁻¹⁴

While there is no doubt to the usefulness of using commercial silicone elastomers with particles for many applications, one major drawback exists; the exact chemical composition of these materials is proprietary and often only reported in broad ranges. Additionally, chemicals other than particles, PDMS polymers, and crosslinker may be present, either intentionally or inadvertently. In Sylgard 184, these include solvents such as toluene, ethylbenzene, and xylene,^{8,9} as well as short-chain siloxane oligomers and cyclics, which are very difficult to purify completely from PDMS. In highly sensitive environments, such as cells exposed to hormones or drugs in microchannels, the effects of these components on cell behavior cannot be ignored.¹⁵⁻¹⁷ While chemical characterization of commercial materials is possible,⁶ it is laborious and requires access to expensive instruments such as Nuclear Magnetic Resonance (NMR) machines and expertise in interpreting the resulting data.

Despite this drawback, Sylgard 184 has been widely adopted for many applications. Numerous researchers have adjusted the prescribed 10:1 B/C ratio in Sylgard 184 to vary mechanical properties, such as Young's modulus, of the material.¹⁸⁻²⁰ This is often done during investigations of cell mobility on substrates with varying degrees of stiffness.²¹⁻²⁴ In other instances, researchers want to create flexible electronics using PDMS as the flexible substrate.²⁵ Sylgard 184 is also used in microelectromechanical systems (MEMS) where various mixing ratios are used to achieve desired properties.^{26,27} Additionally, one group varied the B/C ratio to adjust the Young's modulus of PDMS elastomers while investigating the materials' work of adhesion.²⁸ Clearly, while deviating from Dow Corning's prescribed 10:1 B/C ratio enables access to materials of a broad range of properties, one has to question "at what cost?". This practice also changes the stoichiometry (*i.e.*, ratio of chemicals used in the crosslinking reaction) of the system and makes the chemical reaction imbalanced, resulting in either the polymer or crosslinker becoming the limiting or excess reagent. That is, portions of the network materials are no longer fully reacted. This can result in material defects and significant amounts of chemicals that are not covalently attached to the network relative to materials prepared with balanced stoichiometry.

Therefore, one major goal of this PhD dissertation is to provide researchers with chemical recipes for making materials over a wide range of properties, without the addition of anything other than PDMS polymers, crosslinkers, and catalysts. Making one's own PDMS networks "from scratch" naturally enables knowledge of the precise chemical composition without the need for expensive and intricate chemical analysis.

The goals of this chapter are the following. First, the preparation conditions and precise chemical recipes of model PDMS materials studied throughout this dissertation are conveyed. Next, relationships between changing the molecular weight, stoichiometry, and crosslinking chemistry in silicone elastomer systems, and the degree of chemical crosslinking are elucidated by measuring the gel fraction of the network via the Soxhlet extraction technique. Lastly, the concept of optimal stoichiometry to achieve maximum extent of crosslinking is introduced and the amount of extractable material in model PDMS systems and the commercial Sylgard 184 system is compared.

Background on Crosslinking & Gelation

Gelation involves the transformation of a material from freely flowing moieties (*e.g.*, polymer chains, monomers, colloids, particles) to constrained moieties that can no longer flow freely. One method to constrain polymer chains is through a chemical reaction called crosslinking, also referred to as curing, which covalently attaches polymer chains to each other either directly or through intermediates called crosslinking molecules (or simply crosslinkers). This process creates a 3D net-like molecular structure called a polymer network. Before crosslinking, PDMS is a viscous liquid and in the absence of solvents, it is called a melt. Even though the molecular chains within a PDMS melt are entangled (if indeed, they are above the entangled molecular weight of 12 kDa;²⁹ *cf.* Chapter 3 of this dissertation for details), they can still flow and diffuse past one another over time. In this study, the functional end-groups on PDMS chains chemically attach to crosslinker molecules at nodes called crosslink junctions. The process of polymer chains reacting with crosslinkers is measured by the extent of the crosslinking reaction, p , and is described as gelation. The gelation process transforms a liquid that flows to a gel that is solid. As this reaction proceeds and p increases, a critical extent of reaction is called the gel point p_{gel} , and will be reached wherein one chain of connected polymers and crosslinkers percolates throughout the entire sample volume, called the incipient gel.²⁹ This extended chain (*i.e.*, the incipient gel) has infinite molecular weight³⁰ and will no longer dissolve in solvents. Instead, it will swell when exposed to good solvents. However, the incipient gel still behaves very differently from a fully crosslinked, or well-developed network. Once the reaction progresses to the gel point, there are still many unreacted polymer chains and crosslinkers that have not covalently attached to the network.

A polymer network where the reaction is terminated shortly after the gel point is reached is said to be under-crosslinked because a lot of polymers and crosslinkers are still available to be reacted. All of the material present initially, *i.e.*, polymers and crosslinkers, is categorized into two fractions, one that is and one that is not covalently attached to the incipient gel. These two fractions are called the gel (w_{gel}) and sol (w_{sol}) fractions, respectively. The gel and sol fractions represent a measure of the extent of crosslinking reaction, p , and are used to

precisely calculate p based on the Miller-Macosko^{15,16} model (*cf.* Chapter 3 of this dissertation). The gel fraction is characterized as the fraction of material chemically bound to and permanently trapped in the network. Below the gel point, p_{gel} , the gel fraction is zero; that is, all components will dissolve when exposed to a good solvent. However, after the gel point is reached the Miller-Macosko model³⁰ predicts a rapid increase in gel fraction followed by an asymptotic approach to a value of 1 with further increases in the extent of reaction.

Networks with low gel fraction values, typically between 0-0.8, are considered to be under-crosslinked. At higher extents of reaction, the gel fraction will approach values between 0.95-1, yielding a well-developed network. Depending on the crosslinking chemistry, however, a high gel fraction does not necessarily mean all of the crosslinking molecules have reacted. For instance, in random side-chain crosslinking, such as in the vulcanization of rubber in tires, it only takes two reactions per chain to covalently connect all chains to the network. When that occurs, many more reactive sites may still remain uncrosslinked. Therefore, a well-developed network can be crosslinked further. A fully crosslinked network is one in which it has both a high gel fraction and a high extent of reaction of all available crosslinking sites.

Variables Affecting Gelation

In the PDMS systems investigated throughout this dissertation, gelation can proceed slowly or rapidly, depending on a variety of conditions, as shown in Figure 2.1. The rate of the crosslinking reaction is referred to as the gelation kinetics, while the final result of the crosslinking reaction after long times is referred to as the gelation equilibrium. Both kinetics and equilibrium can change the material properties, and they are influenced by a variety of independent variables.

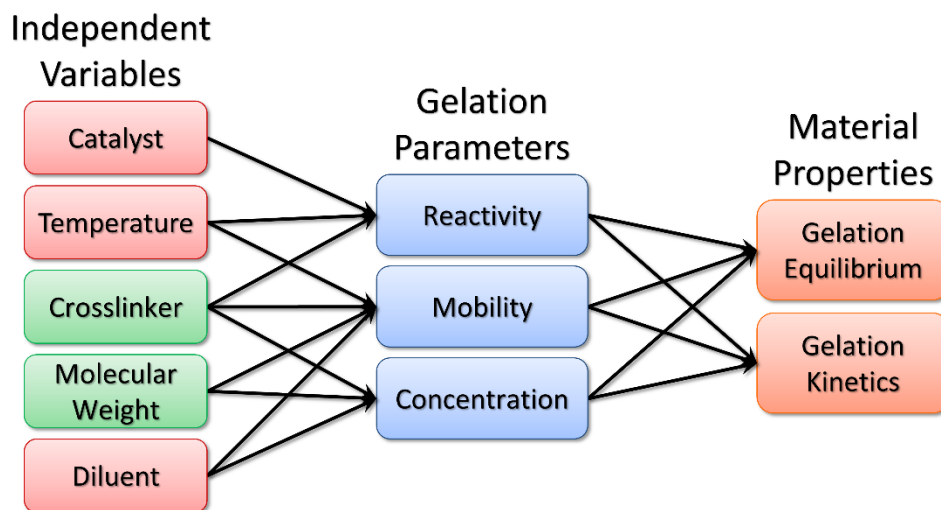


Figure 2.1 – Flow diagram depicting parameters to be considered with preparing silicone elastomers. The independent variables one can control in preparing PDMS networks are given on the left, with the green squares showing variables investigated in this dissertation. The red squares were held constant. The middle blue squares show what gelation phenomena the independent variables can influence. Those parameters then influence both the gelation equilibrium and kinetics, orange squares on the right. Finally, the resulting material properties, such as gel fraction, depend upon the gelation equilibrium and kinetics.

The independent variables in Figure 2.1 are those controlled by the user when preparing silicone materials. First, the amount, type, and activity of the catalyst used can change the kinetics of the reaction. Hence, the catalyst amount and choice directly affect the reactivity of the crosslinkers and polymers in the system. For instance, from this dissertation author’s own experiences, Pt(0) leads to faster gelation than Pt(II) catalysts when all other factors are held constant. However, for the data presented in this Ph.D. dissertation, only Pt(II) was used for the hydrosilylation reaction and Sn(II) was used for the condensation reaction (*vide infra*), but the amount of catalyst was held constant for each type of reaction. Thus, the effects of catalyst on material properties were not reported and it is depicted as a red square in Figure 2.1. Next, increasing the temperature of the crosslinking reaction can speed up kinetics by increasing molecular mobility and the energy of the molecules in the system, which lowers the activation energy of the crosslinking reaction. Different gelation temperatures have been shown to lead to different material properties in Sylgard 184.³² In this investigation,

temperature and duration were held constant (*vide infra*), thus the temperature is also shown in a red square in Figure 2.1.

The molecular architecture and the type of chemical functional groups of the crosslinker are very important parameters that can influence the reactivity, mobility, and concentration of species participating in the crosslinking reaction. They can take the form of a small molecule, as is the case in the model PDMS systems prepared herein, or a copolymer, which is used in Sylgard 184. Different functional groups can also have different reactivity and some are more prone to side reactions than others. In this dissertation, two different polymer end-group/crosslinker combinations are studied. For each system, the ratio of crosslinker to polymer is varied, changing the concentration of the crosslinker in each sample. Crosslinker is shown as a green square in Figure 2.1 because it is thoroughly investigated (*vide infra*). The molecular weight of the polymer is also very important, as this affects the viscosity of the system, which can limit chain mobility and change the concentration of reactive polymer end-groups. Because only the end-groups of the polymer are being reacted, increasing the molecular weight while holding the sample volume constant has the effect of decreasing the concentration of reactive end-groups, which will change the gelation equilibrium and kinetics. A wide range of molecular weights are investigated throughout this dissertation. Hence, molecular weight is also shown as a green square in Figure 2.1. Lastly, increasing the amount of diluent added can increase mobility of chains while also decreasing their concentration. Crosslinking PDMS in the presence of a diluent has been thoroughly investigated by Urayama³³ and co-workers,³⁴ They have found that this leads to a “super-coiled” structure which reduces entanglements and enables very large deformations. The effects of diluent were not investigated in this dissertation, and thus, diluent is shown as a red square in Figure 2.1.

It is evident that gelation is a complex process influenced by many parameters, all of which are important for the resulting material properties. Additionally, many of these parameters, such as concentration, mobility (viscosity) and molecular weight all change during the crosslinking reaction, which can lead to reaction/diffusion limitations. In theory, regardless of the aforementioned parameters, the crosslinking reaction can proceed until all of the available crosslinker and polymer functional end-groups have fully reacted. More accurately,

the crosslinking reaction will take place until a thermodynamic equilibrium is reached between the forward crosslinking reaction and reverse dissociation reactions. In these crosslinking reactions, the equilibrium strongly favors crosslinking over dissociation. Such an equilibrium does exist however, and care should be taken when materials are used over months or years because the properties may change. Typically, researchers do not have time to wait months or years for the true equilibrium reaction conditions to be met. By changing the aforementioned variables to speed up gelation, the resulting materials are being used with a specific history of preparation. They essentially exist as a snapshot of their degree of crosslinking at the particular point in time associated with their characterization based on their specific history. Thus, it is paramount to report gelation conditions when describing properties of PDMS materials.

PDMS Crosslinking Chemistry

The two most common chemical crosslinking reactions for preparing PDMS networks are hydrosilylation and condensation reactions. Both are highly effective at forming PDMS networks and have been studied extensively.

Hydrosilylation

The hydrosilylation reaction occurs between a silicon-hydride functional group (Si-H) and a terminal alkene, or vinyl functional group (R-CH=CH₂) and is frequently catalyzed with platinum, although other transition metals can be used.³⁵ Figure 2.2 shows a simplified mechanism of this crosslinking reaction. A comprehensive review of hydrosilylation is given by Matison³⁵ The most common catalysts used for silicone elastomers are Pt(II) and Pt(0). Platinum(II) is often complexed by sulfur moieties while Pt(0) is frequently complexed by 1,3-divinyltetramethyldisiloxane forming the common Karstedt's catalyst.³⁵ However, the use of Pt(0) complexed with vinyl-functional siloxane ligands may lead to unintended changes in reaction stoichiometry since vinyl-terminated linear PDMS chains are used in the crosslinking reaction.³⁶

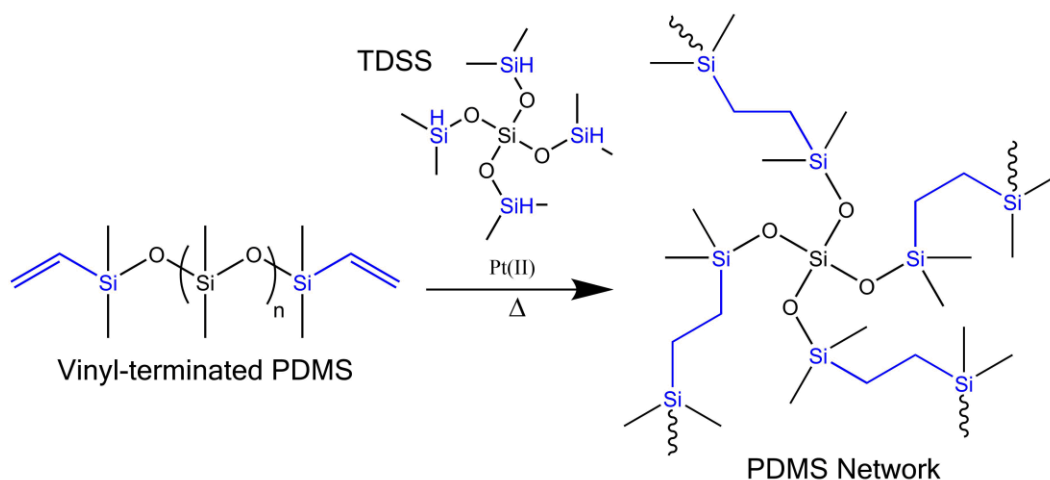


Figure 2.2 – Simplified chemical mechanism of the Pt(II) catalyzed hydrosilylation crosslinking reaction. This example shows the formation of a tetrafunctional crosslink junction through the creation of new Si-C-C-Si covalent linkages.

Hydrosilylation has been used by many researchers in the study of PDMS networks. A brief summary of its use in the literature is given here. In the late 1970s and early 1980s, Miller, Macosko, Valles and co-workers did extensive work on vinyl-terminated PDMS reacted with various silicon-hydride functional crosslinkers to test their gelation model in low stoichiometric ratio regimes.^{37–40} Shortly thereafter, in the mid-to-late 1980s, Chambon, Winter and co-workers used this system to study the sol-gel transition and developed methods for terminating the reaction precisely at the gel point.^{41–45} As mentioned previously, in the late 1990s and early 2000s, Urayama and co-workers used this crosslinking reaction for the study of PDMS networks crosslinked in the presence of a solvent to create highly stretchable materials.^{33,34} In the last couple of years, chemical analysis techniques and instrumentation have advanced, such as double-quantum nuclear magnetic resonance (DQ-NMR). This crosslinking reaction has proved to be a useful model system of study using DQ-NMR in testing gelation theories and determining the contributions of entanglements for improving theories on rubber-like elasticity.^{46,47} Overall, this crosslinking reaction is well-controlled and provides model PDMS network materials that can be used in a variety of applications.

Hydrolysis/Condensation

The other type of crosslinking reaction commonly used in PDMS systems is a hydrolysis/condensation two-step reaction often catalyzed by tin organometallic complexes.⁴⁸ This reaction requires trace amounts of water vapor, usually acquired from humidity in the air, and can proceed without heat, although applying heat increases the reaction rate. Thus, it is often termed room-temperature vulcanization (RTV). Alkoxysilanes serve as tri- or tetrafunctional crosslinkers and have the molecular form of $R'Si(OR)_3$ or $Si(OR)_4$, respectively, where R is an alkane group and R' is some form of hydrocarbon. Pujol and Prébet⁴⁹ investigated systematically the effects of R-group alkyl chain length on curing kinetics and mechanical properties of the resulting PDMS materials. They found that the bulkier R groups resulted in slower reaction kinetics and lower equilibrium in terms of completeness of crosslinking.⁴⁹ They demonstrated a non-uniform gelation reaction, wherein material closest to the air interface crosslinks first and material deeper within the bulk takes longer to crosslink as water must first diffuse through the upper layers of material. Additionally, Mark and co-workers^{50,51} released a series of 12 publications from 1977-1981 that extensively investigated a variety of silicone elastomers made from the hydrolysis/condensation crosslinking scheme.

The simplified mechanism of the hydrolysis/condensation crosslinking reaction is depicted in Figure 2.3.⁴⁸ First, hydrolysis of a siloxy (Si-OR) bond on an alkoxysilane-functional crosslinker occurs in the presence of trace amounts of water. This liberates alcohols (ROH) and forms silanol groups in the form of $Si(OH)_m$, depending on how many m alkoxy groups were originally attached to the crosslinker and how many got hydrolyzed. Then the condensation reaction of silanol groups (Si-OH) on both the crosslinker and polymer chain ends creates new siloxane bonds (Si-O-Si) while liberating water. An example of this simplified mechanism is given for tetraethoxysilane (TEOS) with silanol-terminated PDMS in Figure 2.3.

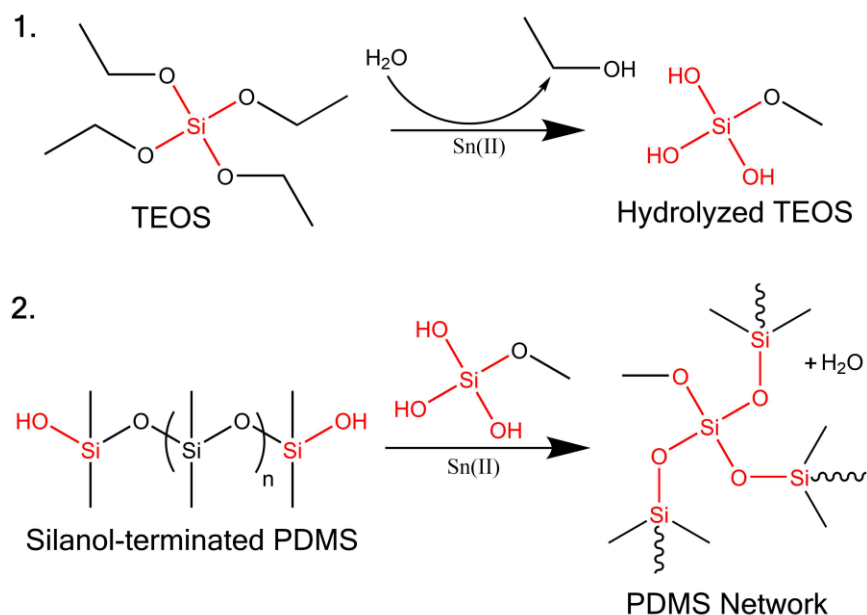


Figure 2.3 – Simplified chemical mechanism of the (1) hydrolysis reaction of tetraethoxysilane (TEOS) and (2) condensation reaction of silanol groups between TEOS and silanol-terminated PDMS, which creates new siloxane (Si-O-Si) bonds and liberates water. This example demonstrates the silanol/alkoxysilane crosslinking reactions for PDMS, forming a trifunctional crosslink junction.

Sylgard 184

Sylgard 184 undergoes the hydrosilylation crosslinking reaction between telechelic vinyl-terminated PDMS and a methylhydrosiloxane-co-dimethylsiloxane copolymer as the crosslinker. In addition to varying the mixing ratios (*vide supra*), researchers have investigated how curing conditions can alter the mechanical properties of Sylgard 184. Johnston *et al.*³² varied the curing temperature from 25 to 200°C and varied the crosslinking time from 18 min to 48 h for a constant 10:1 B/C ratio. They demonstrated that the materials exhibited noticeably different stress-strain curve shapes as well as significantly different ultimate stress and strains in both tensile and compressive modes. By increasing the curing temperature from 25 to 200°C, Young's modulus increased by more than 100%, compressive modulus decreased by more than 60%, and hardness increased by more than 20%.³² These findings strongly indicate that curing at higher temperatures, *i.e.*, faster gelation kinetics, results in strong and harder materials made of the same chemical composition.

Experimental Materials and Methods

Materials

Telechelic poly(dimethylsiloxane) (PDMS) polymers of various molecular weights and end-group functionalities were purchased from Gelest, Inc. and their properties are listed in Table 2.1. The average molecular weights reported by Gelest were used in subsequent calculations. Two different tetrafunctional crosslinker molecules, (*i.e.*, molecules that contain 4 reactive groups, giving them a functionality, f , equal to 4), tetrakis(dimethylsiloxy)silane (TDSS) and tetraethylorthosilicate (TEOS) were also purchased from Gelest, Inc. Two different catalysts, *cis*-dichlorobis(diethyl sulfide)platinum(II) (Pt catalyst), used for hydrosilylation reactions, and tin(II) 2-ethylhexanoate (Sn catalyst), used for hydrolysis/condensation reactions, were purchased from Sigma-Aldrich. A summary of these catalysts and crosslinkers is given in Table A2.1 in the Appendix

Table 2.1 – PDMS Materials and Properties^a Purchased from Gelest, Inc.

Product Code	Molecular Weight Range (kDa)	M_n (kDa) ^b	Viscosity (cSt)	Terminal Group
DMS-S21	5 – 7	6	90 – 120	Silanol
DMS-S27	15 – 20	18	700 – 800	Silanol
DMS-S31	20 – 30	25	800 – 1,200	Silanol
DMS-S35	45 – 55	50	4,000 – 6,000	Silanol
DMS-S45	80 – 130	105	45,000 – 60,000	Silanol
DMS-V21	5 – 7	6	80 – 120	Vinyl
DMS-V25	16 – 18	17	450 – 550	Vinyl
DMS-V31	25 – 30	28	900 – 1,100	Vinyl
DMS-V35	45 – 55	50	4,000 – 6,000	Vinyl
DMS-V41	55 – 70	63	9,000 – 11,000	Vinyl
DMS-V46	100 – 140	117	55,000 – 75,000	Vinyl

^a Properties reported from Gelest, Inc. Safety Data Sheets at the time of purchase.

^b Average molecular weight values reported by Gelest, Inc.

Table 2.2 – Composition of Sylgard 184 (Dow Corning) according to Safety Data Sheets^{8,9}

Function	Component	Base	Curing Agent
Polymer	Vinyl-terminated PDMS	55-75 %	15-35 %
Particles	Dimethylvinylated and trimethylated silica	30-50 %	10-30 %
Crosslinker	Dimethyl, methylhydrogen siloxane, P(DMS-co-MHS)	0 %	55-75 %
Crosslinker	Tetramethyl tetravinyl cyclotetrasiloxane	0 %	1-5 %
Diluent	Tetra(trimethylsiloxy) silane	< 1.0 %	0 %
Diluent	Xylene	0.5 %	0.19 %
Diluent	Ethylbenzene	0.2 %	<0.10 %

Sylgard 184 Silicone Elastomer kit (containing separate Base and Curing Agent components) was purchased from Dow Corning; the composition ranges of each component are given in Table 2.2 according to the Safety Data Sheet (SDS) at the time of purchase. All reactants were used without any further purification.

Network Preparation

To prepare each model PDMS network sample, *ca.* 2.5-3.5 g of PDMS were mixed well with the catalyst in a polypropylene beaker followed by removal of air bubbles under vacuum. For every gram of vinyl-terminated PDMS in each sample, 8 μ L of Pt catalyst solution at a concentration of 0.011 g Pt(II) catalyst per mL of toluene⁵² were added. Sn catalyst was added at a rate of 1% of the total mass of silanol-terminated PDMS polymer plus crosslinker.⁵³ In several instances with particularly high concentrations of TEOS, this amount was reduced to 0.25% of the total mass. Next, a precise mass (and volume) of the crosslinker, TDSS (for vinyl-terminated PDMS) and TEOS (for silanol-terminated PDMS), was added via micropipette over a balance to the PDMS/catalyst mixture yielding a specific desired stoichiometric ratio, r , defined as the initial concentration (mol/vol, n/m^3), of crosslinker functional groups to moles of polymer functional groups in Equation (2.1). This stoichiometric ratio between crosslinker and polymer functional groups has been employed previously^{6,7,36,46,54-58} in the study of silicone elastomer properties. Generally, both crosslinking reactions investigated throughout this dissertation involve A₄ crosslinkers (*i.e.*,

tetrafunctional crosslinker molecules) reacting with B₂ polymers (*i.e.*, end-functional linear polymers) according to the simplified crosslinking reaction of $A_4 + B_2 = network$. The subscripts indicate how many functional groups are available to react per molecule. Thus, the stoichiometric ratio is defined according to Equation (2.1).

$$r = \frac{4[A_4]_0}{2[B_2]_0} = \frac{4 \times \text{initial concentration of crosslinker [mol/vol]}}{2 \times \text{initial concentration of polymer [mol/vol]}} \quad (2.1)$$

After mixing well and degassing again, the solution was carefully poured into a polystyrene or polypropylene Petri dish. If needed, the Petri dish was degassed one last time then covered with a lid and placed on a level surface at room temperature exposed to atmospheric pressure for 1-3 hours of pre-curing, during which the polymer spread evenly throughout the Petri dish, giving a uniform thickness of ~0.7-1.5 mm, depending on how much material was added and the size of the petri dish. Finally, the specimens were placed in a 70°C oven at atmospheric pressure for 24 h. Illustrations of the resulting Vinyl/TDSS networks and Silanol/TEOS networks are provided in Figure 2.5a) and Figure 2.5b). Sylgard 184 samples were prepared in the same manner as model PDMS except the only ingredients used were the base (B) and curing agent (C), which were added together in varying B/C mass ratios. A schematic of its network structure is given in Figure 2.5c)

Kinetics

The work presented in this dissertation does not focus in depth on gelation kinetics. Each reaction was conducted at 70°C and ceased after 24 h by returning the samples to room temperature, effectively creating a snapshot of the extent of gelation 24 h into the reaction. However, the reaction can still proceed at room temperature, albeit at much slower rate. In the Vinyl/TDSS system, it has been shown that crosslinking at 60°C for 24 h is sufficient for achieving high gel fraction materials.³⁶ In the silanol/TEOS system, Pujol and Prébet⁴⁹ found that after 24 h at room temperature, a minimum depth of 3 mm was fully crosslinked. Therefore, 24 h at 70°C is considered to be sufficient. The stoichiometric ratio, r , sets the maximum extent of reaction possible by limiting the number of crosslinker groups or polymer end-groups present in the system. When $r < 1$, the crosslinker groups are the limiting reactant, and, when

$r > 1$, the end-groups on the polymer are the limiting reactant. The results presented in this chapter and throughout this dissertation indicate that curing at 70°C for 24 h is sufficient to form high gel fraction and high modulus networks at crosslinking ratios slightly above the balanced stoichiometric amount needed ($r = 1$).

Gel and Sol Fraction Determination

Soxhlet extraction in toluene, a good solvent for PDMS,⁵⁹ was used to determine the gel (w_{gel}) and sol (w_{sol}) fractions of the networks. The gel fraction, w_{gel} , of the network is defined as the amount of the material chemically bound to and physically trapped in the network²⁹ whereas the sol fraction, w_{sol} , contains all material that can diffuse out of the network. These fractions are determined by measuring the mass of the network in the dry state, m_{Pre} , then exposing it to a continuous rinse of fresh good solvent for 24 h via Soxhlet extraction during which unbound material can diffuse out of the network.²⁹ After extraction, samples were dried first in the fume hood overnight then further dried for 24 h under vacuum before their masses were measured again, m_{Post} . The gel fraction, w_{gel} , is thus mathematically defined as the mass of the network sample after extraction, m_{Post} , divided by the mass prior to extraction²⁹ m_{Pre} . Together, the sol and gel fraction sum to one, as shown in Equation (2.2).

$$w_{gel} = \frac{m_{Post}}{m_{Pre}}, \quad w_{sol} = 1 - w_{gel} \quad (2.2)$$

An example of the Soxhlet extraction experimental setup is shown in Figure 2.4. Briefly, heating mantles provide resistive heating for toluene contained in the round bottom flasks. Toluene vapor travels up to the chamber holder where it is condensed and fills chamber with liquid toluene. After a critical liquid level is reached, the chamber drains by siphon action, removing all liquids but keeping solid samples in the chamber, and then the process repeats. This provides a continuous rinse with clean, good solvent.

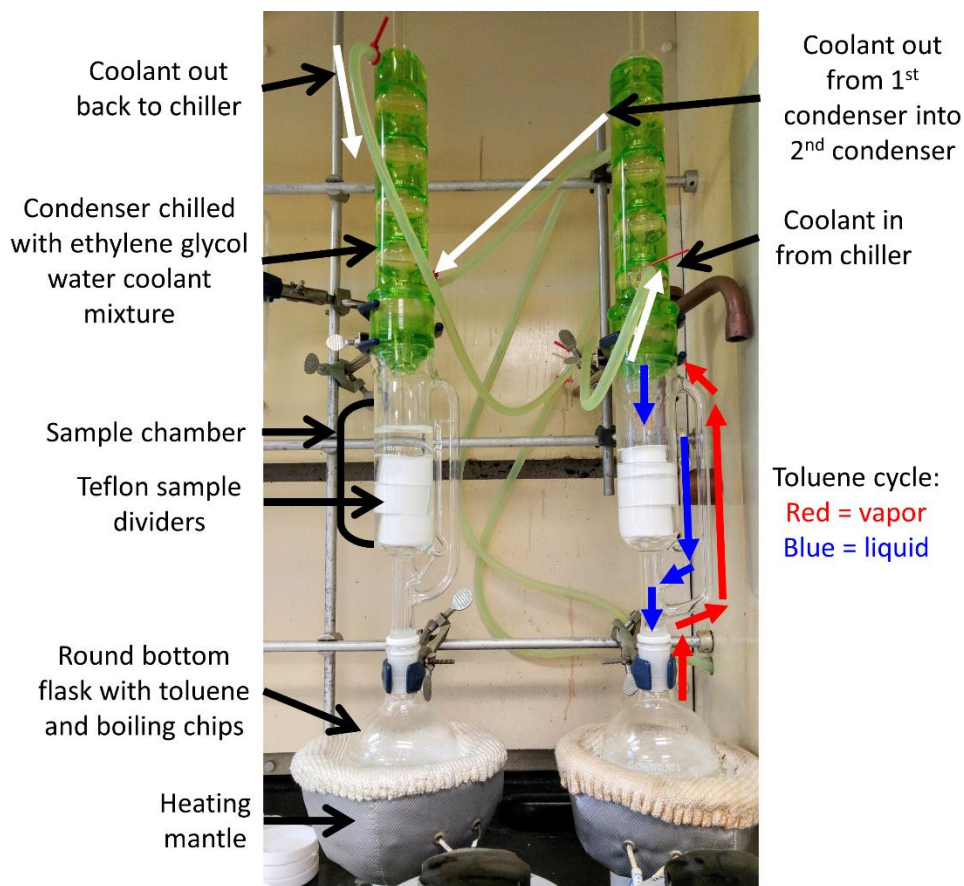


Figure 2.4 – Soxhlet Extraction instrumentation. Samples are separated by porous Teflon holders in the sample chamber, allowing toluene but not the PDMS sample to flow through. A heating mantle uses electrical resistive heating to increase the temperature of toluene and boiling chips in the round bottom flask. The toluene vapor (red arrows) travels within the external glass tube up and into the sample chamber where it is condensed from a water/ethylene glycol coolant mixture (green liquid). The condensed toluene liquid (blue arrows) fills the sample chamber until a critical liquid level is reached, causing the syphon to spill all of the liquid back into round bottom flask. The process is repeated, enabling a continuous rinse with fresh toluene. Coolant from a chiller (white arrows) enters the bottom of right condenser and fills it, exits from the top, and then enters the bottom of the left condenser and fills it before being returned to the chiller.

Scanning Electron Microscopy

Cross-sections of several PDMS samples were analyzed with scanning electron microscopy (SEM) to investigate TEOS aggregation. Prior to analysis, the samples were cut with a razor blade and the cross-section was sputter coated in an argon atmosphere with ~50 nm of a 60%/40% gold/palladium to create conductive surfaces. The Field Emission Verios

460L Scanning Electron Microscope at the Analytical Instrument Facility at North Carolina State University was used.

Results

Crosslinking Chemistry

Model PDMS networks prepared from two different crosslinking reactions, hydrosilylation and hydrolysis/condensation (*vide supra*) are being investigated to determine the impact of the specific crosslinking chemistry used for gelation on the resulting network properties. In the hydrosilylation systems, vinyl-terminated PDMS reacts with a tetrafunctional crosslinker, TDSS. In the hydrolysis/condensation systems, silanol-terminated PDMS is reacted with a different tetrafunctional crosslinker, TEOS. These two model systems are referred to as the Vinyl/TDSS and Silanol/TEOS systems, respectively, and are compared to the commercial Sylgard 184 product throughout this dissertation. All three systems are shown schematically in Figure 2.5.

Both model systems involve α,ω -difunctional terminated PDMS (*i.e.*, telechelic PDMS) being reacted with tetrafunctional crosslinkers. Therefore one may not expect to see any difference in network properties for the same ratios of crosslinker to polymer. However our results suggest otherwise, as will be demonstrated later. In contrast to model networks, Sylgard 184 uses a poly(dimethylsiloxane-co-methylhydrosiloxane) (P(DMS-co-MHS)) copolymer as a crosslinking agent, according to the Safety Data Sheet (*cf.* Table 2.2). This is coupled with vinyl-terminated PDMS to form a network containing much higher functionalities for its crosslinks than the model systems due to side-chain crosslinking along the P(DMS-co-MHS) molecule with vinyl-terminated PDMS chains (the cartoon in Figure 2.5c shows only 4 functional sites per crosslinker molecule, but this can be much higher). Despite the fact that the precise contents of the Sylgard 184 kit are unknown, we can safely hypothesize the crosslinking reaction to involve hydrosilylation due to the presence of both vinyl and silicon-hydrogen bonds and the Pt catalyst.

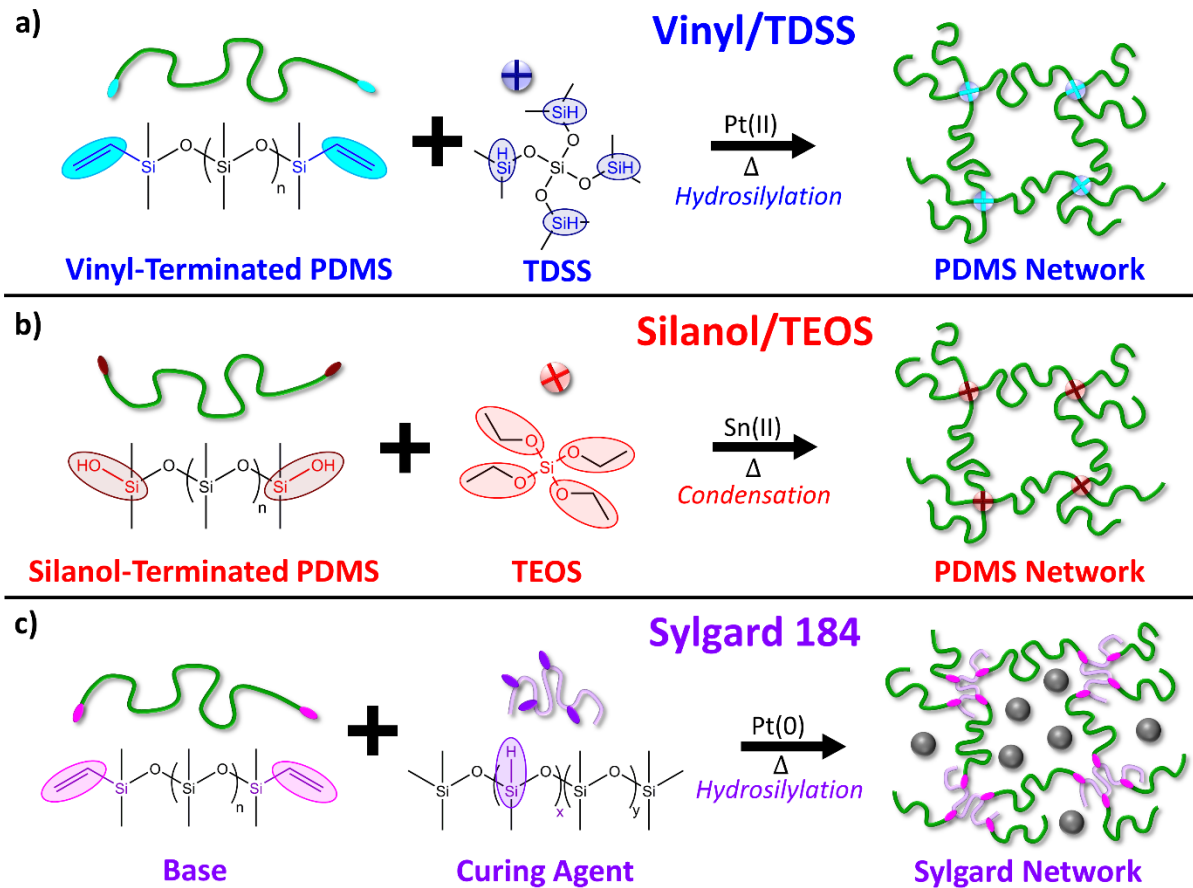


Figure 2.5 – Schematic illustrations of the reactants and products used in each PDMS system studied in this dissertation. The Vinyl/TDSS system crosslinks through Pt(II)-catalyzed hydrosilylation, shown in a). The Silanol/TEOS system crosslinks through a Sn(II)-catalyzed two-step hydrolysis/condensation reaction to create PDMS networks, shown in b). The commercial Sylgard 184 material creates PDMS networks via hydrosilylation of chemicals in the Base and Curing Agent components. The gray spheres represent the filler particles present in both the Base and Curing Agent components of Sylgard 184.

Figure 2.5a depicts the reactants and products of the Pt-catalyzed hydrosilylation reaction⁵² between the vinyl termini of PDMS chains and the silicon-hydride bonds on TDSS. In the mechanism shown in Figure 2.3, TEOS is first hydrolyzed with water moisture in air, forming silanol groups and evolving ethanol. Then Sn catalyzes the condensation reaction between silanol termini of PDMS and silanol groups on TEOS resulting in a new siloxane linkage and the formation of water.⁶⁰ The reactants and products of this crosslinking reaction are shown in Figure 2.5b. Both reactions given in Figure 2.5a and b are examples of a subset of crosslinking reactions called “end-linking”, wherein polymer chains are only crosslinked

through their functional end-groups at the reactive sites on crosslinker molecules. Thus, small molecule crosslinkers can be thought as chemical crosslink junctions. In this model network approach, the molecular weight between chemical crosslinks, M_{CL} , should be no less than the number-averaged molecular weight prior to crosslinking, M_n , for an ideal end-linked network. This method of creating model PDMS networks has been utilized previously to better control of molecular network architecture for accurate testing of theories on swelling and rubberlike elasticity.^{38,40,54,60}

Gel Fraction

Throughout this dissertation, the effects of changing the stoichiometry of the two model systems on the resulting material properties will be investigated. Figure 2.6 Figure 2.7 demonstrate the changes that materials made from different stoichiometric ratios undergo during the Soxhlet extraction process. Changing the relative amounts of crosslinker to polymer, r , can cause dramatic changes in the molecular topology of network materials as seen by comparing structures on the left, pre-extraction vs. those on the right, post-extraction. The red “X” indicates either no network or a degraded network forms under the given stoichiometric conditions. In Figure 2.6 unreacted vinyl end-groups are shown as cyan ovals at the ends of green PDMS chains. TDSS crosslinkers are shown as light blue circles with unreacted groups given by navy blue lines and reacted groups shown as cyan lines. A similar scheme is used in Figure 2.7. Here, unreacted silanol end-groups are brown ovals on the ends of green PDMS chains. TEOS crosslinkers are depicted as light red spheres with unreacted groups shown as red lines and reacted groups shown as brown lines.

Figure 2.6 and Figure 2.7 show schematically how the Soxhlet extraction process changes the structure of PDMS networks at three different r -values. The data providing the rationale behind these schematics are given in Figure 2.8 where the gel fractions of networks prepared according to the Vinyl/TDSS system and the Silanol/TEOS system are plotted as a function of the stoichiometric ratio, r , in a and b, respectively. The gel fraction data for networks made from various molecular weights of PDMS chains prior to crosslinking are given, with short chains shown in violet and longer chains shown in red. These results

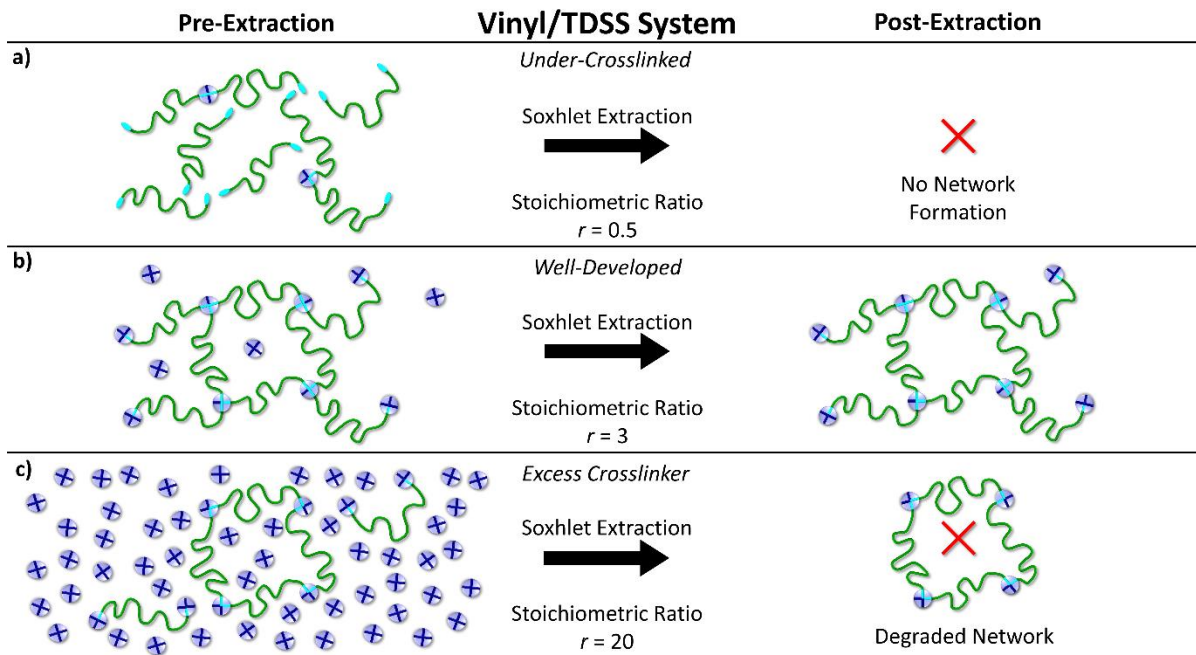


Figure 2.6 – Schematic illustration of different stoichiometric ratios and “end-capping” in the Vinyl/TDSS system. Scenarios corresponding to stoichiometric ratios of $r = 0.5$, 3, and 20 are depicted in a, b, and c, respectively. The left column represents networks before the extraction process while the right column demonstrates how the extraction process removes material not covalently attached to or permanently trapped in the network. PDMS chains are shown as green lines with cyan vinyl end groups and the TDSS crosslinkers are shown as navy blue “+” signs inside light blue circles. Reacted silicon-hydride groups are cyan lines inside the blue circle. The red “X” indicates the failure to form a fully crosslinked network due either insufficient or excess amounts of crosslinker. In c, “end-capped” chains that reacted with TDSS on both ends, but failed to react with the network are extracted, resulting in a degraded network. The size of PDMS chains relative to TDSS crosslinkers is not to scale, but the quantities of each are to scale with respect to r .

demonstrate the predicted behavior from the Miller-Macosko model mentioned earlier. Initially, at very low crosslinker loading, the gel fraction is zero until a critical amount of crosslinker is added. This results in enough available crosslinking sites for the extent of reaction to be equivalent to the gel point, and thus, a small amount of material does not dissolve during the extraction process. From there, a dramatic increase in the amount of material chemically bound to or permanently trapped in the network occurs with only minor increases in r until the networks saturate near $w_{gel} \approx 0.97$ at $r \approx 1.5-6$, depending on molecular weight and crosslinking chemistry. The maximum gel fraction is slightly below a value of 1 due to incomplete crosslinking reactions and impurities in the purchased samples from Gelest

(according to the SDS, sample may contain up to 5% inert cyclic siloxane precursors that were not removed from the polymer before use).

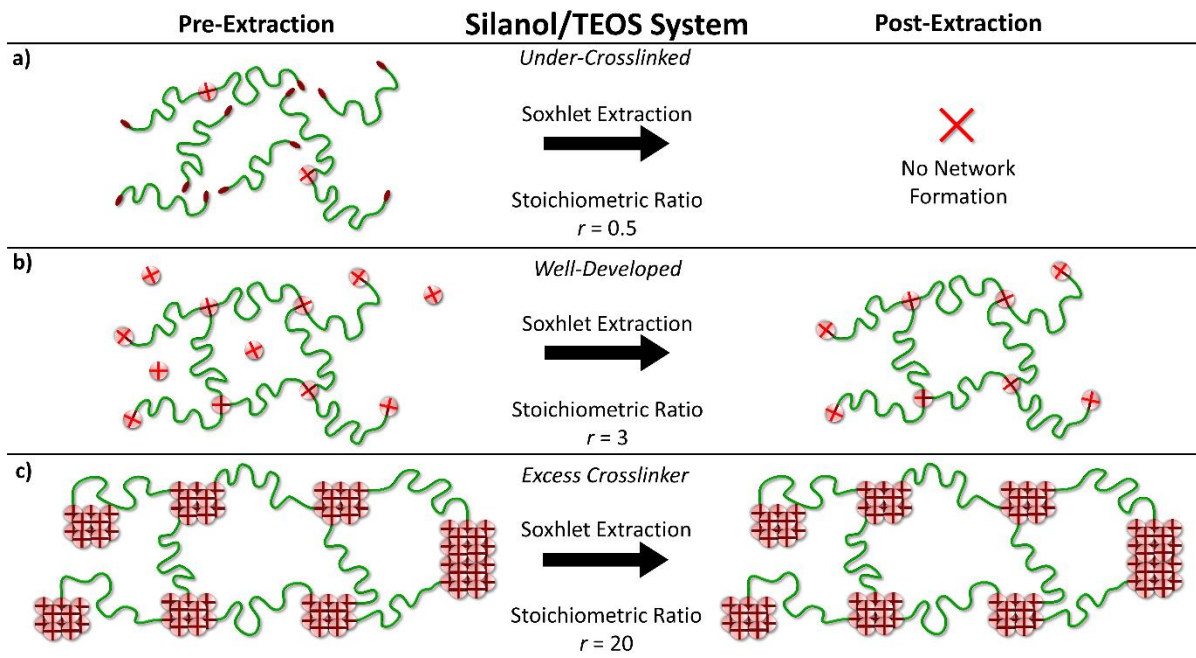


Figure 2.7 – Schematic illustration of different stoichiometric ratios and TEOS aggregation in the Silanol/TEOS system. Scenarios corresponding to stoichiometric ratios, $r = 0.5$, 3, and 20 are shown in a, b, and c, respectively. The left column portrays networks before the extraction process while the right column demonstrates how the extraction process removes material not covalently attached to or permanently trapped in the network. PDMS chains are shown as green lines with brown silanol end groups and the TEOS crosslinkers are shown as red “+” signs inside light red circles. Hydrolyzed and condensed TEOS groups are depicted as brown lines inside the red circle. The red “X” indicates the failure to form a fully crosslinked network. TEOS can react with itself in the presence of moisture and the Sn(II) catalyst, leading to aggregate formation, which is shown in c at a stoichiometric ratio of $r = 20$. This illustration is not meant to imply that the aggregates pack perfectly together. The size of PDMS chains relative to TEOS crosslinkers is not to scale, but the quantities of each are to scale with respect to r .

A similar trend between the Vinyl/TDSS system and the Sylgard 184 is observed in Figure 2.9. That is, with minor increases in Curing Agent to Base Ratio (*i.e.*, decreases in the Base to Curing Agent, B/C, ratio), the gel fraction increases rapidly and then begins to stabilize at a maximum value of ~ 0.95 for both 10:1 and 5:1 B/C ratio mixtures. An optimal ratio of crosslinker to polymer is necessary to achieve the highest gel fraction, as evident by the slight downward turn in gel fraction for additional decreases beyond the 10:1 (B/C) ratio.

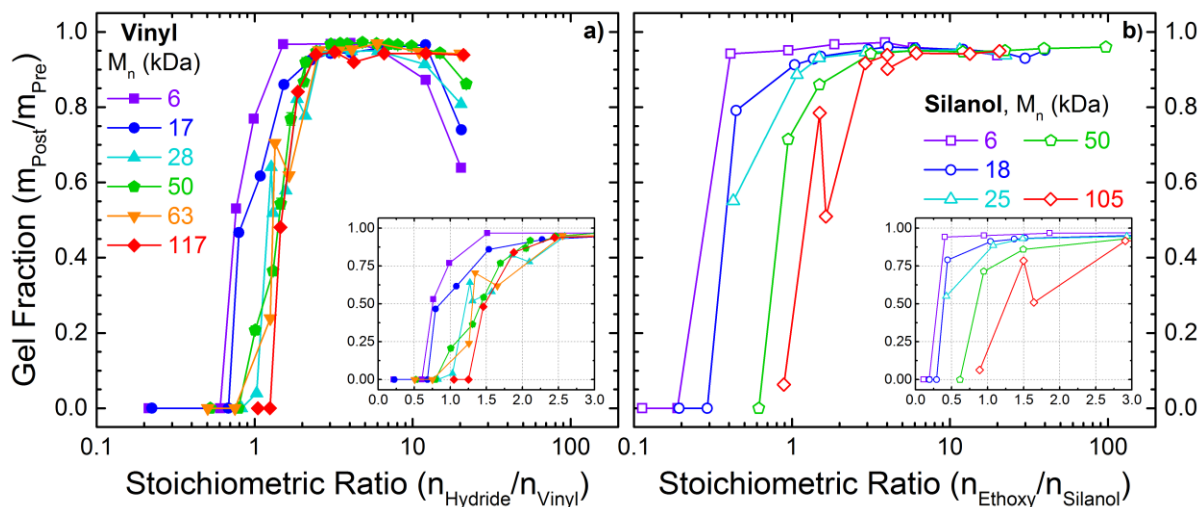


Figure 2.8 – Gel Fraction, w_{gel} , plotted as a function of the stoichiometric ratio, r , prepared in the Vinyl/TDSS systems (a) and Silanol/TEOS systems (b). Molecular weights prior to crosslinking are shown as colors that change from violet to red with increasing molecular weight. Insets show zoomed in regions of low r -values.

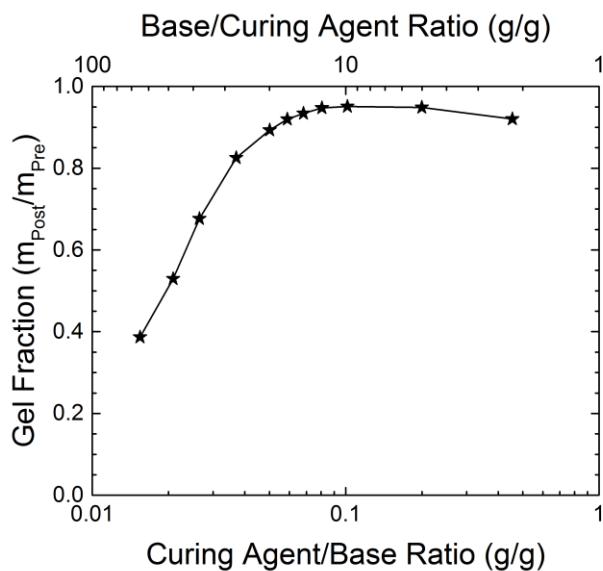


Figure 2.9 – Gel fraction of Sylgard 184 samples as a function of the Curing Agent to Base (C/B) mass ratio. The top abscissa shows the B/C ratio, where B/C=10:1 is the recommended formula in the instructions for the Sylgard 184 kit. The bottom abscissa is the inverse of the top, *i.e.*, the C/B ratio, to demonstrate visual similarity to the model systems with increasing amounts of crosslinker from left to right.

Discussion

Stoichiometry

The trends in the low stoichiometric ratio data match those predicted from the Miller-Macosko model, *i.e.*, a rapid increase in gel fraction with only incremental increases in crosslinker loading. Several other trends in the model PDMS systems warrant further discussion. The first item of interest is the precise optimal stoichiometric ratio that results in maximum gel fraction. Assuming 100% conversion of crosslinking functional groups, a scenario of $r = 1$ should be sufficient to form a fully crosslinked network because the functional groups of TDSS or TEOS are in perfect stoichiometric balance with those on the end-groups of PDMS. Previous studies^{54,61} have shown that a small excess of crosslinker ($1 < r \leq 2$) represented the optimal stoichiometric ratio that yielded the smallest degree of swelling and lowest sol fraction, although those experiments were conducted at different temperatures and for different durations than the current investigation. The data in Figure 2.8 reveal, however, that an excess of crosslinker on the order of $r \approx 2.5$ or greater is required to yield the highest gel fraction for the highest molecular weight systems. From these data, it is apparent that a greater excess in crosslinker loading, *i.e.*, $r > 2$, is necessary to achieve networks with the highest gel fraction for high molecular weights compared to lower molecular weights. That is the optimal stoichiometric ratio for achieve maximum gel fraction is increases with increasing molecular weight.

The data Figure 2.8 indicate that further increases in the crosslinker loading beyond $r \approx 6$, result in a decrease in gel fraction for the vinyl/TDSS systems for several molecular weights, but not in the silanol/TEOS systems. Remarkably, at very high stoichiometric ratios, *i.e.*, as $r > 10$, the gel fraction is similar to that at $r = 1$ in the vinyl/TDSS system for molecular weights less than 28 kDa. For the silanol-terminated networks, no such decrease is observed, even at incredibly high stoichiometric ratios of ~ 100 , which will be discussed later. Despite the inclusion of vinylated fumed silica particles and methylhydrosiloxane as the likely crosslinker, primarily in the Curing Agent component, a slight decrease in gel fraction at higher curing agent ratios still occurs with Sylgard 184 (*cf.* Figure 2.9). This behavior is similar to

the model vinyl/TDSS system, further indicating that hydrosilylation is the leading (if not sole) crosslinking mechanism in Sylgard 184.

Reaction and Diffusion Limitations Necessitate Excess Crosslinker

Recall the discussion of gelation kinetics pertinent to Figure 2.1 in the Introduction to this chapter. Many factors affect the gelation reaction and some can inhibit the reaction from going to completion. Such phenomena can be lumped collectively into the concepts of reaction and diffusion limitations, and these limitations are responsible for the requirement of excess crosslinker beyond the stoichiometric balance to achieve high gel fractions. The reaction mixtures are solvent-free, containing only crosslinker, catalyst, and telechelic polymer chains, which can have very high viscosity at high molecular weight. Thus, the crosslinker molecules must diffuse through tortuous paths of entangled polymer chains (except for low molecular weights at the onset of the reaction) to find a reactive polymer end-group. Once an active end-group of a polymer chain is found, the catalyst must first diffuse to meet these two functional groups, and then a reaction occurs with one of the 4 available functional groups on the crosslinker molecule. From there, 3 more unique chain-ends must then diffuse and find this crosslinker junction before the catalyst leaves or at the same time that another catalyst arrives. Upon being in close enough proximity to the crosslink junction and catalyst, each chain-end must then overcome the activation energy barrier to react in order to achieve a true network junction functionality of $f = 4$. The steric hindrance associated with 4 unique polymer chain ends - all being in close enough proximity to find a single crosslinker molecule and react - creates an additional significant barrier. There are also the issues of unwanted side-reactions using up available crosslinking sites.^{36,62} Therefore, it is not so surprising that such fully reacted crosslink junctions do not occur 100% of the time (see Chapter 3 of this dissertation for data and explanation).

In addition to these reaction limitations, the barriers to diffusion increase dramatically as the reaction proceeds due to increasing viscosity during gelation, which is caused by larger and larger net-like structures chemically reacting and growing until they percolate the entire sample volume, thus forming the incipient gel. As discussed previously, the gel point (*i.e.*, the

extent of reaction such that the incipient gel has formed) is an extent of reaction not sufficiently high to form a fully-crosslinked network. Hence, the crosslinking reaction will still proceed, but with ever growing limitations that slow down the rate. As the viscosity increases, chain-ends and crosslinker molecules may become trapped or immobilized, rendering them inert and thus unable to contribute to gelation. All told, the ever decreasing molecular mobility during gelation consistently diminishes the likelihood of all four reactive groups of a crosslinker molecule reacting with four unique polymer chain-ends.

In systems with low molecular weight PDMS chains, initially there will be a lower diffusion barrier, due to lower viscosity. In fact, holding viscosity constant, the initial reaction rate in low molecular weight systems will likely be much faster than that in higher molecular systems due to there being a greater concentration of polymer end-groups and crosslinker molecules, assuming simple first order kinetics rate law behavior. Despite beginning the reaction with lower viscosity and greater mobility, as the reaction progresses, the chains crosslink and grow, rapidly increasing viscosity until the previously described diffusion limitations become present. Thus, it is unlikely that every available functional group on both polymer chains and crosslinker molecules initially present will react (*cf.* Chapter 3 in this dissertation). These uncrosslinked crosslinker molecules and PDMS chains will be removed during the subsequent Soxhlet extraction, and become part of the sol fraction.

Differences in Molecular Weight

Upon close inspection of Figure 2.8, it appears that lower molecular weight PDMS samples (violet data sets in Figure 2.8) approach a gel fraction value of 1 closer to the theoretically expected stoichiometric ratio of $r = 1$, especially in the silanol/TEOS system, compared to the highest molecular weights tested (red data sets in Figure 2.8). Based on the previous discussion, chain mobility is likely playing a role here. Perhaps more significant than the viscosity effects, when comparing the highest and lowest molecular weights of PDMS tested for both systems, the mixtures at equivalent stoichiometric ratios of $r = 1$ are noticeably different in terms of their composition by mass, as demonstrated in Figure 2.10. This difference only increases with increasing stoichiometric ratios.

Mass Fraction of Crosslinker

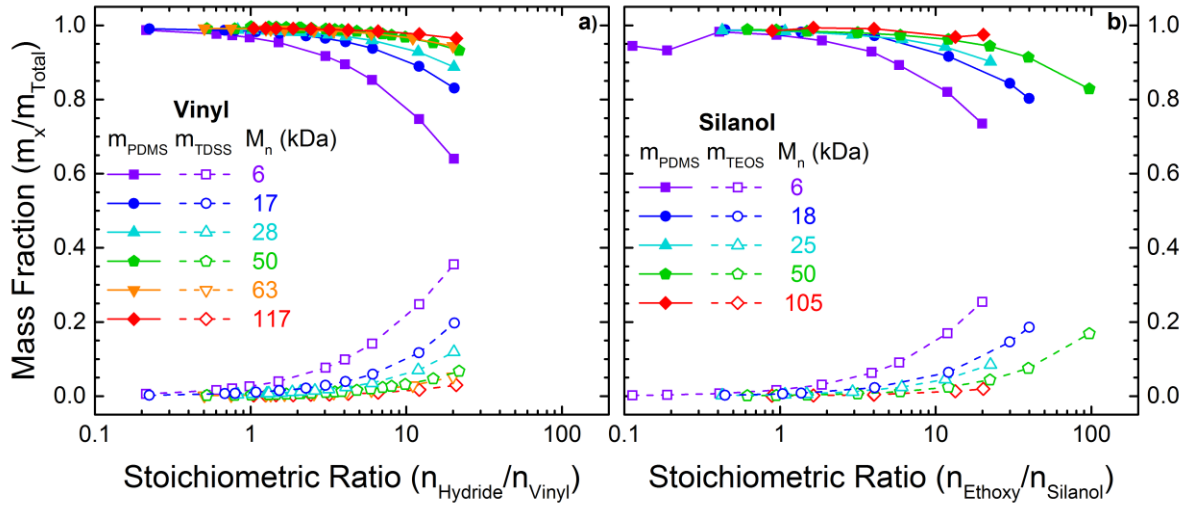


Figure 2.10 – Mass fraction of polymer (filled symbols) and crosslinker (open symbols) for the vinyl/TDSS system (a) and the silanol/TEOS system (b) plotted as a function of the stoichiometric ratio.

In Figure 2.10, the mass fractions of polymer (filled symbols) and crosslinker (open symbols) in the silicone elastomer mixtures are plotted as a function of stoichiometric ratio for the Vinyl/TDSS system (a) and the Silanol/TEOS system (b). In both crosslinking chemistries used, the concentrations of polymer end-groups and crosslinker molecules in the 6 kDa systems are much higher than in the high molecular weight systems. Higher concentrations of reactive groups mean that the probability of a molecular collision that results in a chemical reaction is much greater. Thus, initially, in the lower molecular weight systems, the rate of reaction will be faster due to both lower viscosity and higher concentration of reactive groups. The mass fraction of polymer begins to decrease significantly at high crosslinker loading for all but the highest molecular weights. Therefore, one would expect the gel fraction to begin decreasing dramatically for $r > 10$ at all molecular weights except those greater than 100 kDa due to the excess crosslinker molecules, which essentially act as solvent and simply occupy space without reacting. For this hypothesis to be

true, the crosslinker molecules must be not be able to react with each other, rendering inert excess components that will likely be removed during Soxhlet extraction.

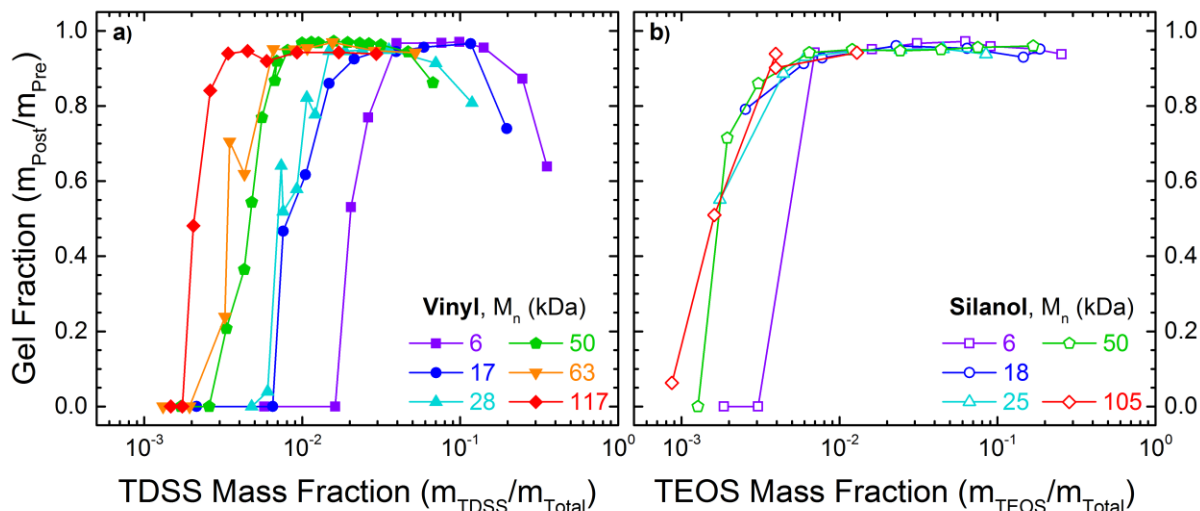


Figure 2.11 – Gel fraction plotted as a function of mass fraction of crosslinker for the vinyl/TDSS systems (a) and the silanol/TEOS systems (b).

In Figure 2.11, the gel fraction is plotted against the TDSS mass fraction for Vinyl/TDSS system (Figure 2.11a), and against the TEOS mass fraction for silanol/TEOS system (Figure 2.11b). For the vinyl/TDSS system, we see that an order of magnitude greater mass fraction of TDSS is required to form a network with a gel fraction of ~ 0.5 for 6 kDa vs. 117 kDa PDMS. The difference in mass fraction of crosslinker needed for gelation in the Silanol/TEOS system over the range of molecular weights tested is not nearly as large as that in the Vinyl/TDSS system. This is, in part, due to the different molecular weights of TDSS and TEOS molecules, which are 328.73 Da and 208.33 Da, respectively. For the same r -value the lower molecular weight of TEOS means that the TEOS will have a smaller mass fraction than TDSS. When high stoichiometric ratios ($r > 10$) are considered, the concentration and mass fraction of crosslinker molecules become rather significant and likely contribute to the decrease in gel fractions observed in the Vinyl/TDSS system. The data are less spread out in the Silanol/TEOS system, which is due, in part, to the difference in molecular weights, as well

as due to the different reaction equilibrium conditions for the two different types of crosslinking chemistries studied. It is apparent that the Silanol/TEOS is more reactive than the Vinyl/TDSS system because less TEOS is needed, in terms of the molar stoichiometric ratio and the mass fraction of TEOS, to form a network with high gel fraction compared to TDSS (*cf.* Figure 2.8). Other plausible explanations for the difference between these two systems are that there are different amounts of catalyst relative to polymer used when we compare the use of Pt(II) in the Vinyl/TDSS system to Sn(II) in the Silanol/TEOS system. Besides different amounts of catalyst, the activity and mechanisms of the catalyst, Pt(II) *vs.* Sn(II), could very well be different, resulting in different extents of reaction in the two systems.

End-Capping Chains vs. Aggregation

The decrease in w_{gel} in the Vinyl/TDSS system may be due to a phenomenon called “end-capping,” which is illustrated in Figure 2.6c. TDSS cannot bond with itself; the only other functional groups present in the system with which it can bond are the vinyl end-groups of the PDMS chains. There is evidence to suggest a side reaction with water, but it is negligible compared to the reaction with alkenes.⁶¹ When a large excess of TDSS with respect to the number of polymer end-groups (*i.e.*, high stoichiometric ratios) is used, individual, unreacted TDSS molecules can react once on each polymer end-group, which diminishes network formation. To promote network formation, an individual TDSS molecule must react with more than one end-group of at least two unique polymer chains. Two end groups on a single chain would form a loop, which is elastically ineffective unless it contains trapped entanglements with other chains (*cf.* Chapter 3 of this dissertation). When many individual and unreacted TDSS molecules react only once with polymer end-groups, this effectively renders polymer chains inert for crosslinking and causes them to be part of the sol fraction. In contrast, for low stoichiometric ratios in which there are not enough TDSS molecules to react with each polymer end-group, unreacted polymer chains are part of the sol fraction (*cf.* Figure 2.6a). In summary, if the crosslinker molecules are incapable of reacting with each other, excess crosslinker loading can result in a network that behaves similarly to one that is “under crosslinked” or not fully developed in the Vinyl/TDSS system.

This behavior does not seem to take place in the Silanol/TEOS systems. TEOS, once hydrolyzed to form silanol groups, can indeed react with itself via condensation, which can lead to *in situ* generation of silica-like aggregates or filler particles in siloxane networks.^{63–66} Therefore, at high stoichiometric ratios, end-capping is highly unlikely to occur and the gel fraction will stay stable and near a value of one, indicating a well-developed network. In principle, these TEOS aggregates can form a more tightly bound network compared to only polymer chains due to TEOS clusters forming silicate-like structures and perhaps even silica particles that are connected chemically to the PDMS chains and to each other. In fact, scanning electron microscopy (SEM) confirmed the presence of these TEOS aggregates, as can be seen in Figure 2.12 as the white dots and clusters in b) while no such spots or clusters are visible in a. The influence of these aggregates can dramatically change the mechanical properties of the material, which will be discussed in Chapters 4 of this dissertation.

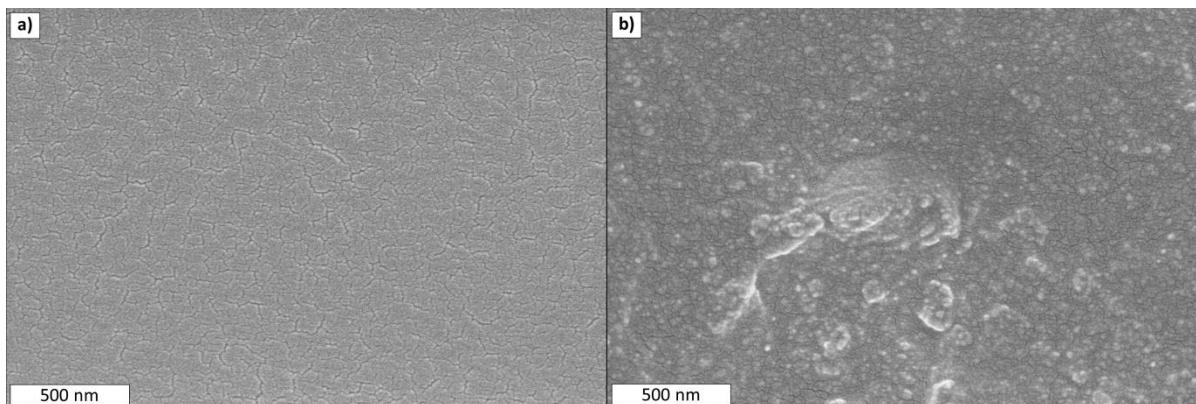


Figure 2.12 – Scanning electron microscopy (SEM) images of cross-sections of Silanol/TEOS PDMS samples of $r = 1.5$ and $r = 40$ in a and b, respectively.

In Figure 2.12, the aggregates were observed in cross-sections of the samples. The effect of TEOS aggregates can also be observed on the surface in the form of topographical wrinkles. For the $r \approx 12$ and $r \approx 20$ samples in the 6 kDa Silanol/TEOS system, wrinkles on the mm length scale are visible to the naked eye, as seen in Figure 2.13. These wrinkles do not occur in the parameter space sampled in the Vinyl/TDSS system or for any other molecular weight in the Silanol/TEOS system. Therefore, there are two parameters necessary for

wrinkling to occur. First TEOS must be present above some critical minimum concentration or mass fraction. Second, PDMS chains must be below some critical maximum molecular weight. Referring back to Figure 2.10, we see that the $r = 12$ sample of 6 kDa has ~15% TEOS by mass. However, at 15% TEOS by mass in higher molecular weight samples, this wrinkling is not observed.

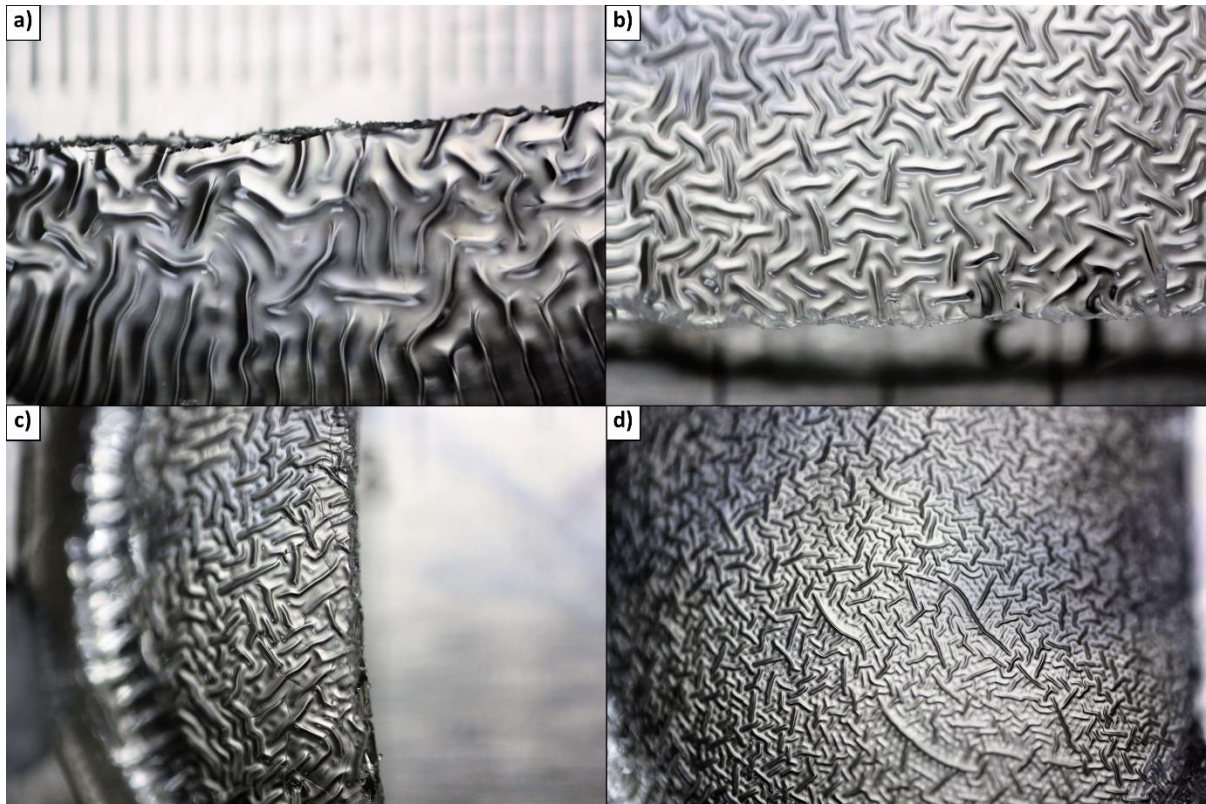


Figure 2.13 – Digital photographs demonstrating the macroscopic (mm length scale) topographical wrinkles at the air interface in certain Silanol/TEOS systems with high TEOS loading and low, 6 kDa molecular weights. Figures a and b correspond to $r = 12$ and c and d correspond to $r = 20$. The tick marks in a) are mm spacers.

This has been observed before⁶⁷ and is likely due to a concentration gradient in TEOS in the vertical direction. During the crosslinking at 70°C, the elevated temperature causes some TEOS molecules to have increased propensity to vaporize, resulting in TEOS molecules diffusing to the air interface. As they crosslink and aggregate with the short PDMS chains near the surface, stress may build up in the material that is not uniform in depth, which could result

in this phenomenon. This is also supported by the water vapor diffusing down from the surface into the material, making a concentration gradient in water. Both of these concentration gradients can result in non-uniform crosslinking from the surface down into the bulk.⁴⁹ With the higher molecular weights tested, it seems as though the stress build-up is not great enough to cause this phenomenon to occur. In fact, this hypothesis predicts a vital criterion for forming such surface wrinkles and instabilities; non-uniform stiffness in the depth-direction of a material. That surface instabilities arise when there are two layers near the surface and the top-most layer has greater stiffness than the underlying layer.^{68,69}

Conclusions

In this chapter, we have laid out the network preparation procedures for making silicone elastomers that will be studied throughout the remainder of this dissertation. Two model systems and one commercial product were prepared over a variety of different crosslinking stoichiometric ratios while maintaining the same curing conditions (temperature and time) and relative amounts of catalyst. The gel fraction of the networks were obtained through Soxhlet extraction in toluene, which allowed molecules that were not covalently attached to or permanently trapped in the network to diffuse out of the gel and into the pure toluene solvent, thus lowering the sample mass. An excess amount of crosslinker above the stoichiometric balance ($r = 1$) was necessary for all systems to reach maximum gelation under reaction conditions of 1-3 h at room temperature followed by 24 h at 70°C, indicating that not all of the available crosslinker sites were reacted. This incomplete reaction of all crosslinking sites will be explored in Chapter 3 of this dissertation. We observed a decrease in gel fraction for the Vinyl/TDSS and Sylgard systems at large excesses of crosslinker, but not for the Silanol/TEOS system. This is due to the TEOS molecule being able to react with itself, but TDSS (and all silicone hydride, Si-H, functional groups) being unable to react with itself. Further, when a massive excess of TDSS is present, these crosslinker molecules can react individually with each polymer chain end, but with no other unique polymer chains, thus creating an “end-capping” effect that causes those chains to become inert and part of the sol fraction. With a massive excess of TEOS, the crosslinker molecules cluster together and form aggregates that

can result in built-in stress in low molecular weight systems and lead to the formation of corrugated surface topographies.

This chapter lays the ground-work for the chapters to come. Now that a sound understanding of what the extraction process does to samples has been established, the extracted samples will be studied further. The next chapter will reveal molecular-level insights of the Vinyl/TDSS system by using the Miller-Macosko model to demonstrate how the system changes with varying amounts of crosslinker relative to polymer. After that, a discussion of the mechanical and swelling properties of extracted samples will take place. This will be followed by an investigation to surface properties of samples both before and after extraction.

Acknowledgements

The author is very grateful to several individuals for their support in the work presented here. Yeongun Ko provided assistance with the PDMS size exclusion chromatography analysis and construction of the universal PS/PMMA calibration curve. Professor Kirill Efimenko gave initial guidance in PDMS network sample preparation. Additionally Zoe Klein and Dr. Edwin Walker helped make some of the PDMS network samples. Professor Julie N. L. Albert was helpful in teaching the Soxhlet extraction technique and provided useful discussions related to the excess crosslinker regime. Lastly, the author thanks Yiliang Lin for help in acquiring and analyzing the SEM micrographs and the Analytical Instrument Facility (AIF) at North Carolina State University for use of their SEM equipment.

Chapter 2 Appendix

Catalysts and Crosslinkers

A summary of the catalysts and crosslinkers used in preparing all of the PDMS samples discussed throughout this dissertation are given below. All reactants were used as received.

Table A2.1 – Catalysts and crosslinkers purchased and used in this research

Vendor	Product Number	Chemical Name	CAS #	Function
Sigma-Aldrich	S3242	Tin(II) 2-ethylhexanoate	301-10-0	Condensation Catalyst
Gelest	SIT7110.0	Tetraethoxysilane (TEOS)	78-10-4	Condensation Crosslinker
Sigma-Aldrich	432849	<i>cis</i> -Dichlorobis(diethyl sulfide)platinum(II)	1544-57-6	Hydrosilylation Catalyst
Gelest	SIT7278.0	Tetrakis(dimethylsiloxo)silane (TDSS)	17082-47-2	Hydrosilylation Crosslinker

Size Exclusion Chromatography

In an attempt to accurately characterize the molecular weight distributions of the PDMS polymer purchases from Gelest, we ran samples through size exclusion chromatography (SEC). All of the PDMS samples acquired from Gelest, Inc. were dissolved in HPLC-grade THF (Fisher) at a concentration of 2 mg/mL and passed through 0.2 μm PTFE filters before being analyzed by SEC. Samples were run through a Waters 2695 separations module and passed through a series of 3 Waters High Resolution (HR) Styragel columns filled with 5 μm particles (Styragel HR 4, Styragel HR 4E, Styragel HR 3) at a flow rate of 0.3 mL/min. A differential refractive index (DRI) detector (Optilab Rex, Wyatt Technology Co.) was used for detection and molecular weight analysis. The columns and detector were maintained at 25°C. A baseline was fit between the peak beginnings and ends in a plot of DRI intensity *vs.* elution time to baseline-correct the data. Polystyrene (PS) and poly(methylmethacrylate) (PMMA) standards (obtained from Fluka) were run with the same HPLC THF to build a universal calibration curve of molecular weight *vs.* elution time. The flow-marker peak, present in all samples due to the HPLC THF solvent, was used to calibrate elution times between all samples and PS and PMMA standards. An interpolation algorithm was run on the DRI *vs.* molecular

weight data to yield equidistant data sampling, which is necessary for accurate analysis. The Mark-Houwink-Sakurada constants for intrinsic viscosity-molecular weight relationships of linear PDMS⁷⁰ were used with the universal calibration curve.

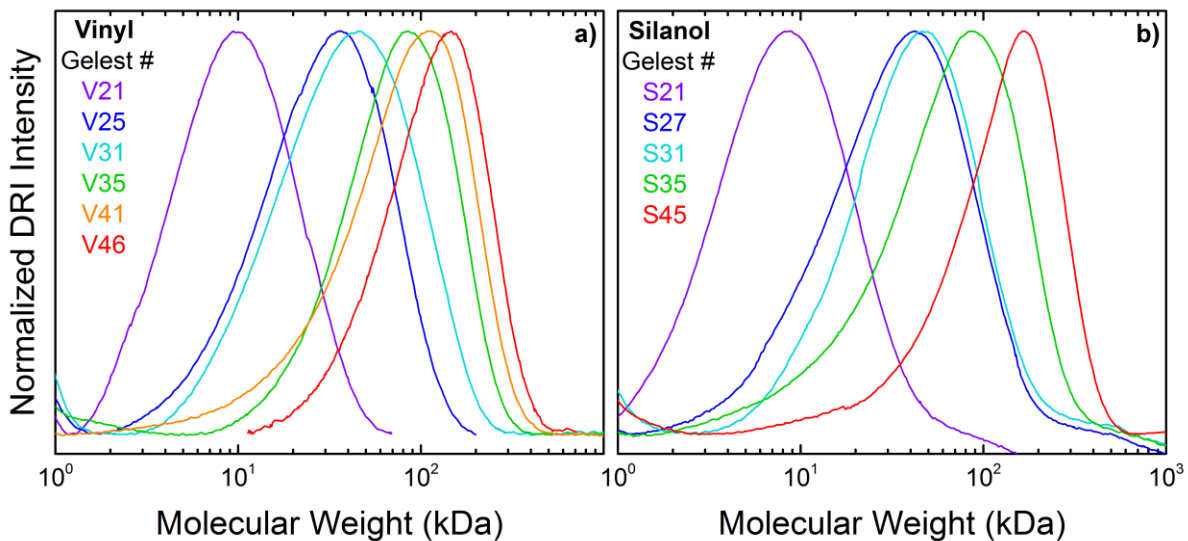


Figure A2.1 – Molecular weight distributions of samples purchased from Gelest, Inc. using size exclusion chromatography. The data were generated from size exclusion chromatography measurements in tetrahydrofuran with monodisperse polystyrene and poly(methylmethacrylate) standards.

The molecular weight distributions are given in Figure A2.1 where normalized DRI intensity is plotted as a function of molecular weight on a log scale. We attempted to calculate the sample number-averaged (M_n) and weight-averaged (M_w) molecular weights and dispersity (M_w/M_n) of the PDMS samples from Gelest. However, our calculated values were different than those reported by Gelest. We decided to use the values specified by Gelest in our subsequent calculations, as other researchers have done.^{71–73}

References

1. Araci, I. E. & Brisk, P. Recent developments in microfluidic large scale integration. *Curr. Opin. Biotechnol.* **25**, 60–68 (2014).
2. Fekete, Z. & Pongrácz, A. Multifunctional soft implants to monitor and control neural activity in the central and peripheral nervous system: A review. *Sensors Actuators B Chem.* **243**, 1214–1223 (2017).
3. Gossweiler, G. R. *et al.* Mechanochemically Active Soft Robots. *ACS Appl. Mater. Interfaces* **7**, 22431–22435 (2015).
4. Daniel, W. F. M. *et al.* Solvent-free, supersoft and superelastic bottlebrush melts and networks. *Nat. Mater.* 1–8 (2015). doi:10.1038/nmat4508
5. Paul, D. R. & Mark, J. E. Fillers for polysiloxane (‘silicone’) elastomers. *Prog. Polym. Sci.* **35**, 893–901 (2010).
6. Delebecq, E. & Ganachaud, F. Looking over Liquid Silicone Rubbers: (1) Network Topology vs Chemical Formulations. *ACS Appl. Mater. Interfaces* **4**, 3340–3352 (2012).
7. Delebecq, E., Hermeline, N., Flers, A. & Ganachaud, F. Looking over Liquid Silicone Rubbers: (2) Mechanical Properties vs Network Topology. *ACS Appl. Mater. Interfaces* **4**, 3353–3363 (2012).
8. Material Safety Data Sheet for Sylgard(R) 184 Silicone Elastomer Kit (BASE). 1–8 (2013). at <http://www.dowcorning.com/applications/search/products/Details.aspx?prod=01064291>
9. Material Safety Data Sheet for Sylgard(R) 184 Silicone Elastomer Kit (CURING AGENT). 1–8 (2014). at <http://www.dowcorning.com/applications/search/products/Details.aspx?prod=01064291>
10. Xia, Y. & Whitesides, G. M. SOFT LITHOGRAPHY. *Annu. Rev. Mater. Sci.* **28**, 153–184 (1998).
11. Qin, D., Xia, Y. & Whitesides, G. M. Soft lithography for micro- and nanoscale patterning. *Nat. Protoc.* **5**, 491–502 (2010).
12. Duffy, D. C., McDonald, J. C., Schueller, O. J. A. & Whitesides, G. M. Rapid prototyping of microfluidic systems in poly(dimethylsiloxane). *Anal. Chem.* **70**, 4974–4984 (1998).
13. McDonald, J. C. *et al.* Fabrication of microfluidic systems in poly(dimethylsiloxane). *Electrophoresis* **21**, 27–40 (2000).
14. McDonald, J. C. & Whitesides, G. M. Poly(dimethylsiloxane) as a material for fabricating microfluidic devices. *Acc. Chem. Res.* **35**, 491–499 (2002).

15. Halldorsson, S., Lucumi, E., Gómez-Sjöberg, R. & Fleming, R. M. T. Advantages and challenges of microfluidic cell culture in polydimethylsiloxane devices. *Biosens. Bioelectron.* **63**, 218–231 (2015).
16. Sackmann, E. K., Fulton, A. L. & Beebe, D. J. The present and future role of microfluidics in biomedical research. *Nature* **507**, 181–189 (2014).
17. Regehr, K. J. *et al.* Biological implications of polydimethylsiloxane-based microfluidic cell culture. *Lab Chip* **9**, 2132 (2009).
18. Rubino, E. & Ioppolo, T. Young's modulus and loss tangent measurement of polydimethylsiloxane using an optical lever. *J. Polym. Sci. Part B Polym. Phys.* **54**, 747–751 (2016).
19. Mata, A., Fleischman, A. J. & Roy, S. Characterization of Polydimethylsiloxane (PDMS) Properties for Biomedical Micro/Nanosystems. *Biomed. Microdevices* **7**, 281–293 (2005).
20. Khanafer, K., Duprey, A., Schlicht, M. & Berguer, R. Effects of strain rate, mixing ratio, and stress-strain definition on the mechanical behavior of the polydimethylsiloxane (PDMS) material as related to its biological applications. *Biomed. Microdevices* **11**, 503–508 (2009).
21. Li, J., Han, D. & Zhao, Y.-P. Kinetic behaviour of the cells touching substrate: the interfacial stiffness guides cell spreading. *Sci. Rep.* **4**, 3910 (2015).
22. Sun, Y., Jiang, L.-T., Okada, R. & Fu, J. UV-Modulated Substrate Rigidity for Multiscale Study of Mechanoresponsive Cellular Behaviors. *Langmuir* **28**, 10789–10796 (2012).
23. Hu, B. *et al.* Orthogonally engineering matrix topography and rigidity to regulate multicellular morphology. *Adv. Mater.* **26**, 5786–5793 (2014).
24. Brown, X. Q., Ookawa, K. & Wong, J. Y. Evaluation of polydimethylsiloxane scaffolds with physiologically-relevant elastic moduli: interplay of substrate mechanics and surface chemistry effects on vascular smooth muscle cell response. *Biomaterials* **26**, 3123–9 (2005).
25. Jeong, S. H., Zhang, S., Hjort, K., Hilborn, J. & Wu, Z. PDMS-Based Elastomer Tuned Soft, Stretchable, and Sticky for Epidermal Electronics. *Adv. Mater.* **28**, 5830–5836 (2016).
26. Schneider, F., Draheim, J., Kamberger, R. & Wallrabe, U. Process and material properties of polydimethylsiloxane (PDMS) for Optical MEMS. *Sensors Actuators, A Phys.* **151**, 95–99 (2009).
27. Schneider, F., Fellner, T., Wilde, J. & Wallrabe, U. Mechanical properties of silicones for MEMS. *J. Micromechanics Microengineering* **18**, 65008 (2008).
28. Yu, Y., Sanchez, D. & Lu, N. Work of adhesion/separation between soft elastomers of different mixing ratios. *J. Mater. Res.* **30**, 2702–2712 (2015).

29. Rubinstein, M. & Colby, R. H. *Polymer Physics*. (Oxford University Press, 2003).
30. Miller, D. R. & Macosko, C. W. A New Derivation of Post Gel Properties of Network Polymers. *Macromolecules* **9**, 206–211 (1976).
31. Macosko, C. W. & Miller, D. R. A New Derivation of Average Molecular Weights of Nonlinear Polymers. *Macromolecules* **9**, 199–206 (1976).
32. Johnston, I. D., McCluskey, D. K., Tan, C. K. L. & Tracey, M. C. Mechanical characterization of bulk Sylgard 184 for microfluidics and microengineering. *J. Micromechanics Microengineering* **24**, 35017 (2014).
33. Urayama, K. Network Topology–Mechanical Properties Relationships of Model Elastomers. *Polym. J.* **40**, 669–678 (2008).
34. Urayama, K., Kawamura, T. & Kohjiya, S. Structure–mechanical property correlations of model siloxane elastomers with controlled network topology. *Polymer* **50**, 347–356 (2009).
35. Matisons, J. *Hydrosilylation: A comprehensive review on recent advances*. (Springer, 2009). doi:10.1007/978-1-4020-8172-9
36. Esteves, A. C. C. *et al.* Influence of cross-linker concentration on the cross-linking of PDMS and the network structures formed. *Polymer* **50**, 3955–3966 (2009).
37. Miller, D. R., Valles, E. M. & Macosko, C. W. Calculation of Molecular Parameters for Stepwise Polyfunctional Polymerization. *Polym. Eng. Sci.* **19**, 272–283 (1979).
38. Valles, E. M. & Macosko, C. W. Properties of Networks Formed by End Linking of Poly(dimethylsiloxane). *Macromolecules* **12**, 673–679 (1979).
39. Valles, E. M. & Macosko, C. W. The Effect of Network Structure in the Equation of Rubber Elasticity. *Rubber Chem. Technol.* **49**, 1232–1237 (1976).
40. Gottlieb, M., Macosko, C. W., Benjamin, G. S., Meyers, K. O. & Merrill, E. W. Equilibrium Modulus of Model Poly(dimethylsiloxane) Networks. *Macromolecules* **14**, 1039–1046 (1981).
41. Chambon, F. & Winter, H. Stopping of crosslinking reaction in a PDMS polymer at the gel point. *Polym. Bull.* **13**, 499–503 (1985).
42. Winter, H. H. & Chambon, F. Analysis of Linear Viscoelasticity of a Crosslinking Polymer at the Gel Point. *J. Rheol. (N. Y. N. Y.)* **30**, 367–382 (1986).
43. Chambon, F. & Winter, H. H. Linear Viscoelasticity at the Gel Point of a Crosslinking PDMS with Imbalanced Stoichiometry. *J. Rheol. (N. Y. N. Y.)* **31**, 683–697 (1987).
44. Winter, H. H., Morganelli, P. & Chambon, F. Stoichiometry effects on rheology of model polyurethanes at the gel point. *Macromolecules* **21**, 532–535 (1988).
45. Venkataraman, S. K., Coynet, L., Chambon, F., Gottliem, M. & Winter, H. H. Critical extent of reaction of a polydimethylsiloxane polymer network. *Polymer* **30**, 2222–2226 (1989).

46. Chassé, W., Lang, M., Sommer, J.-U. & Saalwächter, K. Cross-Link Density Estimation of PDMS Networks with Precise Consideration of Networks Defects. *Macromolecules* **45**, 899–912 (2011).
47. Campise, F. *et al.* Contribution of Entanglements to Polymer Network Elasticity. *Macromolecules* [acs.macromol.6b02784](https://doi.org/10.1021/acs.macromol.6b02784) (2017). doi:10.1021/acs.macromol.6b02784
48. va der Weij, F. W. The Action of Tin Compounds in Condensation-type RTV Silicone Rubbers. *Die Makromol. Chemie* **181**, 2541–2548 (1980).
49. Pujol, J.-M. & Prébet, C. Functional silanes: crosslinkers for silicone elastomers. *J. Adhes. Sci. Technol.* **17**, 261–275 (2003).
50. Mark, J. E. & Sullivan, J. L. Model networks of end-linked polydimethylsiloxane chains. I. Comparisons between experimental and theoretical values of the elastic modulus and the equilibrium degree of swelling. *J. Chem. Phys.* **66**, 1006 (1977).
51. Andradý, A. L. *et al.* Model networks of end-linked polydimethylsiloxane chains. XII. Dependence of ultimate properties on dangling-chain irregularities. *J. Appl. Polym. Sci.* **26**, 1829–1836 (1981).
52. Valles, E. M. & Macosko, C. W. Structure and Viscosity of Poly(dimethylsiloxanes) with Random Branches. *Macromolecules* **12**, 521–526 (1979).
53. Llorente, M. a., Andradý, a. L. & Mark, J. E. Model networks of end-linked polydimethylsiloxane chains. XI. Use of very short network chains to improve ultimate properties. *J. Polym. Sci. Polym. Phys. Ed.* **19**, 621–630 (1981).
54. Patel, S. K., Malone, S., Cohen, C., Gillmor, J. R. & Colby, R. H. Elastic Modulus and Equilibrium Swelling of Poly(dimethylsiloxane) Networks. *Macromolecules* **25**, 5241–5251 (1992).
55. Takeuchi, H. & Cohen, C. Reinforcement of Poly(dimethylsiloxane) Elastomers by Chain-End Anchoring to Clay Particles. *Macromolecules* **32**, 6792–6799 (1999).
56. Lewicki, J. P. *et al.* in *Progress in Silicones and Silicone-Modified Materials* (eds. Clarson, S. J. *et al.*) **1154**, 133–154 (American Chemical Society, 2013).
57. Tordjeman, P., Fargette, C. & Mutin, P. H. Viscoelastic Properties of a Cross-Linked Polysiloxane Near the Sol-Gel Transition. *J. Rheol. (N. Y. N. Y.)* **45**, 995–1006 (2001).
58. Tixier, T., Tordjeman, P., Cohen-Solal, G. & Mutin, P. H. Structural effects on the viscoelasticity of polydimethylsiloxane networks close to the sol-gel threshold. *J. Rheol. (N. Y. N. Y.)* **48**, 39–51 (2004).
59. Lee, J. N., Park, C. & Whitesides, G. M. Solvent Compatibility of Poly(dimethylsiloxane)-Based Microfluidic Devices. *Anal. Chem.* **75**, 6544–6554 (2003).
60. Mark, J. E. & Sullivan, J. L. Model networks of end-linked polydimethylsiloxane chains. I. Comparisons between experimental and theoretical values of the elastic

- modulus and the equilibrium degree of swelling. *J. Chem. Phys.* **66**, 1006–1011 (1977).
61. Macosko, C. W. & Benjamin, G. S. Modulus of Three and Four Functional Poly(dimethylsiloxane) Networks. *Pure Appl. Chem.* **53**, 1505–1518 (1981).
 62. Quan, X. Properties of post-cured siloxane networks. *Polym. Eng. Sci.* **29**, 1419–1425 (1989).
 63. Dewimille, L., Bresson, B. & Bokobza, L. Synthesis, structure and morphology of poly(dimethylsiloxane) networks filled with in situ generated silica particles. *Polymer* **46**, 4135–4143 (2005).
 64. Sur, G. S. & Mark, J. E. Comparisons among some tetraalkoxysilanes in the hydrolytic precipitation of silica into elastomeric networks. *Die Makromol. Chemie* **187**, 2861–2866 (1986).
 65. Ning, Y.-P., Tang, M.-Y., Jiang, C.-Y., Mark, J. E. & Roth, W. C. Particle Sizes of Reinforcing Silica Precipitated into Elastomeric Networks. *J. Appl. Polym. Sci.* **29**, 3209–3212 (1984).
 66. Alexandru, M., Cristea, M., Cazacu, M., Ioanid, A. & Simionescu, B. C. Composite Materials Based on Polydimethylsiloxane and In Situ Generated Silica by Using the Sol–Gel Technique. *Polym. Compos.* **30**, 751–759 (2009).
 67. Li, Q. *et al.* Patterning Poly(dimethylsiloxane) Microspheres via Combination of Oxygen Plasma Exposure and Solvent Treatment. *J. Phys. Chem. B* **119**, 13450–13461 (2015).
 68. Genzer, J. & Groenewold, J. Soft matter with hard skin: From skin wrinkles to templating and material characterization. *Soft Matter* **2**, 310 (2006).
 69. Wang, Q. & Zhao, X. A three-dimensional phase diagram of growth-induced surface instabilities. *Sci. Rep.* **5**, 8887 (2015).
 70. Mrkvičková, L. & Radhakrishnan, N. The SEC estimation of $[\eta]$ -M relationship for linear poly(dimethylsiloxane) in tetrahydrofuran. *Eur. Polym. J.* **33**, 1403–1404 (1997).
 71. Jensen, K. E. *et al.* Wetting and phase separation in soft adhesion. *Proc. Natl. Acad. Sci.* **112**, 14490–14494 (2015).
 72. Cai, L.-H. *et al.* Soft Poly(dimethylsiloxane) Elastomers from Architecture-Driven Entanglement Free Design. *Adv. Mater.* n/a-n/a (2015). doi:10.1002/adma.201502771
 73. Li, C.-H. *et al.* A highly stretchable autonomous self-healing elastomer. *Nat. Chem.* **8**, 618–624 (2016).

CHAPTER 3: Molecular Insights Revealed from Applying the Miller-Macosko Model to the Vinyl/TDSS System

Introduction

In the Context of this Dissertation

In Chapter 2, we provided the preparation details for making the silicone elastomer materials that will be studied throughout this dissertation. In this chapter, we apply the Miller-Macosko model to only samples from the Vinyl/TDSS system to elucidate topological network parameters. The results from this model will be evaluated against independent measurements in subsequent chapters.

Polymer Theories

Polymer physicists have been developing theories to mathematically model and predict the behavior of polymers in various environments since the preeminent work by Flory and others in the 1940s. The well-known Flory-Huggins theory for polymer solutions was developed independently by Huggins¹ and Flory,² in 1942, and Huggins actually published his work a few months before Flory did. This widely used theory represents a simplified, yet robust thermodynamic model to predict phase behavior in polymer solutions and polymer blends. In 1953, Rouse³ developed a model to predict the diffusion of a single chain or chains in a very dilute solutions. The reptation model was developed by de Gennes⁴ in 1971 to expand upon the Rouse model and treated the motion of polymer as snake-like motion. Then, in a series of papers between 1978 and 1979, Doi and Edwards⁵⁻⁸ developed the tube model for reptation to successfully predict diffusion of high molecular weight chains that become entangled with their surroundings.

When it comes to polymer networks, however, the task of predicting the macroscopic mechanical properties from models based on single chains has proved to be very challenging. In 1943, Flory and Rehner presented their theory of rubber-like elasticity,^{9,10} which used statistical mechanics to model elastic deformation of polymer networks when they undergo

isotropic strain due to swelling from a solvent. This was expanded upon to account for defects and trapped entanglements by Langley¹¹ and Graessley¹² in 1968 and 1974, respectively. In 1976, Miller and Macosko^{13,14} published a recursive method that uses probabilities of reactions, initial stoichiometric conditions, and gel fraction data as a way to calculate a variety of topological network parameters that are used in the Langley and Graessley model. The Miller-Macosko model did not account for loop defects but provided a means to calculate the so-called entanglement trapping factor introduced by Langley.¹¹ Research in this area is still ongoing. To quote Zhong *et al.*¹⁵ in a 2016 *Science* article, “Understanding the correlation between the network topology and properties is one of the greatest outstanding challenges in soft materials.”

The challenge arises due to the highly complex nature of polymer networks. Take the human brain, for example, where many neurons are connected to each other at nodes, called synapses. It is estimated that there are many more synapses than stars in the Milky Way galaxy.¹⁶ Somehow this connected network of chemical signals in the brain gives rise to awareness, consciousness, and intelligence that make all living animals unique. We do not yet know how this happens, but the rise of artificial intelligence based on computer neural networks is proving to be one way we are quickly learning. Polymer networks can be thought of in a similar fashion. Polymer physicists can successfully model single polymer chains, dilute polymer solutions, and even densely packed polymer blends. However, massive complexity rapidly arises when many individual polymer chains are all connected to each other at junctions. These junctions cause restrictions in chain mobility and conformations and result in non-linear responses to surrounding chains when one local region is perturbed, making modeling and prediction a very challenging problem to solve.

The purpose of this chapter is to demonstrate the value of information gained when applying the Miller-Macosko model to polymer networks. Although not perfect, many insights to network topology can be elucidated from this model to gain a deeper understanding about the molecular architecture of the networks prepared in the preceding chapter of this dissertation. By applying this model, one is able to draw stronger conclusions about observed macroscopic properties and relate those observations back to molecular-level network

structure, consequently elucidating structure-property relationships. Without this model, many properties of the network would remain unknown and thus, conclusions about material properties would be made with incomplete information. It is prudent for researchers conducting investigations with polymer networks to apply either this model or other network theories to relate molecular network structure to their macroscopic observations and draw more sound conclusions.

Entanglements

One of the greatest challenges to developing accurate theories of polymer networks is the concept of entanglements. The current understanding of entanglements is that they arise due to the physical barriers of chains, which prevent them from crossing each other. That is, polymer chains cannot pass through each other. This results in the confinement of single-chain polymer motion to snake-like reptation (*vide infra*) When chains are highly concentrated and sufficiently long enough, polymers become entangled. This concept is analogous to cooked spaghetti noodles that have been poured through a strainer and allowed to dry. It is nearly impossible to pull just one noodle out of the entire bunch of noodles; instead, pulling one noodle results in many other noodles being pulled as well, due to entanglements among the noodles. When polymer chains are short (think penne noodles) and present in dilute environments, they are free to exist in highly globular conformations and, thus, are unentangled. In this regime, the Rouse³ model predicts accurately their motion. This model assumes a bead-and-spring design that connects monomer units to each other with a friction coefficient assigned to each bead. The time it takes for a polymer chain to move the equivalent of its own size is given by the Rouse time, τ_R . In contrast, in a highly concentrated environment with long chains, such as a polymer melt, polymers will be highly entangled. In this scenario, a single polymer chain within a polymer melt can be thought of as a snake inside a confined tube. The reptation model^{4,5} treats polymers according to this analogy where the confined tube is the result of all the other chains surrounding the chain of interest. There are multiple types of motion the snake-like chain can make and each type of motion has an associated time scale. The time it takes the chain (snake) to move (slither) out of its original confinement tube is

called the reptation time, τ_{rep} . The characteristic reptation time is greater than the characteristic Rouse time.

How does one know when polymer chains are long enough to become entangled? There are two different values of molecular weights that trigger the onset of behavior associated with entanglements. One value is obtained by performing either stress relaxation or oscillatory shear rheology experiments to determine the plateau modulus, G_e , of a polymer melt. The modulus is simply the stress (force per unit area on which the force is acting) required to deform a material divided by the strain or deformation of the material. Strain is often reported as a percent of initial material dimensions, thus giving the modulus units of pressure. The plateau modulus, G_e , is a region on the modulus vs. frequency (or time) graph wherein the modulus is constant over a wide range of frequency (or time-scales), hence the term “plateau.” An example of this is given in Figure 3.1, which is reproduced here from Macosko and Benjamin¹⁷ and for PDMS gives a plateau modulus value of 0.24 ± 0.02 MPa. This frequency-independent modulus is due to a temporary network-like structure formed solely from temporarily trapped entangled chains that do not relax over the time-scale of the measurement.¹⁸ The time-scale for which this temporary network exists is called the Rouse

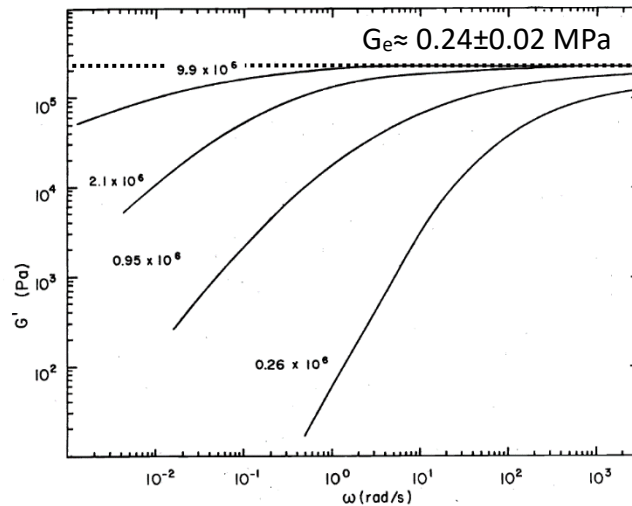


Figure 3.1 – Adapted from Macosko and Benjamin.¹⁷ Shear storage modulus, G' , plotted as a function of angular frequency, ω , for PDMS weight-average molecular weights of 9.9×10^6 , 2.1×10^6 , 0.95×10^6 , and 0.26×10^6 g/mol. The plateau modulus is extrapolated down to zero frequency from the plateau region in the high frequency portion of the graph.

time for entanglement strands, τ_e . Rubinstein and Colby¹⁸ define the number-average molecular weight of an entanglement strand as M_e , which can be thought of as the molecular weight between entanglements. Therefore, the relationship between shear plateau modulus and entanglement molecular weight is given by Equation (3.1).

$$G_e \approx \frac{\rho RT}{M_e} \quad (3.1)$$

Here, ρ is the polymer melt density (0.97 g/cm³ for PDMS), R is the universal gas constant, and T is the absolute temperature. Others have reported the plateau modulus for PDMS be ~ 0.20 MPa, giving an entanglement molecular weight of $M_e = 12$ kDa.¹⁸

There is another way to define entanglement molecular weight in polymer melts using viscometry. The critical molecular weight for entanglement effects in viscosity, M_c , is usually 2 to 4 times larger than the entanglement molecular weight, M_e .¹⁸ This is because in typical viscosity experiments, measured polymer chains must move along the entire contour length of their confining tube according to the reptation model. Viscosity is inversely proportional to strain rate while the plateau modulus is inversely proportional to strain. The reptation model thus predicts the following relationship between viscosity and plateau modulus.

$$\eta \approx G_e \tau_{rep} \quad (3.2)$$

Longin *et al.*¹⁹ compiled many viscometric measurements and normalized for different temperatures at which the experiments were performed. The compilation of data is reproduced in Figure 3.2 below. The classical determination of critical molecular weight of entanglement, M_c , is done by plotting zero-shear viscosity, η_0 , as a function of weight-averaged molecular weight, M_w , on a log-log scale. Below the critical molecular weight of entanglement, M_c , the viscosity increases linearly with increasing molecular weight. The critical entanglement molecular weight is defined as the molecular weight where the slope changes to a value of 3.4 with zero shear viscosity plotted against molecular weight on a log-log scale. The data shown by Longin *et al.*¹⁹ estimates $M_c = 28$ kDa. This is in agreement with predictions by Graessley and Edwards,²⁰ who demonstrated that for PDMS, the plateau modulus detects ~ 2.4 times as many interactions as viscous flow, or mathematically, $M_c/M_e \approx 2.4$. In other words, a molecular weight ~ 2.4 times greater is needed in viscometric tests to change the slope from ~ 1 to ~ 3.4

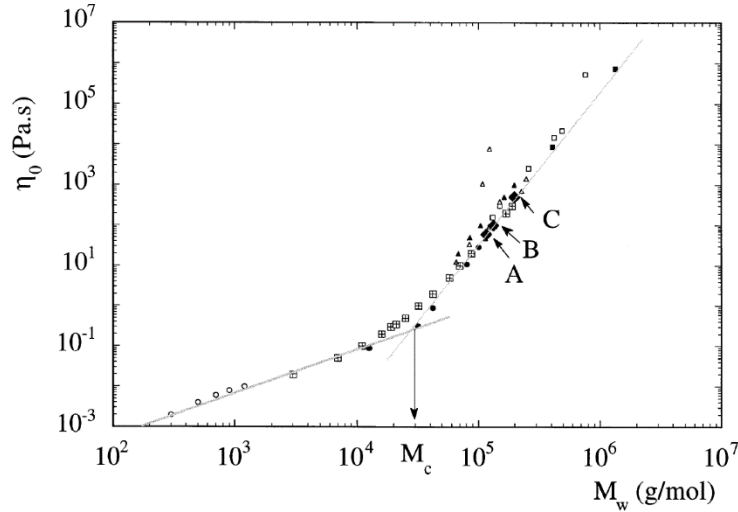


Figure 3.2 – Adapted from Longin *et al.*¹⁹ Zero-shear viscosity, η_0 , plotted as a function of weight-averaged molecular weight. Data was compiled by Longin *et al.*¹⁹ and normalized for temperature differences.

compared to the molecular weight that forms a temporary network-like structure in dynamic mechanical testing. To recap, the molecular weight between entanglements, M_e , given by Rubinstein and Colby¹⁸ is 12 kDa and when multiplied by 2.4 yields 28.8 kDa, which is in excellent agreement with the critical molecular weight of entanglements, M_c , of 28 kDa given by Longin *et al.*¹⁹ Additionally, an earlier investigation and compilation of existing data by Kataoka and Ueda²¹ gave critical molecular weight of entanglements, M_c , of 30 kDa, which is also consistent with the value quoted by Longin.

While the preceding discussion may seem tangential to the theme of this chapter, it is vitally important to understand the concepts of entanglements within polymer systems, the different time scales associated with different types of polymer motions, and the methods for determining two distinct values of molecular weight that correspond to the onset of behavior caused by entanglements. The critical molecular weight of entanglement, M_c , which for PDMS is 28 kDa, will be important in the discussions to follow throughout this dissertation.

Real Elastic Network Theory – Loop Defects

In addition to entanglements, the concept of loop defects in networks has been challenging to model. A first order loop occurs when both ends of a polymer chain covalently

attach to the same crosslinker molecule. Higher order chains can exist, however, which will be more elastically effective, but not as elastically effective as chains with no loops (*cf.* Figure 3.3). Recently, Zhong *et al.*¹⁵ created well defined hydrogels by utilizing azide-terminated poly(ethylene glycol) (PEG) telechelic polymers chains and mixing them with alkyne-based crosslinkers that contained either three or four functional alkyne groups. The generic system they studied was end-linking of $A_2 + B_3$ ($f = 3$) and $A_2 + B_4$ ($f = 4$) systems, where A is the telechelic polymer chain, B refers to the crosslinkers, and f is the number available functional groups per crosslinker molecule. The deuterated end-groups permitted quantification of loop defects using a technique called symmetric isotopic labeling disassembly spectrometry (SILDaS). The size of the loop was measured in terms of the loop order, which is the number of chains in the loop (*cf.* Figure 3.3).

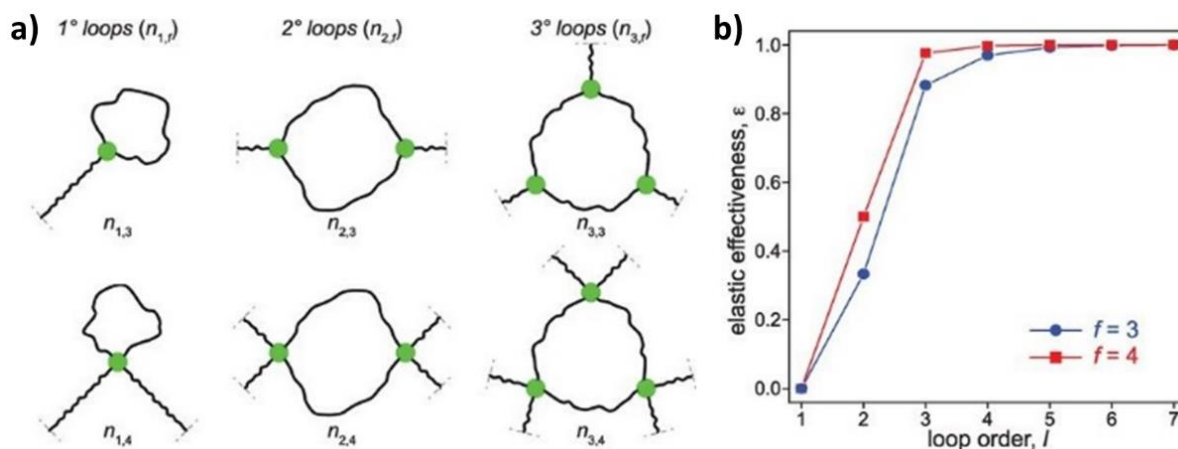


Figure 3.3 – Adapted from Zhong *et al.*¹⁵ In a), loops of the first (1°), second (2°), and third (3°) order are depicted in columns from left to right for 3- and 4-functional crosslinkers on the top and bottom rows, respectively. Nomenclature of $n_{x,y}$ refers to x -order loop with y -functionality crosslinker. In b), elastic effectiveness, ϵ , of chains within loops is plotted as a function of the loop order, l , for 3- (blue) and 4- (red) functional crosslinkers.

To quantify the loop defects and their effect on shear modulus, they derived a term called the elastic effectiveness, ϵ , which measures the relative elasticity of a chain. A value of 0 elastic effectiveness means the chain contributes no entropic restoring force and a value of 1 is the equivalent of an ideal elastically effective chain. Zhong and colleagues found that loops

of higher order than 5° loops for $f = 3$ systems and 3° loops for $f = 4$ systems had no significant decrease in elastic effectiveness (*cf.* Figure 3.3). However, loops of lower order had dramatic decreases in elastic effectiveness ultimately reaching 1° loops (a single chain with both ends attached to a crosslinker) that had zero elastic effectiveness. By measuring shear storage modulus, G' , as a function of quantity and type of loop defects, they were able to develop a new model titled the “Real Elastic Network Theory” (RENT), which accurately predicts their measured shear storage modulus values using accurate quantities of loop defects as inputs. One crucial note in this study is that all of the polymer chains before crosslinking were below their critical entanglement molecular weight, which eliminated the issue of dealing with entanglements during their analysis.

Miller–Macosko Model

The Miller-Macosko model was developed based on the recursive nature of polymer networks and thus uses branching theory and conditional probability laws to directly calculate a variety of topological network parameters. The step-by-step derivation of their original model is given in the literature,^{13,14} and the final equations used in this analysis are shown in the following section. There are several key assumptions to their approach. First, all functional groups of the same type are equally reactive. Second, all functional groups react independently of one another. This means that the last functional group on the crosslinker to react will be just as reactive as the first group on the crosslinker that reacted. Lastly, they assume that no intramolecular reactions occur in finite species. Here, “finite species” refers to material in the sol fraction. Thus, their model does not account for loop formation of chains that are not connected to the network. Additionally, Miller and Macosko do not explicitly account for first order loops as Zhong *et al.*¹⁵ were the first who accurately predicted the quantitative effect of topological loop defects on network elasticity. However, a rich understanding of topological network parameters and their relationships to initial crosslinking conditions can be gleaned from this analysis, which provides greater insight to the molecular network architecture.

Recently, Chassé *et al.*²² demonstrated the accuracy of the Miller-Macosko model. They used PDMS copolymers that contained random distributions of vinyl groups, which

allowed for random crosslinking along the side-groups with difunctional silicon-hydride crosslinkers. The overall extent of reaction, p , is defined as the fraction of total number of functional crosslinking groups that have reacted, *i.e.*, the fraction of silicon-hydride (Si-H) groups that have reacted out of all of the crosslinking molecules initially present in the system. They verified that the calculated p was very close to the experimentally determined p with double quantum NMR measurements. Although this system is different than the end-linking scheme employed in this dissertation, the crosslinking chemical reaction is the same. Therefore, the Miller-Macosko model is applied within this dissertation to calculate the extent of reaction and other network parameters under the assumption of its validity.

Most of the topological network parameters to be calculated from the Macosko-Miller model are depicted in Figure 3.4. Networks can be categorized into elastic, w_{el} , and pendant, w_{pen} , fractions, which are shown as green and red chains in Figure 3.4, respectively. The elastic fraction, w_{el} , is composed of elastically effective chains and junctions, which have concentrations of ν and μ , respectively. Elastically effective chains are polymers that are covalently attached to two different elastically effective crosslinker junctions. A crosslink junction is considered to be elastically effective if it connects two or more elastically effective chains. Defects that cause chains to be elastically ineffective (*i.e.*, pendant chains) can take several forms. Pendant material in which a chain is only connected to a crosslinker molecule at one end is called a dangling end. Pendant material can also be in the form of first order loops, which are chains that have both ends attached to the same crosslinking molecule. For a loop to be considered pendant and elastically ineffective, it must not contain any trapped entanglements. Therefore, dangling ends, loops without trapped entanglements, and lower order loops¹⁵ discussed previously are all defects that result in elastically ineffective chains and are thus encompassed by the pendant fraction.²²⁻²⁷

Elastically effective chains contribute an entropic restoring force similar to a spring when strain is applied. A chain has higher entropy when it is in a more globular configuration with many more possible conformation states as opposed to when it is elongated and has fewer possible allowed conformations. From a thermodynamic perspective, there is always a balance between entropy and enthalpy and the system wants to be in the lowest energy state possible.

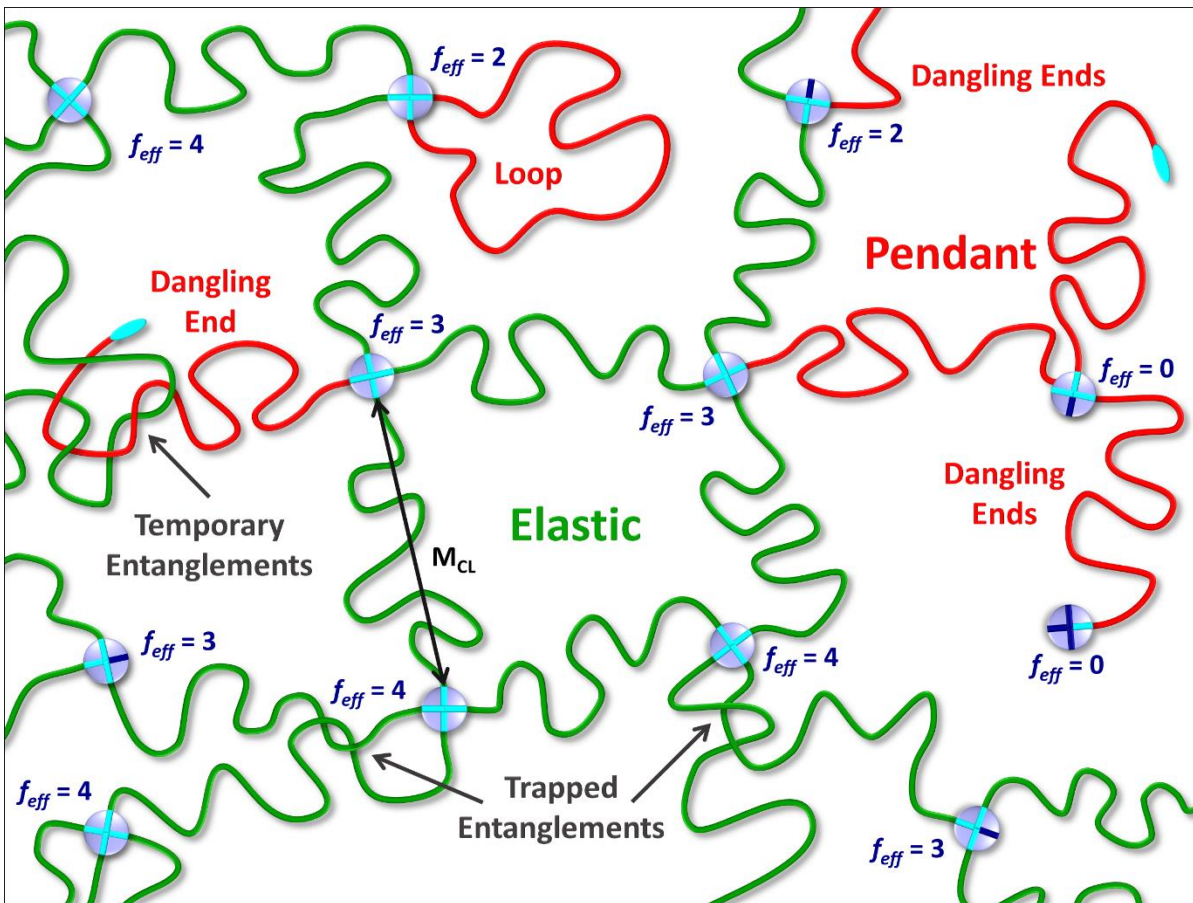


Figure 3.4 – Illustration of topological network parameters calculated from the Miller-Macosko model. Elastically effective chains are shown in green and pendant chains, as either dangling ends or loops, are shown in red. Trapped entanglements occur when all four ends of the two entangled chains are covalently bound to elastically effective crosslinks. Temporary entanglements occur with dangling ends and can disentangle. Molecular weight between elastically effective chemical crosslinks, M_{CL} , is shown as the black line with arrows at both ends. Crosslinker sites that have reacted are depicted as cyan lines inside light blue circles. Unreacted crosslinker sites are shown as navy blue lines inside the light blue circles. Effective crosslinker functionality, f_{eff} , is given for each crosslinker. Unreacted polymer end-groups are depicted as cyan ellipses.

This balance is encompassed by the Gibbs free energy, ΔG , equation, $\Delta G = \Delta H - T\Delta S$, where ΔH is the change in enthalpy and ΔS is the change in entropy. The Δ refers to a change from a reference state. To minimize the Gibbs free energy, the entropy should be maximized, thus chains do not like to be elongated and prefer to be restored to their globular configuration.

The functionality of crosslinker molecules used for model PDMS systems in this study has been held constant at a value of $f = 4$, but the functionality of the curing agent in Sylgard

184 is unknown. In both instances, however, not every available site on the crosslinker molecule will react with an elastically effective chain. Effective functionality, f_{eff} , is accordingly defined as the average number of functional groups per crosslinker molecule that have reacted with elastically effective chains. The molecular weight (in kDa) of elastically effective chains that span two elastically effective crosslink junctions is rightly called the molecular weight between elastically effective chemical crosslinks, $M_{CL,MM}$. The subscript “MM” is used to denote M_{CL} calculated from the Miller-Macosko model to distinguish it from the same parameter that will be calculated from other theories in subsequent chapters.

Furthermore, the Miller-Macosko model is used to calculate the so-called entanglement trapping factor, T_e . The entanglement trapping factor, T_e , as described by Miller and Macosko¹⁴ represents the probability that all four chain ends coming from an entanglement lead to the network. That means when two chains cross and form an entanglement, both ends of both chains must eventually be connected to an elastically effective chemical crosslink junction with $f_{eff} \geq 3$. The entanglement trapping factor changes from 0 when the extent of reaction equals the gel point, $p = p_{gel}$, and increases to a value of 1 for fully developed networks that have very few defects. Trapped entanglements, *i.e.*, those which cannot disentangle because the chain ends are covalently attached to a chemical crosslink junction, contribute some elasticity to the network in the form of quasi-tetra functional crosslink junctions. They do not contribute the same magnitude of elasticity as chemical crosslink junctions because the trapped entanglements can slide along chains until they hit another topological constraint.

Based on this abundance of topological network information to be gained, the application of the Miller-Macosko model to a polymer network system is highly advantageous and should be used whenever possible to draw stronger conclusions from macroscopic measurements and observations.

Experimental Methods

Miller-Macosko Model Calculations

According to the previous discussion of the Miller-Macosko model, there are many topological network parameters to be computed. The following section outlines the final forms of the equations used in their model. The density of elastically effective chains, ν (in mol/m³), and junctions, μ (in mol/m³), as well as the pendant, w_{pen} , and elastic, w_{el} , fractions of material present in the network after extraction (*i.e.*, present in the gel fraction, w_{gel} , portion of the material) were calculated according to the Appendix of Patel *et al.*²⁸ and the Appendix of Valles & Macosko.²⁹ Patel *et al.*²⁸ applied the Miller-Macosko^{13,14,30} model to the system of A₄ + B₂ (tetrafunctional crosslinker + difunctional polymer) networks, which is valid for the vinyl/TDSS system in the present investigation.

First, the extent of reaction, p , is calculated. To determine this quantity, the composition of the sol fraction is considered. The measured sol fraction, w_{sol} , comprises both unreacted crosslinker and polymer. In these calculations, the mass of catalyst is not considered due to it being present in negligible quantities. Therefore, the composition of the sol fraction is given in Equation (3.3).¹⁴

$$1 - w_{gel} = w_{sol} = w_{0,A_4} \alpha^4 + w_{0,B_2} \beta^2 \quad (3.3)$$

Here $w_{0,i}$ refers to the mass fraction of species i present in the initial mixture of polymer and crosslinker prior to crosslinking. The probability that a crosslinker molecule chosen at random, and all molecules covalently connected to it, are not connected to the network (*i.e.*, it is part of the sol fraction) is given by α . The probability of the same outcome when a polymer molecule is chosen at random is given by β . These probabilities are related both to the stoichiometric ratio, r , and the extent of reaction, p . Equations (3.4) and (3.5) give those relationships as follows.²⁹

$$\alpha = \sqrt{\frac{1}{rp^2} - \frac{3}{4}} - \frac{1}{2} \quad (3.4)$$

$$\beta = 1 - \frac{1}{p}(1 - \alpha) \quad (3.5)$$

The initial mass fractions, $w_{0,A4}$, $w_{0,B2}$, stoichiometric ratio, r , and sol fraction, w_{sol} , are all known or measured quantities as outlined in Chapter 2 of this dissertation. The only unknown is the extent of reaction of crosslinker groups, p . To proceed, we simultaneously solve the system of non-linear equations (3.3)-(3.5) using Solver in Microsoft Excel under the constraints that α , β , and p all be values between 0 and 1 since they are probabilities and an extent of reaction. To facilitate convergence to a solution, initial guesses for each of those parameters should also be between 0 and 1.

Next, the density of elastically effective chains, ν (in mol/m³), and junctions, μ (in mol/m³) are given by Equations (3.6) and (3.7).²⁸

$$\nu = \frac{[A_4]_0}{w_{gel}} [6\alpha(1 - \alpha)^3 + 2(1 - \alpha)^4] \quad (3.6)$$

$$\mu = \frac{[A_4]_0}{w_{gel}} [4\alpha(1 - \alpha)^3 + (1 - \alpha)^4] \quad (3.7)$$

Here $[A_4]_0$ is the initial concentration (in mol/m³) of crosslinker A₄ molecules present in the reaction mixture. Once the densities of elastically effective chains, ν , and junctions, μ , have been determined, the effective functionality of the chemical crosslink junctions, f_{eff} , can be calculated according to Equation (3.8).³¹

$$f_{eff} = 2\nu/\mu \quad (3.8)$$

Recall that α is the probability that a crosslinker molecule chosen at random, and all molecules connected to it, is part of the sol fraction, and that β is the same probability except when a polymer molecule is chosen at random. Combining these probabilities with the extent of reaction, p , enables calculation of bulk network parameters. These probabilities serve as inputs to calculating the pendant, w_{pen} , and elastic fractions, w_{el} , of material remaining in the gel fraction, w_{gel} , of the network after extraction. They are determined according to Equations (3.9) and (3.10), respectively.^{28,30}

$$w_{pen} = 2w_{0,B2}\beta(1 - \beta) + w_{0,A4} \left[4\alpha^3(1 - \alpha) + 12\alpha^2(1 - \alpha)^2 \frac{M_A}{M_{A4}} + 4\alpha(1 - \alpha)^3 \frac{M_A}{M_{A4}} \right] \quad (3.9)$$

$$w_{el} = w_{0,B2}(1 - \beta)^2 + w_{0,A4} \left[(1 - \alpha)^4 + 4 \left(1 - \frac{M_A}{M_{A4}} \right) (1 - \alpha)^3 \alpha + 6 \left(1 - 2 \frac{M_A}{M_{A4}} \right) (1 - \alpha)^2 \alpha^2 \right] \quad (3.10)$$

Here, M_A is the molecular weight (in g/mol) of one arm of an A_4 (crosslinker) molecule and M_{A_4} refers to the molecular weight (in g/mol) of one A_4 crosslinker molecule. The gel fraction of the network (*i.e.*, material remaining after Soxhlet extraction) consists of elastically effective, w_{el} , and pendant, w_{pen} , fractions that together sum to the value of the gel fraction w_{gel} , according to Equation (3.11).³⁰

$$w_{el} + w_{pen} = w_{gel} = 1 - w_{sol} \quad (3.11)$$

Next, the number-average molecular weight between effective chemical crosslink junctions, $M_{CL,MM}$, is determined according to Equation (3.12).³⁰

$$M_{CL,MM} = 2M_A + \frac{M_{B_{2n}} + [M_{A_4} - (f_{eff} - 2)M_A]C}{1 - C} \quad (3.12)$$

Here, $M_{B_{2n}}$ refers to the number-average molecular weight of the polymer prior to crosslinking. The term C represents the probability that a part of a chain chosen at random (either a monomer unit of PDMS or a crosslinker molecule) is connected to the gel at both ends (*i.e.*, is connected to an elastically effective junction). This probability is given by Equation (3.13).³⁰

$$C = \frac{3(1-\alpha)\alpha^2}{3(1-\alpha)\alpha^2 + 3(1-\alpha)^2\alpha + 3(1-\alpha)^3} \quad (3.13)$$

Lastly, the entanglement trapping factor, T_e , is determined according to Equation (3.14).¹⁴

$$T_e = (1 - \beta)^4 \quad (3.14)$$

Materials

In this chapter, the Miller-Macosko model is applied only to the Vinyl/TDSS model networks prepared according to the procedure described in Chapter 2 of this dissertation. The data from stoichiometry, molecular weight, and gel fraction are used as inputs to the Miller-Macosko formulas in this chapter. To briefly recap the network preparation details, vinyl-terminated, telechelic PDMS polymers of various molecular weights were purchased from Gelest, Inc. (*cf.* Table 3.1). A tetrafunctional crosslinker molecule (*i.e.*, one having 4 reactive groups per molecule), tetrakis(dimethylsiloxy)silane (TDSS) was also purchased from Gelest, Inc. A hydrosilylation catalyst, *cis*-dichlorobis(diethyl sulfide)platinum(II) (Pt catalyst) was purchased from Sigma-Aldrich. All reactants were used as received.

Table 3.1 – Vinyl-Terminated PDMS Materials Purchased from Gelest, Inc.

Product Code	Number-Averaged Molecular Weight, M_n (kDa)	Viscosity (cSt.)
DMS-V21	6	80 – 120
DMS-V25	17	450 – 550
DMS-V31	28	900 – 1,100
DMS-V35	50	4,000 – 6,000
DMS-V41	63	9,000 – 11,000
DMS-V46	117	55,000 – 75,000

Network Preparation & Gel Fraction Determination

To prepare each model Vinyl/TDSS PDMS network sample, *circa* 2.5-3.5 g of PDMS were mixed well with the Pt(II) catalyst solution in a polypropylene beaker followed by removal of air bubbles under moderate vacuum. For every gram of vinyl-terminated PDMS in each sample, 8 μ L of Pt(II) catalyst solution at a concentration of 0.011 g Pt (II) catalyst per mL of toluene were added. Next, a precise mass (and volume) of the crosslinker, TDSS, was added via micropipette over a balance to the PDMS/catalyst mixture yielding a specific desired stoichiometric ratio, r , defined in Chapter 2 of this dissertation.

After mixing well and degassing again, the solution was carefully poured into a polystyrene or polypropylene Petri dish. If needed, the Petri dish was degassed one last time. The sample in dish was then covered with a lid and placed on a level surface at room temperature exposed to atmospheric pressure for 2-3 hours of pre-curing, during which the polymer spread evenly throughout the Petri dish, giving a uniform thickness of \sim 0.7-1.5 mm (depending on how much polymer was added to the dish). Finally, the networks were placed in a 70°C oven at atmospheric pressure for 24 hrs. Soxhlet extraction in toluene, a good solvent for PDMS,³² was used to determine the gel (w_{gel}) and sol (w_{sol}) fractions of the networks according to the same method described in Chapter 2 of this dissertation.

In Chapter 2 of this dissertation, we discussed the methods of preparing networks and acquired corresponding gel fraction data, which are reproduced here in Figure 3.5. The gel

fraction data, along with molecular weight and stoichiometric ratio, r , are inputs into the Miller-Macosko model, which reveals insights into the molecular-level architecture of the networks that were prepared.

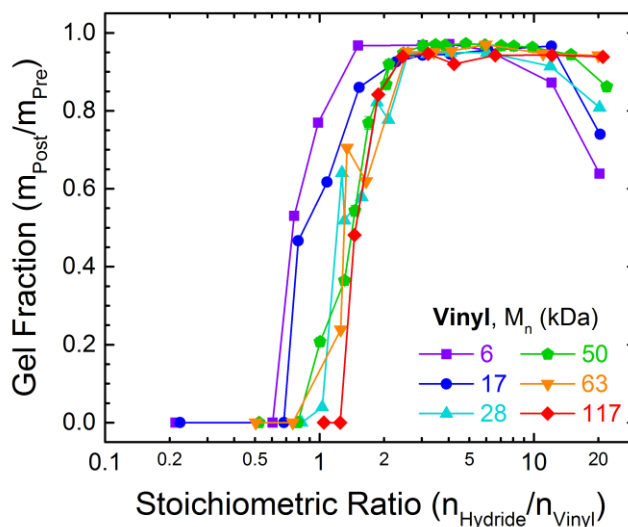


Figure 3.5 – Gel fraction as a function of stoichiometric ratio, r , for molecular weights ranging from 6 (violet) to 117 (red) kDa.

Results & Discussion

From a few simple inputs of molecular weight and stoichiometric ratio, r , and by determining the gel fraction of the networks through Soxhlet extraction, the Miller-Macosko model reveals a plethora of details about the molecular architecture of the networks. All of the data plotted in this chapter will be shown with number-average molecular weights of PDMS before crosslinking increasing from 6 kDa (violet squares), 17 kDa (blue circles), 28 kDa (cyan up-facing triangles), 50 kDa (green pentagons), 63 kDa (orange down-facing triangles), to 117 kDa (red diamonds) according to the visible light spectrum. The shortest chains are violet and longest chains are red. Additionally, the lines connecting data points are intended only to guide the eye. The lines do not represent any fitting functions or equations related to the Miller-Macosko model.

Reactivity Insights

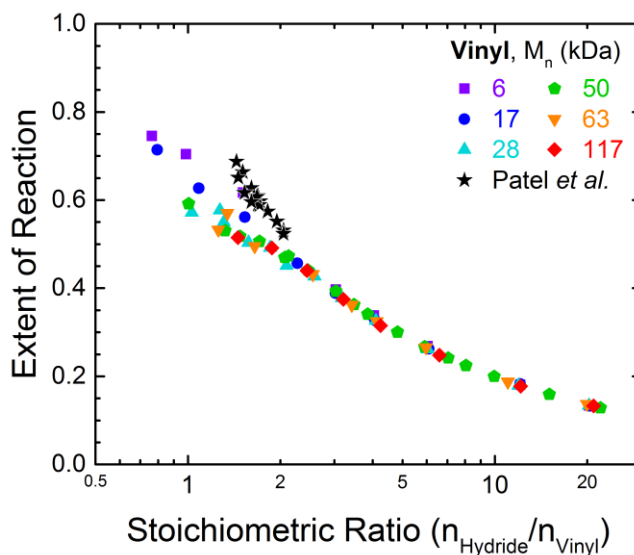


Figure 3.6 – Extent of reaction, p , plotted as a function of stoichiometric ratio, r , on a semi-log scale. The black stars are extents of reaction calculated from data reported by Patel *et al.*²⁸ In their study, only optimal stoichiometric ratios were reported, between values of $r = 1$ and $r = 2$, for a variety of molecular weights between 2.5 and 58 kDa.

We begin by plotting the extent of reaction of crosslinker groups, p , as a function of the stoichiometric ratio, r , on a semi-log scale in Figure 3.6. As higher stoichiometric ratios are used, fewer and fewer of the available Si-H groups react because the crosslinker becomes in greater and greater excess above $r = 1$; therefore p decreases with increasing r for $r > 1$. Even at the theoretical balanced stoichiometric ratio of $r = 1$, still not all of the functional groups in our samples have reacted. This is likely due to diffusion and steric hindrance limitations discussed in Chapter 2 of this dissertation. If the data from Patel *et al.*²⁸ are extrapolated, the point $r = 1$ and $p = 1$ may be reached. Additional sources of incomplete reactivity could be due to reaction duration and temperature not being sufficient, low molecular weight impurities, side reactions, as well as catalyst amount, type, and activity. All of these factors may contribute to the incomplete reaction of all silicon-hydride groups and are challenges present whenever one works with PDMS using hydrosilylation crosslinking

chemistry. Nonetheless, the following relationships between initial chemical conditions and network topology are still insightful because it is often impractical for researchers to wait long enough for 100% conversion when using PDMS materials.

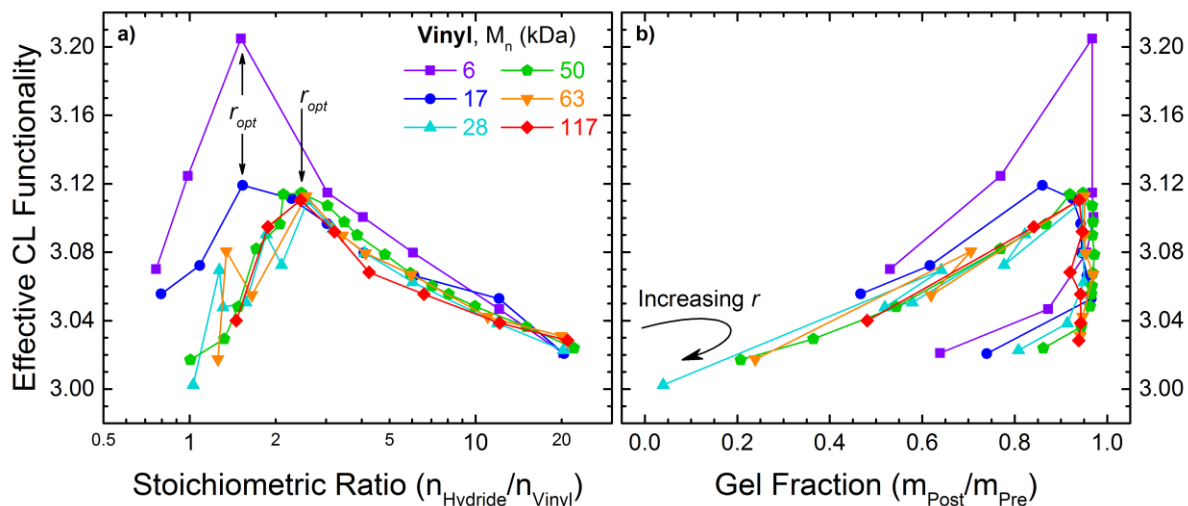


Figure 3.7 – Effective crosslinker functionality, f_{eff} , plotted as a function of stoichiometric ratio, r , and gel fraction, w_{gel} , in a and b, respectively. The stoichiometric ratio, r , increases in a clockwise fashion, depicted by the arrow in the bottom left corner of b.

Next, we investigate details about the crosslinker molecules individually, beyond just the overall extent of reaction of all of the crosslinker molecules. The effective functionality, f_{eff} , of the crosslinker is plotted as a function of stoichiometric ratio, r , and gel fraction, w_{gel} , in Figure 3.7. Based on this analysis, the effective functionality, f_{eff} , is between 3.0 and 3.2 in all of the tested vinyl/hydride samples, as seen in Figure 3.7. In each molecular weight system, an optimal stoichiometric ratio, r_{opt} , exists that maximizes f_{eff} . The 6 and 17 kDa systems have the same optimal stoichiometric ratio, $r_{opt} = 1.5$, but the 6 kDa system also has a significantly higher maximum effective crosslinker functionality of $f_{eff} = 3.21$, which is the highest out of all materials tested. For molecular weights greater than 6 kDa, all systems had same highest effective functionality, $f_{eff} \approx 3.12$. Additionally, for all of these molecular weights, this maximum f_{eff} value occurs at an optimal stoichiometric ratio, $r_{opt} \approx 2.5$, except for 17 kDa in which $r_{opt} \approx 1.5$. At high crosslinker loading, all of the data sets, regardless of molecular

weight, approximately converge for $r \geq 3$, meaning the effective functionality is mostly independent of molecular weight with increasing r beyond this optimal stoichiometric ratio. When a large excess of TDSS molecules are initially present, the probability of both polymer end-groups on a single chain reacting with two unique TDSS molecules that have not reacted with other chains is greater (*cf.* “End-Capping” discussion in Chapter 3 of this dissertation). This has the effect of lowering the reactivity per TDSS molecule, and decreasing f_{eff} . The gel fraction does not uniquely lead to a single f_{eff} value. The data show directionality with increasing stoichiometric ratio. Thus, gel fraction alone cannot be used as a criterion for determining maximum f_{eff} .

There are several factors contributing to the molecular weight dependence on f_{eff} including effects of concentration and kinetics, viscosity, diffusion, and steric hindrance. Not only do the higher molecular weight systems (> 17 kDa) possess the same r_{opt} , they all seem to collapse onto the same curve in Figure 3.7a) regardless of r . This may be due to them being equal to and above the critical entanglement molecular weight, $M_c = 28$ kDa.¹⁹ For these systems equal to and above the critical entanglement molecular weight, the chain mobility is initially stifled due to entanglements which results in higher viscosities. When chains are above M_c , they move according to reptation, which is slower than Rouse motion. This slower motion could contribute to diminished chances of chain ends finding a reactive crosslink site. The chains whose molecular weights are below M_c (*i.e.*, the 6 kDa and 17 kDa systems) exhibit faster motion that is directly proportional to the molecular weight. It therefore makes sense that, for chains below M_c , the shorter chains could find reactive sites with greater frequency for the same stoichiometric ratio.

On the macro level, the 6 kDa material has a viscosity that is approximately five-fold lower than the 17 kDa PDMS (*cf.* Table 3.1). The 6 kDa system exhibits the highest f_{eff} due to the initial lowest viscosity (*i.e.*, fastest motion), but also (perhaps more significantly) due to the initial highest concentration of both polymer end groups and crosslinking sites. All of these factors contribute to initial faster kinetics relative to the other systems, allowing more reactions to occur before the viscosity increases sharply as the reaction approaches the gel point. At the gel point, the viscosity has approached infinity and chain lengths have spanned the entire

sample volume. Since the molecular weights are much greater than those initially present before crosslinking, the chains may become entangled. Both entanglements and viscosity dramatically reduce chain mobility, and hence the ability to find reactive sites. Overall, these data reveal that not every available functional group on both polymer chains and crosslinker molecules initially present has reacted. Thus, the assumption of complete reaction of all groups under the conditions used in this study is invalid.

Elastic and Pendant Fractions

Recall that none of the networks prepared reached a gel fraction of 100% (*cf.* Figure 3.5). Additionally, the previous discussion of effective crosslinker functionality revealed that very few crosslinkers fully reacted with four unique elastically effective chains (*cf.* Figure 3.7). Both of these facts indicate that some material must be elastically ineffective. That is, the model networks prepared through end-linking are not immune to network defects. Figure 3.4 provided a schematic as to what types of defects may occur that cause chains to be elastically ineffective. In the example shown in Figure 3.4, when one counts only the 15 fully visible chains (excluding those that continue beyond the figure border), the pendant fraction is $w_{pen} = 5/15 = 33.33\%$ and the elastic fraction is $w_{el} = 10/15 = 66.67\%$. Based on this simplified example, one can readily see how a network can form with an average effective crosslinker functionality of $f_{eff} < 4$ or even $2 < f_{eff} < 3$, which results in significant fractions of pendant material.

The Miller-Macosko model enables quantification of elastic and pendant fractions according to Equations (3.9) and (3.10), respectively. In Figure 3.8, the composition of the gel fraction is broken down into its constituent parts of elastic, w_{el} , and pendant, w_{pen} , fractions for each molecular weight studied as a function of stoichiometric ratio, r . Initially at low stoichiometric ratios, most of the material present after extraction (*i.e.*, remaining within the gel fraction) takes the form of pendant material. Eventually, as r increases, the elastic fraction, w_{el} , only becomes the majority component at some crossover r -value. From here, additional increases in r result in further increases in w_{el} and decreases in w_{pen} until a plateau is reached in both fractions, which coincides with a plateau in w_{gel} . When r is increased further, the elastic

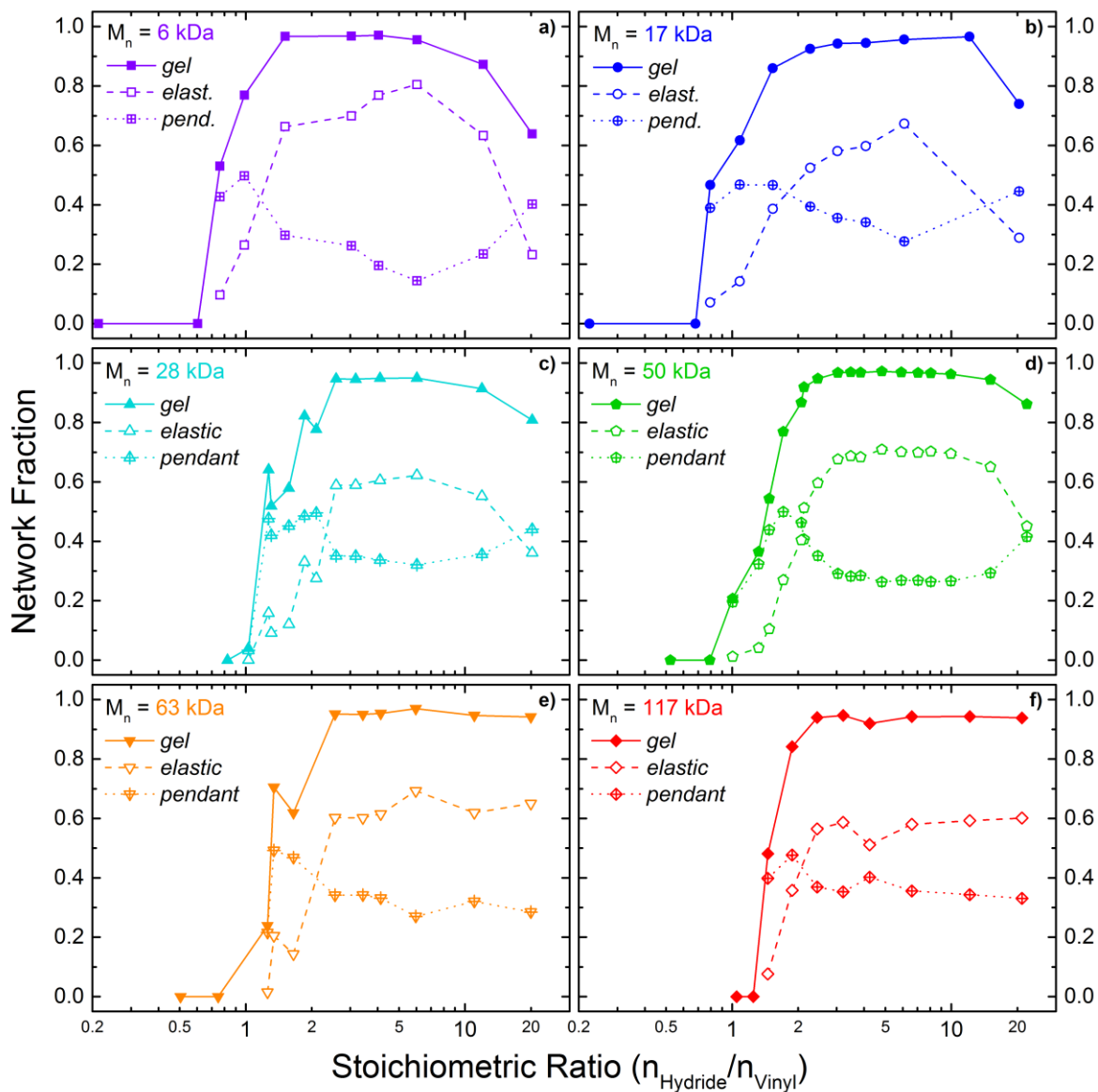


Figure 3.8 – Gel fractions, w_{gel} , (filled symbols, solid lines), elastic fractions, w_{el} , (open symbols, dashed lines) and pendant fractions, w_{pens} (open symbols with “+” sign, dotted lines) are plotted as a function of stoichiometric ratio, r , for molecular weights prior to crosslinking of 6 (violet), 17 (blue), 28 (cyan), 50 (green), 63 (orange), and 117 kDa (red) in a) through f), respectively.

fraction starts decreasing and the pendant fraction increases again. This is due to a massive excess of crosslinking molecules; *i.e.*, fewer and fewer of the crosslink junctions have more than two connections to elastically effective chains, resulting in more pendant material.

To infer how all molecular weights relate to each other, we collapse the data from Figure 3.8 onto the same graphs and plot them in Figure 3.9 where the elastic fraction is shown in a and b and the pendant fraction is shown in c and d. These fractions are plotted against the stoichiometric ratio, r , in a and c and against the gel fraction, w_{gel} , in b and d. The black curves in b and d are merely used to guide the eye. As a function of stoichiometric ratio, the elastic fraction rapidly increases with incremental increases in r until it plateaus, followed by a decrease at very high crosslinker loading. This behavior is similar to the gel fraction (*cf.* Figure 3.5). The pendant fraction never exceeds 50% in the samples tested. After an initial

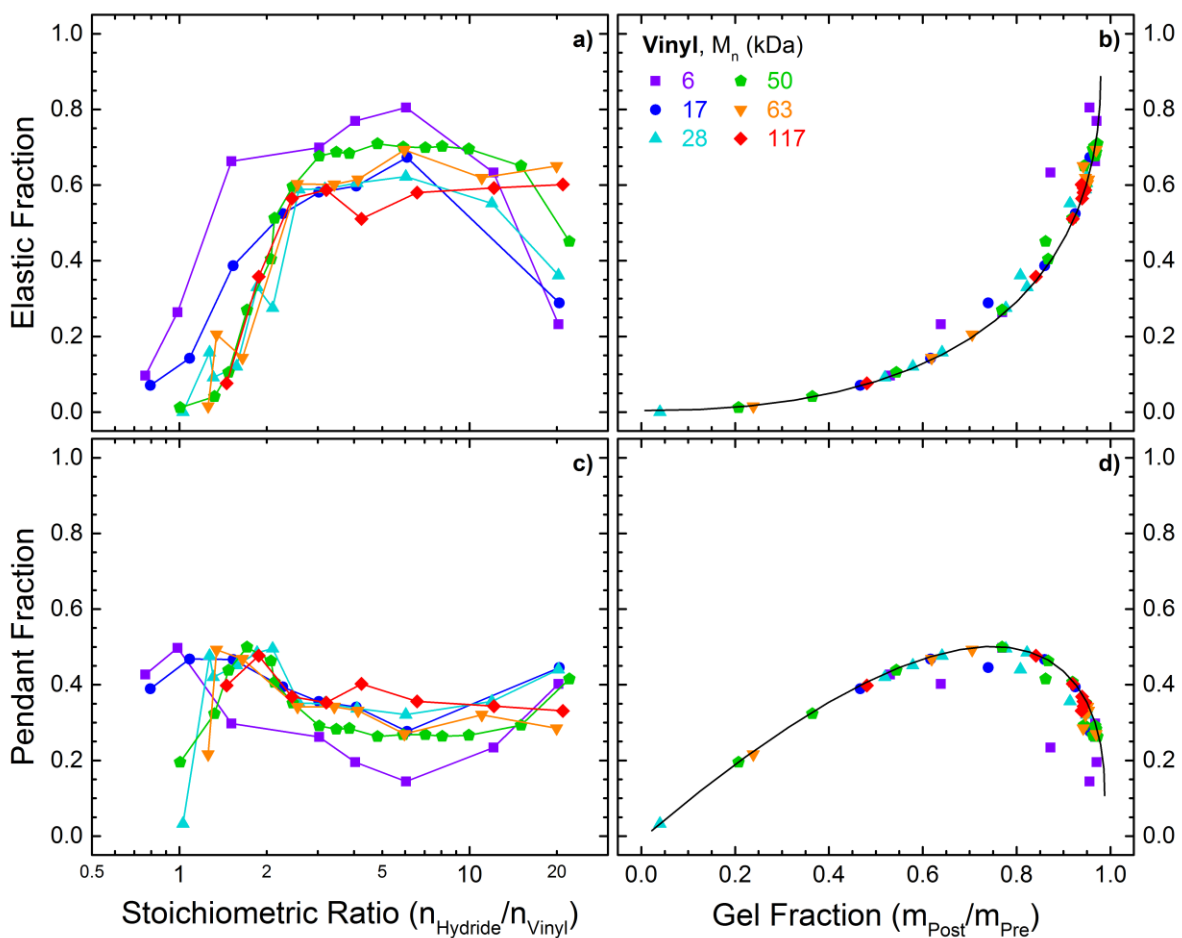


Figure 3.9 – Elastic (top row) and pendant (bottom row) fractions shown as a function of stoichiometric ratio, r , (left column) and gel fraction, w_{gel} , (right column) in a) through d). The curved lines in b) and d) are only to guide the eye.

increase with r , the pendant fraction begins decreasing beyond r_{opt} until finally increasing again with excess crosslinker. The shortest chains (6 kDa, violet squares) achieve greater elastic and correspondingly lesser pendant fractions compared to the other molecular weights studied. Interestingly, the 50 kDa system exhibits the second highest elastic fraction in the plateau region. This is due to this molecular weight system also achieving slightly greater gel fractions for this range of stoichiometric ratios (*cf.* Figure 3.5).

Despite these molecular weight differences, the data collapse onto a master curve when elastic and pendant fractions are plotted against gel fraction, indicating that molecular weight prior to crosslinking does not appear to have any significant influence on the overall elastic or pendant fractions of materials. More important, instead, is the ability to achieve the highest possible gel fraction to maximize elastic fraction. To emphasize the relationships between gel, elastic, and pendant fractions further, we collapse the data from Figure 3.9b and d onto the same graph in Figure 3.10, which displays again the elastic fraction, w_{el} (filled symbols) and pendant fraction, w_{pen} (open symbols), plotted as a function of the gel fraction, w_{gel} , for the Vinyl/TDSS system. Together, the sum of the elastic and pendant fractions equal the gel fraction, while all other material is contained in the sol fraction, as shown in Equation (3.11) and in the $y = x$ diagonal line in Figure 3.10.

At low gel fractions right beyond the gel point, the incipient network contains predominantly pendant material and very little elastic material. As the crosslinking reaction continues (or, in this study, as more crosslinker is added, *i.e.*, increasing r), the gel fraction increases, which is accompanied by an increase in both w_{gel} and w_{pen} . Near ~70% gel fraction, the pendant fraction begins to level off while the elastic fraction rapidly increases. Samples with these fractions are representative of imperfect and under-crosslinked networks that contain many dangling ends and elastically ineffective material. At ~80% gel fraction, the composition of the network finally begins to show a decrease in the amount of pendant material, and the network begins to fully develop. It requires a network to have ~87% gel fraction before the majority component is elastically effective (*i.e.*, the crossover point between elastic and pendant fractions in Figure 3.10). The highest gel fraction of all Vinyl/TDSS samples tested in this study was ~97% and occurred with the 6 kDa system at $r = 1.5$. This

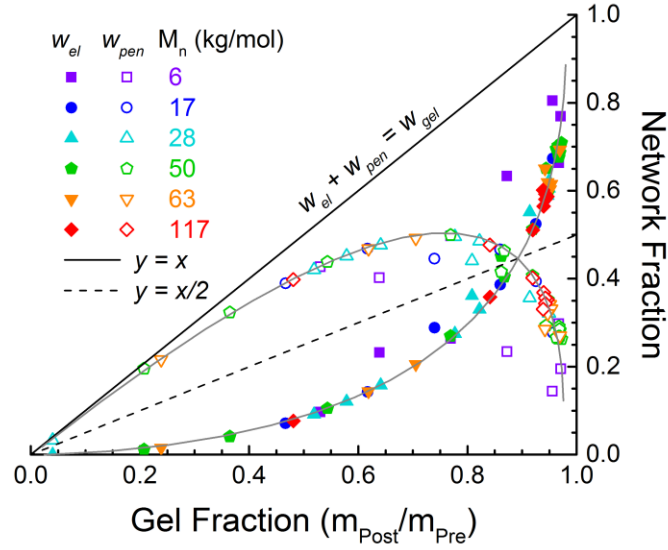


Figure 3.10 – Elastic, w_{el} , (filled symbols) and pendant, w_{pen} (open symbols) fractions plotted as a function of the gel fraction for all molecular weights. The $y = x$ line represents the sum of the elastic and pendant fractions to equal the gel fraction, according to Equation (3.11). The $y = x/2$ dashed line represents the line of symmetry for the elastic and pendant fractions. The gray solid lines are guides to the eye.

sample, however, was composed of only ~80% elastic material. Perhaps not so coincidentally, this is the same fraction for the ratio of the maximum f_{eff} observed divided by the theoretical maximum of $f = 4$, *i.e.*, $3.21/4 \approx 80\%$ (*cf.* Figure 3.7) This demonstrates the relationship between maximizing all available crosslinker sites to achieve maximum elastic fraction. Further, this is a cautionary sign that even model PDMS networks prepared with very precise stoichiometric ratios will still contain defects resulting in pendant material.

Density of Elastically Effective Chains, ν

In the preceding discussion, we revealed macroscopic information about the networks in terms of what proportion of the entire sample, post-extraction, is elastic and pendant. To offer more detailed insight into the network structure, we now plot the density of elastically effective chains, ν , as calculated from Equation (3.6), as a function of r and w_{gel} in Figure 3.11a and b, respectively. As expected, the shorter chains contain a greater density of elastically effective chains by virtue of having more moles of chains in a given unit volume. Figure 3.11b shows that the highest density of elastically effective chains occurs at the lowest sol fraction,

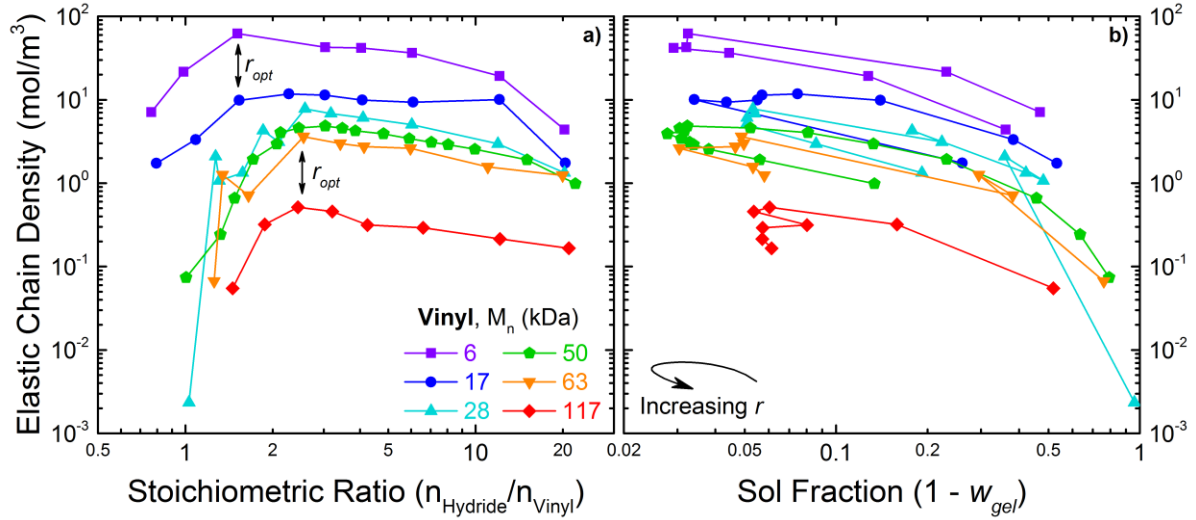


Figure 3.11 – Density of elastically effective chains, ν , (mol/m^3) plotted as a function of stoichiometric ratio, r , and gel fraction in a and b, respectively. The stoichiometric ratio, r , increases in a clockwise fashion, as depicted by the arrow in the bottom right corner of b.

(or greatest gel fraction), as expected. In Figure 3.11a, for each molecular weight, there exists an optimal stoichiometry at which the density of elastically effective chains reaches a maximum. As before, both the 6 and 17 kDa systems achieve a greater maximum ν at a lower r_{opt} , closer to the balanced ratio of 1.

When ν is plotted against f_{eff} , in Figure 3.12, this r_{opt} observed for ν is, in fact, the same r_{opt} value to that identified for maximum effective crosslinker functionality in Figure 3.7. There is one exception where there seems to be an unusually high value of ν at $r \approx 12$ in the case of 17 kDa system, but this is only a minor deviation. Overall, the greatest effective crosslinker functionality corresponds with the greatest density of elastically effective chains in nearly all systems. This relationship is expected because a greater amount of reacted groups on the crosslinkers means that there are greater amounts of chains connecting those crosslinkers. We find it somewhat unexpected that a system can exhibit two different values of ν for the same value of f_{eff} . This is possible because a system with the same amount of connectivity (*i.e.*, same f_{eff}) can have different distances between those crosslink junctions. This leads to the next parameter to be discussed, *i.e.*, the molecular weight between elastically effective chemical crosslinks, $M_{CL,MM}$.

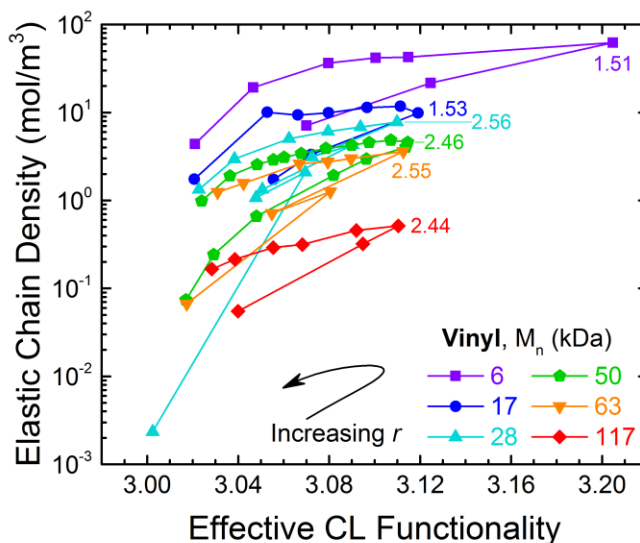


Figure 3.12 – Density of elastically effective chains, ν , (mol/m^3) plotted as a function of effective functionality of the crosslinker molecule, f_{eff} , for various molecular weights of PDMS. The stoichiometric ratio, r , increases in a counter clockwise fashion, depicted by the arrow in the bottom right corner. The numerical labels indicate r_{opt} .

Molecular Weight between Elastically Effective Chemical Crosslinks

The Miller-Macosko model allows for the calculation of molecular weights between elastically effective chemical crosslinks, $M_{CL,MM}$. The physical meaning of this value is shown schematically in Figure 3.4 as the mass of a linear polymer chain (in kDa) that spans two elastically effective chemical crosslink junctions. One may at first assume that the molecular weight between chemical crosslinks must always be equal to the number-averaged molecular weight, M_n , since only the reactive end-groups of the polymer can participate in the crosslinking reaction. This would be true only if all of the available crosslinking and polymer end-groups reacted in a system with balanced stoichiometry, thus giving $r=1$, $p=1$, and $f_{\text{eff}}=4$. Based on the previous discussions, this is not the case. However, the minimum value of $M_{CL,MM}$ must be M_n because of the end-group crosslinking scheme. When $f_{\text{eff}} < 4$ and for balanced stoichiometry, *i.e.*, $r=1$, the molecular weight between effective chemical crosslinks must be greater than M_n due to chain extension, which is illustrated schematically in Figure 3.13. Chain extension occurs when a crosslinker molecule only reacts twice with two unique

chains, thus creating a new chain that is twice as long as the initial chain. The example illustrated in Figure 3.13 shows when chain extension results in $M_{CL,MM} = 3M_n$.

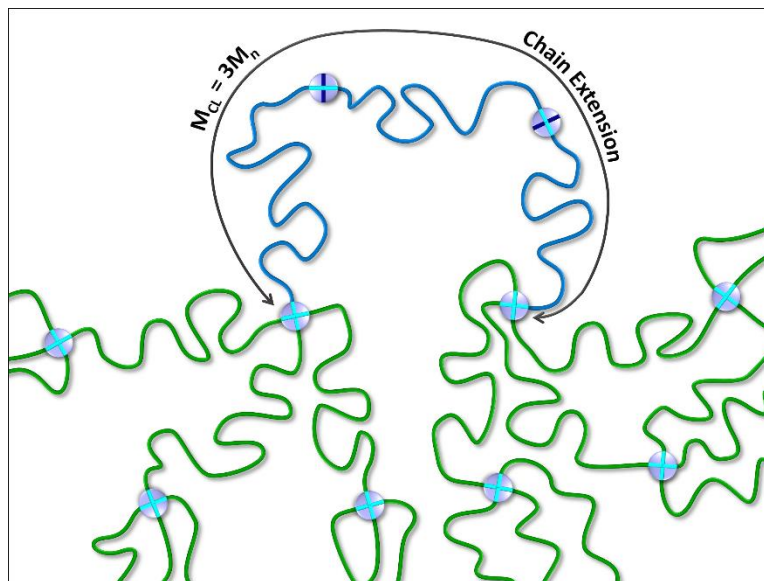


Figure 3.13 – Chain Extension shown by the three blue chains that are connected by two 2-functional crosslinkers ($f_{eff} = 2$). This has the effect of extending the molecular weight between elastically effective chemical crosslinking junctions to $M_{CL,MM} = 3M_n$.

One can imagine a network that consists of many chains connected to each other in a linear fashion, forming longer linear chains (*i.e.*, “chain extension”), with only a few branching sites where 3 or more chains meet. Queslel and Mark³³ describe this situation by saying that effective junctions must have “any combination of functionalities $f \geq 2$, at least some of which have functionalities $f > 2$.” Miller and Sarmoria³⁴ describe elastically effective junctions to be crosslink sites “from which it is possible to follow at least three independent paths to the infinite network.” However, recently Goff *et al.*³⁵ demonstrated materials that exhibited network-like elasticity formed purely by chain extension using a system that only contained $f = 2$ functionality. Nevertheless, this concept of “chain extension” relates to the parameter of the molecular weight between elastically effective chemical crosslink junctions, $M_{CL,MM}$. In the Vinyl/TDSS system studied here, there can be many chains where both ends are connected

to junctions of $f_{eff} = 2$ resulting in high degrees of chain extension. This is permissible as long as a few junctions have $f_{eff} > 2$.

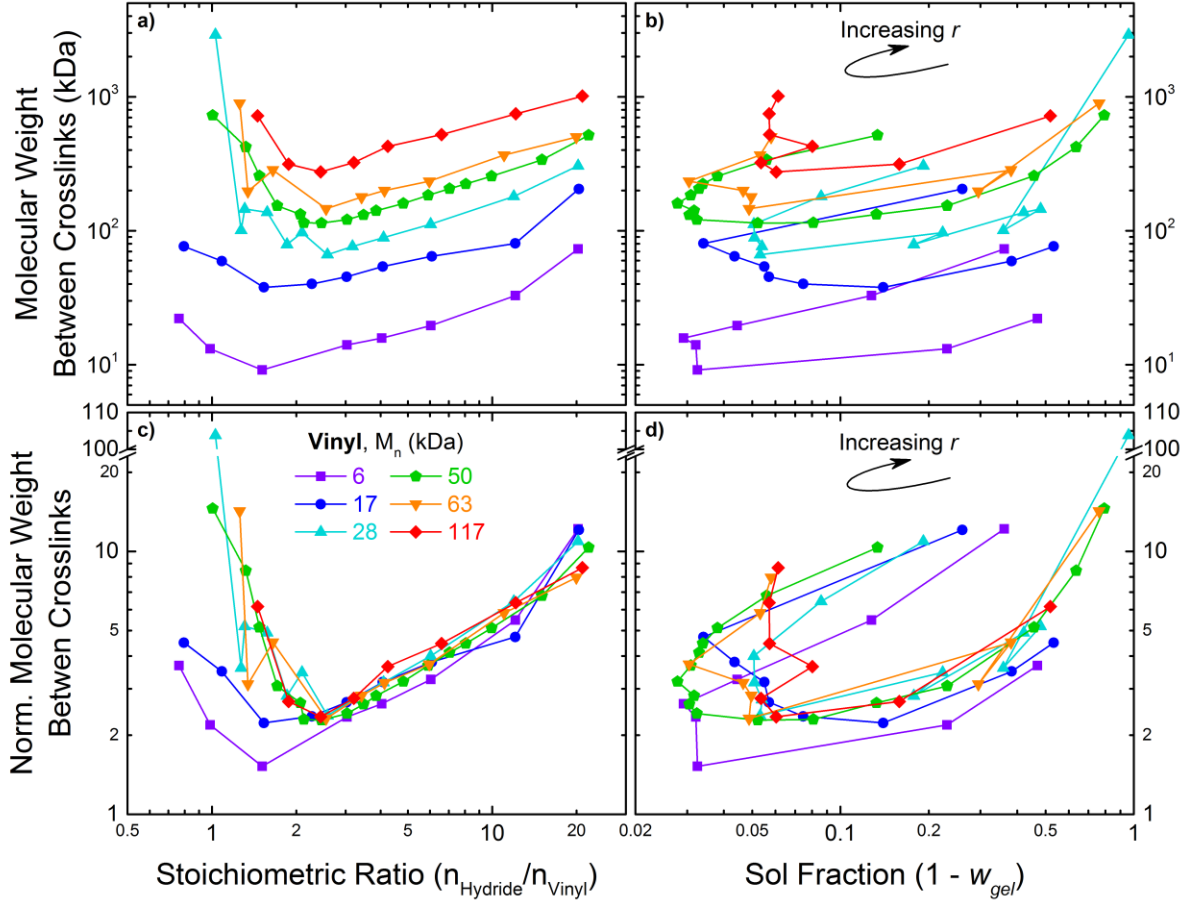


Figure 3.14 – Molecular weight between elastically effective chemical crosslinks, $M_{CL,MM}$, plotted as a function of stoichiometric ratio, r , and sol fraction, w_{sol} , in a) and b), respectively. $M_{CL,MM}$ normalized by number-averaged molecular weight, M_n , is plotted as a function of stoichiometric ratio, r , and sol fraction, w_{sol} , in c) and d), respectively. Black arrows in b) and d) indicate increasing stoichiometric ratios in the counter clockwise direction.

In Figure 3.14, we plot $M_{CL,MM}$ as a function of the stoichiometric ratio, r , and sol fraction, w_{sol} , in a) and b), respectively, and the quantity of $M_{CL,MM}$ normalized by M_n as a function of r and w_{sol} in c) and d), respectively. At the same optimal r -value for f_{eff} and ν determined previously, we observe $M_{CL,MM}$ is at a minimum. However, $M_{CL,MM}$ is always greater than M_n , meaning chain extension indeed occurs in all elastomers prepared. Figure

3.14a looks similar to Figure 3.11a except the ordinate appears to be inverted. This is because the molecular weight between elastically effective chemical crosslinks is inversely proportional to the density of elastically effective chains. In other words, for the same initial moles of polymer chains of a given molecular weight, as the concentration of elastically effective chains, ν , increases, the length of those chains, $M_{CL,MM}$, must decrease.

The parameter of $M_{CL,MM} / M_n$ elucidates the degree of chain extension occurring in these systems. On average, based on Figure 3.14c, for most molecular weights at the optimal r -value, there are only $\sim 2-3$ chains between chemical crosslinks junctions of $f_{eff} \geq 3$, meaning at r_{opt} , $M_{CL,MM} \approx 2M_n$ or $3M_n$. For extremely under-crosslinked samples and those with massive excesses of crosslinker, $M_{CL,MM}/M_n$ increases significantly, indicating multiple linear chain extensions of elastically effective chains in between network junctions of $f_{eff} \geq 3$. It appears that for free PDMS chains whose molecular weights are greater than or equal to the critical entanglement molecular weight of $M_c = 28$ kDa,¹⁹ the data collapse onto a master curve in Figure 3.14c. From these data, we conclude that for a given stoichiometric ratio, the degree of chain extension is constant for polymers having $M_n \geq M_c$ prior to crosslinking. Additionally chain extension can be reduced by forming networks from polymers initially having $M_n < M_c$. Furthermore the data for 6 kDa in Figure 3.14a indicate that most of the stoichiometric ratios used these networks exhibit $M_{CL,MM} \geq 10$ kDa, which is near the entanglement molecular weight of $M_e = 12$ kDa.¹⁸ This means that even if the polymer molecular weight prior to crosslinking is less than the entanglement molecular weight, it is still possible for entanglements to occur and to become trapped during the gelation process. More evidence of these trapped entanglements in systems made from chains below M_e will be discussed in Chapter 5 of this dissertation during an analysis of the swelling behavior of these materials.

For stoichiometric ratios greater than r_{opt} , $M_{CL,MM}$ monotonically increases and is even greater than values for under-crosslinked materials at low r -values as seen in Figure 3.14a. This means that massive amounts of excess crosslinker cause chain extension to occur more frequently than reactions involving limiting amounts of crosslinker. This observation was perplexing to us at first because the under-crosslinked region was initially expected to have greater molecular weights between crosslinks. However, this does make sense considering

that as the ratio of crosslinkers to polymers increases, the amount of sites reacted per crosslinker molecule will decrease. Stated differently, when the crosslinker is the limiting reagent, *i.e.*, there are fewer crosslinker groups than polymer groups, the amount of sites reacted per crosslinker will be greater, resulting in less chain extension, compared to when the polymer is limiting.

One might suspect that molecular weight between elastically effective chemical crosslinks would be directly proportion to the gel or sol fraction, which is a measure of degree of gelation. However, according to Figure 3.14b this is not the case. Unlike the elastic and pendant fractions, which collapsed onto master curves when plotted against gel fraction (*cf.* Figure 3.10), $M_{CL,MM}$ seems to depend more strongly on r and molecular weight of the polymer prior to crosslinking. Even when eliminating the latter factor by normalizing for M_n prior to crosslinking, the data still exhibit r -dependence and one must follow the black arrows indicating the trajectory of increasing r -values in Figure 3.14b and d. This demonstrates that given 2 networks with the same gel fraction and the same precursor molecular weight, they can have different $M_{CL,MM}$ values depending on how each network was prepared. That is, whether the network was prepared with a $r < r_{opt}$ or $r > r_{opt}$ will more strongly dictate $M_{CL,MM}$ than just the gel (or sol) fraction of the network alone does.

While the data do not collapse on a master curve as a function of sol fraction, the effective functionality tells a different story. Upon close examination to Figure 3.14c one may recall that it bears a striking resemblance to the effective crosslink functionality, f_{eff} , plotted as a function of stoichiometric ratio, r (*cf.* Figure 3.7a), except inverted. That is, beyond r_{opt} , the chain extension is independent of molecular weight prior to crosslinking. Therefore, it is likely that f_{eff} plays a very crucial role in determining $M_{CL,MM}$. Figure 3.15 depicts such a relationship.

In Figure 3.15, we plot the molecular weight between elastically effective chemical crosslinks, $M_{CL,MM}$, as a function of the effective crosslinker functionality, f_{eff} , and the density of elastic chains, ν , in a and b, respectively. We also plot the quantity of $M_{CL,MM}$ normalized by M_n as a function of the same variables in c and d, respectively. The color-coded and black lines are guides to the eye in a and c. The black arrows in b and d indicate a counter clockwise trajectory for increasing stoichiometric ratios. As expected, greater crosslink junction

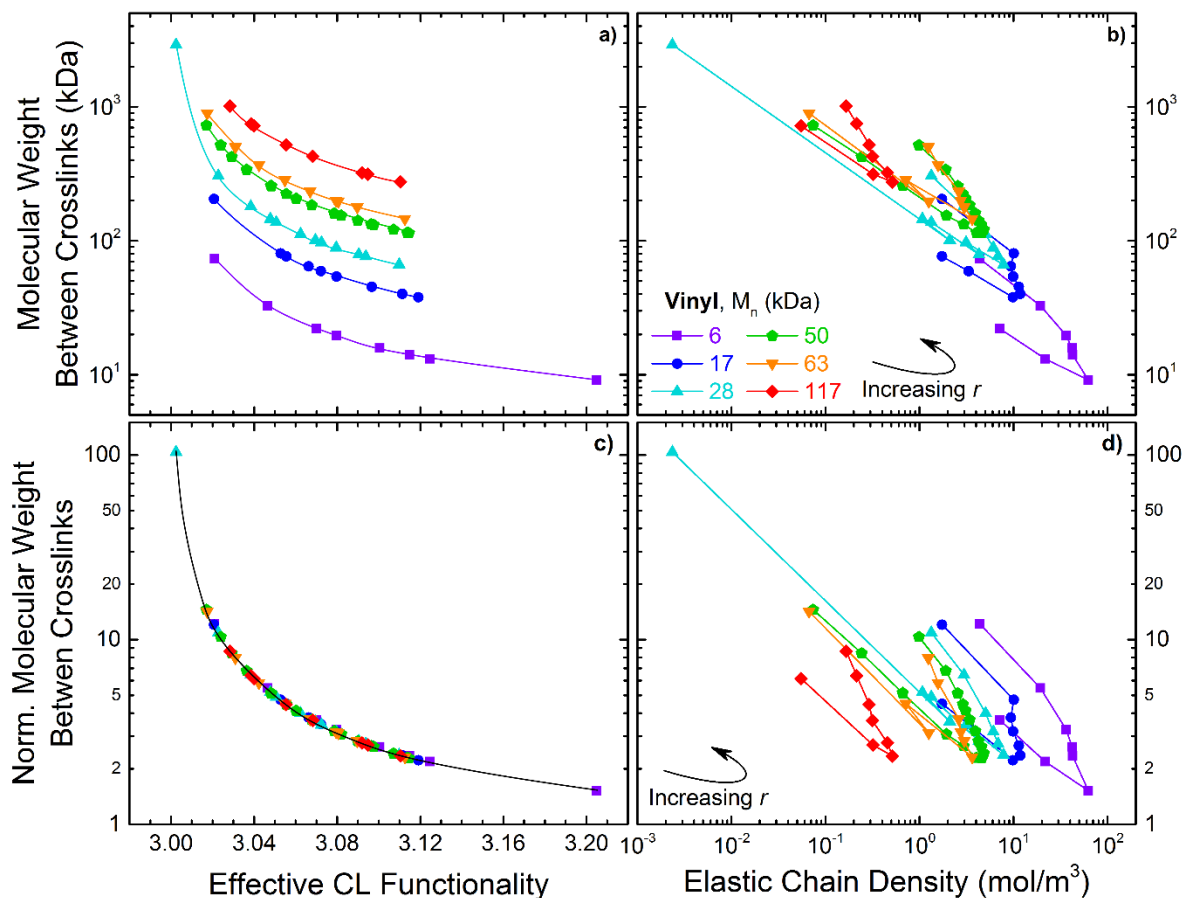


Figure 3.15 – Molecular weight between elastically effective chemical crosslinks, $M_{CL,MM}$, plotted as a function of the effective crosslinker functionality, f_{eff} , and the density of elastic chains, ν in a and b, respectively. $M_{CL,MM}$ normalized by M_n is plotted against the same variables in c and d, respectively. The colored and black curves are guides to the eye in a and c. The black arrows in b and d indicate counter clockwise directionality for increasing stoichiometric ratios.

functionality, f_{eff} , results in lower molecular weights between elastically effective chemical crosslinks, $M_{CL,MM}$, due to the diminishing amounts of chain extension. This direct relationship between $M_{CL,MM}$ and f_{eff} (*i.e.*, a relationship that is not cyclic with respect to r like many other relationships) is not necessarily obvious based on the equations for determining $M_{CL,MM}$ and the C parameter (recall Equations (3.12) and (3.13)). However, when pausing to think and reflect, the molecular weight between elastically effective crosslinks should depend most strongly on the amount of sites per crosslinker molecule that have reacted. This relationship

should be more strongly correlated than a relationship between stoichiometric ratio or gel fraction with $M_{CL,MM}$.

The density of elastically effective chains, ν , is expected to be inversely related to the molecular weight between elastically effective chemical crosslinks, which is demonstrated in Figure 3.15b. Generally, as the molecular weight between crosslinking junctions, $M_{CL,MM}$, decreases the concentration of chains, ν , increases. However, the graph in Figure 3.15b has a cyclic nature with respect to r . As r is increased beyond r_{opt} , greater chain length, $M_{CL,MM}$, is observed for the same density of elastically effective chains, ν , compared to that below r_{opt} . Stated differently, for the same molar concentration of chains on the abscissa, one encounters two different values of molecular weight between crosslinks of those chains in Figure 3.15b and d with the greater $M_{CL,MM}$ value occurring when $r > r_{opt}$. For this to be true, chain extension (*i.e.*, $f_{eff} = 2$) would have to occur more frequently than forming crosslink junctions (*i.e.*, $f_{eff} = 3$ or 4.) when there is a greater amount of crosslinker molecules present in the system. This makes sense because as the ratio of crosslinkers to polymers increase, the amount of sites reacted per crosslinker molecule will decrease.

Now that the parameters related to effective crosslinker functionality, density of elastically effective chains, and molecular weights between elastically effective chemical crosslinks have been discussed, we revisit the concepts of elastic and pendant fractions. Previously, these fractions were analyzed with respect to only the stoichiometric ratio and gel fraction. Here, the elastic, w_{el} , and pendant, w_{pen} , fractions are plotted as a function of effective crosslinking functionality, f_{eff} , and molecular weight between effective chemical crosslinks, $M_{CL,MM}$, in Figure 3.16. We observe the cyclic nature of the data again manifesting itself here with respect to stoichiometric ratio where different behavior occurs below and above r_{opt} . When the elastic fraction is plotted against f_{eff} , it increases with increasing f_{eff} until some maximum value is reached, at r_{opt} . Then the data loops back and decreases in the counter-clockwise direction. This reveals that networks with the same f_{eff} can have two different elastic and pendant fractions. The same is true of $M_{CL,MM}$ as shown in Figure 3.16b and d. It is important to note that the highest elastic fraction does not correlate with the shortest $M_{CL,MM}$ for each molecular weight prior to crosslinking. There appears to be an optimal $M_{CL,MM}$ value

for each molecular weight system studied that corresponds to a maximum in elastic fraction. Overall, the elastic and pendant fractions depend more strongly on the gel fraction than on f_{eff} and $M_{CL,MM}$.

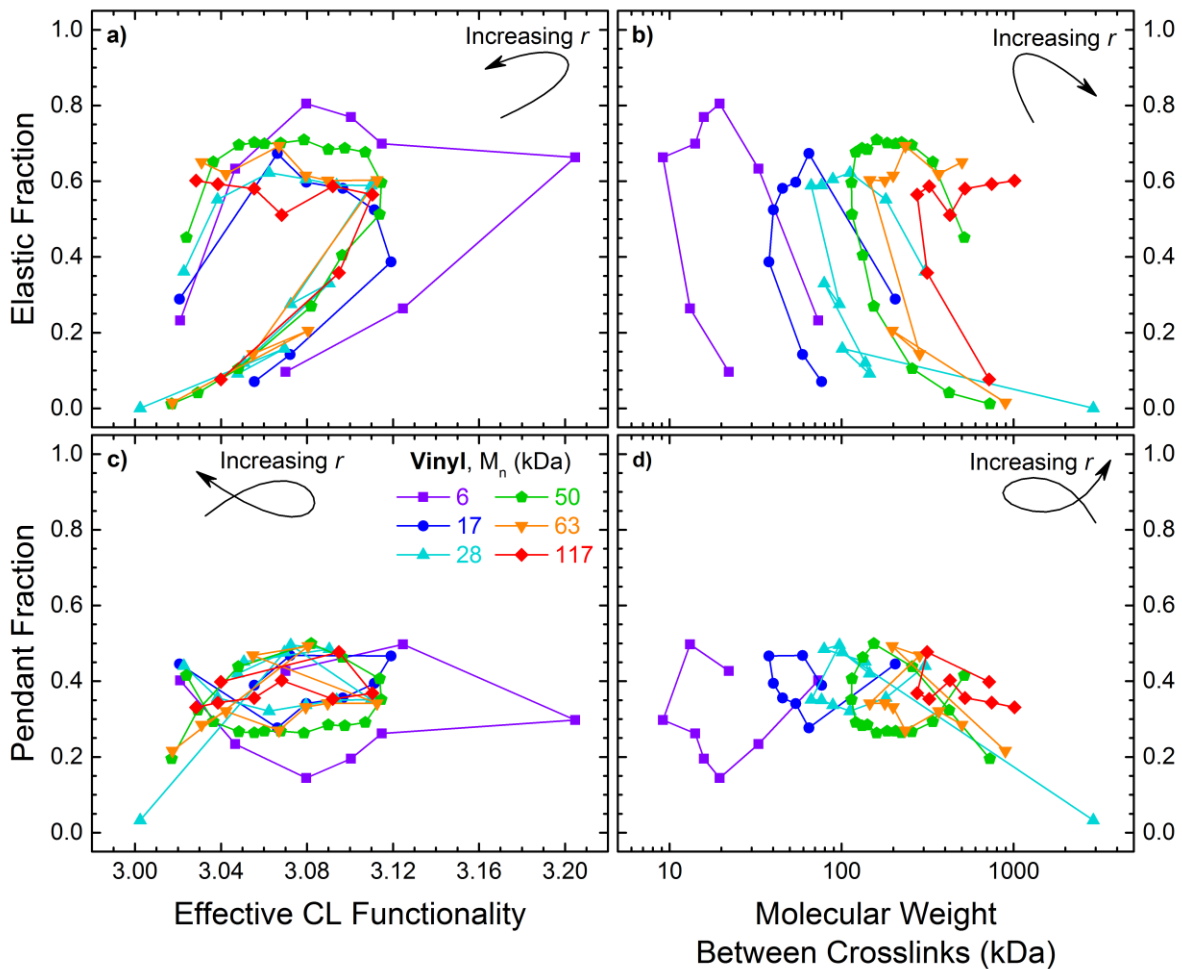


Figure 3.16 – Elastic (top row) and pendant (bottom row) fractions plotted as a function of effective functionality (left column) and molecular weight between elastically effective chemical crosslinks (right column). The black arrows indicate the directionality for increasing stoichiometric ratios. The black arrows in a and d indicate counter-clockwise directionality for increasing stoichiometric ratios while clockwise directionality is shown in b and c.

Entanglement Trapping Factor

In the introduction to this chapter we discussed concepts related to entanglements in macromolecular systems. The importance of the critical molecular weight of entanglement, M_c , was demonstrated throughout the results and discussion sections in this chapter. Some of the behavior described in the preceding sections could be categorized according molecular weights above and below M_c . Systems having molecular weights below M_c achieved the highest effective crosslinker functionality, f_{eff} , and elastic fraction, w_{el} , while systems having molecular weights above M_c often overlapped with each other and behaved similarly. In the Introduction to this chapter we discussed the meaning of the entanglement trapping factor, T_e . Recall that this parameter gives the probability that entanglements, if present, cannot disentangle. This is the difference between temporary and trapped entanglements depicted in Figure 3.4. To elucidate the effects of entanglements, we plot T_e as a function of stoichiometric ratio and gel fraction in Figure 3.17a and b, respectively.

Recall the preceding discussion related to effective crosslinker functionality in Figure 3.7a and molecular weight between effective chemical crosslink junctions in Figure 3.14c. With those parameters, data for systems having molecular weight equal to and above M_c seemed to overlap. A similar situation is apparent when the entanglement trapping factor is plotted as a function of stoichiometric ratio, as seen in Figure 3.17a. For systems above M_c , the data tend to collapse onto a master curve and there is very little molecular weight dependence. Remarkably, for the same stoichiometric ratios, the data for molecular weight systems below M_c show higher entanglement trapping factors than for those above M_c . This is another indication that just because a system is crosslinked with polymer chains initially below M_c , it does not mean that it is impossible to trap entanglements during the crosslinking reaction.

When compared to the gel fraction, the entanglement trapping factor shows a nearly exponential increase with linear increases in gel fraction until stoichiometric ratios increase beyond the optimal level. This is indicated by the data turning back towards lower gel fractions and T_e values after previously reaching maxima and is more visible in the lower molecular weight systems. A high gel fraction corresponds to a fully developed network, which will

likely have an entanglement trapping factor near 1. This means that if there are any entanglements in the system, they are certain to become trapped and contribute elastically to the network properties.

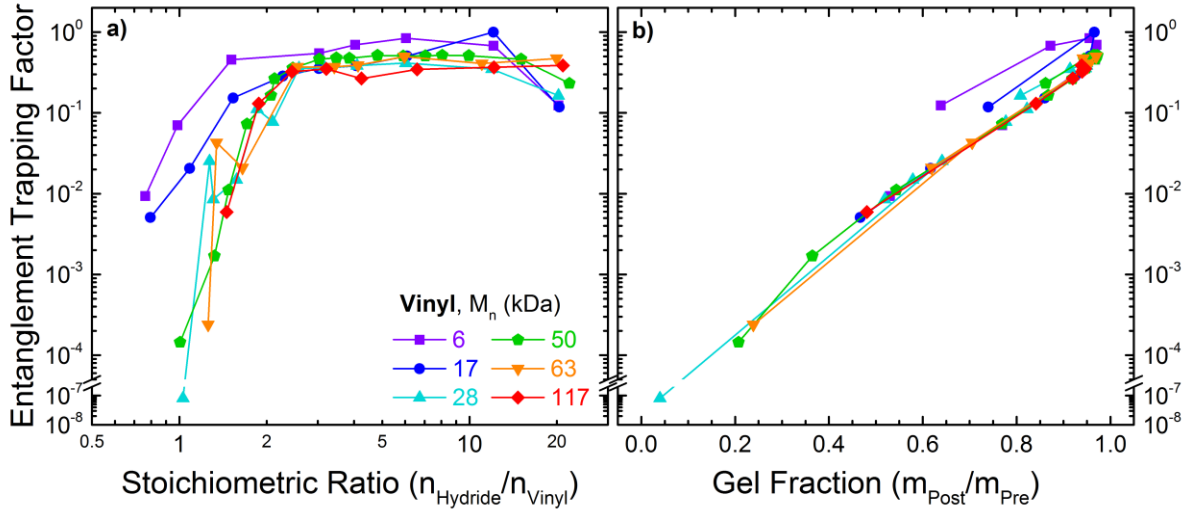


Figure 3.17 – Entanglement trapping factor, T_e , plotted as a function of stoichiometric ratio, r , in a and as a function of gel fraction, w_{gel} , in b.

Lastly, to investigate the effects of trapped entanglements on elastic and pendant fractions we plot T_e as a function of those parameters in Figure 3.18a and b, respectively. From these data, we conclude that the entanglement trapping factor is strongly correlated to the elastic and pendant fractions. The entanglement trapping factor exhibits a very strong correlation with the elastic fraction. This is expected because when all of the material is elastically effective, there is no pendant material or dangling ends, which would be the only source of temporary entanglements after extraction. Entanglements that occur between dangling ends can become disentangled over time. Such entanglements do not contribute any elasticity to the network. At first, we find it surprising that a maximum pendant fraction does not correspond to a minimum in entanglement trapping factor as shown in Figure 3.18b). Recalling the discussion regarding Figure 3.10, however, this is due to the maximum pendant fraction occurring for networks that have achieved $\sim 70\%$ gel fraction. This means that although the pendant fraction is high, the elastic fraction is also non-negligible for these

samples. Once the pendant fraction is normalized by the gel fraction, illustrating the proportion of the material remaining after extraction that is pendant, the trend becomes more clear, as shown is the inset in Figure 3.18c. Here, the maximum entanglement trapping factor occurs at minimum normalized pendant fraction.

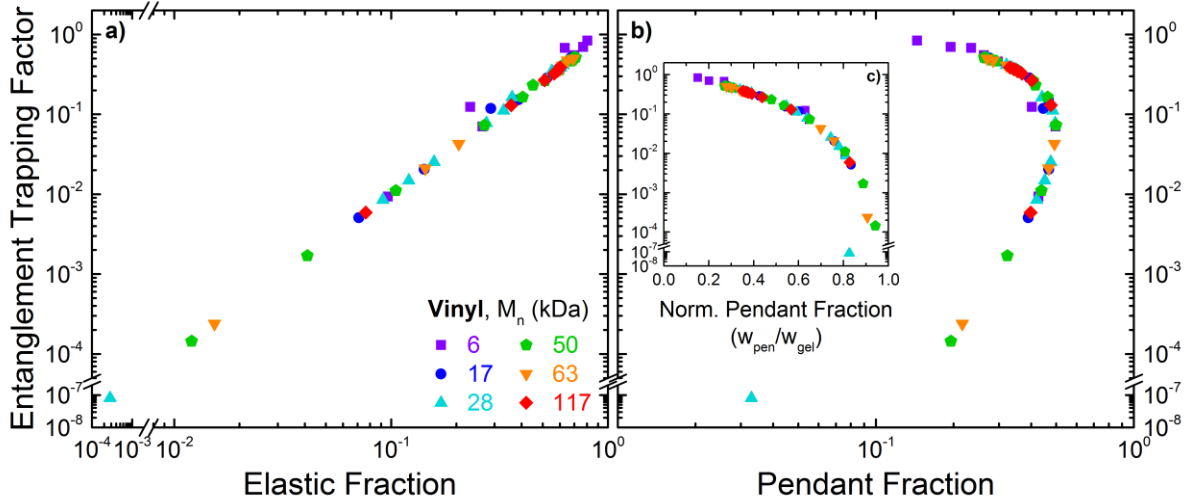


Figure 3.18 – Entanglement trapping factor, T_e , plotted as a function of the elastic fraction w_{el} , in a and the pendant fraction, w_{pen} , in b. The inset, c, shows the entanglement trapping factor as a function of pendant fraction normalized by elastic fraction.

Conclusions

In this chapter, we applied the Miller-Macosko model to the Vinyl/TDSS PDMS system for 6 different molecular weights of linear PDMS prior to crosslinking. Two of those molecular weights were below the critical entanglement molecular weight, M_c , of 28 kDa (*i.e.*, 6 and 17 kDa), one was approximately equal to M_c , (*i.e.*, 28 kDa), and 3 were above M_c , (*i.e.*, 50, 63, and 117 kDa). Throughout this chapter, we plotted and discussed many relationships among molecular network properties to demonstrate correlations. We observed optimal stoichiometric ratios, r_{opt} , that yielded maximum effective crosslinker functionalities, f_{eff} , (*cf.* Figure 3.7), maximum density of elastically effective chains, ν , (*cf.* Figure 3.11), and minimum molecular weight between elastically effective chemical crosslinks, M_{CLMM} (*cf.* Figure 3.14).

In some instances, the molecular weight of the polymer prior to crosslinking played a big role. For example, the systems below M_c exhibited the highest effective crosslinker functionality, f_{eff} , and highest elastic fraction, w_{el} (*cf.* Figure 3.7 and Figure 3.9, respectively). Thus, networks prepared from these recipes provide means to achieving a greater extent of reaction and utilizing all available functional groups per crosslinker molecule. In cases for samples prepared from molecular weights greater than M_c , the data collapsed onto a single master curve, such as in Figure 3.7a, Figure 3.9a, and Figure 3.14c, which demonstrated the influence of stoichiometric ratio, r , on effective crosslinker functionality, f_{eff} , elastic fraction, w_{el} , and normalized molecular weight between elastically effective chemical crosslinks, $M_{CL,MM}/M_n$.

In contrast, we noted several relationships that did not seem to exhibit any dependence on molecular weight or stoichiometric ratios, r , and all the data collapsed onto master curves. Such examples include the following. The gel fraction, w_{gel} , seems to influence most profoundly the elastic, w_{el} , and pendant, w_{pen} , fractions (*cf.* Figure 3.10) while the elastic fraction, w_{el} , most strongly influences the entanglement trapping factor, T_e (*cf.* Figure 3.18a). In both of these plots, there is no clear dependence on molecular weight or stoichiometric ratios. The effective crosslinking functionality, f_{eff} , seemed to most strongly influence the density of elastically effective chains ν (*cf.* Figure 3.12) and the molecular weight between elastically effective chemical crosslinks, $M_{CL,MM}$ (*cf.* Figure 3.15).

Overall, in this chapter, we have demonstrated the power of applying the Miller-Macosko model, which has facilitated numerous insights to the molecular level architecture and topology of PDMS networks. The advantages of elucidating these topological network parameters will be demonstrated in subsequent chapters of this dissertation where they are correlated with macroscopic material properties and observations determined from independent experiments. As was discussed in Chapters 1 and 2 of this dissertation, PDMS is a material used broadly in many scientific disciplines. Our hope is that the demonstration of this model, which is based on a few easily acquired inputs, will promote it and other models to researchers outside of the polymer physics community. By learning more about topological PDMS network properties and using this knowledge to help explain observed phenomena and

reach more sound conclusions, we believe that precisely such researchers stand to benefit the most though use of this model.

Acknowledgements

The author thanks Professor Kirill Efimenko for initial guidance in making PDMS networks via hydrosilylation and Dr. Edwin Walker for helping to prepare some of the 50 kDa Vinyl/TDSS PDMS networks.

References

1. Huggins, M. L. Solutions of Long Chain Compounds. *J. Chem. Phys.* **9**, 440–440 (1941).
2. Flory, P. J. Thermodynamics of High Polymer Solutions. *J. Chem. Phys.* **10**, 51–61 (1942).
3. Rouse, P. E. A Theory of the Linear Viscoelastic Properties of Dilute Solutions of Coiling Polymers. *J. Chem. Phys.* **21**, 1272–1280 (1953).
4. de Gennes, P. G. Reptation of a Polymer Chain in the Presence of Fixed Obstacles. *J. Chem. Phys.* **55**, 572–579 (1971).
5. Doi, M. & Edwards, S. F. Dynamics of concentrated polymer systems. Part 1.—Brownian motion in the equilibrium state. *J. Chem. Soc., Faraday Trans. 2* **74**, 1789–1801 (1978).
6. Doi, M. & Edwards, S. F. Dynamics of concentrated polymer systems. Part 2.—Molecular motion under flow. *J. Chem. Soc., Faraday Trans. 2* **74**, 1802–1817 (1978).
7. Doi, M. & Edwards, S. F. Dynamics of concentrated polymer systems. Part 3.—The constitutive equation. *J. Chem. Soc., Faraday Trans. 2* **74**, 1818–1832 (1978).
8. Doi, M. & Edwards, S. F. Dynamics of concentrated polymer systems. Part 4.—Rheological properties. *J. Chem. Soc., Faraday Trans. 2* **75**, 38–54 (1979).
9. Flory, P. J. & Rehner, J. Statistical Mechanics of Cross-Linked Polymer Networks I. Rubberlike Elasticity. *J. Chem. Phys.* **11**, 512–520 (1943).
10. Flory, P. J. & Rehner, J. Statistical Mechanics of Cross-Linked Polymer Networks II. Swelling. *J. Chem. Phys.* **11**, 521–526 (1943).
11. Langley, N. R. Elastically Effective Strand Density in Polymer Networks. *Macromolecules* **1**, 348–352 (1968).
12. Graessley, W. in *Advances in Polymer Science* **16**, 1–179 (Springer Berlin Heidelberg, 1974).
13. Macosko, C. W. & Miller, D. R. A New Derivation of Average Molecular Weights of Nonlinear Polymers. *Macromolecules* **9**, 199–206 (1976).
14. Miller, D. R. & Macosko, C. W. A New Derivation of Post Gel Properties of Network Polymers. *Macromolecules* **9**, 206–211 (1976).
15. Zhong, M., Wang, R., Kawamoto, K., Olsen, B. D. & Johnson, J. A. Quantifying the impact of molecular defects on polymer network elasticity. *Science (80-.)*. **353**, 1264–1268 (2016).

16. Voytek, B. Are There Really as Many Neurons in the Human Brain as Stars in the Milky Way? | Brain Metrics. *Nature Education* 1–5 (2013). at <https://www.nature.com/scitable/blog/brain-metrics/are_there_really_as_many>
17. Macosko, C. W. & Benjamin, G. S. Modulus of Three and Four Functional Poly(dimethylsiloxane) Networks. *Pure Appl. Chem.* **53**, 1505–1518 (1981).
18. Rubinstein, M. & Colby, R. H. *Polymer Physics*. (Oxford University Press, 2003).
19. Longin, P. ., Verdier, C. & Piau, M. Dynamic shear rheology of high molecular weight polydimethylsiloxanes: comparison of rheometry and ultrasound. *J. Nonnewton. Fluid Mech.* **76**, 213–232 (1998).
20. Graessley, W. W. & Edwards, S. F. Entanglement interactions in polymers and the chain contour concentration. *Polymer* **22**, 1329–1334 (1981).
21. Kataoka, T. & Ueda, S. Viscosity–molecular weight relationship for polydimethylsiloxane. *J. Polym. Sci. Part B Polym. Lett.* **4**, 317–322 (1966).
22. Chassé, W., Lang, M., Sommer, J.-U. & Saalwächter, K. Cross-Link Density Estimation of PDMS Networks with Precise Consideration of Networks Defects. *Macromolecules* **45**, 899–912 (2011).
23. Hild, G. Model Networks Based on ‘Endlinking’ Process: Synthesis, Structure and Properties. *Prog. Polym. Sci.* **23**, 1019–1149 (1998).
24. Urayama, K., Kawamura, T. & Kohjiya, S. Structure–mechanical property correlations of model siloxane elastomers with controlled network topology. *Polymer* **50**, 347–356 (2009).
25. Villar, M. A. & Vallés, E. M. Influence of Pendant Chains on Mechanical Properties of Model Poly(dimethylsiloxane) Networks. 2. Viscoelastic Properties. *Macromolecules* **29**, 4081–4089 (1996).
26. Andrady, A. L. *et al.* Model Networks of End-Linked Polydimethylsiloxane Chains. XII. Dependence of Ultimate Properties on Dangling-Chain Irregularities. *J. Polym. Sci.* **26**, 1829–1836 (1981).
27. Larsen, A. L. *et al.* Elastic Properties of Nonstoichiometric Reacted PDMS Networks. *Macromolecules* **36**, 10063–10070 (2003).
28. Patel, S. K., Malone, S., Cohen, C., Gillmor, J. R. & Colby, R. H. Elastic Modulus and Equilibrium Swelling of Poly(dimethylsiloxane) Networks. *Macromolecules* **25**, 5241–5251 (1992).
29. Valles, E. M. & Macosko, C. W. Properties of Networks Formed by End Linking of Poly(dimethylsiloxane). *Macromolecules* **12**, 673–679 (1979).
30. Miller, D. R., Valles, E. M. & Macosko, C. W. Calculation of Molecular Parameters

- for Stepwise Polyfunctional Polymerization. *Polym. Eng. Sci.* **19**, 272–283 (1979).
31. Gottlieb, M., Macosko, C. W., Benjamin, G. S., Meyers, K. O. & Merrill, E. W. Equilibrium Modulus of Model Poly(dimethylsiloxane) Networks. *Macromolecules* **14**, 1039–1046 (1981).
 32. Lee, J. N., Park, C. & Whitesides, G. M. Solvent Compatibility of Poly(dimethylsiloxane)-Based Microfluidic Devices. *Anal. Chem.* **75**, 6544–6554 (2003).
 33. Queslel, J. P. & Mark, J. E. in *Analysis/Networks/Peptides* **65**, 135–176 (Springer-Verlag, 1984).
 34. Miller, D. R. & Sarmoria, C. "In-Out" Recursive Probability Modeling of Branched Step-Growth Polymerizations. *Polym. Eng. Sci.* **38**, 535–557 (1998).
 35. Goff, J., Sulaiman, S., Arkles, B. & Lewicki, J. P. Soft Materials with Recoverable Shape Factors from Extreme Distortion States. *Adv. Mater.* **28**, 2393–2398 (2016).

CHAPTER 4: Mechanical Properties of Silicone Elastomers

Introduction

In the Context of this Dissertation

In Chapter 2, we discussed the preparation details for making the silicone elastomers studied throughout this dissertation. We completed a thorough analysis of the influence of stoichiometric ratio and molecular weight on gel fraction. Then, in Chapter 3, we used those parameters as inputs to gain a deep understanding of the molecular level network topology. In this chapter, we will determine the mechanical properties of the many silicone elastomer materials prepared and described hitherto. Several key topological network parameters calculated in Chapter 3 will be used in assessing the mechanical properties of PDMS materials in the current chapter.

Mechanical Properties of Soft Materials

There is an exciting growing trend of interdisciplinary research occurring at present among biologists, chemists, physicists, materials scientists, and chemical and electrical engineers. Such teams have goals of developing soft materials for a variety of applications that have ramifications for potentially all human beings. Figure 4.1 shows the Young's modulus, a measure of how soft or hard a material is, for a variety of biological (blue) and engineered (red) materials. The term "soft" materials refers to those structures that exhibit a Young's modulus less than ~ 1 GPa, which is roughly the equivalent of tendons found in our bodies. PDMS materials prepared and studied in this dissertation are shown in the green region.

The applications of soft materials range broadly. Neural system implants in either the spinal cord or brain, for example, have the potential to help patients suffering from paralysis and/or dementia to regain control of their bodies and minds.^{2,3} The goal of one of Elon Musk's latest start-ups, Neuralink, is to create neural implants that can augment human intelligence and help our species keep pace with the looming age of artificial intelligence. In addition to

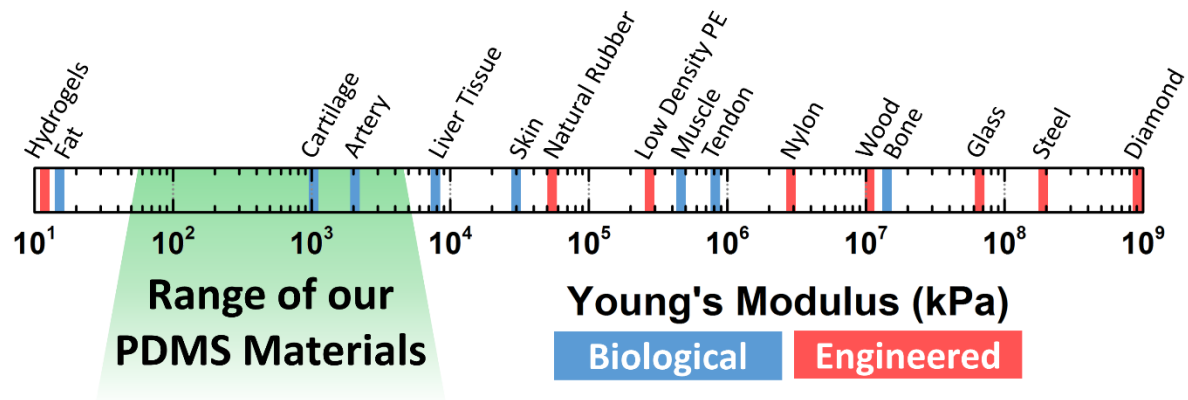


Figure 4.1 – Adapted from Rus and Tolley.¹ The range of Young’s modulus values for a variety of biological (blue) and engineered (red) materials. The green region corresponds to silicone elastomers prepared and studied in this dissertation.

creating synthetic links for the transmission of signals in an artificial neural-like material, soft materials have the potential to serve as artificial muscles and actuators in the field of tissue engineering.^{4,5} Artificial muscles can help patients recover from injuries or illnesses, but can also be employed to enhance human performance. Instead of implanting artificial muscles in a body, other research has focused on applying the same principles to the advancement of soft robotics¹ for an entirely new paradigm in what we traditionally conceive of as robots. To make all of the preceding applications possible, materials must be soft and flexible, but also, vitally, electronically conductive for sending and receiving signals. Consequently, research in the area of flexible electronics is also rapidly expanding.^{6,7} PDMS is a promising candidate material in all of these applications.

For those previously mentioned biological applications, one growing area of material development is in so-called double network hydrogels, which are very tough, relatively strong yet soft materials that contain anywhere from 50%-90% water.⁸ This work was pioneered by Gong and co-workers⁹ and is still a vibrant field of study.^{8,10} Hydrogels have the advantage that they can be prepared from biocompatible polymers and strongly resemble biological materials, since most tissues in our bodies are also some sort of hydrogel. PDMS polymers have also been shown to be biocompatible and have demonstrated promise in the aforementioned applications where biocompatibility is a concern.

One area where PDMS excels greatly over hydrogels is in microfluidics and “lab on a chip” technology due to their resistance to swelling in aqueous and alcoholic solutions and relative ease at which micro-scale features can be imparted onto the surface of PDMS materials. This is accomplished through the process of so-called soft lithography, which was pioneered by Whitesides and co-workers.¹¹⁻¹⁴ and has led to an outburst in microfluidic research. There is strong potential to create cheap and small devices for a variety of diagnostic applications for disease detection, cell-based screening technologies, and single-cell research.^{15,16}

In order for these technical advancements to reach fruition, precise control over the mechanical properties of materials is of the utmost importance. Therefore, in this chapter, we present a cookbook of recipes for making model PDMS materials over a wide range of mechanical properties. By utilizing dynamic mechanical analyses, richer information about the mechanical performance of these materials is elucidated compared to solely performing stress-strain experiments. In many of our experiments, we compare our model PDMS materials to the commercial silicone elastomer, Sylgard 184, to demonstrate the strengths and weaknesses of each type of material. Lastly, in addition to providing recipes or chemical formulations that produce materials of a given nature, the correlations between molecular-level network topological structure and bulk mechanical properties are illuminated. These relationships offer insights that enable materials for a given application to be designed more efficiently as opposed to the “guess-and-check” approach.

Theoretical Background

Entropic Origins of Rubber-Like Elasticity

Theories of polymer rubber-like elasticity have been developing for nearly 8 decades. Elasticity arises due to entropy; when chains undergo deformation, they exhibit an entropic restoring force similar to a spring that counters the force causing the deformation. A polymer chain has higher entropy when it is in a more globular conformation with many more possible confirmation states as opposed to when it is elongated and has fewer possible allowed

conformations. From a thermodynamic perspective, there is always a balance between entropy and enthalpy and the system tends to reach the lowest energy state possible. This balance is encompassed by the Gibbs free energy, ΔG , relationship between the change in enthalpy, ΔH , and entropy, ΔS , given by, $\Delta G = \Delta H - T\Delta S$, where T is the temperature. The Δ refers to a change from a reference state. To minimize the Gibbs free energy, the entropy should be maximized, accordingly, chains do not like to be elongated and prefer to be restored to their globular configuration. As a side note, since elasticity arises from entropy, elastomers exhibit higher moduli with increased temperature. That is, they get stronger and tougher at elevated temperatures, in contrast to conventional solid materials that become softer when temperature is increased since they are being brought closer to their melting points.¹⁷

As discussed in Chapter 3 of this dissertation, an important phenomenon in polymers is their ability to entangle and form temporary topological network-like structures. These temporary states exist on time scales that are short enough where elasticity can be observed before the chains relax and disentangle. Experiments to determine the onset of entanglements are typically done in shear rheological experiments where oscillatory shear strain is applied to polymers of various molecular weights over a range of frequencies. At high molecular weights and high enough frequencies (*i.e.*, short enough time-scales), the modulus ceases to increase as frequency continues to increase, resulting in a frequency, ω , independent shear storage modulus, G' . Hence, the plateau modulus, G_{eq} , defines the onset of entanglements.

An example of the determination of plateau modulus for PDMS was given in Chapter 3 of this dissertation and is reproduced here in Figure 3.1. These data have been reproduced from Macosko and Benjamin¹⁸ and give a plateau modulus value of 0.24 ± 0.02 MPa. This frequency-independent modulus is due to a temporary network-like structure formed solely from temporarily trapped entangled chains that do not relax over the time-scale of the measurement.¹⁷ The shear plateau modulus is related to the entanglement molecular weight, M_e , according to Equation (4.1).

$$G_{eq} \approx \frac{\rho RT}{M_e} \quad (4.1)$$

Here, ρ is the polymer melt density (0.97 g/cm^3 for PDMS), R is the universal gas constant, and T is the absolute temperature. Others have reported the plateau modulus for PDMS to be $\sim 0.20 \text{ MPa}$, giving an entanglement molecular weight of $M_e \approx 12 \text{ kDa}$.¹⁷

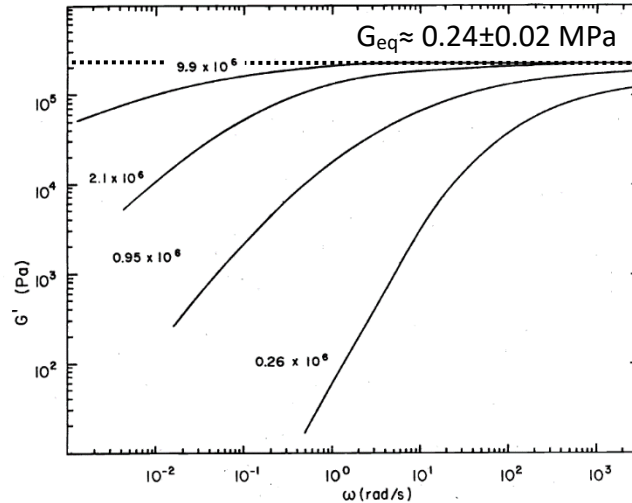


Figure 4.2 – Adapted from Macosko and Benjamin.¹⁸ Shear storage modulus, G' , plotted as a function of angular frequency, ω , for PDMS weight-average molecular weights of 9.9×10^6 , 2.1×10^6 , 0.95×10^6 , and $0.26 \times 10^6 \text{ g/mol}$. The plateau modulus is extrapolated down to zero frequency from the plateau region in the high frequency portion of the graph.

The previous example of shear rheology was for polymer melts, *i.e.*, the polymers were not crosslinked, and only exhibited a temporary network-like structure. Since the network-like structure was formed from temporary entanglements, over long enough time-scales (*i.e.*, low frequencies), the storage modulus is lower, demonstrating chain relaxation and disentanglement of the temporary network-like structure. This is because entropy increases with time and chains have greater entropy when they are not elongated to form temporary networks. Thus, over long time-scales, the free energy of the system is minimized due to maximizing entropy as the chains relax from their temporary elongated form of a network-like structure. The same type of shear rheological experiments can also be applied to polymer networks to develop theories of rubber-like elasticity. These theories relate molecular weight between crosslinks, which is inversely proportional to the crosslink density, to the material's modulus. Here, both entanglements and chemical crosslinks contribute to restrictions in chain

motion. Therefore, for fully crosslinked networks, the storage modulus is independent of frequency since the chains cannot disentangle over long time-scales. In other words, the highest entropy (and lowest energy) state of the system is greater in crosslinked networks than in polymer melts because chains are permanently trapped in those conformations due to chemical crosslinks. This gives rise to viscoelastic properties of polymer networks. In the next section, we provide a brief background on the two most common theories of rubber-like elasticity in polymer networks.

Affine and Phantom Models

The affine model for rubber-like elasticity was originally proposed by Kuhn¹⁹ and is the simplest model that addresses the challenge of predicting bulk elastomeric behavior from molecular-level structure. The primary assumption in this model is that polymer chains and crosslink junctions deform relative to the macroscopic strain applied to them.¹⁷ This means that if a strain of 50% is applied to the sample, the chains and junctions will also be deformed by 50% in the direction of strain. It is as if the crosslink junctions are fixed in space, connected to a background object that does not allow them to fluctuate, and when that background object is deformed, the junctions deform by relatively the same amount.¹⁷ The relationship between modulus and molecular weight between crosslinks for the affine model is given by:^{17,20}

$$G_{Aff} = \nu RT = \frac{\rho RT}{M_{Aff}} \quad (4.2)$$

Here, the shear modulus as predicted from the affine model, G_{Aff} , is directly proportional to the density of elastically effective strands, ν (mol/m³) (see Chapter 3 of this dissertation for more information on this parameter), and inversely proportional the molecular weight between crosslinks predicted from the affine model, M_{Aff} . The density of the polymer is given by ρ , R is the universal gas constant, and T is the absolute temperature.

The obvious limitation of the affine model is that polymers and crosslinkers are molecules, and hence, they undergo diffusion, Brownian motion, and thermal fluctuations. Restraining the crosslink junctions to be fixed in space, relative to a hypothetical background object, consequently limits their motion and creates artificial restraints, resulting in predictions of a higher modulus and shorter molecular weight between crosslinks (*i.e.*, a greater crosslink

density). To address the limitation of fixed crosslink junctions, the phantom model was developed. Here, the crosslink junctions are permitted to fluctuate, which results in an overall lowering of the free energy since the junctions can move to more favorable energy states upon deformation.¹⁷ The relationship between modulus and molecular weight between crosslinks in the phantom model depends on the densities of both elastically effective chains, ν , and junctions, μ (see Chapter 3 of this dissertation for explanations). Recall from Chapter 3 of this dissertation that ν and μ are related to the effective crosslinker functionality, f_{eff} , according to $f_{eff} = 2\nu/\mu$.²¹ Thus, the relationship between modulus and molecular weight between crosslinks as determined from the phantom model is given in Equation (4.3).^{17,22}

$$G_{Ph} = (\nu - \mu)RT = \left(1 - \frac{2}{f_{eff}}\right) \left(\frac{\rho RT}{M_{Ph}}\right) \quad (4.3)$$

In the phantom model, if a perfect tetrafunctional crosslinker is used and it reacts completely, *i.e.*, $f_{eff} = 4$, then Equation (4.3) reduces to one half the value of the affine model in Equation (4.2).

In summary, the affine model is limited due to crosslink junctions being unable to fluctuate, making them deform proportionally to the macroscopic deformation. The phantom model relaxes this assumption, permitting crosslink junction fluctuations, and thus enabling lower energy states when deformed. The relationships between the models are summarized in the following relationships:

$$\text{for given } M, G_{Ph} < G_{Aff} \text{ \& for given } G, M_{Ph} < M_{Aff} \quad (4.4)$$

Tensile and Shear Moduli

In this dissertation, we report tensile storage and loss moduli, E' and E'' , respectively. The relationships between shear storage and loss moduli, G' and G'' , respectively, and tensile moduli arise from the material's Poisson's ratio, ν_P . This is a measure of how the sample deforms during uniaxial extension wherein the two dimensions perpendicular to the force shrink while the dimension parallel to the force grows. For uniaxial compression, the opposite is true; the dimension parallel to the force shrinks while the two dimensions perpendicular to the force expand. For silicone elastomers, the Poisson's ratio is 0.5.²³ This means that the

amount of decrease in a dimension perpendicular to the applied force is half the amount of increase in the dimension parallel to the applied force. The relationship between shear and tensile moduli for PDMS is given by Equation (4.5):²⁴

$$E = 2G(1 + \nu_p) = 3G \quad (4.5)$$

This relationship between shear and tensile module will be used to calculate molecular weight between crosslinks in the aforementioned affine and phantom models. The molecular weights between crosslinks predicted from the affine model, M_{Aff} , and the phantom model, M_{Ph} , are not the same as the molecular weight between chemical crosslinks predicted from the Miller-Macosko model,²⁵ $M_{CL,MM}$ (see Chapter 3 of this dissertation). Instead, they are both an average chain length that results in a sufficient crosslink density to give the equilibrium shear modulus observed. That is, they are hypothetical chain lengths that would result in the observed behavior and are independent of the chemistry of the system, except for the functionality of crosslinker in the phantom model. These values will all be compared towards the end of this chapter.

Previous Research on Dynamic Mechanical Properties of PDMS Networks

A considerable amount of research has focused on using model PDMS networks to study the gelation process via *in situ* dynamic mechanical experiments monitoring shear storage and loss moduli. Many of these examples were given in the previous chapters of this dissertation. Less work has been done on fully characterizing the dynamic mechanical behavior of PDMS networks after the crosslinking reaction has completed. Langley and Ferry²⁶ did early work in the late 1970s analyzing dynamic mechanical responses and used the Time-Temperature-Superposition (TTS) principle to elucidate the full viscoelastic response of PDMS over wide frequency ranges. Similar work using TTS was done by Takahashi more recently in 2006.²⁷ Other investigations have focused on understanding the influence of pendant material, such as dangling ends, on the loss modulus of PDMS networks for the development of efficient damping materials.^{28,29} Additionally, several researchers have characterized the dynamic viscoelastic response for PDMS/silica composite materials.³⁰⁻³⁴

However, to the best of our knowledge, a comprehensive evaluation and comparison of model PDMS networks made from both hydrosilylation and hydrolysis/condensation crosslinking reactions coupled with a comparison to the commercial Sylgard 184 system has not been reported. Based on the results in previous chapters of this dissertation, we believe the differences in gel fraction with respect to molecular weights and stoichiometric ratios between the two model systems will reveal different dynamic mechanical responses within these materials. Providing the recipes for creating such materials will be beneficial to the community at large.

Experimental Materials and Methods

Materials

In this chapter, the mechanical properties were determined for both the Vinyl/TDSS and Silanol/TEOS model PDMS networks, as well as Sylgard 184 materials prepared according to the procedure described in Chapter 2 of this dissertation. The data from stoichiometry, molecular weight, and gel fraction are the same as those used in Chapter 2 of this dissertation. To briefly recap, telechelic PDMS polymers of various molecular weights and having vinyl and silanol end-group functionalities were crosslinked with two different tetrafunctional crosslinker molecules (*i.e.*, each molecule has 4 reactive groups) to form model PDMS networks. For the vinyl system, tetrakis(dimethylsiloxy)silane (TDSS) was the crosslinker and *cis*-dichlorobis(diethyl sulfide)platinum(II) (Pt catalyst) was the catalyst. For the silanol system, tetraethoxysilane (TEOS) was the crosslinker and tin(II) 2-ethylhexanoate (Sn catalyst) was the catalyst. PDMS materials were also made from the Sylgard 184 Silicone Elastomer kit (Dow Corning), which contains separate Base (B) and Curing Agents (C) that simply need to be mixed together in different mass ratios (*i.e.*, B/C ratio). The composition of both components is reproduced from Chapter 2 of this dissertation in Table 4.1 as a reminder of the large fraction of silica particles present, which will greatly influence mechanical properties discussed in this chapter.

Table 4.1 - Composition of Sylgard 184 (Dow Corning) according to Safety Data Sheets^{36,37}

Function	Component	Base	Curing Agent
Polymer	Vinyl-terminated PDMS	55-75 %	15-35 %
Particles	Dimethylvinylated and trimethylated silica	30-50 %	10-30 %
Crosslinker	Dimethyl, methylhydrogen siloxane (PDMS-co-HMS)	0 %	55-75 %
Crosslinker	Tetramethyl tetravinyl cyclotetrasiloxane	0 %	1-5 %
Diluent	Tetra(trimethylsiloxy) silane	< 1.0 %	0 %
Diluent	Xylene	0.5 %	0.19 %
Diluent	Ethylbenzene	0.2 %	<0.10 %

Methods

Network Preparation

To prepare each model PDMS network sample, *circa* 2.5-3.5 g of PDMS were mixed well with the catalyst in a polypropylene beaker followed by removal of air bubbles under moderate vacuum. For every gram of vinyl-terminated PDMS in each sample, 8 μ L of Pt(II) catalyst solution at a concentration of 0.011 g Pt(II) catalyst per mL of toluene were added. In the Silanol/TEOS samples, Sn(II) catalyst was added at a rate of 1% of the total mass of silanol-terminated PDMS polymer plus crosslinker. In several instances with particularly high concentrations of TEOS, this amount was reduced to 0.25% of the total mass to slow down the reaction. Next, a very precise mass (and volume) of the crosslinker, TDSS (for vinyl-terminated PDMS) and TEOS (for silanol-terminated PDMS), was added via micropipette over a balance to the PDMS/catalyst mixture yielding a specific desired stoichiometric ratio, r , defined in Chapter 2 of this dissertation.

After mixing well and degassing again, the solution was carefully poured into a polystyrene or polypropylene Petri dish. If needed, the Petri dish was degassed one last time. The sample in the Petri dish was then covered with a lid and placed on a level surface at room temperature exposed to atmospheric pressure for 2-3 h of pre-curing, during which the polymer spread evenly throughout the Petri dish, giving a uniform thickness of \sim 0.7–1.5 mm (depending on the amount of polymer added to the dish). Finally, the networks were placed in

a 70°C oven at atmospheric pressure for 24 h. Sylgard 184 samples were prepared in the same manner as model PDMS except the only ingredients used were the base and curing agent, which were added together in varying Base/Curing Agent (B/C) mass ratios. Soxhlet extraction in toluene, a good solvent for PDMS,³⁸ was used to determine the gel (w_{gel}) and sol (w_{sol}) fractions of the networks according to the same method described in Chapter 2 of this dissertation. Those data are reproduced in Figure 3.5.

Background on Dynamic Mechanical Analysis

We performed a dynamic mechanical analysis of each sample to elucidate the materials' responses on different time scales. Typical behaviors of purely elastic Hookean elastic solids and viscous Newtonian liquids, along with polymers, which exhibit viscoelastic behaviors, are shown in Figure 4.3. The tensile storage modulus, E' , is a measure of how elastic- or solid-like the material is, meaning the material obeys Hooke's law. That is, the force required to deform the material is proportional to the deformation or strain.³⁹ To normalize for the area on which the force is acting, stress is used and is defined as the force applied per unit area on which it is acting. Elastomers generally behave as Hookean solids at low strains < 10%. When a force acts on an elastic material, 100% of that force is used to deform the material, or induce a strain in the material. When the force is removed, the material returns rapidly back to the original shape, releasing the energy that was stored, thus behaving elastically. The resistance to motion on a molecular level determines how much stress must be applied to induce a strain. For instance, when atoms are arranged on a crystal lattice, the atoms have an extremely high resistance to motion due to strong ionic bonding holding them in place, and thus, crystals have very high storage moduli. As seen in Figure 4.3a, there is no lag between stress and strain when a sinusoidal force acts to deform an elastic solid. The phase angle, δ , separating a sinusoidal stress from the resultant strain is zero.³⁹

The tensile loss modulus, E'' , provides a measure of how liquid-like the material behaves, *i.e.*, the material's ability to dissipate energy. This is specific to Newtonian liquids, in which the stress is proportional to the strain rate and the strain exhibited by the material lags the applied stress due to viscosity. Liquids have the ability to dissipate forces that act on them

because the molecules comprising the liquid are able to flow freely past one another (at least, much more so than crystalline solids). In a solid, the molecules are bound in space and cannot flow readily. The liquid's viscosity is a measure of the forces required to make molecules flow past one another and to absorb and dissipate the force being applied. Purely viscous materials exhibit a perfectly out of phase response between applied stress and induced strain, resulting in a phase angle of $\delta = 90^\circ$, as can be seen in Figure 4.3a.

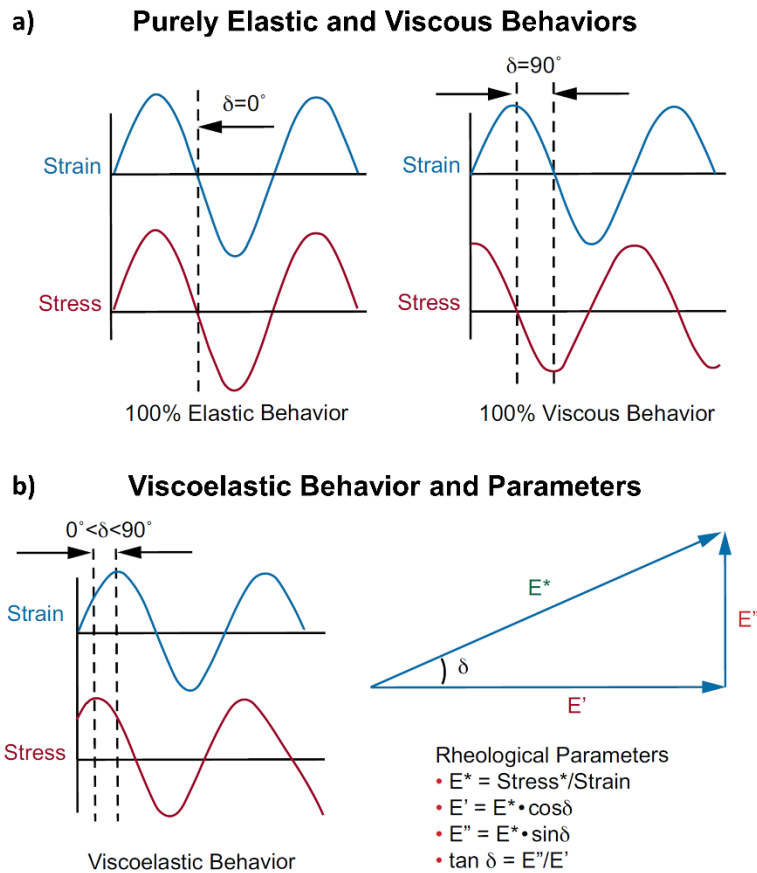


Figure 4.3 – Adapted from the RSA-G2 Solids Analyzer Brochure from TA Instruments.⁴⁰ For elastic materials, when oscillatory stress is applied, the strain is perfectly in phase (*i.e.*, the phase angle, $\delta = 0^\circ$) as shown in the left plot in a. In purely viscous materials, the strain lags the stress by a phase angle of $\delta = 90^\circ$ (right, a). In b, polymers exhibit viscoelastic behavior, where the lag between stress and strain is somewhere in between the two ideal elastic and viscous cases. The complex modulus, E^* , is the vector sum of the storage modulus, E' , and loss modulus, E'' , which are related to the phase angle according to the equations in the figure. The phase angle, δ , is often reported as the loss tangent, $\tan(\delta)$, which is defined as the ratio of loss modulus to storage modulus, E''/E' .

The phase angle, δ , represents the time delay between applied force per unit of cross-sectional area (or stress) and observed deformation (or strain) of the material. When the stress and strain are completely in phase, the phase angle will be nearly zero, and thus, $\tan(\delta)=E''/E'$, will be near zero, indicating solid, elastic-like behavior where energy is stored. The lower the value of $\tan(\delta)$, the more solid- and elastic-like the material will behave because it has no means to dissipate forces, *i.e.*, no viscous component. When the strain lags the stress by $\delta = 90^\circ$ (*i.e.*, they are completely out of phase from one another), $\tan(\delta)$ approaches infinity and the material behaves like a liquid.

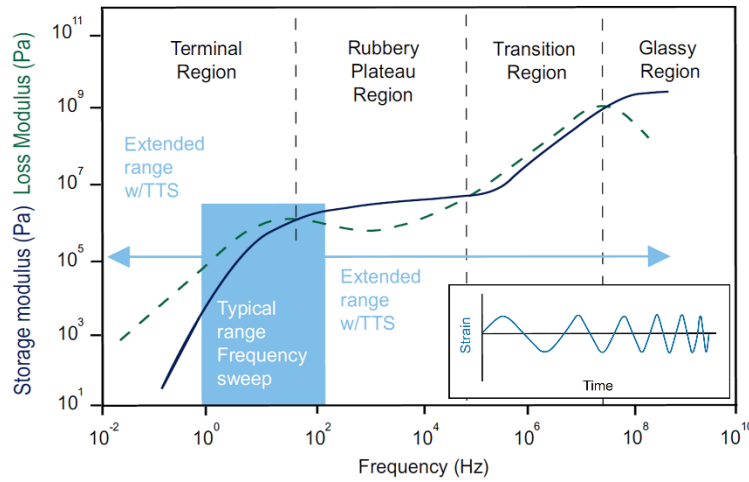


Figure 4.4 – Adapted from the RSA-G2 Solids Analyzer Brochure from TA Instruments.⁴⁰ Typical plot of storage and loss moduli, E' and E'' , respectively for a viscoelastic polymer as a function of frequency of applied strain. The inset demonstrates a constant strain amplitude applied at an increasing frequency with over the time of the experiment. The frequencies used in this dissertation were such that the rubbery plateau region of PDMS was investigated, which does not correspond to those in this example.

Silicone elastomers, among many polymers above their glass transition temperature, T_g , exhibit viscoelastic, *i.e.*, both solid-like and liquid-like, behavior. The polymers behave more like solids for short time scales and more like liquids over long time scales. A typical viscoelastic response of a polymeric material is depicted in Figure 4.4 where the storage (solid navy line) and loss (dashed green line) moduli are plotted as a function of frequency of applied strain. The inset shows a schematic demonstrating how a constant amplitude sinusoidal strain is applied with increasing frequency over the course of the experiment. Machine and time

limitations prevent one from acquiring the full spectrum of material responses over such a large frequency range. However, by testing the same frequency range over many different temperatures, the data can be shifted according to the TTS principle, which yields the full frequency material response spectrum.

In amorphous polymeric elastomers, the polymer chains are free to move, to some extent, within the free volume available in the material. Furthermore, if the temperature is above the glass transition temperature, T_g , of the polymer, additional motion of the molecules is permissible. These factors allow the polymer chains to flow somewhat when a force is applied, depending on the crosslinking density, and other parameters such as the molecular rigidity of the repeat unit. If the force caused only elastic deformation (*i.e.*, small strain), then once the force is removed, the chains will return to their original conformation over a characteristic time scale, characterized by the relaxation time, which depends on the liquid-like properties of the material. However, if the strain is large enough such that the material is stretched beyond the region of elastic deformation, then the material deforms plastically, from which it cannot return to its original shape.

Dynamic Mechanical Experiments

An RSA-G2 Solids Analyzer from TA Instruments, commonly referred to as a Dynamic Mechanical Thermal Analyzer (DMTA) instrument, was used to determine the dynamic mechanical properties of the PDMS network materials. From each PDMS network batch (various stoichiometric ratios for each molecular weight), two extracted samples were cut into rectangles (approximately 1 mm thick by 5-8 mm wide by 7-20 mm long) and the dimensions of each sample were determined with digital calipers. Sylgard 184 samples were tested pre- and post-extraction. Using the Tension Fixture attachment, small rectangular pieces of extracted PDMS networks were subjected to angular frequency, ω , sweeps from 0.1–100 rad/s, ($\omega = 2\pi f$, where f is the frequency in Hz or s^{-1}). Both the applied strain and the force required to induce the strain were monitored as a function of frequency to yield the dynamic behavior of the material. The tests were conducted at room temperature ($20\pm 1^\circ\text{C}$) with a constant strain of 1% applied at each frequency value. All samples were subjected to

0.05 - 0.1 N of axial force for ~30 s (until the force stabilized to ± 0.005 N) before beginning the mechanical experiments to negate human error and differences in sample loading. The tensile storage (E') and tensile loss (E'') moduli, as well as the loss tangent ($\tan(\delta) = E''/E'$) were recorded for each sample at each frequency.

Stress-Strain Experiments

Sylgard 184 samples were tested on an Instron extensometer to elucidate uniaxial stress-strain curves and ultimate material properties. Ultimate properties refer to ultimate tensile stress or strength, which is the maximum measured stress, and ultimate strain, which is the strain at which ultimate tensile strength occurs. For the silicone elastomers tested, these two parameters coincide with the stress and strain at rupture. However, this is not the case for all materials since necking and crazing phenomena can occur before rupture. Neither of these was observed on the measured samples. Dog bone molds ~1.5 mm in depth were machined from a Teflon slab for curing the Sylgard 184, which allowed for testing according to the ASTM D412 test standard for Vulcanized Rubber and Thermoplastic Elastomers-Tension.⁴¹ The smallest mold from the ASTM D412 standard, Type D, is shown in Figure 4.5 and was chosen to reduce material consumption. All experiments were performed at a strain rate of 5 mm/min until samples ruptured and three different samples at each B/C ratio were tested. In a typical stress-strain curve, the small strain region (<10%) is due to elastic deformation, *i.e.*, the shape of the sample can be recovered upon release of stress. Increased strain beyond that the elastic deformation region results in plastic deformation, where the shape of the sample is permanently deformed. The silicone elastomers tested did not exhibit plastic deformation.

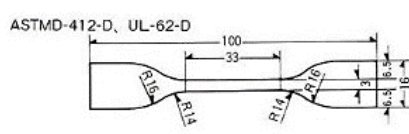


Figure 4.5 – ASTM-D412 Type D⁴¹ mold for performing tensile stress-strain experiments on silicone elastomers. Units are in mm. Depth of mold is ~1.5 mm.

During these uniaxial experiments, a force, F , is applied to stretch the sample. This force acts on the cross-sectional area, A , normal to it, which in the case of the Type D molds, corresponds to an initial cross-sectional area, A_0 , of $1.5 \times 3 = 4.5 \text{ mm}^2$. However, the sample deforms during uniaxial extension with the two dimensions perpendicular to the force shrinking while the dimension parallel to the force grows. As previously discussed, the Poisson's ratio for silicone elastomers is 0.5,²³ meaning the amount of decrease in dimensions perpendicular to the force is half the amount of increase in the dimension parallel to the force. This makes the real-time area difficult to measure. Thus, the true stress, $\sigma_T = F/A$, acting on the material, defined as the force (F) per unit cross-sectional area in real-time (A), is also difficult to assess. Instead, the engineering stress, $\sigma_E = F/A_0$, is often reported using the force (F) per initial cross-sectional area, A_0 . Engineering stress is often plotted as a function of engineering strain, ϵ_E , defined as the change in length divided by the initial length, $\epsilon_E = \Delta L/L_0$. The initial length of the sample, L_0 , is 33 mm for the Type D dog bone mold, and ΔL is the change in length at any given time, t , during the experiment, $\Delta L = L(t) - L_0$. The true strain, ϵ_T , is the sum of all instantaneous engineering strains. The derivations of the relationships between true and engineering values of stress and strain are provided by Khanafer *et al.*⁴² and the final results are given in Equation (4.6):⁴²

$$\sigma_T = \sigma_E(1 + \epsilon_E), \quad \epsilon_T = \ln(1 + \epsilon_E) \quad (4.6)$$

The Young's modulus, or tensile elastic modulus, E , is defined as the slope of the true stress-strain curve in the small strain region where the material has only undergone elastic deformation. Young's modulus is a measure of the force necessary to deform a material to a small degree via uniaxial elongation. Sometimes Young's modulus is reported from the engineering stress-strain curve. In the small strain regions, there is very little difference between true and engineering stress-strain curves (*vide infra*). However, it is judicious to report the specific types of stress and strain used when determining Young's modulus. Since stress has units of pressure and strain is unit-less, the Young's modulus has units of pressure according to Equation (4.7):

$$E = \sigma_T/\epsilon_T \quad (4.7)$$

For a viscoelastic solid, in the limit of long time scales or low frequencies, the value of tensile storage modulus, E' , approaches the value of Young's modulus, E .¹⁷

Results & Discussion

Raw data from the dynamic experiments showing mechanical properties as a function of angular frequency are provided for Sylgard 184 samples in the Appendix. All values of storage modulus, loss modulus, and loss tangent reported in this chapter are given at angular frequencies of $\omega = 1$ rad/s unless otherwise noted. Additionally, values at $\omega = 1$ rad/s are used in any subsequent calculations of properties and parameters that require mechanical properties as inputs. This value was chosen because in most samples the properties within this frequency range demonstrate a constant dependence on frequency of applied strain, *i.e.*, the slope in this range is constant. For the model Vinyl/TDSS and Silanol/TEOS systems, all data are reported for post-extraction samples. For Sylgard 184, dynamic mechanical data for pre- and post-extraction samples are provided while only pre-extraction data are provided for stress-strain experiments.

Model PDMS Systems

Brief Recap of Gel Fraction

The gel fraction data for the model PDMS systems are reproduced from Chapter 2 of this dissertation and plotted in Figure 3.5 for reference. While the gel and sol fractions and stoichiometric ratio provide parameters from which a great deal of information about the networks can be calculated and inferred, the networks are not yet fully characterized. To gain a more comprehensive understanding, the mechanical properties must be measured.

Stoichiometric Ratio Effects

Given so many different stoichiometric ratios and molecular weights tested for model PDMS, plots directly comparing the systems as a function of frequency would be rather crowded. Instead, in Figure 4.7, the values of E' , E'' , and $\tan(\delta)$ ($=E''/E'$), at a frequency of $\omega = 1$ rad/s are all plotted as a function of the stoichiometric ratio, r , for both vinyl and silanol

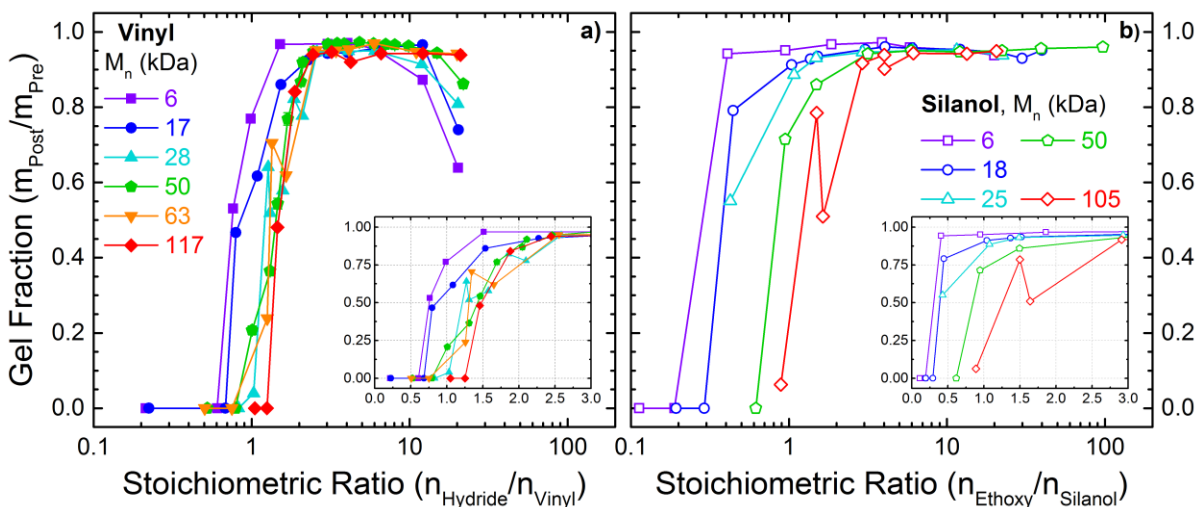


Figure 4.6 – Gel fraction plotted as a function of stoichiometric ratio, r , for the Vinyl/TDSS system (a) and the Silanol/TEOS system (b) for various molecular weights of PDMS prior to crosslinking. The insets show the region zoomed into low stoichiometric ratios.

systems. We note that in the cases of 6 kDa for both vinyl and silanol systems, dynamic measurements of samples at relatively high cross-linker loading were not possible due sample limitations. Strain appeared to be trapped in these samples during curing, which resulted in curved, rigid samples from which uniform rectangular prism-shaped samples could not be made for testing. Loss modulus data, and thus $\tan(\delta)$, were not readily acquired by our instrument for highly rigid samples.

Figure 4.7 provides a summary of the mechanical properties of networks as a function of the stoichiometric ratio for the Vinyl/TDSS system in plots a, b, and c and the Silanol/TEOS system in plots d, e, and f. Generally, the data for the Vinyl/TDSS system are more compact, *i.e.*, there is less spread in the data with respect to stoichiometric ratio and particularly weak molecular weight dependence compared to the Silanol/TEOS system. The data for storage modulus of the Vinyl/TDSS system given in Figure 4.7a show that, initially, very minor increases in stoichiometric ratio result in rapid increases in storage modulus until an optimal stoichiometric ratio with respect to storage modulus has been reached. This region of rapid increases in storage modulus corresponds to the same under-crosslinked region for gel fraction (*cf.* Figure 3.5a). As stoichiometric ratio continues to increase, it becomes difficult to

distinguish any significant differences in maximum storage modulus values with molecular weight and stoichiometric ratio as the data appear to plateau somewhat over a range of

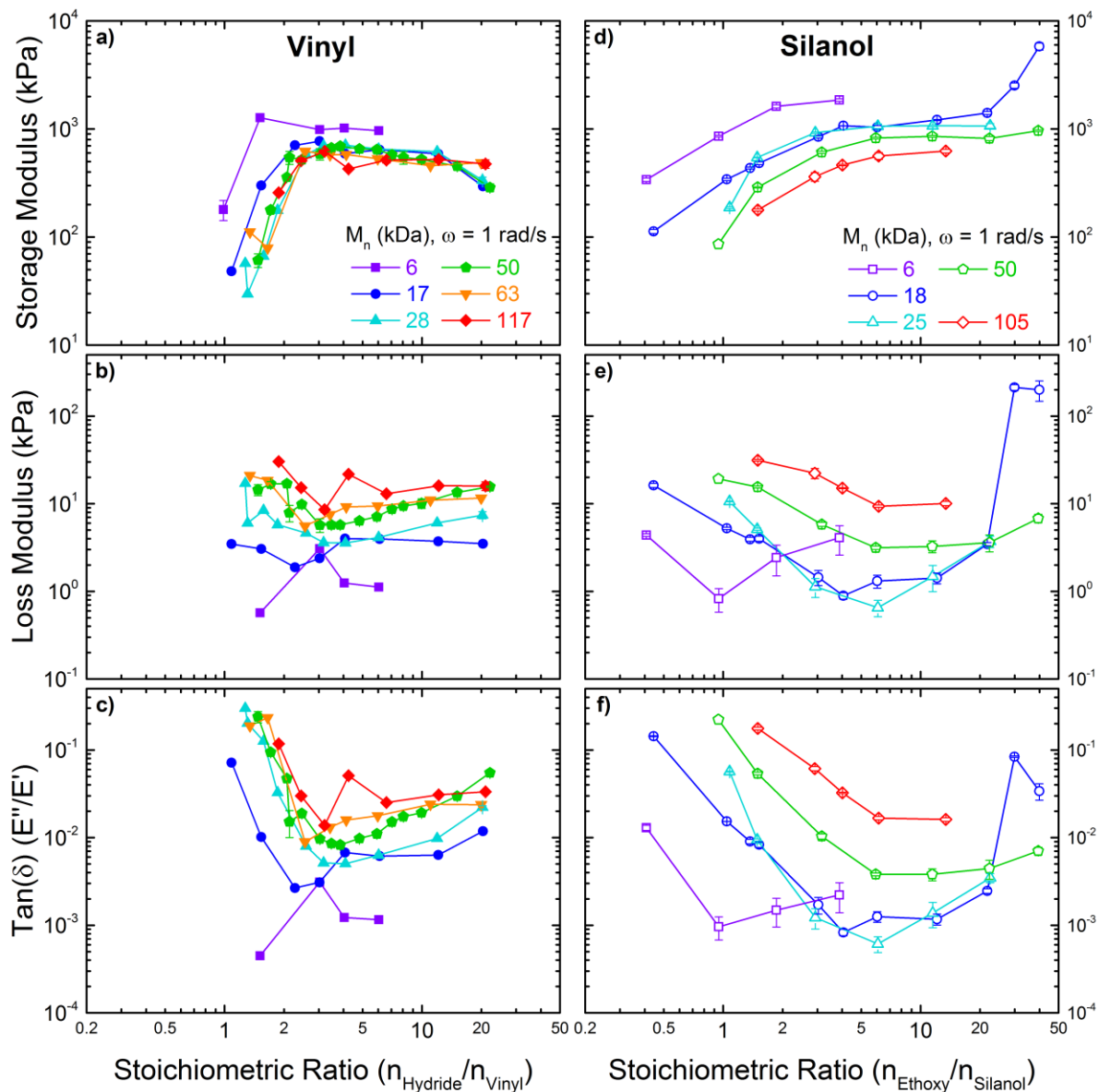


Figure 4.7 – Dynamic mechanical properties at an angular frequency of 1 rad/s of model PDMS systems plotted as a function of stoichiometric ratios for constant molecular weight series. Mechanical properties at an angular frequency of $\omega = 1$ rad/s for all model PDMS samples prepared in this investigation are plotted as a function of the stoichiometric ratio, r . Plots a, b, and c show the storage modulus, loss modulus, and the loss tangent, respectively, for vinyl-terminated PDMS networks. Plots d, e, and f show the storage modulus, loss modulus, and the loss tangent, respectively, for silanol-terminated PDMS networks.

stoichiometric ratios similar to the fully-crosslinked region in gel fraction data (*cf.* Figure 3.5a). However, when zoomed in, minor - but non-negligible - distinctions do become apparent (*cf.* Figure A4.4 in the Appendix). With yet further increases in stoichiometric ratio, the storage modulus begins to decrease in the excess crosslinker region, again mirroring the trend with gel fraction (*cf.* Figure 3.5a).

The storage modulus data of the Silanol/TEOS system in Figure 4.7d demonstrate more significant dependence on molecular weight and stoichiometric ratio. There are clear differences in storage modulus that result from preparing networks from a given molecular weight PDMS. This trend is similar to that in Figure 3.5b wherein greater molecular weights require greater stoichiometric ratios to achieve maximum gel fraction. Here, the 6 kDa sample is clearly the molecular weight that yields the greatest storage modulus, similar to the 6 kDa samples in the Vinyl/TDSS system. Other than the 6 kDa data, however, distinction between molecular weights is difficult (*cf.* Figure 4.7a) in the Vinyl/TDSS system. In contrast, there are more noticeable gaps in maximum storage modulus values for each value of molecular weight prior to crosslinking. Further details with respect to molecular weight will be discussed in the next section. The Silanol/TEOS system requires noticeably larger increases in the stoichiometric ratio to increase the storage modulus, hence a broadening of the data in Figure 4.7d with respect to stoichiometric ratio, which is also comparable to the gel fraction dependence on stoichiometric ratio (*cf.* Figure 3.5b).

In the fully-crosslinked region, there exists a plateau in storage modulus where no additional increases in storage modulus are observed with increasing the stoichiometric ratio. However, as the data enter the excess crosslinker region, the storage exhibits a significant increase instead of continuing to plateau with increasing stoichiometric ratios, as is the case for gel fraction. A dramatic increase in storage modulus occurs with very high crosslinker loading for the 18 kDa silanol-terminated PDMS system and a slight upturn is also evident for the 50 kDa system. Thus, there is no optimal stoichiometric ratio with respect to storage modulus for the Silanol/TEOS system since storage modulus continuously increases with increasing stoichiometric ratio. This provides evidence that the *in situ* formation of silica

particles discussed previously in Chapter 2 of this dissertation is effecting significantly the mechanical properties (*vide infra*), which is in accordance with previous findings.^{33,43,44}

In most samples, minima in loss modulus and in $\tan(\delta)$ are observed at some stoichiometric ratio that sometimes, but not always, corresponds with the highest storage modulus value observed in the Vinyl/TDSS system. The 6 kDa silanol PDMS is noteworthy due to the minimum in $\tan(\delta)$ at precisely the stoichiometric balance of $r = 1$. However, this does not correlate with the highest storage modulus. Additionally, if more stoichiometric ratios were prepared with smaller increments, a more precise value of the minimum could be determined. The loss modulus data for the Vinyl/TDSS system exhibits weak but clear dependence on molecular weight, and also, fairly weak dependence on the stoichiometric ratio. Minima in loss moduli are observed for the Vinyl/TDSS system, but not as deep of minima compared to the Silanol/TEOS system, indicating that the stoichiometric ratio in the Silanol/TEOS system more greatly influences the materials' ability to dissipate energy compared to Vinyl/TDSS system. Furthermore, the minima in $\tan(\delta)$ are spread out over a larger stoichiometric ratio for the Silanol/TEOS system compared to the Vinyl/TDSS system.

Overall, the Silanol/TEOS system enables one to create PDMS elastomers with a broader range of mechanical properties than does the Vinyl/TDSS system and the properties of such elastomers depend more strongly on the molecular weight and stoichiometric ratio of the elastomer mixture before crosslinking. The Vinyl/TDSS system is able to make softer materials with lower storage moduli while the Silanol/TEOS system can achieve more rigid and stronger materials with higher storage moduli. As will be seen, the Silanol/TEOS system can also achieve samples of high strength and flexibility that approach the properties of Sylgard 184.

Molecular Weight Effects

To more directly investigate the molecular weight influence on mechanical properties, the same data from Figure 4.7 are plotted as a function of molecular weight for data series consisting of approximately constant stoichiometric ratios in Figure 4.8. The same phenomena described in the discussion of Figure 4.7 are applicable here. For instance, one immediately

notices a weak dependence of storage modulus on molecular weight for fully crosslinked Vinyl/TDSS systems, *i.e.*, the slope of the data is very shallow. Additionally, the data seem to

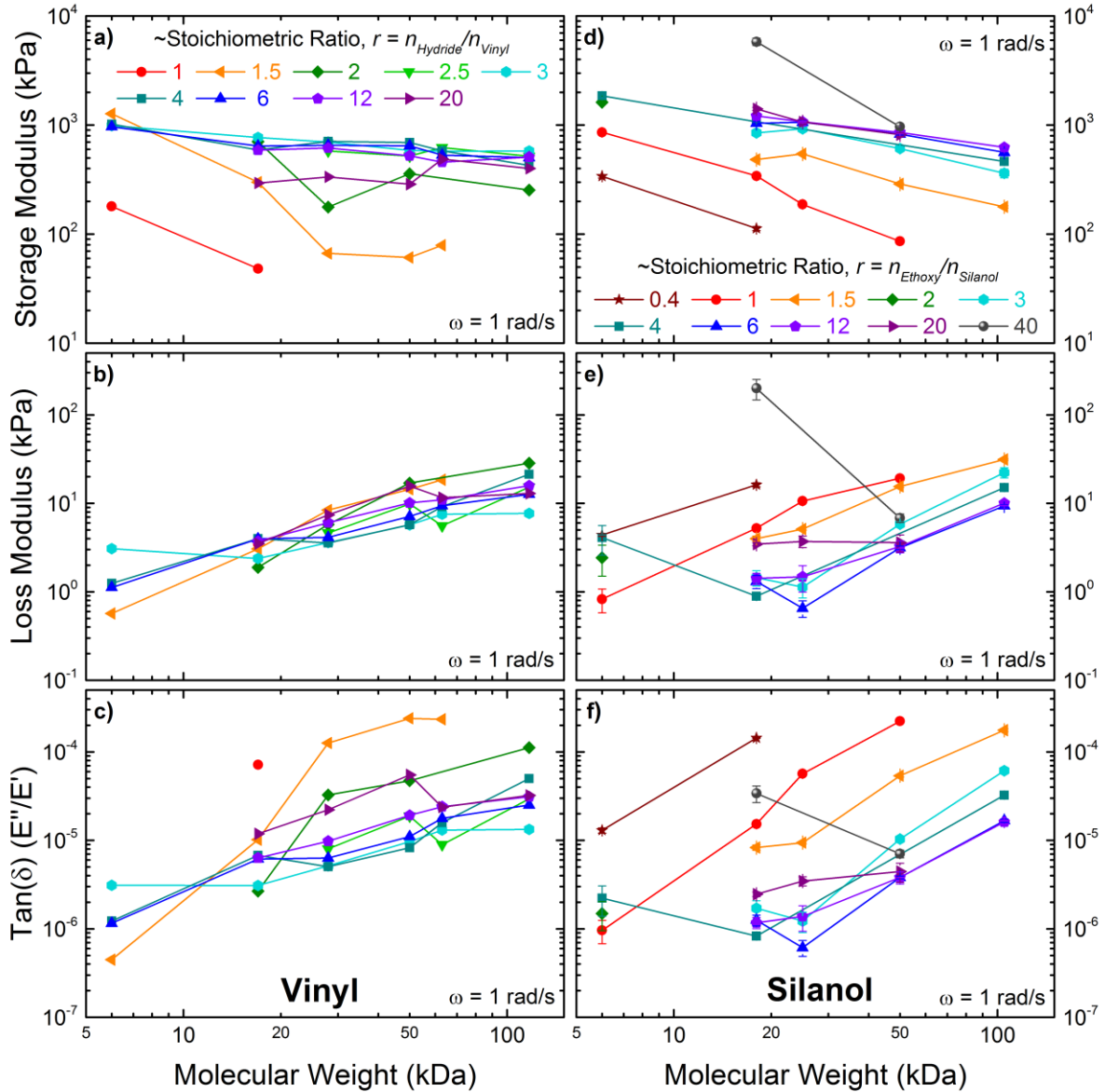


Figure 4.8 – Dynamic mechanical properties at an angular frequency of 1 rad/s of model PDMS systems plotted as a function of molecular weight for constant stoichiometric ratio series. Storage modulus is plotted in a and d, loss modulus is plotted in b and e and Tan(δ) is plotted in c and f as a function of molecular weight prior to crosslinking for the Vinyl/TDSS system in plots a, b, c and the Silanol/TEOS system in plots d, e, f for various stoichiometric ratios. The legends are the same for plots a, b, and c in the vinyl system and for plots d, e, and f in the silanol system. Samples were extracted prior to testing.

fall on a master curve for the loss modulus of the Vinyl/TDSS system, indicating rather weak stoichiometric ratio dependence and but modest molecular weight dependence, as evidenced by the slightly positive slope. The same is true for $\tan(\delta)$ in the Vinyl/TDSS system, albeit with a greater dependence on stoichiometric ratio as evidenced by the increased spread in the data.

The Silanol/TEOS system demonstrates strong dependence on stoichiometric ratio, as seen by the general lack of crossing of each stoichiometric ratio data series. For instance, the red circles, corresponding to a stoichiometric ratio of $r \approx 1$, seem to demonstrate a power-law relationship (linear on the log-log scale) between mechanical properties and molecular weight. Compared to other stoichiometric ratios, the slopes are roughly similar but the absolute values of mechanical properties are shifted. Generally, it is notably easy to distinguish the trend of mechanical properties with molecular weight for each stoichiometric ratio in the Silanol/TEOS system while such a distinction is not readily apparent in the Vinyl/TDSS system.

In the Silanol/TEOS system, the under-crosslinked stoichiometric ratios (dark red, red, and orange data sets) tend to yield soft materials with lower storage moduli and higher $\tan(\delta)$ for a given molecular weight. Generally, storage modulus decreases and loss modulus and $\tan(\delta)$ increase with increasing molecular weight. The only data series that exhibits peculiar behavior is that for a stoichiometric ratio of $r = 40$, shown as dark gray spheres. The reason the slope is descending for this series as opposed to ascending for all other series in plots of loss modulus and $\tan(\delta)$ is due to a step-change behavior that occurs when some critical mass fraction of TEOS is added to the system. This critical mass fraction is likely independent of molecular weight, but occurs at significantly different stoichiometric (*i.e.*, molar) ratios due to molecular weight. For example, a stoichiometric ratio of $r = 40$ for both the 18 and 50 kDa samples corresponds to mass fractions of TEOS equal to 18.5 and 7.5%, respectively (*cf.* Chapter 2 of this dissertation). Thus, a critical mass fraction of TEOS upon which silica-like aggregates form has not yet been reached in the 50 kDa system, which explains the lack of upturn in mechanical properties. A particular stoichiometric ratio of TEOS, different for each molecular weight, defines the point when TEOS begins aggregating. At this point, it becomes more practical to monitor amount of TEOS in terms of a mass fraction instead of mole ratio.

Unfortunately, this parameter space was not thoroughly explored during this research and only the 18 kDa molecular weight has been studied.

Sylgard 184 Dynamic Mechanical Properties

The commercial product, Sylgard 184, which contains up to 50 wt% chemically treated fumed silica filler particles,³⁶ was investigated at different base/curing agent (B/C) ratios and data was gathered both before and after performing Soxhlet extraction. The primary crosslinker in Sylgard 184 is a random copolymer consisting of an unknown fraction of methylhydro-siloxane repeat units with the remaining repeat units being dimethylsiloxane. This results in an unknown crosslinker functionality,³⁷ but one that is likely greater than 4, which is used in both model systems. It is similar to the Vinyl/TDSS system because both crosslinking chemical reactions occur via hydrosilylation. Thus, it displays some similar behavior compared to the Vinyl/TDSS system, as will be demonstrated below.

In Figure 4.9, dynamic mechanical properties at an angular frequency of 1 rad/s are plotted as a function of the B/C ratio in plot a and as a function of the sol fraction in plot b. Pre-extraction data are shown as filled symbols and solid lines while post-extraction data are displayed as open symbols and dashed lines. Storage (blue) and loss (red) moduli are both plotted on the left ordinates while $\tan(\delta)$ is given on the right ordinates. An optimal B/C ratio of 5:1, which is markedly different than the 10:1 ratio prescribed by the manufacturer, gives the highest storage modulus. However, the prescribed B/C ratio of 10:1 produces the maximum loss modulus. Preparing materials at B/C ratios other than the optimal ratio of B/C = 5 results in a lower storage modulus, as is the case when non-optimal stoichiometry is used in the Vinyl/TDSS system (*vide supra*). From Figure 4.9a, it is evident that the storage and loss moduli follow the same trend with respect to stoichiometry. That is, they both generally decrease when deviating from optimal stoichiometry. Conversely, in the model systems, the storage and loss moduli act inversely to each other with respect to stoichiometry (*i.e.*, when E' increases, E'' decreases and vice-versa for model PDMS). The $\tan(\delta)$, displays less regular behavior compared to the storage and loss moduli. With Sylgard 184, there appears to be a plateau in $\tan(\delta)$ over which small changes in B/C ratio between ~10-20 do not cause

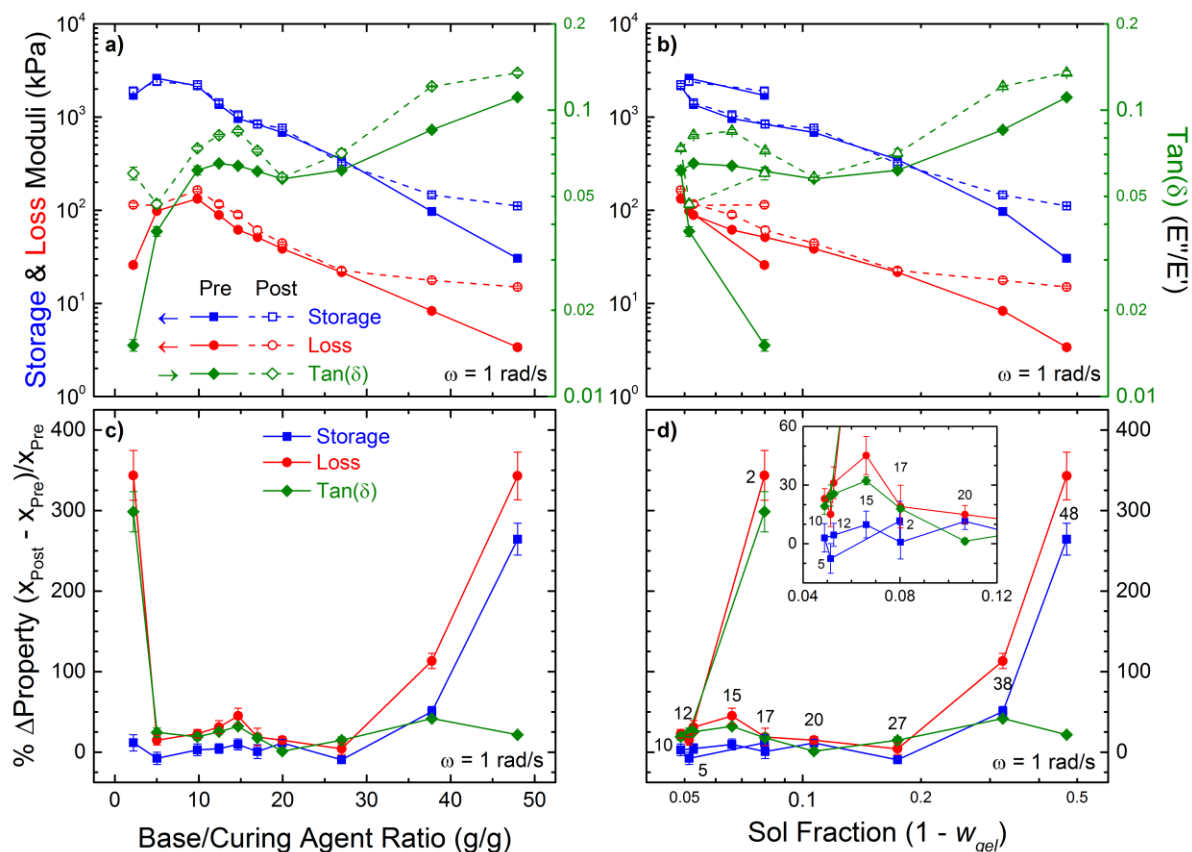


Figure 4.9 – Dynamic mechanical properties of Sylgard 184 commercial PDMS at an angular frequency of $\omega = 1$ rad/s. In a and b, the storage modulus (blue squares, left ordinates), loss modulus (red circles, left ordinates), and $\tan(\delta)$ (green triangles, right ordinates), prior to (filled symbols, solid lines) and after (open symbols, dashed lines) Soxhlet extraction are plotted as a function of the B/C ratio and sol fraction, respectively. The percent change in storage modulus (blue squares), loss modulus (red circles) and loss tangent (green diamonds) is plotted as a function of stoichiometric ratio in c and sol fraction in d. The inset, shows a zoomed in region of d. The percent change in mechanical properties is defined as the quantity of value post-extraction minus the value pre-extraction divided by the value pre-extraction. Thus, negative percent changes correspond to smaller values post-extraction. The data labels in d correspond to B/C ratios and align vertically with the data in b.

any changes in $\tan(\delta)$. However, when the B/C ratio decreases dramatically, $\tan(\delta)$ decreases while at larger B/C values, it increases. The $\tan(\delta)$ is a measure of a material's ability to dampen forces acting on it, *i.e.*, a material's ability to dissipate energy. The under-crosslinked samples at high B/C ratios are goeey materials that freely deform when a force is applied, which means they can readily dissipate energy and show very little resistance to applied forces.

The effect of degree of gelation on Sylgard 184 samples is demonstrated in Figure 4.9b. Materials that contain large sol fractions, which correspond to very high B/C ratios and under-

crosslinked materials, generally exhibit relatively lower values of both the storage and loss moduli, compared to those with small sol fractions. These samples are also accompanied by the highest $\tan(\delta)$ values observed. As the material becomes fully crosslinked and achieves a low sol fraction, the highest storage and loss moduli are achieved. The mechanical properties of Sylgard 184 loop back down as the B/C ratio is decreased below 10, resulting in higher sol fractions and lower mechanical properties. Generally, $\tan(\delta)$ remains in the range of $\sim 0.01 - 0.2$ for Sylgard 184 regardless of sol fraction, which is 1-2 orders of magnitude greater than $\tan(\delta)$ observed in the model PDMS systems (*vide supra*). The relatively high range of $\tan(\delta)$ values coupled with high storage and loss moduli demonstrate the very impressive ability of Sylgard 184 to exhibit both high strength and ease of deformability. The role filler particles play in this observation will be discussed later.

Changes Due to Extraction

While the plots in Figure 4.9a and b demonstrate similar trends pre- and post-extraction for each mechanical property as a function of B/C ratio and sol fraction, to take into account the magnitude of the properties being tested, one can examine the percent change before and after extraction. Such data are presented in Figure 4.9c and d. A discussion and accompanying plots related to the absolute change in mechanical properties is given in the Appendix (*cf* Figure A4.3), while only the percent change in properties is discussed here. In Figure 4.9, the percent change of each mechanical property, (storage modulus in blue, loss modulus in red, and $\tan(\delta)$ in green), with respect to its value prior to extraction is plotted as a function of the B/C ratio in plot c and as a function of the sol fraction in plot d. The labels in plot d correspond to B/C ratios and the inset shows a zoomed in region for the smallest sol fraction data. The labels align vertically with the data in b.

Interesting trends emerge from these plots. First, it is apparent that significant relative changes in properties occur when deviating far from the prescribed 10:1 B/C ratio. In fact, the largest changes occur when deviating ~ 5 -fold from the B/C ratio of 10:1, *i.e.*, when $B/C \approx 2$ or 48. For under-crosslinked samples, *i.e.*, excess polymer and $B/C \gg 10$, the storage and loss moduli both undergo very large changes after extraction on the order of 250-350%. Because

both of these properties change with similar orders of magnitude, $\tan(\delta)$ does not change significantly. On the other hand, when excess crosslinker is present, *i.e.*, $B/C \ll 10$, only the loss modulus changes in excess of 300% while the storage modulus shows minimal change. This results in $\tan(\delta)$ also changing significantly. Extraction removes the material not chemically bound to or permanently trapped in the network. Before extraction, the unbound material acts like a plasticizer, helping to dissipate forces acting on the material. Once that material is removed, the storage modulus increases. Taken alone, this would indicate that the material becomes more elastic. However, the loss modulus also shows an increase after extraction. The explanation for this change will be given shortly, but in short, this is due to the presence of filler silica particles.

These changes in mechanical properties before and after extraction cannot be attributed to the degree of crosslinking alone. In examining Figure 4.9d, the sol fraction of the $B/C = 2$ sample is ~ 0.07 , which is similar to that of $B/C = 17$. This means that despite both systems having 7% of material removed during extraction (or, conversely, 93% material remaining in the gel), the mechanical properties of the $B/C = 2$ sample change dramatically pre- vs. post-extraction while $B/C = 17$ does not change significantly. Thus, different types of material must be removed during the extraction process to cause such a change. In the $B/C = 17$ sample, there is a slight excess of polymer, resulting in an under-crosslinked network. In this scenario long polymer chains would be the primary component extracted. In contrast, the $B/C = 2$ sample has an excess of short-chain crosslinkers, thus they would be the majority of material removed. As a result of extracting the short chain crosslinkers, the loss modulus increases significantly. Although one would expect the loss modulus to decrease after extraction of oligomers and polymer chains, which are liquid-like and can dissipate energy, this observation is due to the presence of fumed silica particles.

The Role of Filler Particles Influence in Dynamic Mechanical Properties

When filler particles are present in high enough concentrations *i.e.*, above the percolation threshold, they tend to associate into a connected secondary network structure within the polymer matrix due to filler-filler interactions.⁴⁵ This leads to nonlinear

viscoelasticity in polymer-filler composite materials where the strain amplitude in the small-strain region can strongly influence the storage and loss moduli measured, unlike in unfilled polymers where there is a linear viscoelastic response in the small-strain region.⁴⁶ The so-called Payne effect, first observed by Payne in the early 1960s with carbon black fillers in natural rubber,^{47,48} is the observation of storage modulus decreasing and loss modulus peaking at some critical value as strain amplitude is increased from $\sim 10^{-5}$ to $10^{-1}\%$. The decrease in storage modulus and simultaneous maximum in loss modulus was attributed to the breakdown of filler particle secondary network structure, or de-agglomeration, which both weakens the material and dissipates energy. The precise reinforcement mechanism of fillers in elastomers is still not completely understood and is a topic of ongoing research. Other competing theories are that the filler-polymer interactions play a bigger role because the Payne effect has been observed in systems below the percolation threshold.^{49,50} This bonding and de-bonding, in a physical, not covalent, sense between the polymer and filler particle surface can also contribute to dissipative mechanisms in composite materials.

An explanation for the dramatic change in loss modulus in the $B/C = 2$ sample compared to the $B/C = 17$ sample is due to the filler particles and the type of material removed during extraction. The ability for filler particles to dissipate energy by multiple mechanisms likely renders them better suited in dissipating energy than the short-chain crosslinker oligomers. Despite losing the oligomers to extraction, this has the effect of increasing the concentration of filler particles remaining in the polymer matrix. If the particles are more efficient at dissipating energy than oligomers, this would explain the increase in loss modulus as a result of extraction. In the $B/C = 17$ sample, longer PDMS chains are in excess and are thus the majority component removed. Longer chains would be better at dissipating energy than shorter oligomers, so by removing them one expects a decrease in loss modulus and energy dissipating abilities. However, removing the long chains also increases the concentration of fillers, resulting in no significant increase in loss modulus. That is, the two mechanisms of energy dissipation (*i.e.*, filler-filler and filler-matrix interactions *vs.* excess viscous long chains) both approximately cancel each other out as a result of the extraction process.

The hypothesis that a greater concentration of filler particles increases loss modulus is supported by the trends in Figure 4.7d where both the storage and loss moduli of the 18 kDa silanol-terminated PDMS/TEOS system increase as more TEOS, and thus silica aggregates, are added. Increases in storage and loss moduli as a result of increased filler content have been observed previously in similar precipitated silica-PDMS composite materials.³⁰ The incorporation of silica-like aggregates formed *in situ* due to excess TEOS results in an increased loss modulus over just a pure polymer. This is directly observed by comparison of the 17 and 18 kDa samples (blue data) in the Vinyl/TDSS system vs. the Silanol/TEOS system in Figure 4.7b and e. For stoichiometric ratios of $r = 20$, both systems exhibit loss moduli at 1 rad/s equal to ~ 3.5 kPa. However, upon additional increases in TEOS, the loss modulus rapidly increases for the Silanol/TEOS system, which is not predicted from the trend of the lower stoichiometric ratios leading up to $r = 20$. This upturn is not likely in the Vinyl/TDSS system.

Slope of Frequency Curves

In addition to analyzing mechanical properties at a particular frequency, the slopes of the mechanical properties vs. frequency curves can reveal useful information. For the storage modulus, slopes of zero with respect to frequency are indicative of fully crosslinked networks.⁵¹ Thus, such samples have a constant storage modulus value over a wide range of frequency. Slopes greater than zero indicate material that is not fully crosslinked. At the gel point, the storage and loss moduli should have the same slopes with respect to frequency, *i.e.*, they are parallel.^{52,53,51} With additional crosslinking, the slope of the storage modulus decreases and approaches zero for a fully crosslinked sample. It is typical for the loss modulus to have a positive slope in the range of $\sim 0.3-0.7$ for very soft silicone elastomer materials.⁵⁴ Under-crosslinked materials with higher sol fractions exhibit steeper slopes while more fully crosslinked materials with lower sol fractions exhibit more shallow slopes.⁵⁴ Thus, the minimum in slope of loss modulus for $B/C = 10$ corresponds to a near-fully crosslinked network. This is also supported by data plotted in Figure 4.10b wherein the minimum slope

of loss modulus occurs at the minimum sol fraction and for B/C = 10, indicating optimal crosslinking.

The slope of the storage modulus generally increases after extraction while the slope of loss modulus decreases after extraction, as indicated in Figure 4.10c and d where the blue squares representing the slope of the storage modulus are greater than 0 while the red circles representing slope of loss modulus are less than zero. This is in agreement with others who

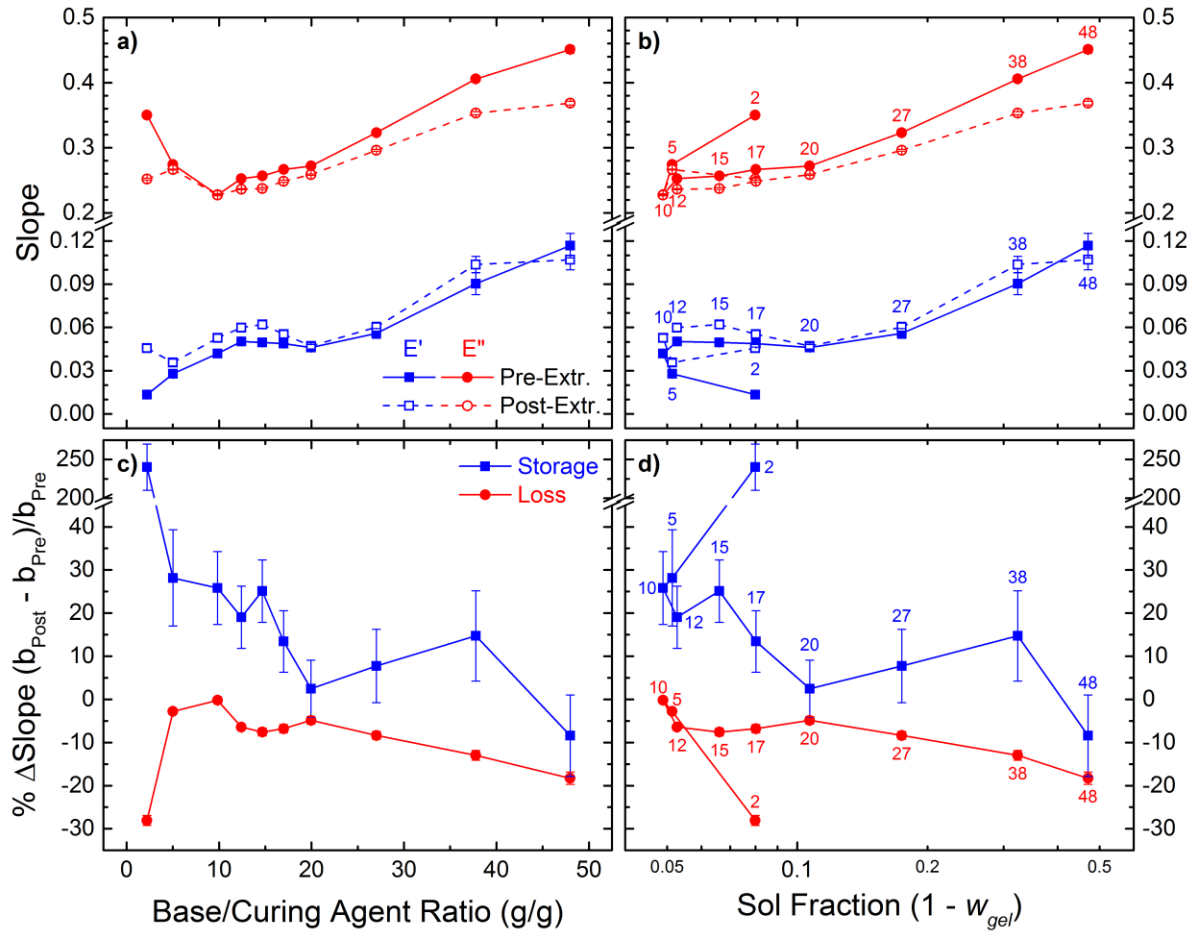


Figure 4.10 - Mechanical properties vs. angular frequency curves were fit with power-law functions according to $y = A\omega^b$, as shown in Figure A4.2 in the Appendix. The slopes of the curves, b , are plotted for the storage (blue squares) and loss (red circles) moduli pre-extraction (filled symbols, solid lines) and post-extraction (open symbols, dashed lines) as a function of stoichiometric ratio and sol fraction in plots a and b, respectively. The legend is the same for a) and b). In plots c and d, the percent change in the slope as a result of extraction is plotted for storage (blue square) and loss (red circle) moduli as a function of B/C ratio and sol fraction, respectively. The legend is the same for plots c and d. Labels in plots b and d correspond to B/C values.

have observed the loss modulus slope decrease after extraction.⁵⁵ Only minor changes in slope of storage modulus occur for most B/C ratios except for the 5-fold excess crosslinker sample of B/C = 2. Similar to the preceding discussion, this is not simply a matter of removing ~7% of the material during the extraction process since the B/C = 17 sample has the same sol fraction but does not exhibit dramatic changes. Instead, as before, it is a matter of what type of material is removed during the extraction process. The removal of the excess crosslinker short-chain oligomers leads to strong changes in the magnitude of the loss modulus (*cf.* Figure 4.9) and the slopes of the storage and loss moduli (*cf.* Figure 4.10). This suggests that removing short chains and long chains results in different changes to the material.

In this section, Sylgard 184 mechanical properties were studied extensively. It was shown that the storage and loss moduli follow the same trends with respect to stoichiometry and sol fraction. Additionally, the extraction process results in dramatic changes to both the magnitude and slope of the loss modulus data for samples made from ~5-fold deviations from optimal stoichiometry (*i.e.*, B/C = 2 & 48). On the other hand, the majority of the B/C ratios tested, $5 < B/C < 27$, show significant stability to the extraction process, resulting in only minor changes in mechanical properties.

Comparison between Sylgard 184 and Model PDMS Systems

Now we present direction comparisons between the two model PDMS systems and Sylgard 184. The model PDMS cannot be directly compared to Sylgard 184 in terms of stoichiometry since Sylgard 184 is prepared based on a mass ratio of two proprietary mixtures and model PDMS networks are prepared based on molar ratios of crosslinker and polymer. However, they can be compared based on their extent of crosslinking, as measured by the gel and sol fractions.

Sol Fraction Effects

The similarities and differences between Sylgard 184, Vinyl/TDSS, and Silanol/TEOS PDMS systems are demonstrated in Figure 4.11 where all mechanical properties for extracted samples are plotted against the sol fraction of the sample. The highest storage and lowest loss

moduli occur in model systems at the lowest sol fraction, or highest degree of crosslinking. Conversely, Sylgard 184 exhibits the highest storage and highest loss moduli simultaneously at the lowest sol fraction, thus providing high elasticity and flexibility. There appear to be two regimes wherein the sol fraction influences the mechanical properties of the networks. For the

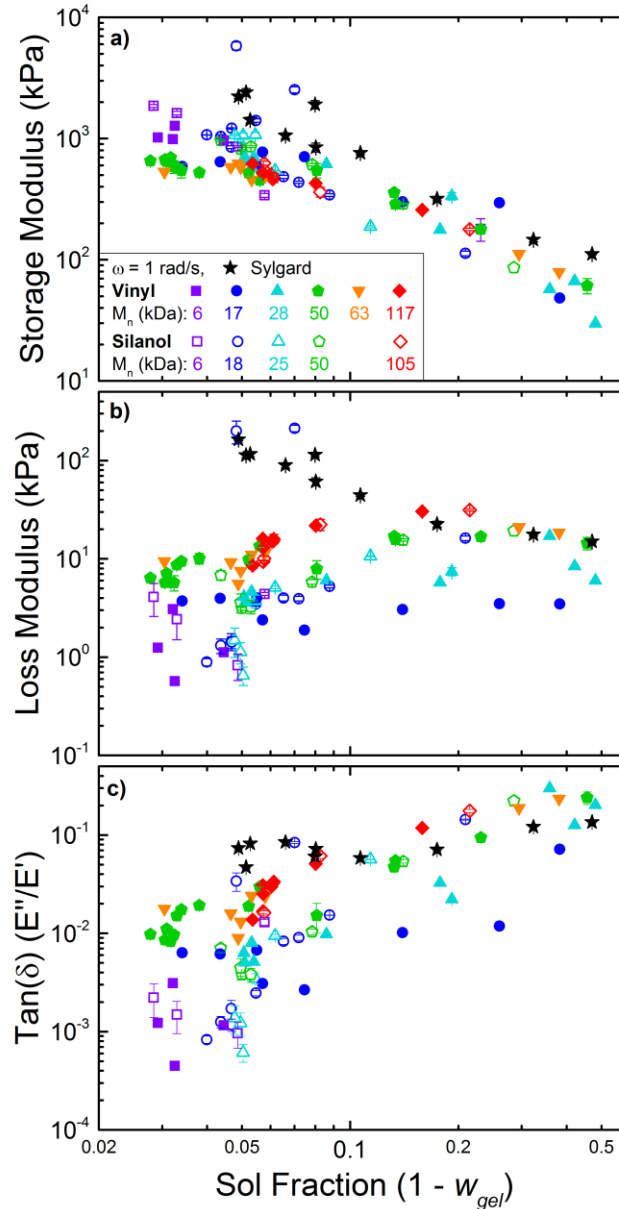


Figure 4.11 – Plots of storage modulus, loss modulus, and $\text{Tan}(\delta)$ in plots a, b, and c, respectively, at an angular frequency of $\omega = 1$ rad/s for post-extraction samples as a function sol fraction for all model networks and Sylgard 184 samples tested.

storage modulus, when the sol fraction is greater than ~ 0.07 , E' decreases. As sol fraction decreases less than ~ 0.07 , E' changes less significantly, demonstrating only very minor increases and almost plateauing, thus showing very little dependence on sol fraction. The exception is with Sylgard 184 and two samples of the 18 kDa Silanol/TEOS ($r = 30$ & 40) system that exhibited sharp upturns in storage modulus in Figure 4.7d. This is due to the presence of filler particles.

The loss modulus seems to be fairly independent of sol fraction for most samples with slight increases in E'' occurring with increases in sol fraction. There is an exception, again, with Sylgard 184 and the two model 18 kDa Silanol/TEOS samples, which steadily decrease as sol fraction increases. Additionally, for samples of low molecular weight and low sol fractions, the data tend to exhibit downturns showing sharp decreases in loss modulus with incremental decreases in sol fraction. Lastly, Sylgard 184 exhibits different behaviors from the model systems with respect to the $\tan(\delta)$. The behavior of $\tan(\delta)$ also follows two regimes of influence where it increases with increasing sol fraction for $w_{sol} > 0.07$ and decreases more sharply with decreasing sol fraction for $w_{sol} < 0.07$. Broadly, there seems to be a slight molecular weight dependence, wherein the violet and blue data (short chains, below the entanglement molecular weight of $M_c = 28$ kDa⁵⁶) tend to give higher storage moduli and lower loss moduli compared to the green, orange and red data, which are of greater molecular weight than M_c . Generally, Sylgard 184 samples (black stars) display higher mechanical properties in all three parameters compared to most data from the model systems.

Mechanical Property Possibilities

Our discussion of the influence of particles or aggregates in Sylgard 184 and a few model Silanol/TEOS samples has been limited thus far. The most direct demonstration of aggregate and particle influences is now presented in Figure 4.12. Here, to further demonstrate the mechanical behavior of all the silicone elastomers tested, $\tan(\delta)$ is plotted as a function of both the storage and loss moduli in Figure 4.12a and b, respectively. The loss modulus is plotted as a function of the storage modulus in Figure 4.12c. Digital photographs depict the 117 (top) and 6 kDa (bottom) Vinyl/TDSS samples being bent. The SEM images show the 18

kDa Silanol/TEOS samples for stoichiometric ratios of $r = 40$ (d) and $r = 1.5$ (e)

These plots illustrate vividly the difference between model tetrafunctional crosslinked PDMS systems and the commercially available Sylgard 184 that contains filler particles and is crosslinked at higher functionality with a random short-chain copolymer. As the storage modulus increases, with model systems, $\tan(\delta)$ drops nearly two orders of magnitude lower

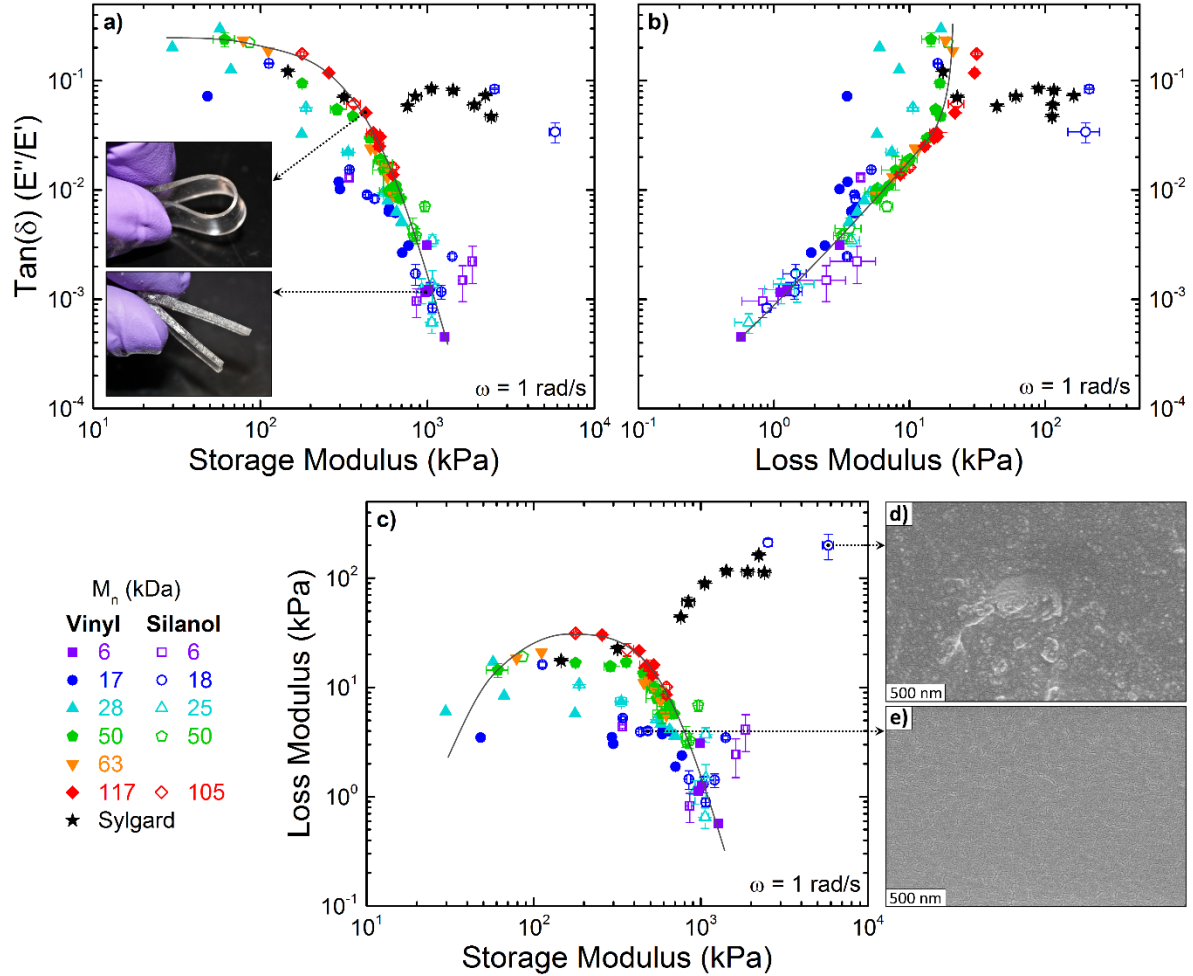


Figure 4.12 – Comparison of all dynamic mechanical properties for samples all model PDMS and Sylgard 184 samples post-extraction. $\tan(\delta)$, is plotted against the storage modulus in a, and loss modulus in b. The loss modulus is plotted as a function of the storage modulus in c. Insets show digital photographs demonstrating the flexibility of Vinyl/TDSS systems of 117 kDa (top) and 6 kDa (bottom). SEM images of 18 kDa PDMS from the Silanol/TEOS system at stoichiometric ratios of $r = 40$ and $r = 1.5$ are shown in d and e, respectively. All mechanical data is taken at an angular frequency of $\omega = 1$ rad/s. Gray lines are to guide the eye according to all model PDMS (*i.e.*, particle-free samples).

than Sylgard 184. Practically, this means that while one can achieve a high storage modulus from unfilled PDMS material, especially with the Silanol/TEOS system, it will be very brittle and inflexible. The higher $\tan(\delta)$ values inherent in Sylgard 184 give it both flexibility and high storage modulus, which render it a tough material capable of undergoing large amounts of strain without breaking (*vide infra*). Similarly, the model PDMS cannot achieve both high loss modulus and high $\tan(\delta)$, unless silica particles are precipitated into the matrix via excessively high TEOS loading. Thus, these data demonstrate a range of possibilities for mechanical properties that can be made from model PDMS networks without adding filler particles. This range is depicted by gray lines that guide the eye to match the trends in the model PDMS data. Sylgard 184 pushes out past that range of mechanical property possibilities, making it a composite elastomeric material with impressive mechanical properties.

The ability for Sylgard 184 and two Silanol/TEOS samples that formed particles *in situ* to exhibit both high loss and storage moduli indicates their ability to dissipate energy and readily deform, albeit with high amounts of stress required due to their high storage modulus. This means that particles are excellent energy dissipaters, just as excess long polymer chains and pendant material are. As discussed previously, there are two mechanisms by which particles dissipate energy. One is due to the breakdown of the filler secondary network structure, primarily controlled by filler-filler interactions. The other is due to breakdown of physical bonds at polymer-filler interfaces. Conversely, liquids and rubbery polymers dissipate energy by viscous means, *i.e.*, flowing and readily deforming their shape. Higher molecular weight systems exhibit viscous dissipative mechanisms and excess TEOS loading results in filler-related mechanisms.

In summary, model PDMS materials that contain no particles or aggregates give an “either-or” range of material properties. That is, materials can be either strong and brittle, or soft and flexible. On the contrary, the inclusion of particles and/or aggregates enhances greatly material properties by enabling high degrees of deformability coupled with high strength.

Network Topology Effects

One of the major goals of this dissertation is to determine relationships between molecular-level architecture of polymer networks (*i.e.*, network topology) and macroscopic material properties. Thus, now that the macroscopic, or bulk, mechanical network properties have been demonstrated, the data gleaned from Chapter 3 of this dissertation will be used to elucidate structure-property relationships between the molecular and macro scales in these materials.

Molecular Weight between Effective Crosslinks – Affine Model

One key topological network parameter is the molecular weight between crosslinks, which is inversely proportional to the crosslink density of the network. As discussed in Chapter 3 of this dissertation, both trapped entanglements and chemical crosslinks can contribute to the elasticity of a network material. Thus, the mechanical properties measured in this chapter will depend on both of those phenomena.

Young's tensile modulus, E , is approximately equal to the storage modulus, E' , in the limit of $\omega \rightarrow 0$.¹⁷ This is used to approximate the molecular weight between effective crosslinks from the affine model, M_{Aff} , by applying a Poisson's ratio for PDMS equal to 0.5²³ according to Equation (4.8).¹⁷ Recall, the main assumptions in the affine model are that the chains and junctions both expand proportionally to the macroscopic deformation and that crosslink junctions are fixed in relative to the background.¹⁷

$$M_{Aff} = 3\rho RT/E' \quad (4.8)$$

The molecular weight between effective crosslinks according to the affine model, M_{Aff} , is plotted as a function of stoichiometric ratio for the vinyl and silanol systems in Figure 4.13a and b, respectively. These data mirror the data for storage moduli of the same systems (*cf.* Figure 4.7a and d since they are inversely proportional to the storage modulus). The samples that exhibit the highest storage moduli also exhibit the lowest molecular weight between effective crosslinks. There is a large decrease in M_{Aff} for the 18 kDa, $r = 40$ Silanol/TEOS sample which has the silica-like aggregates. This suggests that aggregates serve as obstacles

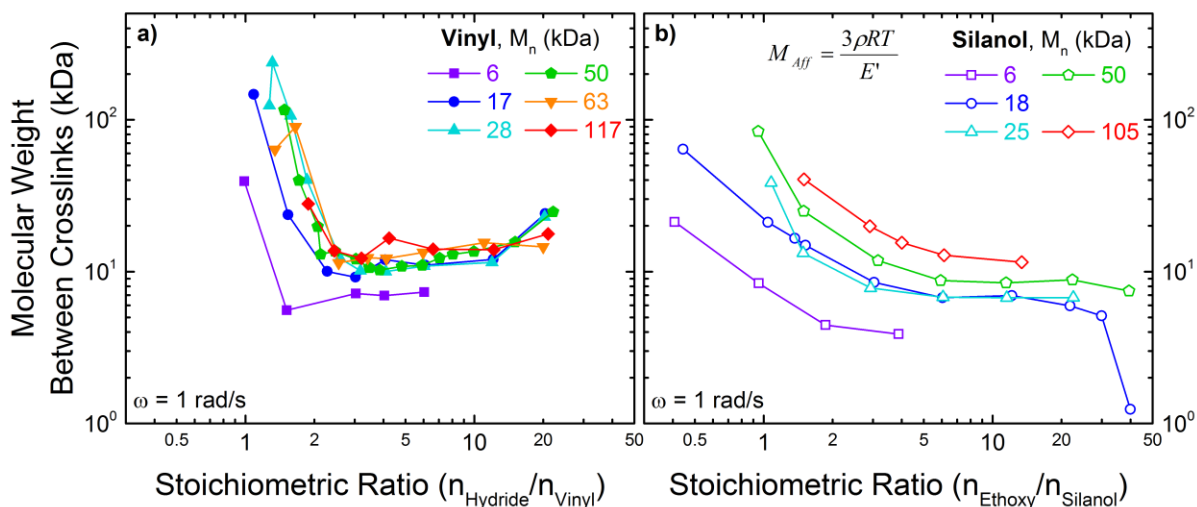


Figure 4.13 – Molecular weight between effective crosslinks according to the affine model, M_{Aff} , plotted as a function of stoichiometric ratio for the Vinyl/TDSS system in plot a and the Silanol/TEOS system in plot b.

that restrain chain motion in a similar manner to entanglements. Unlike entanglements, however, due to the chemical nature of TEOS, the silanol end-groups of PDMS in this system can attach covalently to the aggregates. This would restrain polymer motion to a greater degree than entanglements because of the covalent bond, as opposed to entanglements, which can slide along the chain.

Influence of Miller-Macosko Topological Network Parameters

The results from applying the Miller-Macosko model^{25,57,58} to the Vinyl/TDSS system were useful in gaining a deeper understanding of network topology. Here they will be related to the bulk dynamic mechanical properties. The derivation^{57,59} of the Miller-Macosko model and equations for topological network parameters are independent of mechanical properties. Therefore, comparing those parameters to mechanical properties is a strong way to assess the validity of the model and to understand the molecular level topology that results in observed bulk dynamic mechanical properties.

The storage modulus, loss modulus, and $\tan(\delta)$ are plotted as a function of the elastic fraction in Figure 4.14a, b, and c and as a function of the pendant fraction in Figure 4.14d, e, and f, respectively, for the Vinyl/TDSS system after extraction. The elastic fraction seems to

influence directly the storage modulus, as seen by the monotonic increase in storage modulus with elastic fraction in Figure 4.14a. It is not surprising that the material with the highest elastic fraction also exhibits the highest storage modulus. For the most part, as the pendant fraction increases, the storage modulus increases except at relatively high pendant fractions.

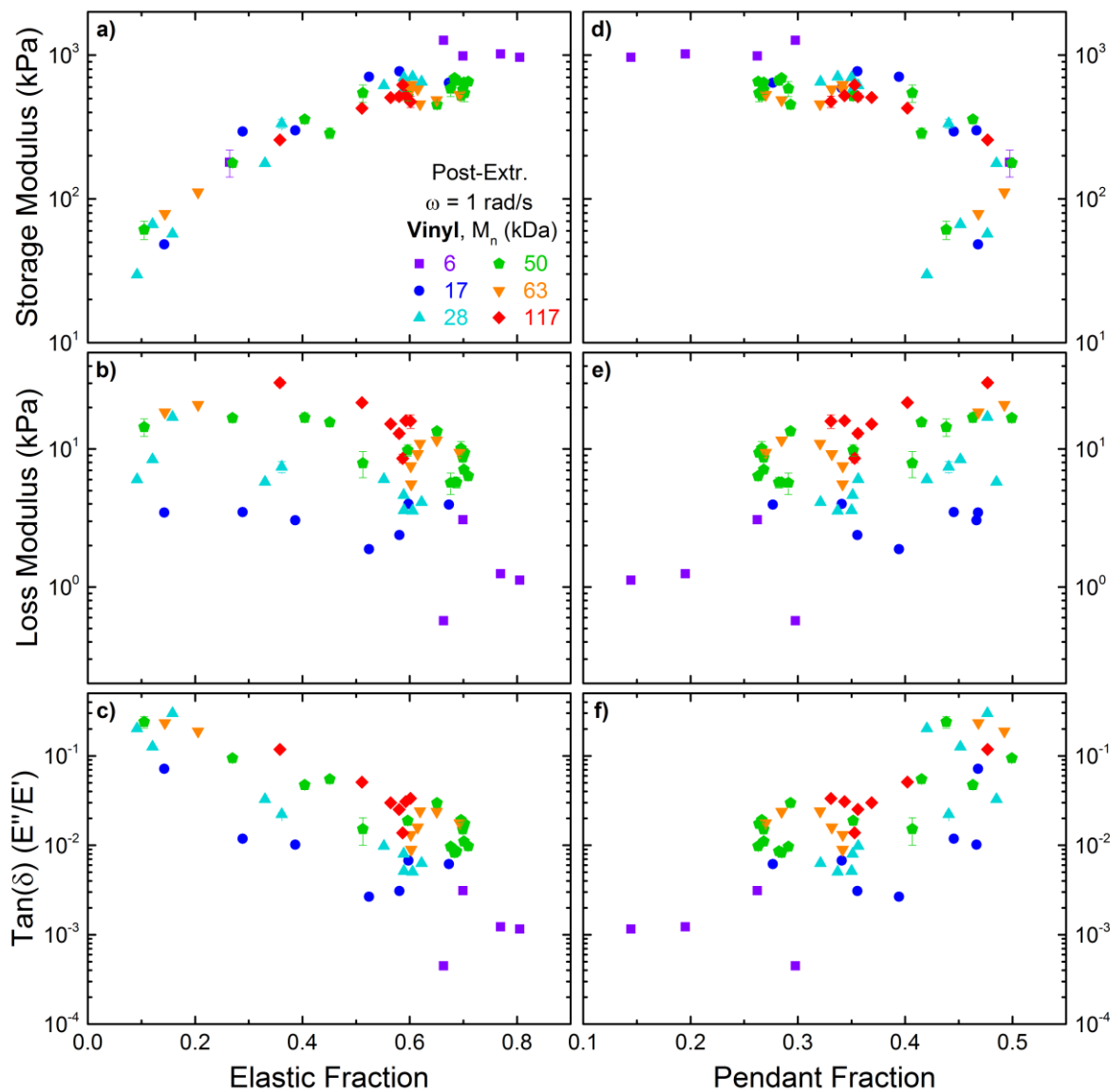


Figure 4.14 – Plots a, b, and c show the storage modulus, loss modulus, and the loss tangent, respectively, as a function of the elastic fraction. Plots d, e, and f show the same properties, respectively, as a function of the pendant fraction. Dynamic mechanical properties are reported at an angular frequency of 1 rad/s for post extraction samples.

The loss modulus displays weaker dependence on both the elastic and pendant fractions. Generally, the loss modulus decreases with increasing elastic fraction and decreasing pendant fraction, but there is greater spread in the data relative to the storage modulus. There appears to be a significant molecular weight dependence between loss modulus and elastic and pendant fractions. That is, lower loss modulus values are observed for shorter chains, which correspond to higher elastic and lower pendant fractions. Greater values of loss modulus are apparent with longer chains, which generally have lower elastic and greater pendant fractions. The $\tan(\delta)$ displays a stronger relationship to the elastic and pendant fractions compared to the loss modulus. Here it is readily apparent that greater elastic fractions and smaller pendant fractions results in smaller $\tan(\delta)$ values, which is in accordance with previous results.²⁹

Recall from Chapter 3 of this dissertation that elastically effective chains are defined as those which connect on both ends to the network whereas pendant chains are those attached only at one end to the network, or those that form small loops by attaching both ends to the same crosslinker molecule. The pendant material should be responsible for dissipating energy in the system while the elastic material should be responsible for storing energy in the system. Chains in the elastic fraction will supply the entropic restoring force when a strain is applied. Chains in the pendant fraction have much greater degrees of freedom of motion, since they are only covalently attached to the network at one end, which allows them to more readily dissipate energy.

These same ideas are supported by plotting the mechanical properties as a function of the effective crosslinker functionality and the entanglement trapping factor, which is shown in Figure 4.15. Recall from Chapter 3 that effective crosslinker functionality is the average number of functional groups per crosslinker molecule that have reacted with elastically effective chains. The entanglement trapping factor, a value between 0 and 1, is a measure of how many entanglements, if present, are permanently trapped. Thus, when the entanglement trapping factor is equal to 1, then 100% of entanglements present are trapped.

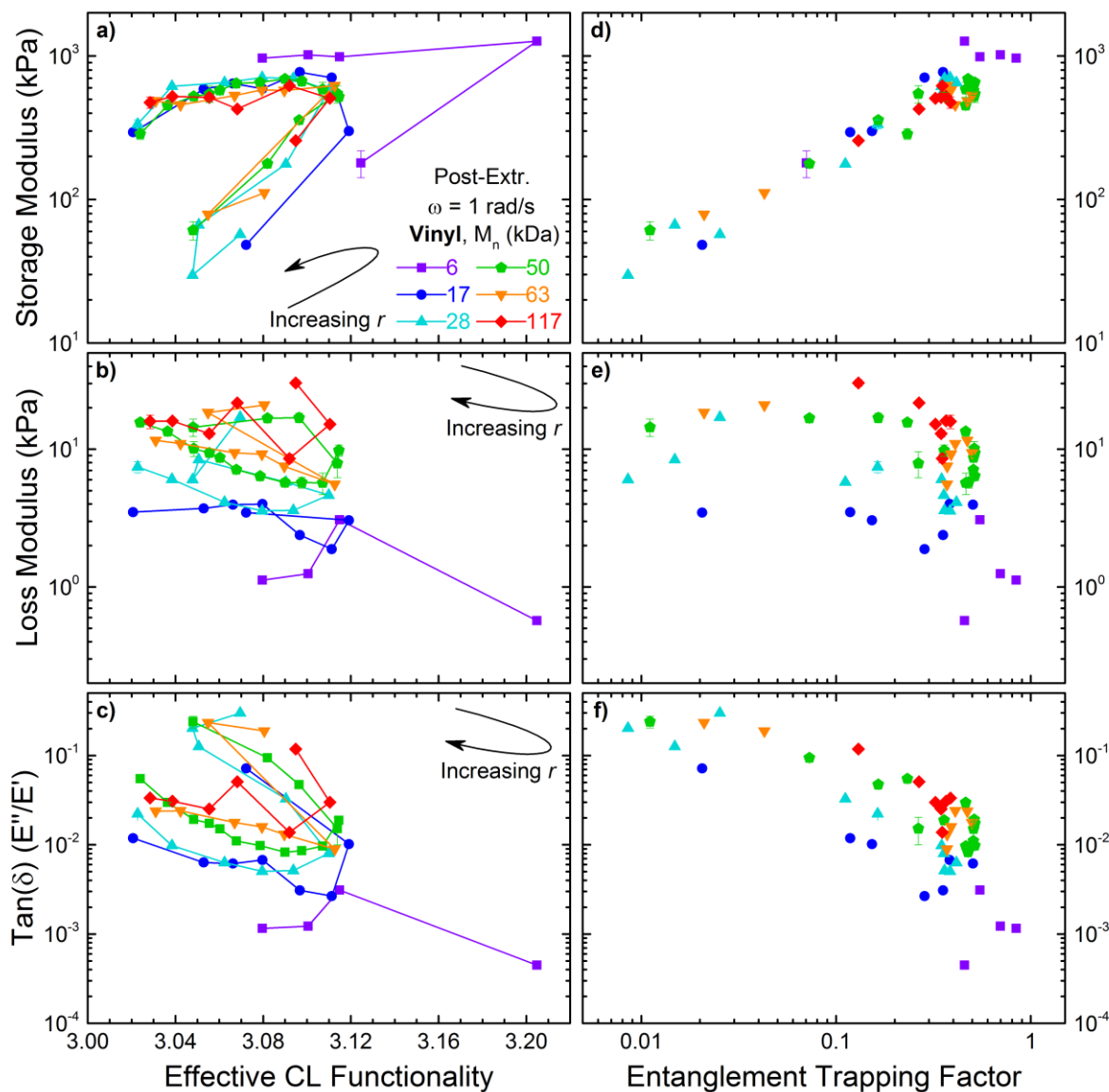


Figure 4.15 – Plots a, b, and c show the storage modulus, loss modulus, and the loss tangent, respectively, as a function of effective crosslinker functionality. Plots d, e, and f show the same properties, respectively, as a function of entanglement trapping factor. Dynamic mechanical properties are reported at an angular frequency of 1 rad/s for post extraction samples. Black curve demonstrates direction of increasing stoichiometric ratio.

In nearly all samples, the maximum effective crosslinker functionality corresponds to the maximum storage modulus, as shown in Figure 4.15a). Furthermore, the maximum storage modulus is achieved with the maximum entanglement trapping factor and storage modulus shows a monotonic increase with respect to entanglement trapping factor. All of the

mechanical properties exhibit cyclic behavior when plotted as a function of effective crosslinker functionality. This is due to the stoichiometric ratio changing from one that yields an under-crosslinked network, to fully-crosslinked, then to one that gives excess crosslinker, which is non-optimal. This means that networks with the same fraction of reacted functional groups per crosslinker can exhibit two different mechanical properties, depending on whether the stoichiometric ratio is sub- or super-optimal.

The $\tan(\delta)$ is low when the entanglement trapping factor is high, as expected. When more entanglements are permanently trapped, those chains cannot relax fully and disentangle, resulting in a greater loss of entropy and less ability to dissipate energy (recall Introduction to this chapter). Conversely, when the entanglement trapping factor is low, the materials achieve greater damping abilities, which is shown for higher values of $\tan(\delta)$.

Now that several relationships between mechanical properties and topological properties of elastic and pendant fractions, the effective crosslinker functionality, and the entanglement trapping factor, have been established, a common parameter between the two methods will be assessed. From the storage modulus, the affine and phantom models can be applied to calculate the molecular weight between effective crosslinks, M_{Aff} and M_{Ph} , respectively. These values are compared to the molecular weight between chemical crosslinks calculated from the Miller-Macosko model in Figure 4.16.

The values calculated from the affine and phantom models are plotted as a function of the value from Miller-Macosko in Figure 4.16a and b, respectively. In the vast majority of samples prepared, the values of molecular weight between crosslinks calculated from the Miller-Macosko model are greater than the values determined by either the affine or phantom models. This is due to chain extension that occurred readily in nearly all samples prepared (see Chapter 3). Thus, the values given by Miller-Macosko may be several times greater than the original number-averaged molecular weight prior to crosslinking. This makes it possible for samples well below the critical molecular weight of entanglement of 28 kDa⁵⁶ prior to crosslinking to create trapped entanglements during the crosslinking reaction. That is, values below the $y = x$ line in Figure 4.16a and b are due to additional topological constraints other

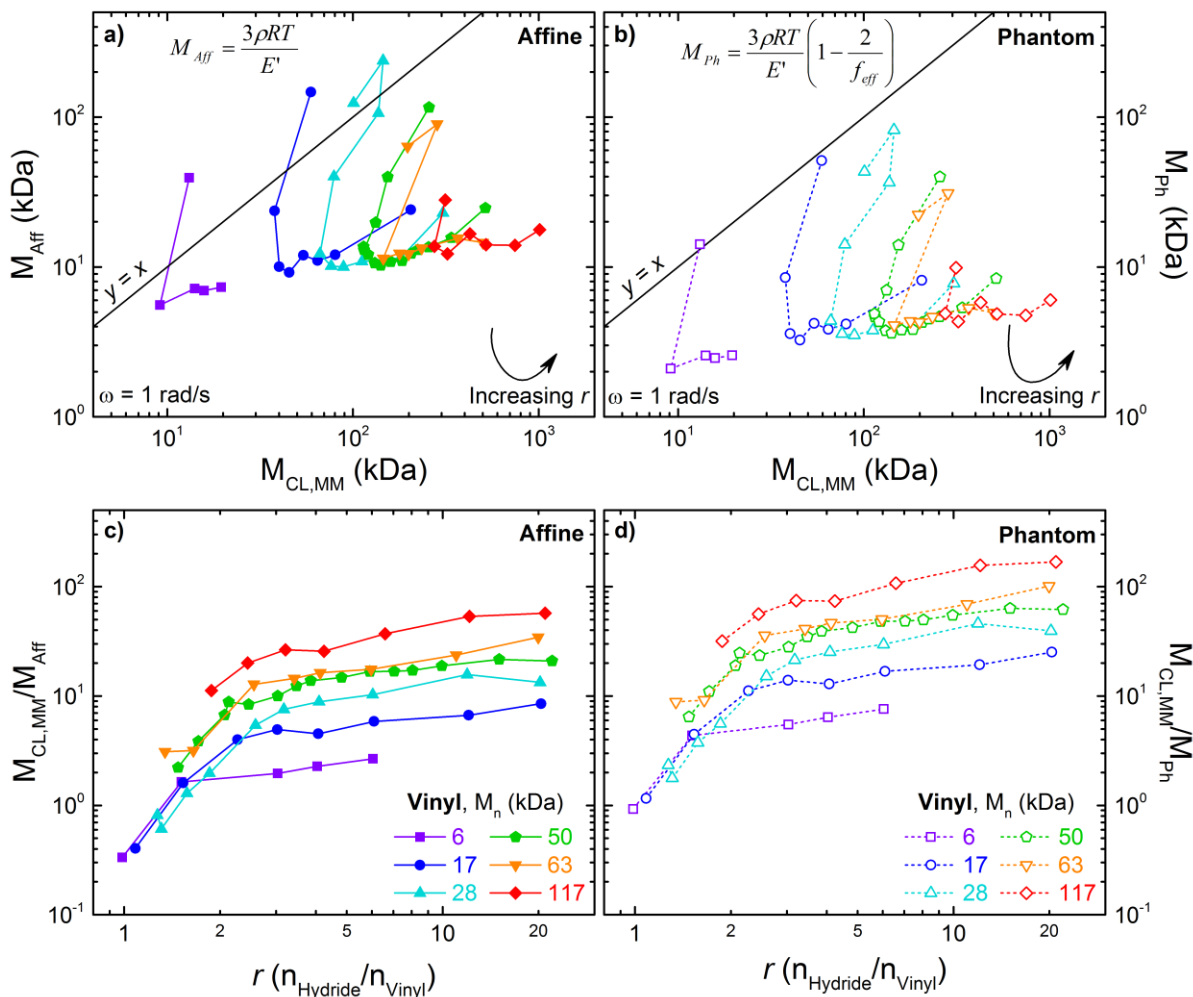


Figure 4.16 – Molecular weights between effective crosslinks as calculated from the affine model, M_{Aff} , and from the phantom model, M_{Ph} , are plotted as a function of the molecular weight between elastically effective chemical crosslinks according to the Miller-Macosko model, $M_{CL,MM}$, in plots a and c, respectively. The value from the Miller-Macosko model is normalized by the affine and phantom values in plots b and d, respectively, and plotted as a function of the stoichiometric ratio. All data shown is for the Vinyl/TDSS system after extraction.

than chemical crosslinks, *i.e.*, trapped entanglements. The phantom model is shifted lower than the affine model due to the effective crosslinker functionality being taken into account.

Both models show a dependence on the stoichiometric ratio and molecular weight. That is, in low molecular weight samples under-crosslinking results in effective molecular weight calculated from the affine model to predict a greater value than one caused only by elastically effective chemical crosslinks. The phantom model shows no such cases in the

samples tested here. At high molecular weights, values calculated from the Miller-Macosko model are always greater than those calculated from affine and phantom models regardless of stoichiometric ratio. With respect to stoichiometric ratio, a cyclic behavior in r is apparent. For each molecular weight prior to crosslinking, the Miller-Macosko value stays constant while the affine and phantom values decrease until some minimum is reached, corresponding to the optimal stoichiometric ratio that maximizes storage modulus. From there, additional increases in stoichiometric ratio result in roughly constant values in affine and phantom models but gradual increases in values calculated from the Miller-Macosko model. This corresponds to the plateau of storage modulus values observed in Figure 4.7a.

The affine and phantom models predict hypothetical molecular weights between crosslinks that would give sufficient crosslink density to achieve the measured modulus value. Thus, when values from affine and phantom models are lower than those from Miller-Macosko, there are effectively multiple shorter chains that comprise one longer chain between chemical crosslinks. These can represent the contribution of entanglements, which is shown schematically in Figure 4.17. Although trapped entanglements do not act exactly the same way as chemical crosslinks, they do impart a resistance to motion on the chain that results in additional elasticity.

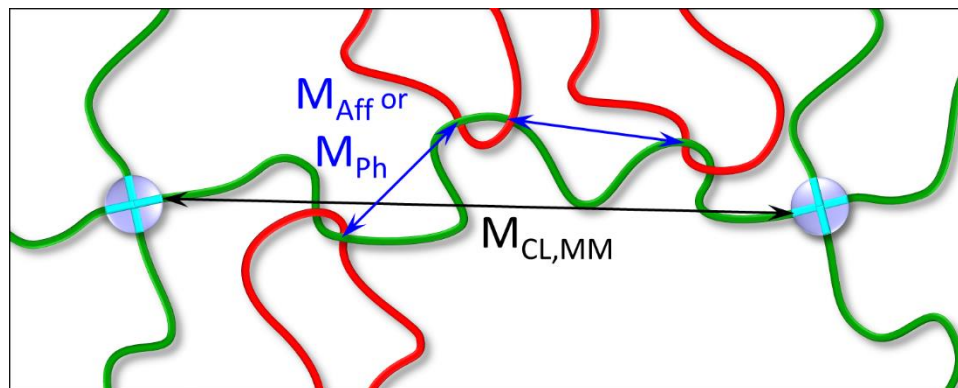


Figure 4.17 – Schematic illustrating the different values of molecular weight between crosslinks calculated from the affine, M_{Aff} , phantom, M_{Ph} , and Miller-Macosko, $M_{CL,MM}$, models. Chemical crosslink junctions are depicted as light blue circles with cyan lines.

In Figure 4.16c and d, the molecular weights between crosslinks as calculated from the Miller-Macosko model are normalized by the affine and phantom model, respectively, and plotted against the stoichiometric ratio. Here two distinct regimes exist where the normalized value on the ordinate increases with a steeper slope until the stoichiometric ratio reaches the optimal value associated with the maximum storage modulus, r_{opt} . Beyond that, additional increases in stoichiometric ratio result in more shallow increases in the normalized value. Normalizing the Miller-Macosko value by the affine and phantom values reveals how many short elastically effective chains there are per chain length between chemical crosslinks, as depicted in Figure 4.17.

The reason for the two regimes of different slopes is due to multiple effects in both the mechanical testing and the Miller-Macosko model. Recall from Chapter 3 of this dissertation, initially at low stoichiometric ratios, $r < r_{opt}$, the value calculated from the Miller-Macosko model, M_{CLMM} , decreased rapidly as a function of r when the networks were still forming and there were limiting amounts of crosslinker. This coincides with the region of rapid increase in storage modulus as a function of r given in Figure 4.7a. Beyond r_{opt} , chain extension occurs, which increases more slowly than initially growing a gel when $r < r_{opt}$. In the same vein, the storage modulus, from which the affine and phantom values are calculated, increases rapidly in the sub-optimal stoichiometric ratio regime before plateauing and slowly decreasing for stoichiometric ratios greater than the optimal value. Thus, both systems, *i.e.*, the mechanical testing and the Miller-Macosko model, undergo rapid and gradual changes in the same regions of stoichiometric ratio, which results in two distinct regions in Figure 4.16c and d.

Overall, the trends observed from comparisons between mechanical properties and topological network parameters calculated from the Miller-Macosko model are in good agreement. This has revealed the importance of the elastic and pendant fractions and the entanglement trapping factor to help design materials of greater strength of damping abilities. Additionally, comparison of various methods for determining molecular weight between crosslinks provided insights to the relative amount of trapped entanglements occurring in between chemical crosslinks.

Stress-Strain Properties of Sylgard 184

Hitherto, the dynamic mechanical properties of various silicone elastomers were determined. These provided insights to the different types of material responses, such as their ability to dampen forces acting on them and dissipate energy. While helpful in some applications such as shock absorbers, in other applications, such as soft robotics, a material's ultimate stress and strain may be necessary information. In such a situation, knowing how a material behaves under large deformations is helpful. Thus, in the following section, a brief overview of stress-strain behavior of 4 different B/C ratios of Sylgard 184 prior to Soxhlet extraction is presented.

The raw data for both engineering and true stress-strain curves are presented Figure 4.18 for 3 replicates (solid, dashed, and dotted lines) of each B/C ratio (5 in red, 10 in blue, 20 in green, and 40 in orange). The insets are zoomed in regions of 10% strain from which the slope of the curve reveals the Young's modulus. All samples underwent deformation at a constant strain rate of 5 mm/min. Despite some differences from trial to trial for the same B/C ratio, some trends can still be elucidated. The regions of small strain (*i.e.*, < 10%) show fairly

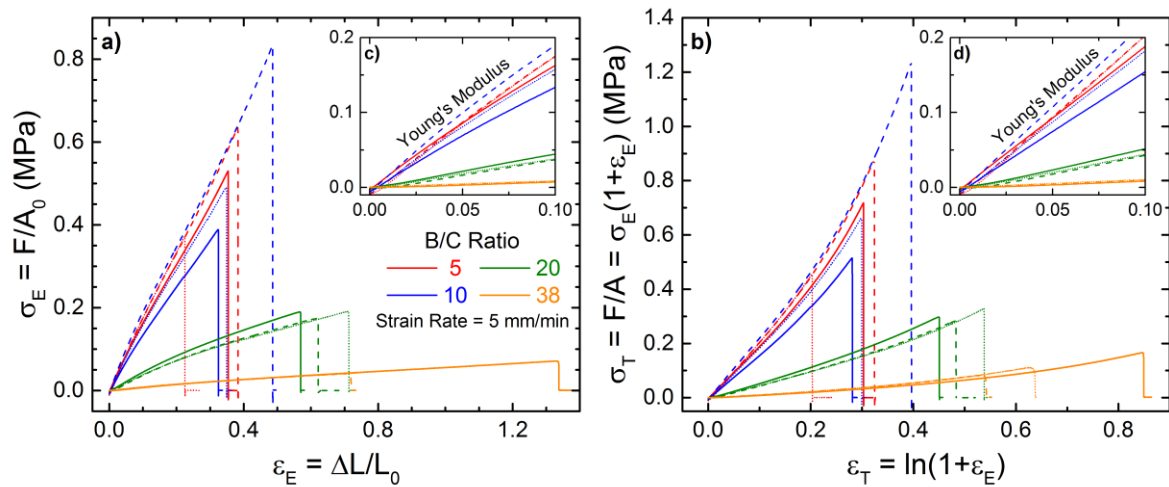


Figure 4.18 – Stress-strain responses for pre-extraction Sylgard 184 samples. In a), the engineering stress-engineering strain curves for 4 different B/C ratios (5:1 in red, 10:1 in blue, 20:1 in green, and 38:1 in orange) at 3 trials each (solid, dashed, and dotted lines). In b) the data have been converted to true stress-true strain curves for the same samples. Insets c) and d) show the zoomed in regions of 10% strain, the slopes of which are used to determine Young's modulus. A strain rate of 5 mm/min was used for all samples.

consistent slopes for each B/C ratio. However, the values of stress and strain at rupture demonstrate noticeable variation among trials. This indicates that more replicates are needed to acquire more precise values of ultimate properties.

Bearing that in mind, an analysis of the stress-strain curves follows. At first glance, the B/C ratios of 5 and 10 behave similarly, with steeper slopes than the B/C = 20, which has a steeper slope than B/C = 40. Additionally, B/C ratios of 5 and 10 require much greater stress to induce the same amount of strain compared to the other two ratios. It requires very little stress to strain the B/C = 40 samples, and they can deform to much greater strains than the B/C = 5 and 10 samples. When converting from engineering stress to true stress, the magnitude of the values increases significantly. This is to be expected because the cross-sectional area is shrinking as the material is strained. Therefore, with the same force applied to a smaller area, the stress will clearly increase. The true stress-strain curves display an increase in slope at higher strains, whereas in the engineering stress-strain curves the slope is roughly constant beyond the initial small strain region. This increase in slope means that a greater force is required to induce a smaller strain compared to the small-strain region of the graph. This phenomenon is termed “strain-hardening” wherein the polymer chains have become unentangled and begin to align. They are reaching the point of brittle failure. This chain alignment can result in strain-induced crystallization, which further increases the resistance to strain, resulting in a steeper curve.⁶⁰ The increase in stress when converted from engineering to true coincides with a decrease in strain when doing the same conversion; the true strain values also change significantly, revealing true strain at rupture to be less than the engineering strain at rupture for nearly all trials.

The averages and standard deviations of stress and strain at rupture (*i.e.*, the ultimate properties) and Young’s modulus were determined from these stress-strain data and are presented Figure 4.19. Here, the values determined from the engineering stress-strain curve are given by filled symbols with solid lines while those determined from the true stress-strain curve are represented by open symbols and dashed lines. The inverse relationship between ultimate stress and strain is clearly visible. For low Young’s modulus materials, relatively little stress is needed to impart a large strain at rupture, as evidenced by the data for the

B/C = 38 sample. As Young's modulus increases, a greater amount of stress is required to impart strain. The B/C = 10 and 5 samples exhibit much smaller ultimate strains while requiring greater force to cause rupture. Thus, it is challenging to create materials with both high ultimate stress and strain. Here, it is evident that the prescribed B/C ratio of 10:1 does exhibit the strongest material properties, *i.e.*, greatest ultimate stress.

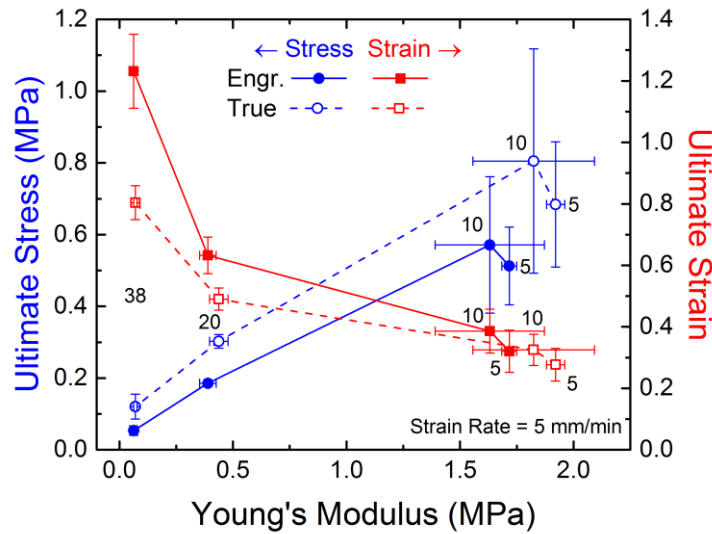


Figure 4.19 – Ultimate properties of Sylgard 184 samples. Ultimate stress (MPa) is shown on the left ordinate as blue circles and is plotted as a function of the Young's modulus as determined from the slope in the small-strain (< 10%) region. Ultimate strain is given as red squares on the right ordinate and is also plotted as a function of Young's modulus. Values of Young's modulus, ultimate stress, and ultimate strain determined from the engineering stress-strain curves are given as filled symbols with connected by dotted lines. The same values determined from the true stress-strain curve are shown as open symbols with dashed lines.

The relationship between the storage modulus, acquired from dynamic mechanical experiments, and the Young's modulus, acquired from stress-strain curves, is the following. The storage modulus extrapolated to a frequency of zero (*i.e.*, long times) is approximately equal to the Young's modulus.¹⁷ Since the data for Sylgard 184 is roughly independent of frequency, the data exist in the rubbery plateau region and have a slope of zero with respect to frequency. Thus, the values at an angular frequency of 1 rad/s are representative of values extrapolated to zero frequency. The values of Young's modulus determined from the engineering and true stress-strain curves, in orange pentagons and green diamonds,

respectively, are plotted as a function of the storage modulus for each B/C ratio in Figure 4.20. Here it is evident that storage modulus is not the same parameter as Young's modulus since storage modulus is consistently greater than the Young's modulus. When using the true stress-strain curve, the values of Young's modulus are closer to the values of storage modulus. Nevertheless, a linear relationship between the two parameters does exist. The linear best fit equations and corresponding R^2 values are given in the figure.

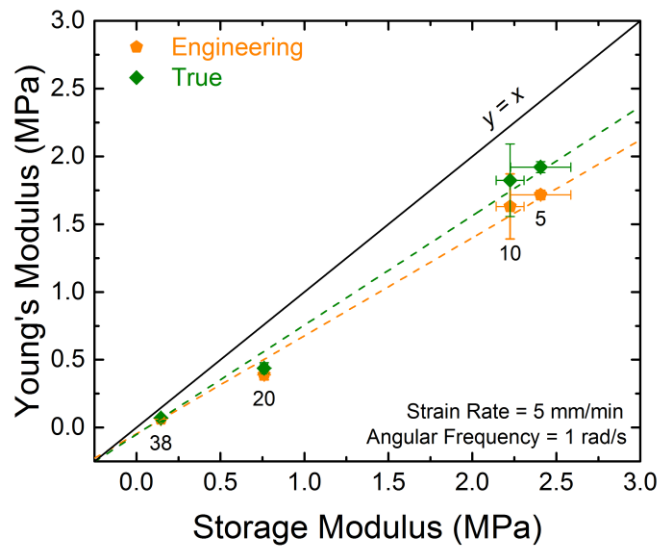


Figure 4.20 – Comparison of Young's modulus from stress-strain experiments and storage modulus from dynamic experiments. The Young's modulus as determined from the engineering and true stress-strain curves are shown in orange pentagons and green diamonds, respectively. Stress-strain tests were performed at a strain rate of 5 mm/min. Dynamic storage modulus values are given at a frequency of $\omega = 1$ rad/s. All data were acquired on samples prior to Soxhlet extraction. Linear best fit curve equations are given for engineering and true data in orange and green, respectively. The equation for the linear best fit curve for Young's modulus determined from engineering stress-strain is $y = 0.723x - 0.046$ (orange dashed line), and that for true stress-strain is $y = 0.806x - 0.051$ (green dashed line).

This brief section on stress-strain analysis of Sylgard 184 samples pre-extraction has revealed the importance of reported which type of data is being presented, whether true or engineering. Additionally, adjusting the B/C ratio can tune the mechanical properties of Sylgard 184 giving it vastly different stress-strain responses.

Conclusions

In this chapter, we presented a cookbook of recipes for making model PDMS materials over a wide range of mechanical properties. By utilizing dynamic mechanical analyses, richer information about the mechanical performance of these materials was elucidated compared to solely performing stress-strain experiments. Through comparisons of the model PDMS materials to the commercial silicone elastomer, Sylgard 184, it was shown that the effects of filler particles serve to increase damping ability and allow for high strength and deformation. Such materials made from model PDMS with no silica-like aggregates could not be made within this parameter space. Furthermore, the stress-strain behavior of a few Sylgard 184 elastomers was presented to identify Young's modulus and ultimate properties of the material. Lastly, the correlations between molecular-level network topological structure and bulk mechanical properties were elucidated. It was shown that the storage modulus depends greatly on the elastic fraction, the entanglement trapping factor, and the effective crosslinker functionality. The $\tan(\delta)$ showed strong correlations with the pendant fraction and entanglement trapping factor. A gauge of how many trapped entanglements may be occurring between chemical crosslinks was elucidated by comparison between the Miller-Macosko and affine and phantom models for determining molecular weight between crosslinks. Overall, these relationships provide insights to more efficiently design materials for a given application.

Acknowledgements

The author is grateful to several individuals for their help in producing the results that were presented in this chapter. Professor Julie N. L. Albert trained the author on using the RSA-G2 DMTA instrument. Zoe Klein helped prepare the Silanol/TEOS samples and performed some of the dynamic mechanical characterization of these materials. Dr. Edwin Walker helped prepare some of the Vinyl/TDSS samples. Dr. Duncan Davis provided training on the Instron extensometer and Professor Michael Dickey graciously provided the author time on this instrument for the Sylgard 184 stress-strain data to be acquired.

Chapter 4 Appendix

Sylgard 184 Data

Data Interpretation

A typical example of our analysis is shown in Figure A4.1. Values of E' , E'' and $\tan(\delta)$ are obtained at each frequency and averaged over 3-4 trials to produce mean values and standard deviations. The data are plotted on a log-log scale, which means a linear trend would follow a power law function. Therefore, we have fitted storage and loss moduli data in the form of $y = A\omega^b$ where y can represent either E' or E'' , ω represents angular frequency (rad/s), and A and b are fitting parameters. On the log-log scale, b corresponds to the slope of the best-fit line and A the y-intercept.

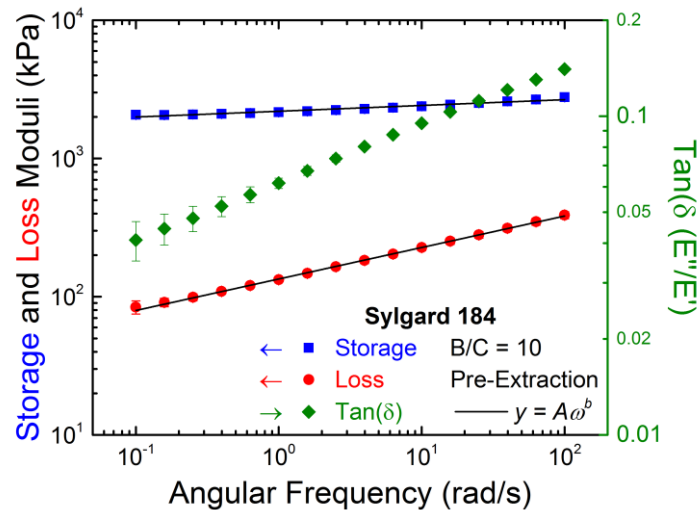


Figure A4.1 – Storage (blue squares) and loss (red circles) moduli shown on the left ordinate and $\tan(\delta)$ (E''/E' , green diamonds) on the right ordinate all plotted as a function of angular frequency. This plot is a representative example of data gathered from dynamic mechanical analysis of PDMS samples. The moduli (E' , E'') are fit with a power law function, as shown in the legend. The exponent value, b , is the slope of the line (black lines) on this plot.

Raw Data Fitting

The next figure provides the raw data from Sylgard 184 samples of different B/C ratios as a function of angular frequency. Mechanical properties pre-extraction are given in the left column and properties post-extraction are given in the right column.

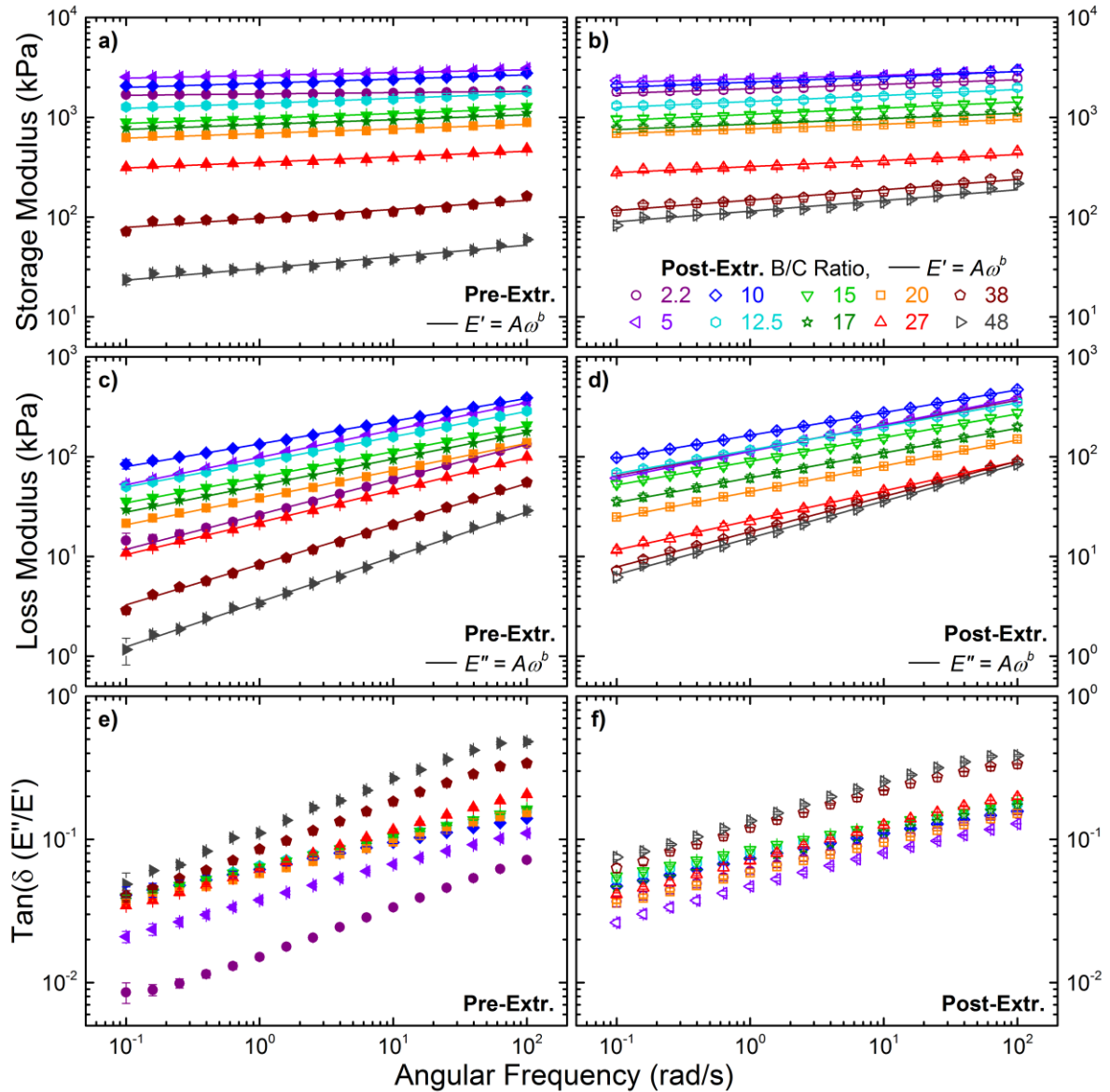


Figure A4.2 – Raw dynamic mechanical data of Sylgard 184 shown for various B/C ratios pre-extraction (left) and post-extraction (right). Storage modulus a) and b), loss modulus c) and d), and loss tangent e) and f) are plotted as a function of angular frequency.

Dynamic Mechanical Properties Pre- and Post-Extraction

The dynamic mechanical properties of Sylgard 184 were assessed both before and after the samples underwent Soxhlet extraction. The data presented in Figure 4.9a and b show similar trends pre- and post-extraction with respect to B/C ratio and sol fraction. To more directly compare changes the extraction process cause, the post-extraction properties (ordinates) are plotted as a function of the pre-extraction properties (abscissae) in Figure A4.3. Here, data for storage modulus, loss modulus and $\tan(\delta)$ is given in the left middle and right columns. The top row depicts a linear relationship while the bottom row shows the same data on a log-log scale. The data are fit with a linear best-fit line whose equation and R^2 value are given in each plot. The $\tan(\delta)$ were not well fit by a linear best-fit line. The black solid line represents no change in properties due to extraction and is thus the $y = x$ line. The labels correspond to the B/C ratios.

The data presented with linear scaling can deceive one into believing the changes induced by the extraction process are fairly small since there are no dramatic deviations from the $y = x$ line for most B/C ratios, with the exception of B/C = 2 in the loss modulus and $\tan(\delta)$. However, typically, mechanical data are plotted on a log-log scale. Changes between a value of *e.g.*, 0.01 and 0.1 would not be visible on a linear scale but readily present themselves on a log scale. Two different scales are used to demonstrate the changes in the high and low ends of the data, where smaller values would not be readily visualized on a linear scale.

The storage modulus is the only property that shows a slight decrease post-extraction for certain B/C ratios, particularly B/C = 5 and 27. All of the other ratios result in seemingly minor increases after extraction. With respect to the storage modulus, most of the data are fit well by line, indicating that B/C ratio does not strongly dictate the change in storage modulus resulting from the extraction process. However, this is an artifact caused by the linear scaling. In contrast, when the same data are plotted on a log-log scale, shown in the bottom row, the large changes at different B/C ratios become apparent.

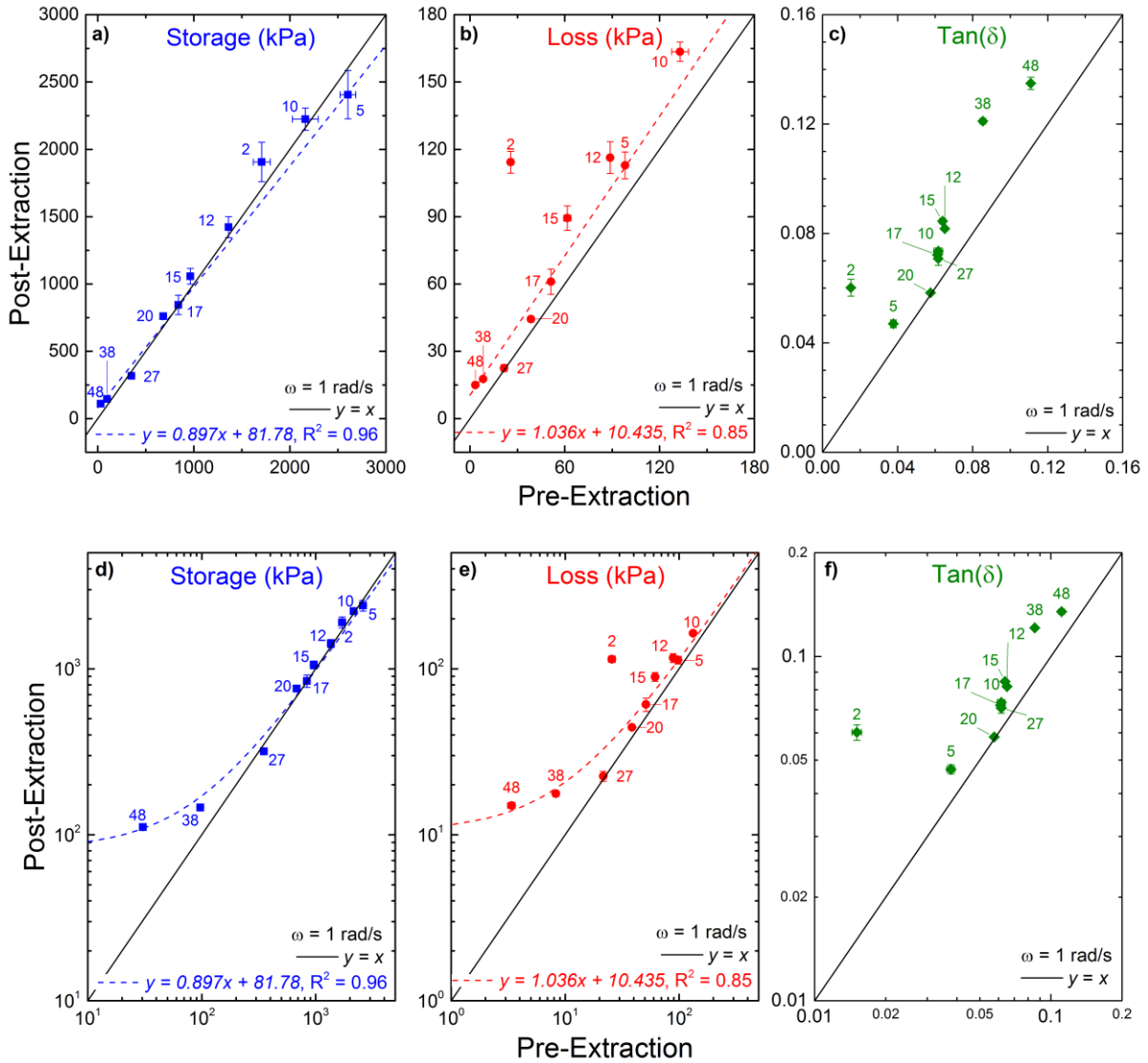


Figure A4.3 – Post-extraction properties (ordinates) plotted as a function of the pre-extraction properties (abscissae) for storage modulus, loss modulus, and $\tan(\delta)$ in the left, middle, and right columns, respectively. The data are plotted on linear scales in the top row and log-log scales in the bottom row. The data are fit with a linear best-fit line whose equation and R^2 value are given in each plot. The black solid line represents no change in properties due to extraction and is thus $y = x$.

When it comes to the loss modulus and $\tan(\delta)$, the linear-best fit does not capture the trend in the data as well. For the loss modulus, all of the data show an increase in magnitude resulting from the extraction process, which is indicated by the best fit line and all data falling to the left of the $y = x$ line. The same is true for $\tan(\delta)$, but the linear fit does not capture well

the observed trend. It is noteworthy that the B/C = 2 sample results in large deviations from the $y = x$ line and the linear best-fit line in both the loss modulus and $\tan(\delta)$. This sample has a 5-fold excess in crosslinker and thus behaves abnormally. The extraction process will remove the short-chain excess crosslinker, primarily in this sample, as opposed to the excess long-chain PDMS in most other samples that are under-crosslinked.

Vinyl/TDSS Data

The following figure provides a semi-log plot for storage modulus as a function of stoichiometric ratio in the Vinyl/TDSS system. This enables one to distinguish maximum values of storage modulus for each molecular weight.

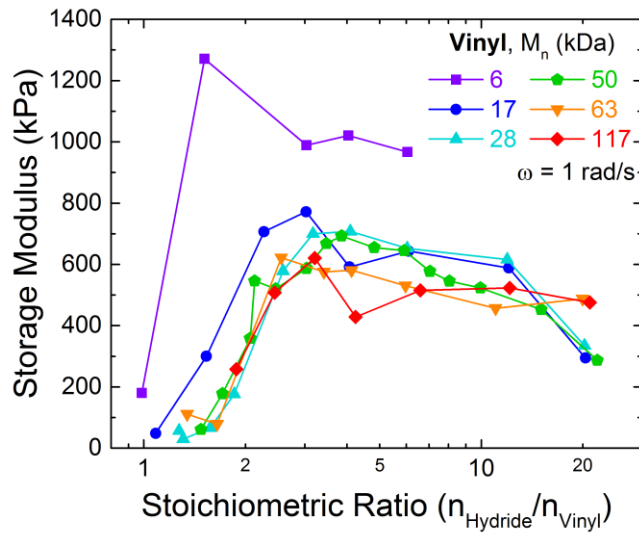


Figure A4.4 – Storage modulus at an angular frequency of 1 rad/s plotted against the stoichiometric ratio for the Vinyl/TDSS system on a semi-log scale to visualize differences in maximum storage modulus.

References

1. Rus, D. & Tolley, M. T. Design, fabrication and control of soft robots. *Nature* **521**, 467–475 (2015).
2. Fekete, Z. & Pongrácz, A. Multifunctional soft implants to monitor and control neural activity in the central and peripheral nervous system: A review. *Sensors Actuators B Chem.* **243**, 1214–1223 (2017).
3. Hassler, C., Boretius, T. & Stieglitz, T. Polymers for neural implants. *J. Polym. Sci. Part B Polym. Phys.* **49**, 18–33 (2011).
4. Carpi, F., Kornbluh, R., Sommer-Larsen, P. & Alici, G. Electroactive polymer actuators as artificial muscles: are they ready for bioinspired applications? *Bioinspir. Biomim.* **6**, 45006 (2011).
5. Romasanta, L. J., Lopez-Manchado, M. A. & Verdejo, R. Increasing the performance of dielectric elastomer actuators: A review from the materials perspective. *Prog. Polym. Sci.* **51**, 188–211 (2015).
6. Rogers, J. A., Someya, T. & Huang, Y. Materials and Mechanics for Stretchable Electronics. *Science (80-.)*. **327**, 1603–1607 (2010).
7. Khan, S., Lorenzelli, L. & Dahiya, R. S. Technologies for printing sensors and electronics over large flexible substrates: A review. *IEEE Sens. J.* **15**, 3164–3185 (2015).
8. Chen, Q., Chen, H., Zhu, L. & Zheng, J. Fundamentals of double network hydrogels. *J. Mater. Chem. B* **3**, 3654–3676 (2015).
9. Gong, J. P., Katsuyama, Y., Kurokawa, T. & Osada, Y. Double-network hydrogels with extremely high mechanical strength. *Adv. Mater.* **15**, 1155–1158 (2003).
10. Haque, M. A., Kurokawa, T. & Gong, J. P. Super tough double network hydrogels and their application as biomaterials. *Polymer* **53**, 1805–1822 (2012).
11. Xia, Y. & Whitesides, G. M. SOFT LITHOGRAPHY. *Annu. Rev. Mater. Sci.* **28**, 153–184 (1998).
12. Duffy, D. C., McDonald, J. C., Schueller, O. J. A. & Whitesides, G. M. Rapid prototyping of microfluidic systems in poly(dimethylsiloxane). *Anal. Chem.* **70**, 4974–4984 (1998).
13. McDonald, J. C. *et al.* Fabrication of microfluidic systems in poly(dimethylsiloxane). *Electrophoresis* **21**, 27–40 (2000).

14. McDonald, J. C. & Whitesides, G. M. Poly(dimethylsiloxane) as a material for fabricating microfluidic devices. *Acc. Chem. Res.* **35**, 491–499 (2002).
15. Whitesides, G. M. The origins and the future of microfluidics. *Nature* **442**, 368–73 (2006).
16. Hou, X. *et al.* Interplay between materials and microfluidics. *Nat. Rev. Mater.* **2**, 17016 (2017).
17. Rubinstein, M. & Colby, R. H. *Polymer Physics*. (Oxford University Press, 2003).
18. Macosko, C. W. & Benjamin, G. S. Modulus of Three and Four Functional Poly(dimethylsiloxane) Networks. *Pure Appl. Chem.* **53**, 1505–1518 (1981).
19. Kuhn, W. Dependence of the average transversal on the longitudinal dimensions of statistical coils formed by chain molecules. *J. Polym. Sci.* **1**, 380–388 (1946).
20. Patel, S. K., Malone, S., Cohen, C., Gillmor, J. R. & Colby, R. H. Elastic Modulus and Equilibrium Swelling of Poly(dimethylsiloxane) Networks. *Macromolecules* **25**, 5241–5251 (1992).
21. Gottlieb, M., Macosko, C. W., Benjamin, G. S., Meyers, K. O. & Merrill, E. W. Equilibrium Modulus of Model Poly(dimethylsiloxane) Networks. *Macromolecules* **14**, 1039–1046 (1981).
22. Gottlieb, M., Macosko, C. W. & Lepsch, T. C. Stress-Strain Behavior of Randomly Crosslinked Polydimethylsiloxane Networks. **19**, 1603–1617 (1981).
23. Seghir, R. & Arscott, S. Extended PDMS stiffness range for flexible systems. *Sensors Actuators, A Phys.* **230**, 33–39 (2015).
24. Johnston, I. D., McCluskey, D. K., Tan, C. K. L. & Tracey, M. C. Mechanical characterization of bulk Sylgard 184 for microfluidics and microengineering. *J. Micromechanics Microengineering* **24**, 35017 (2014).
25. Miller, D. R., Valles, E. M. & Macosko, C. W. Calculation of Molecular Parameters for Stepwise Polyfunctional Polymerization. *Polym. Eng. Sci.* **19**, 272–283 (1979).
26. Langley, N. R. & Ferry, J. D. Dynamic Mechanical Properties of Cross-Linked Rubbers. VI. Poly(dimethylsiloxane) Networks. *Macromolecules* **1**, 353–358 (1968).
27. Takahashi, H. Viscoelastic behavior of scarcely crosslinked poly (dimethyl siloxane) gel. *Nihon Reoroji Gakkaishi* **34**, 135–145 (2006).
28. Villar, M. A. & Vallés, E. M. Influence of Pendant Chains on Mechanical Properties

- of Model Poly(dimethylsiloxane) Networks. 2. Viscoelastic Properties. *Macromolecules* **29**, 4081–4089 (1996).
29. Urayama, K., Miki, T., Takigawa, T. & Kohjiya, S. Damping Elastomer Based on Model Irregular Networks of End-Linked Poly(Dimethylsiloxane). *Chem. Mater.* **16**, 173–178 (2004).
 30. Shim, S. E. & Isayev, A. I. Rheology and structure of precipitated silica and poly(dimethyl siloxane) system. *Rheol. Acta* **43**, 127–136 (2004).
 31. Clément, F., Bokobza, L. & Monnerie, L. Investigation of the Payne Effect and its Temperature Dependence on Silica-Filled Polydimethylsiloxane Networks. Part I: Experimental Results. *Rubber Chem. Technol.* **78**, 211–231 (2005).
 32. Clément, F., Bokobza, L. & Monnerie, L. Investigation of the Payne Effect and its Temperature Dependence on Silica-Filled Polydimethylsiloxane Networks. Part II: Test of Quantitative Models. *Rubber Chem. Technol.* **78**, 232–244 (2005).
 33. Alexandru, M., Cristea, M., Cazacu, M., Ioanid, A. & Simionescu, B. C. Composite Materials Based on Polydimethylsiloxane and In Situ Generated Silica by Using the Sol–Gel Technique. *Polym. Compos.* **30**, 751–759 (2009).
 34. Delebecq, E., Hermeline, N., Flers, A. & Ganachaud, F. Looking over Liquid Silicone Rubbers: (2) Mechanical Properties vs Network Topology. *ACS Appl. Mater. Interfaces* **4**, 3353–3363 (2012).
 35. Chambon, F. & Winter, H. H. Linear Viscoelasticity at the Gel Point of a Crosslinking PDMS with Imbalanced Stoichiometry. *J. Rheol. (N. Y. N. Y.)* **31**, 683–697 (1987).
 36. Material Safety Data Sheet for Sylgard(R) 184 Silicone Elastomer Kit (BASE). 1–8 (2013). at <http://www.dowcorning.com/applications/search/products/Details.aspx?prod=01064291>
 37. Material Safety Data Sheet for Sylgard(R) 184 Silicone Elastomer Kit (CURING AGENT). 1–8 (2014). at <http://www.dowcorning.com/applications/search/products/Details.aspx?prod=01064291>
 38. Lee, J. N., Park, C. & Whitesides, G. M. Solvent Compatibility of Poly(dimethylsiloxane)-Based Microfluidic Devices. *Anal. Chem.* **75**, 6544–6554 (2003).
 39. Graessley, W. W. *Polymeric Liquids & Networks: Dynamics and Rheology*. (Taylor & Francis Group, LLC, 2008). at

<<http://www.garlandscience.com/product/isbn/9780815341710>>

40. TA Instruments. RSA-G2 Solids Analyzer Brochure. 1–28 (2014). at <<http://www.tainstruments.com/wp-content/uploads/RSA-G2.pdf>>
41. Standard Test Methods for Vulcanized Rubber and Thermoplastic Elastomers —. *Annu. B. ASTM Stand.* 1–14 (2012). doi:10.1520/D0412-06AE02.2
42. Khanafer, K., Duprey, A., Schlicht, M. & Berguer, R. Effects of strain rate, mixing ratio, and stress-strain definition on the mechanical behavior of the polydimethylsiloxane (PDMS) material as related to its biological applications. *Biomed. Microdevices* **11**, 503–508 (2009).
43. Sur, G. S. & Mark, J. E. Comparisons among some tetraalkoxysilanes in the hydrolytic precipitation of silica into elastomeric networks. *Die Makromol. Chemie* **187**, 2861–2866 (1986).
44. Dewimille, L., Bresson, B. & Bokobza, L. Synthesis, structure and morphology of poly(dimethylsiloxane) networks filled with in situ generated silica particles. *Polymer* **46**, 4135–4143 (2005).
45. Meier, J. G. & Klüppel, M. Carbon Black Networking in Elastomers Monitored by Dynamic Mechanical and Dielectric Spectroscopy. *Macromol. Mater. Eng.* **293**, 12–38 (2008).
46. Sternstein, S. S. & Zhu, A.-J. Reinforcement Mechanism of Nanofilled Polymer Melts As Elucidated by Nonlinear Viscoelastic Behavior. *Macromolecules* **35**, 7262–7273 (2002).
47. Payne, A. R. Dynamic properties of heat-treated butyl vulcanizates. *J. Appl. Polym. Sci.* **7**, 873–885 (1963).
48. Payne, A. R. A note on the conductivity and modulus of carbon black-loaded rubbers. *J. Appl. Polym. Sci.* **9**, 1073–1082 (1965).
49. Ramier, J., Gauthier, C., Chazeau, L., Stelandre, L. & Guy, L. Payne effect in silica-filled styrene–butadiene rubber: Influence of surface treatment. *J. Polym. Sci. Part B Polym. Phys.* **45**, 286–298 (2007).
50. Gauthier, C., Reynaud, E., Vassoille, R. & Ladouce-Stelandre, L. Analysis of the non-linear viscoelastic behaviour of silica filled styrene butadiene rubber. *Polymer* **45**, 2761–2771 (2004).
51. Scanlan, J. & Winter, H. Composition dependence of the viscoelasticity of end-linked poly (dimethylsiloxane) at the gel point. *Macromolecules* **24**, 47–54 (1991).

52. Tordjeman, P., Fargette, C. & Mutin, P. H. Viscoelastic Properties of a Cross-Linked Polysiloxane Near the Sol-Gel Transition. *J. Rheol. (N. Y. N. Y.)* **45**, 995–1006 (2001).
53. Friedrich, C. & Heymann, L. Extension of a Model for Crosslinking Polymer at the Gel Point. *J. Rheol. (N. Y. N. Y.)* **32**, 235–241 (1988).
54. Cai, L.-H. *et al.* Soft Poly(dimethylsiloxane) Elastomers from Architecture-Driven Entanglement Free Design. *Adv. Mater.* n/a-n/a (2015). doi:10.1002/adma.201502771
55. Takahashi, H., Ishimuro, Y. & Watanabe, H. Viscoelastic Behavior of Scarcely Crosslinked Poly(dimethyl siloxane) Gels: 2. Effects of Sol Component and Network Strand Length. *Nihon Reoroji Gakkaishi* **35**, 191–198 (2007).
56. Longin, P. ., Verdier, C. & Piau, M. Dynamic shear rheology of high molecular weight polydimethylsiloxanes: comparison of rheometry and ultrasound. *J. Nonnewton. Fluid Mech.* **76**, 213–232 (1998).
57. Miller, D. R. & Macosko, C. W. A New Derivation of Post Gel Properties of Network Polymers. *Macromolecules* **9**, 206–211 (1976).
58. Valles, E. M. & Macosko, C. W. Properties of Networks Formed by End Linking of Poly(dimethylsiloxane). *Macromolecules* **12**, 673–679 (1979).
59. Macosko, C. W. & Miller, D. R. A New Derivation of Average Molecular Weights of Nonlinear Polymers. *Macromolecules* **9**, 199–206 (1976).
60. Argon, A. S. & Cohen, R. E. Toughenability of polymers. *Polymer* **44**, 6013–6032 (2003).

CHAPTER 5: Dynamic Water Wetting on PDMS Materials Due to Uncrosslinked Species

Introduction

In the Context of this Dissertation

In Chapter 2 of this dissertation, we discussed the preparation details for making the silicone elastomers studied throughout this dissertation. We completed a thorough analysis of the influence of stoichiometric ratio and molecular weight on gel fraction. Then, in Chapter 3, we used those parameters as inputs to gain a deep understanding of the molecular-level network topology by applying the Miller-Macosko model to the Vinyl/TDSS system. In Chapter 4, we analyzed the dynamic mechanical properties of model silicone elastomers and Sylgard 184 and additionally studied the stress-strain behavior of Sylgard 184. We used the outputs from the Miller-Macosko model to relate key topological network parameters to mechanical properties. Here, in the last results chapter of this dissertation, we present an analysis of the surface wetting properties of silicone elastomers. We will demonstrate relationships between the surface wetting properties and the molecular network composition and bulk dynamic mechanical properties.

Wetting

On the surface, wettability may seem like a simple phenomenon. If favorable interactions exist between the liquid and the surface, the liquid drop will spread out and wet the surface completely such as water on clean glass or metals. An example of this is shown in Figure 5.1a) for water on a clean silicon wafer. If there are unfavorable interactions, the drop will bead up and may roll off the surface, like raindrops on leaves, as seen in Figure 5.1b). In extreme cases, those statements are true. However, this oversimplification ignores the subtleties and complexities that go in to making surface science such a challenging and interesting topic. Surfaces are indeed complicated. To quote¹ the Nobel Prize winner in Physics, Wolfgang Pauli, “God made the bulk; surfaces were invented by the devil.” And as

the saying goes, “the devil is in the details.” Therefore, the details that contribute to making surface science so complex and interesting will be investigated in this chapter with regard to how water droplets behave on the surfaces of PDMS network materials.

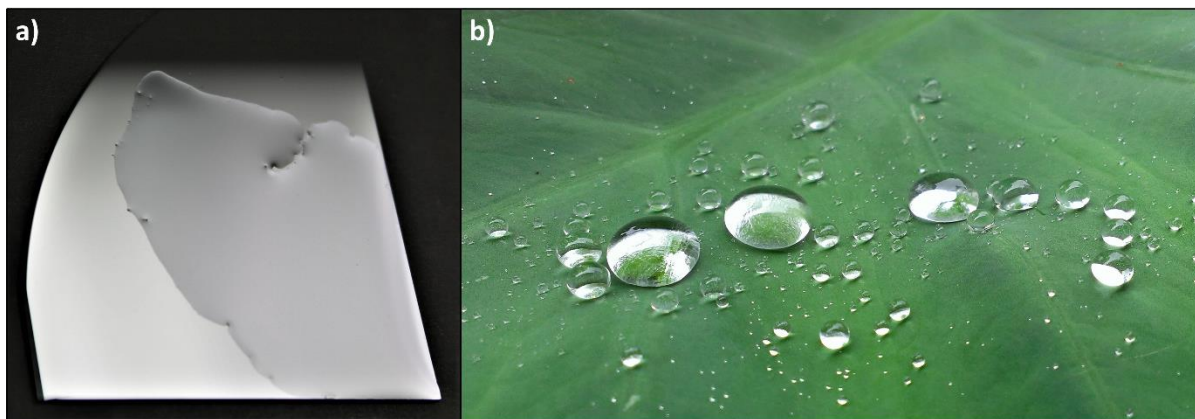


Figure 5.1 – a) A water droplet spreads out and fully wets a cleaned, polished silicon wafer. A defect or dust particle is present in the top-right where water does not fully spread. The bottom horizontal dimension of the wafer is about 1 inch. b) Water droplets beading up and minimally wetting a *colocasia* leaf, which is commonly referred to as an “elephant ear” plant. The leaves are about 3 feet in length and 1 foot in width. Digital photographs were taken by the author of this dissertation.

Surface Energy and Surface Tension

To explain how water can wet two surfaces so differently, we will introduce the concepts of surface energy and surface tension based largely on the excellent descriptions given by Jacob Israelachvili in his book *Intermolecular and Surface Forces*.² The surface wettability by a probing liquid refers to the extent to which the liquid spreads on the surface. Water can wet two surfaces differently, as shown in Figure 5.1, because they have different surface energies. Surface energy can be thought of as the price a surface must pay for existing and expanding. It is a positive perturbation in the overall free energy of the system, and systems like to minimize their free energy. In the bulk, there exists a cohesive energy that arises from intermolecular forces between like molecules. A given molecule in the bulk is interacting equally in all directions with like molecules surrounding it resulting in a net force of zero acting on it, as shown by the bottom two circles in Figure 5.2. In order to separate like

species from each other, a surface must be formed that exposes a portion of the bulk species to a vacuum. The molecules at the surface exposed to the vacuum are no longer surrounded by like molecules in all directions, and therefore, the forces acting on them do not cancel out, as seen in the top two circles in Figure 5.2. The positive change in free energy due to creating this new area that is exposed to a vacuum (*i.e.*, the penalty or cost of creating it) is the surface energy. For solids, the surface energy typically has SI units of mJ/m^2 and is denoted as γ_s . For liquids, the same concept of surface energy is typically referred to as surface tension, γ_L , and has units of mN/m . Both terms correspond to the same thermodynamic concept and have the same fundamental units.

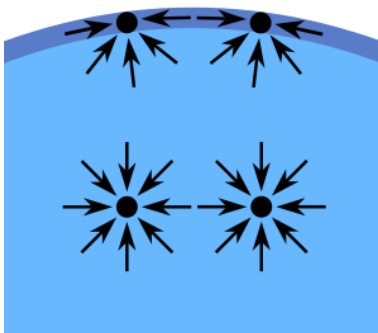


Figure 5.2 – Diagram depicting different forces acting on species in the bulk and near the surface.³

For liquids, which have weaker intermolecular forces than solids, this imbalance of forces acting on molecules near the surface results in a net force inward that is strong enough to induce curvature at the surface. Dividing this force by the interfacial area on which it acts gives the Laplace pressure, which compresses the molecules inside the droplet. This is why drops are round. The surface area, and thus surface tension and change in free energy, is minimized by forming a sphere.

Most of the time, surfaces do not appear in a vacuum. In practice, separating the bulk to create a new surface will result in a surface that is exposed to another medium, either a gas, liquid, or another solid. When this occurs, the term used to describe the change in free energy to create the surface is called interfacial energy (or interfacial tension) between the two media.

For the case of a solid (S) and a liquid (L), this is denoted as γ_{SL} . The Dupré equation describes the change in free energy that occurs when creating an interface between two media and is given for the example of solids and liquids in Equation (5.1):

$$\gamma_{SL} = \gamma_S + \gamma_L - W_{SL} \quad (5.1)$$

Here, W_{SL} is the work of adhesion, or free energy change, required to bring the two surfaces into contact with one another. To good approximation, the work of adhesion can be estimated from the dispersion forces associated with the two interacting surfaces, according to Equation (5.2).

$$\gamma_{SL} \approx \gamma_S + \gamma_L - 2\sqrt{\gamma_S^d \gamma_L^d} \quad (5.2)$$

Here, γ_i^d is the component of surface tension due to dispersion forces for either the solid or liquid. The surface tension of water in air, $\gamma_{\text{water-air}}$, at room temperature (20°C) is 72.8 mN/m, which is relatively high compared to most liquids in large part due to the high polarity and large amount of hydrogen bonding associated with water.² The temperature must be specified because surface energy and surface tension depend on intermolecular forces, which change with temperature. The dispersion components are sufficient for this discussion since PDMS primarily interacts with its surrounding through dispersion forces.

Polymer Surface Tension

For polymers, the surface tension not only depends on temperature, but also depends on molecular weight and chemical end-group functionality. This is because the end groups of the polymer chain are in greater concentration for low molecular weight (LMW) polymers and the end groups may interact with the media at the surface differently than the rest of the chain. The end groups' influence on surface tension becomes negligible as their concentration decreases for higher molecular weights. Thus, the surface tension for many polymers (in air) often takes the form⁴ of Equation (5.3) where k is a constant different for each polymer and γ_∞ is the surface tension at infinite molecular weight.

$$\gamma = \gamma_\infty - k/(M_n)^{\frac{2}{3}} \quad (5.3)$$

In the case of PDMS, the reported values of k and γ_∞ vary slightly based on measurement technique and method of normalizing data for different collection temperatures. Kobayashi and Owen⁵ reported k and γ_∞ equal to 161 mN/m*(Da^{2/3}) and 20.69 mN/m, respectively, based on the pendant drop technique carried out at 25°C. The pendant drop technique determines surface tension of a liquid by fitting the shape of a drop suspended from a needle in air to the Young-Laplace equation, which balances gravitational and interfacial forces with capillary pressure.⁶ Legrand and Gaines⁴ reported k and γ_∞ equal to 166 mN/m*(Da^{2/3}) and 21.25 mN/m, respectively based on data they compiled from the literature and adjusted to 20°C. The data they reported were collected with a different technique called the du Noüy ring technique. In these experiments, a metal ring (usually platinum) is slowly withdrawn from a liquid surface, and the force measured to do so is related to the surface tension of the liquid.^{7,8} Even after accounting for temperature adjustments, it seems that the pendant drop and du Noüy ring techniques may give slightly different values for surface tension. The techniques may be the culprit for differences, but another factor is also at play; the presence of lower molecular weight (LMW) impurities may skew results. LMW molecules can diffuse more quickly and have lower surface energies. Thus, they will segregate to the interface. The surface tension values and other useful properties of LMW PDMS linear and cyclic oligomers are reported in Table A5.1 of the Appendix. These molecules will be of importance in later discussions.

The previous discussion of constants for Equation (5.3) focused only on one type of PDMS, one which had trimethyl termini. Jalbert *et al.*⁹ investigated the effects of chemical end-group functionality and molecular weight simultaneously by carrying out pendant drop experiments at 30°C. They demonstrated that the surface tension of trimethyl-terminated PDMS decreased from ~20.5 to ~15 mN/m with decreasing molecular weights, the surface tension of silanol-terminated PDMS remained nearly constant at ~20.2 mN/m regardless of molecular weight, and the surface tension of aminopropyl-terminated PDMS increased from ~20.2 to ~22 mN/m with decreasing molecular weight. This is because trimethyl groups have favorable interactions with air, silanol groups apparently have neutral interactions with air, and the aminopropyl groups have unfavorable interactions with air. Jalbert and coworkers also concluded that the surface tension does not depend on the molecular weight dispersity.⁹

One may question how the surface tension changes when PDMS is crosslinked and transformed from a liquid to a solid. Crosslinking has the effect of removing the influence of end groups and reducing chain mobility. The composition also changes because crosslinked materials contain more than just pure PDMS; they also contain crosslinker. For a fully crosslinked system, Chaudhury and Whitesides¹⁰ directly measured the interfacial energy between PDMS and air. They used a different formulation from Dow Corning called Sylgard 170, which contains both base and curing agent components and filler particles. However, they allowed for particle settlement out of solution and used only the clear, pure polymer layers in their experiments. They determined $\gamma_{\text{PDMS-air}}$ to be equal to 21.1 ± 0.2 mN/m, which is in very good agreement with the γ_{∞} values for uncrosslinked PDMS discussed previously. Thus, there is only negligible change in surface energy between high molecular weight (HMW) liquid PDMS and fully crosslinked PDMS.

Contact Angle Measurements

Young's Law and Rigid Substrates

Now that the concepts of interfacial energy/tension for the two-phase systems of water-in-air and PDMS-in-air have been separately established, they can be used to quantitatively interpret wettability data for the three-phase system of water droplets placed on a PDMS substrate in air. For this system, there exist three different interfacial tensions that, when balanced, will reveal the equilibrium contact angle, θ , the water droplet makes with the substrate that minimizes the free energy of the system, as shown in Figure 5.3a), which has been reproduced from Genzer and Efimenko.¹¹ The three interfacial tensions at play are those for the substrate-vapor, γ_{SV} , substrate liquid, γ_{SL} , and liquid-vapor, γ_{LV} . When the forces are balanced in the horizontal direction, one arrives at the well-known Young's equation given by Equation (5.4), which Thomas Young first published in 1805.¹²

$$\cos \theta = \frac{\gamma_{\text{SV}} - \gamma_{\text{SL}}}{\gamma_{\text{LV}}} \quad (5.4)$$

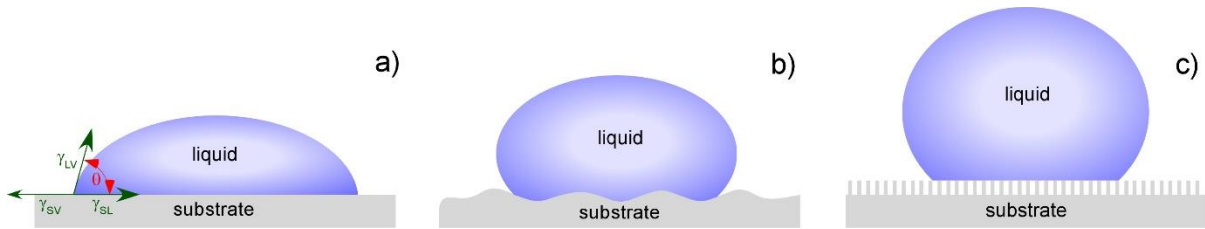


Figure 5.3 – Various wetting states between a liquid droplet and a substrate. a) Depicts the ideal case with an atomically flat substrate. Surface roughness is depicted in b) where the droplet is in the Wenzel state. When the roughness aspect ratio is increased, the droplet enters the Cassie-Baxter state, shown in c). This figure is reproduced from Genzer and Efimenko.¹¹

This equilibrium relationship that minimizes the Gibbs free energy has several key assumptions that make it less applicable in certain situations. For this equation to hold true, the substrate must be an ideal solid surface, *i.e.*, it is atomically smooth, non-deformable, chemically homogenous, insoluble in the probing liquid, and non-reactive with the probing liquid. These assumptions are met in certain situations, such as cleaned glass or metal substrates, but often, substrates are not atomically smooth. Surfaces can have roughness on the macro or nano scale and the scale of the roughness, in part, dictates how the liquid will wet the substrate. There can also be impurities that cause chemical heterogeneities. Nevertheless, Young’s equation has enjoyed wide use as a reasonable approximation for surface energies of various substrates.

When a surface contains roughness, the probing liquid may penetrate into the crevasses and still fully wet the substrate, resulting in the so-called Wenzel state,¹³ as in Figure 5.3b. However, when the aspect ratio of the roughness features becomes large, and the surface tension of the liquid is high enough to maintain the droplet’s shape, the liquid will not completely wet the surface, resulting in the Cassie-Baxter regime,¹⁴ in Figure 5.3c. The development of nano-engineered surface roughness has led to advancements in creating superhydrophobic surfaces by trapping air “pockets” within the voids of the substrate, which strongly repels water.¹⁵

Deformable Substrates

One major assumption with the three possible wetting states previously described is that the surface is rigid. For the case of polymeric surfaces, especially soft ones, this does not always hold true. If the substrate is deformable, the topographical features resulting in roughness may not withstand the capillary forces of the probing liquid, which will diminish their functionality. Furthermore, for a smooth, flat, deformable substrate, the vertical component of the probing liquid surface tension can pull the substrate up at the 3-phase contact line. The so-called wetting ridge height, h_{wr} , of such a deformation has been reported to be on the order of $h_{wr} \approx \gamma_{LV} \sin(\theta)/E$, where θ is the contact angle between the liquid and substrate and E is Young's modulus of the substrate.^{16,17} Thus, the wetting ridge height is proportional to a quantity called the elastocapillary length, $l = \gamma/E$, where γ and E are the same quantities as previously mentioned. An example of this deformation is given in Figure 5.4c, where the variable d is used to describe the wetting ridge height.¹⁸

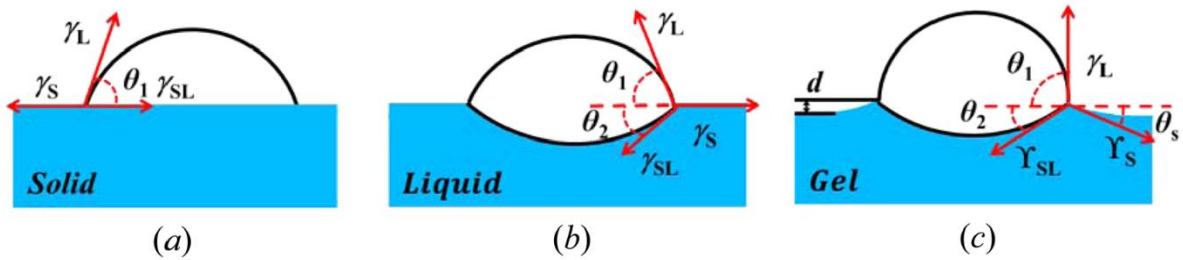


Figure 5.4 – Reproduced from Cao and Dobrynin.¹⁸ Three different systems are depicted. In system a), a solid, rigid substrate is described well by Young's law. For two immiscible liquids, as shown in b), Neumann's triangle accurately describes the system. For a soft deformable substrate, such as a gel, the system is complex and the subject of on-going research.

A high-resolution X-ray microscopy image of this wetting ridge was captured recently for the first time by Park *et al.* in 2014.¹⁹ They confirmed experimentally that the height of the deformation was indeed on the order of $\gamma_{LV} \sin(\theta)/E$, but interestingly, they found that the deformation was asymmetric.

As depicted in Figure 5.4, the wetting of soft substrates can be described as something in between Young's Law and Neumann's triangle. Neumann's triangle describes two immiscible liquids and is a vector balance of the 3-liquid interfacial tensions, thus taking into account forces acting in both the horizontal and vertical directions.²⁰ Instead of a soft substrate completely deforming due to the surface tension of the probing liquid, as is the case in the Neumann triangle situation, the elastic nature of the soft substrate counteracts the vertical component of surface tension, reaching an equilibrium with a certain degree of deformation near the 3-phase contact line, *i.e.*, the wetting ridge.

Understanding the 3-phase contact line in liquid/soft-solid systems has been an area of considerable research. Shanahan and Carré produced significant findings in the 1990s and early 2000s related to the development of models for the dynamics of drops spreading on soft substrates and de-wetting phenomena.^{17,21–26} More recently, in the 2010s, Style and Dufresne have contributed greatly to this field through their analysis of surface stresses and the role they play in liquid droplets deforming soft substrates.^{27–32}

Microfluidics

Wettability is an important topic due to its relevance in a variety of applications. This chapter specifically focuses on coatings and materials that use PDMS as an integral ingredient. PDMS is employed to create superhydrophobic surfaces³³ that have contact angles greater than 150° and are endowed with self-cleaning abilities.³⁴ PDMS-based coatings can also offer surfaces anti-biofouling capabilities that either prevent biological moiety adhesion (*i.e.*, anti-biofouling surfaces),^{11,35–38} or provide for facile release^{39,40} of such moieties (*i.e.*, foul-release surfaces) due to the inherent low surface energy of PDMS. Additionally PDMS finds use as emulsifying and anti-foaming agents, as sealants and adhesives, and as lubricants for plastics, fibers, molds, and metals. To make all of these applications possible, a sound understanding of surface science with PDMS is needed.

A rapidly growing area of research is in the field of microfluidics or “lab on a chip” technology. George Whitesides and coworkers^{41–46} played a big role in pioneering the fabrication of microfluidic devices from PDMS near the turn of the millennium. They

developed “soft lithography” techniques which enabled the fairly simple creation of micron-sized surface features on a PDMS matrix. Specifically, microchannels within a PDMS matrix were developed for laminar flow of small liquid volumes. A crucial step in the fabrication of microfluidic devices is the adhesion of two sheets of PDMS, one of which contains the micropattern and the other is flat. To minimize leaking of liquid reagents, a strong seal must be made between the two PDMS surfaces. This is often accomplished by plasma, ultraviolet (UV), or ultraviolet/ozone (UV/O₃) treating the surfaces of the PDMS. These types of treatment create a thin silica-like layer at the air-interface of the substrate that is terminated with “sticky” silanol groups. Depending on the power of the UV lamp used, this silica-like layer will penetrate into the substrate on the order of 5 nm but material up to 60 nm below the surface can still be modified somewhat for 60 min exposure times.⁴⁷ The silica-like layer forms due to chain scission and radical formation, which tightly covalently attaches short siloxane chains. These hydroxyl groups have high surface energy due to their polarity and ability to hydrogen bond. When contacted with a similar surface, the two surfaces quickly and strongly adhere to each other. This is further characterized as having an extremely low water contact angle, on the order of 10° for exposure times greater than 60 min.⁴⁷

Hydrophobic Recovery

This silica-like layer that forms, however, is not permanent, as surfaces have been shown to display increases in water contact angles hours~days after UV/O₃, UV or plasma treatment. Consequently, the so-called “hydrophobic recovery” phenomenon exists in treated PDMS materials and has been investigated thoroughly by Hillborg and coworkers.⁴⁸⁻⁵¹ Not surprisingly, the dose of the surface treatment (both exposure time and source dosage) influences the initial increase in surface energy after treatment (and decrease in contact angle). The dose also influences the subsequent duration of the hydrophobic recovery process (*i.e.*, increase in contact angle), wherein the surface energy decreases back to the original hydrophobic PDMS.

As discussed in preceding chapters of this dissertation, when not using optimal stoichiometry, uncrosslinked molecules remain present in the network. These will likely

contribute to the hydrophobic recovery process. However, even well extracted samples have been shown to exhibit hydrophobic recovery, albeit at slower rates.⁵² This is for several reasons. First, it is extremely difficult to extract all unbound material within a PDMS network. More importantly, however, the surface treatment process itself causes chain scission, which creates many LMW siloxanes that are responsible for the hydrophobic recovery. These LMW siloxanes act according to the mechanism depicted in Figure 5.5. Upon mechanical strain or deformation and/or with excess plasma treatment, cracks can form in the silica-like layer, permitting easier and faster mobility of LMW siloxanes to the silicone/air interface.

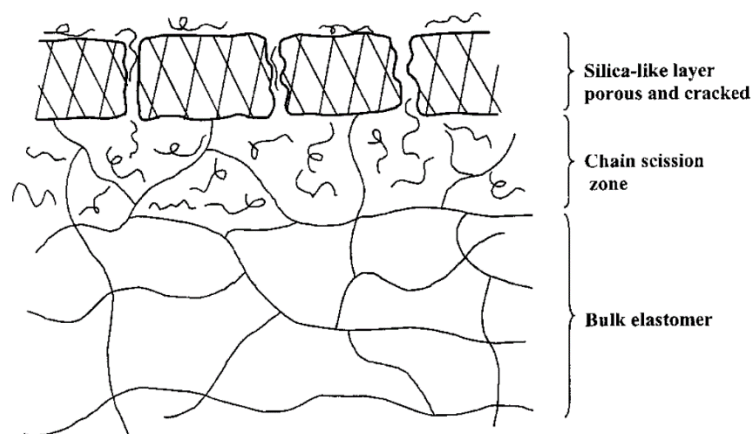


Figure 5.5 – Reproduced from Kim, J., Chaudhury, M., and Owen, M. J.⁵² Schematic illustration of the cross-sectional section of PDMS after exposed to surface treatment.

In the past 15+ years, interdisciplinary research has taken off between the fields of materials science and biology wherein PDMS is used as the material to make microfluidic devices^{44,46} for studying biological phenomena. Micron-sized features are very relevant in the field of biology and can be created using soft lithographic techniques with PDMS.⁴¹ Additionally, PDMS in its macromolecular form, *i.e.*, HMW linear chains, have been found to be biocompatible,^{53,54} with biomedical implants being stable *in vivo* for up to 25 years.⁵⁵ In microchannel fabrication, quite frequently the commercial material, Sylgard 184 is used rather than pure PDMS, due to its commercial availability and to its favorable mechanical properties that readily allow for the creation of micro-scale surface features. The trends in the growing

use of Sylgard 184 in both the microfluidic and biological fields are presented in Figure 1.2. Note that the two fields are not mutually exclusive.

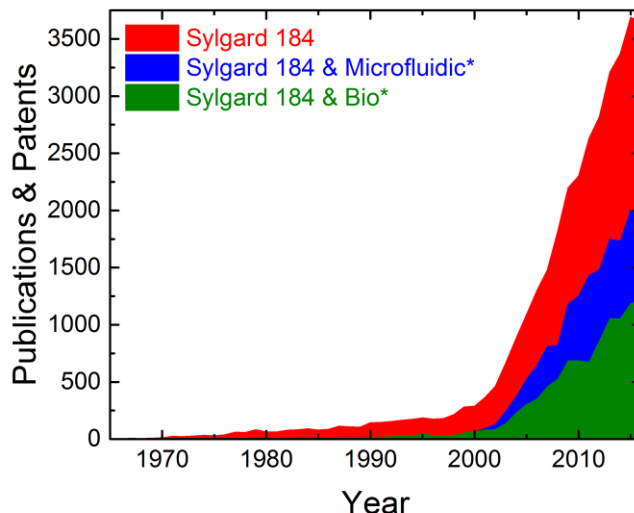


Figure 5.6 – Publications and patents awarded per year that mention “Sylgard 184” (red), “Sylgard 184 and Microfluidic” (blue), and “Sylgard 184 and Bio” (green) plotted as a function of year. Data acquired from Google Scholar on April 28, 2017.

As more research involves proteins and cells in microfluidic devices, the surface properties of PDMS become of paramount interest. In such confined volumes, the cells may be sensitive to any impurities that could be leaching out of the underlying PDMS substrate, particularly small PDMS precursors such as cyclic and linear oligomers mentioned earlier.⁵⁶ The cyclic volatile methylsiloxanes (D₃, D₄), in particular, have been shown to lead to DNA damage after 30 weeks of exposure, which could lead to the development of breast cancer.⁵⁷ Another challenge is that PDMS may absorb hydrophobic molecules, such as hormones and drugs, that are introduced to the cell media, which may skew the dosages and thus, the cell responses.⁵⁴

Given the need for using a microfluidic devices composed of well-crosslinked materials that do not leach small molecule impurities, we will demonstrate a simple technique for qualitatively measuring such leaching phenomena in this chapter. We have utilized time-

dependent water contact angle measurements to demonstrate the amount of leaching of siloxane molecules that can occur when optimal stoichiometry in crosslinking is not used.

Chapter Goals

Based on the previous discussion, the surface science of PDMS materials interfacing with water has broad applicability. In this chapter we present a thorough analysis of the dynamic water droplet behavior on PDMS substrates prepared from various molecular weights and crosslinking stoichiometries, and the commercial Sylgard 184 material prepared in different B/C ratios. We will discuss relationships between the wetting behavior and such variables. Crucially, we will demonstrate how the Soxhlet extraction process changes the dynamic wetting behavior of the system. That is, the influence of the sol fraction, or uncrosslinked material, on the wetting behavior will be elucidated. Additionally, we will tie observed wetting behavior to the contact area over which the drop is interacting with the substrate, *i.e.*, the interfacial area between water and PDMS and discover how these two parameters are entwined. The wetting parameters will be compared briefly to the substrate mechanical properties to determine what, if any, relationships exist between the bulk and the surface. A brief analysis of the wetting ridge height phenomenon will be addressed at the end of this chapter. This was not a major topic of focus since most of our materials were not soft enough to exhibit relatively large (> 1 micron) deformations. Lastly, we show how to control the dynamic spreading behavior by intentionally adding silicone oils of various molecular weights to the polymer networks during crosslinking using optimal stoichiometry. That is, we control the amount and type of material present in the sol fraction and monitor its influence on the dynamic wetting behavior.

Experimental Materials and Methods

Materials

Silicone Elastomers

In this chapter, we are only conducting the dynamic water wetting experiments on Vinyl/TDSS model networks and Sylgard 184 samples prepared according to the procedure described in Chapter 2 of this dissertation. Samples from the same batch of materials used in the preceding chapters are used in this chapter. We tested dynamic wetting behavior on samples both pre- and post-extraction. Vinyl-terminated, telechelic PDMS polymers of various molecular weights were purchased from Gelest, Inc. A tetrafunctional crosslinker molecule (*i.e.*, one having 4 reactive groups per molecule), tetrakis(dimethylsiloxy)silane (TDSS) was also purchased from Gelest, Inc. A hydrosilylation catalyst, *cis*-dichlorobis(diethyl sulfide)platinum(II) (Pt catalyst) was purchased from Sigma-Aldrich. The Sylgard 184 Silicone Elastomer kit was purchased from Dow Corning, and contains separate Base (B) and Curing Agents (C) that simply need to be mixed together in different mass ratios (*i.e.*, B/C ratio). All reactants were used without any further purification.

Benchmark Materials

We benchmarked our results against polymers that do not exhibit as high of molecular mobility as PDMS. Further, these polymers should not contain LMW species that can leach out of them. We tested two different sheets of Teflon (poly(tetrafluoroethylene) or PTFE) purchased from McMaster-Carr, a poly(ethylene terephthalate) (PET) stand-alone film supplied by Eastman Chemical (called PET Mylar), a pure PET film spin-coated on a silicon wafer, and polypropylene (PP) and polystyrene (PS) Petri dishes purchased from VWR. These samples were not rinsed with any liquids prior to testing. Instead, they were sprayed with high-pressure nitrogen gas to remove any dust or debris prior to testing. All of these materials have glass transition temperatures well above room temperature except polypropylene. At room temperature, PP is amorphous, like PDMS. However, PP showed no signs of non-linear

dynamic wetting behavior, indicating a lack of LMW impurities and significantly less chain mobility than the PDMS samples. The dynamic wetting behavior of these materials is provided in Figure A5.1 of the Appendix.

Methods

Network Preparation & Gel Fraction Determination

Samples were prepared according to the procedure described in Chapter 2 of this dissertation. To recap, for each model Vinyl/TDSS PDMS network sample, *circa* 2.5-3.5 g of PDMS were mixed well with the Pt(II) catalyst solution in a polypropylene beaker followed by removal of air bubbles under moderate vacuum. For every gram of vinyl-terminated PDMS in each sample, 8 μL of Pt(II) catalyst solution at a concentration of 0.011 g Pt (II) catalyst per mL of toluene were added. Next, a precise mass (and volume) of the crosslinker, TDSS, was added via micropipette over a balance to the PDMS/catalyst mixture yielding a specific desired stoichiometric ratio, r , defined in Chapter 2 of this dissertation.

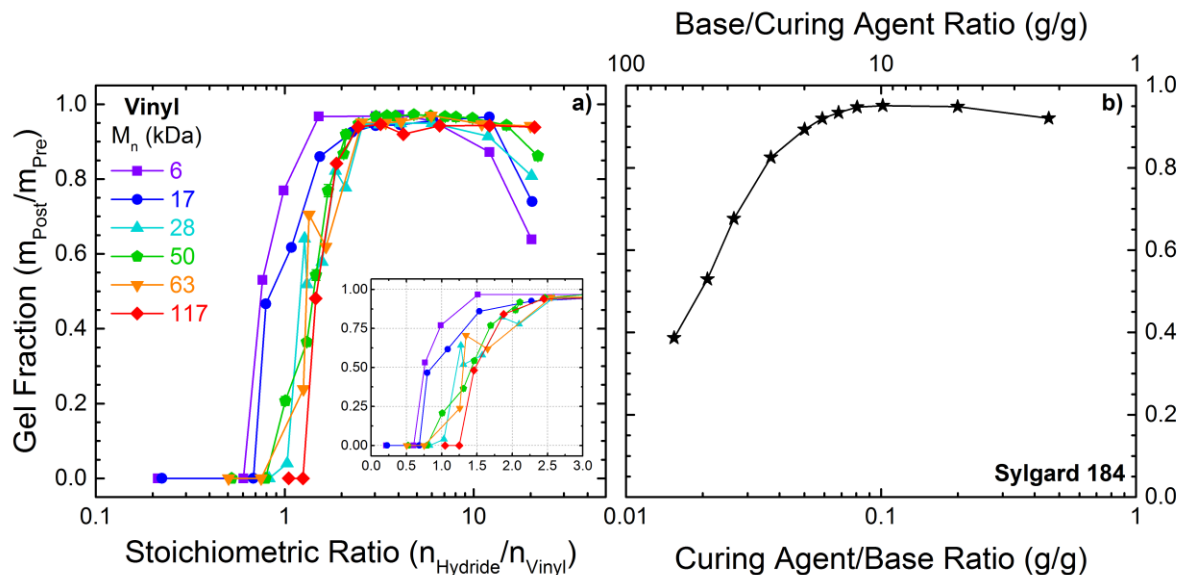


Figure 5.7 – Gel fraction as a function of stoichiometric ratio, r , for molecular weights ranging from 6 (violet) to 117 (red) kDa in the Vinyl/TDSS system plotted in a. Gel fraction is plotted against the curing agent/base ratio (bottom abscissa) and against the base/curing agent (B/C) ratio (top abscissa) for Sylgard 184 (b).

After mixing well and degassing again, the solution was carefully poured into a polystyrene or polypropylene Petri dish. If needed, the Petri dish was degassed one last time. The sample in dish was then covered with a lid and placed on a level surface at room temperature exposed to atmospheric pressure for 2-3 h of pre-curing, during which the polymer spread evenly throughout the Petri dish, giving a uniform thickness of ~ 0.7 -1.5 mm (depending on how much polymer was added to the dish). Finally, the networks were placed in a 70°C oven at atmospheric pressure for 24 h. Sylgard 184 samples were prepared in the same manner as model PDMS except the only ingredients used were the base and curing agent, which were added together in varying Base/Curing Agent (B/C) mass ratios. Soxhlet extraction in toluene, a good solvent for PDMS,⁵⁸ was used to determine the gel (w_{gel}) and sol (w_{sol}) fractions of the networks according to the same method described in Chapter 2 of this dissertation. Those data are reproduced in Figure 5.7.

Contact Angle Experiments

To elucidate a value of contact angle between water and PDMS networks that is close to the true equilibrium value, the sessile drop method was used wherein droplets were placed on the surface of PDMS and allowed to settle for a period of 6-8 minutes. This revealed the dynamic behavior of the water/PDMS interface. The experiments were conducted using a goniometer (Model-No. 100-00, Ramé-Hart, Inc. Mountain Lakes, NJ). First, the samples were cleaned with a high pressure stream of nitrogen gas to remove any debris that may have settled on the surface. Samples were not rinsed with any liquid to prevent the removal of any unbound molecules. Next, the samples were placed on the stage and the stage angle was adjusted to produce a level interface between PDMS and air. A droplet was manually dispensed by hand to a volume of 6 μ L and the needle was lowered such that the droplet was just above the PDMS sample. Then the stage was lifted slightly to bring the water into contact with the PDMS, which instantly distorted the droplet shape by pulling it towards the substrate. The needle was then rapidly lifted until it was withdrawn from the water droplet. At this point, the software began acquiring images every 20 seconds.

In the data shown in this chapter, the contact time, t , refers to the time (min) after the needle was withdrawn from the droplet, which occurred very quickly after the droplet contacted the substrate. The experiments were not conducted in a controlled atmosphere, thus the droplets did evaporate slightly throughout these experiments. Benchmark experiments were conducted on solid polymer surfaces (PET, Teflon, PP, PS) that underwent the similar volume changes due to evaporation. Despite this slight evaporation, the change in droplet volume did not prove to be a factor that influenced the contact angle and droplet shape on PDMS samples and the glassy polymers did not display the same behavior with respect to change in contact angle. See Appendix for data regarding non-PDMS substrates.

Matlab Image Analysis Codes

Matlab codes were developed for rapid, nearly fully automated image analysis. This ensured consistency across samples and minimized human error in droplet shape analysis and contact angle determination. Two separate codes were developed, one for hydrophobic ($\theta > 90^\circ$) and one for hydrophilic ($\theta < 90^\circ$) substrates due to slightly different droplet analysis techniques used in each scenario. The full codes for each are provided in the Appendix. A representative output of the image analysis is given in Figure 5.8.

The algorithms used in the code act according to the following protocol. All images were converted from goniometer software output file type of Bitmap (.bmp) to 8-bit TIFF (.tiff) using ImageJ software before being read in to Matlab. The Matlab code first reads in

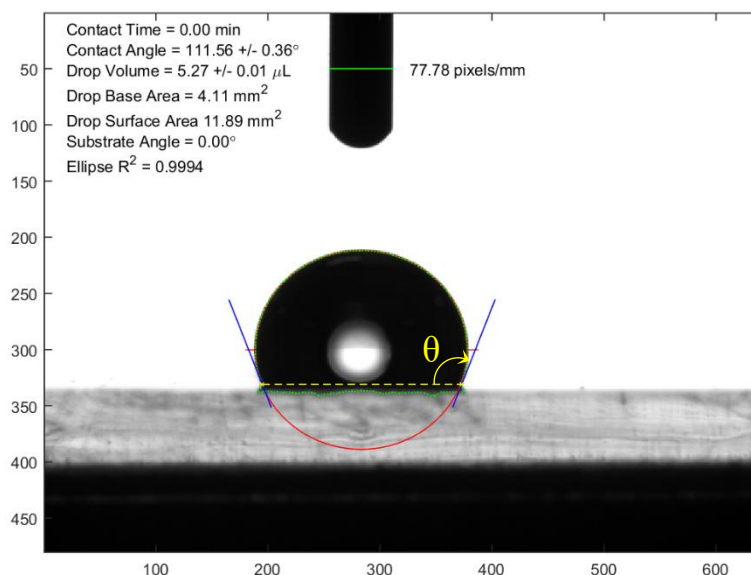


Figure 5.8 – Representative result of droplet image analysis performed with Matlab code. The raw data is a side-view image of the droplet on the surface with a small amount of droplet reflection visible on the surface below the droplet. The code returns the contact time (based on the file naming scheme used in saving images from the goniometer) between water and the substrate along with droplet parameters given in the top left of the image. The tick labels on the left and bottom axes in the image represent pixels. The green horizontal line on the needle is the scale factor of pixels to mm. The green dotted line is the boundary of the droplet as determined by a built-in Matlab function. The red line is the ellipse that has been fitted to the droplet boundary. Yellow “x” marks indicate the user-defined 3-phase contact points. The yellow dashed line connects the two 3-phase contact points and serves as the diameter of the interfacial circular area between water and the substrate. The blue lines indicate the lines tangent to the ellipse at the 3-phase contact points. The slope of the tangent lines is used to calculate the contact angle, θ , which is shown in yellow as the angle between the water-PDMS interface and the blue tangent lines. Full codes are given in the Appendix.

information from the filename, all of which ended with values in seconds that denoted the contact time, t , between the droplet and surface that had elapsed when the image was taken. This value is converted to minutes and shown in the top-left corner of the output image. Next, the image is converted to black and white according to a certain gray pixel threshold value. For each pixel, a value of 1 is white and a value of 0 is black. The gray threshold value between 0 and 1 sets the level above which gray pixels turn white and below which they turn black. This threshold can be adjusted as needed according to the lighting and any artifacts in the photograph that may interfere with the analysis. The needle is then found and a scale factor is determined to convert pixels to millimeters based on the needle outer diameter of 0.78 mm, depicted as a horizontal green line in Figure 5.8. After that the code scans below the needle to find the next black pixel, which is near the top of the droplet. From there, a built-in boundary

command determines the droplet boundary between black and white pixels shown as a green dotted line surrounding the droplet and its reflection in Figure 5.8.

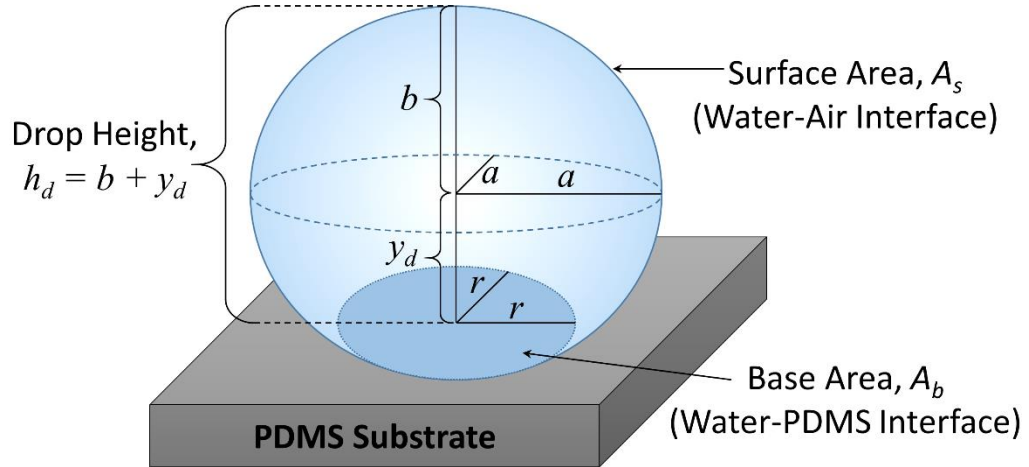


Figure 5.9 – Schematic of a water droplet in the shape of an oblate spheroidal cap showing variables used in calculating droplet parameters. The two major radii that are parallel to the substrate are given by a while the minor radius that is perpendicular to the substrate is given by b . The distance between the substrate and the major diameter of the drop is given by y_d . The total drop height, h_d , is the sum of the minor radius, b , and y_d . The radius of the circular interfacial area between water and PDMS, referred to as the Base Area, A_b , is given by r . The interfacial area between water and air is referred to as the surface area, A_s .

Based on the boundary, a rough idea of the shape of the droplet emerges. Every droplet analyzed had an oblate spheroidal shape, as shown in Figure 5.9. When viewed from above, the droplet is circular, but when viewed from the side, it is elliptical with the horizontal dimension being greater than the vertical dimension. That is, in three dimensions, the two radii parallel to the substrate (a in Figure 5.9) are the same and the radius perpendicular to the substrate (b in Figure 5.9) is smaller than those. The side-view could be fitted according to the equation of an ellipse, given in Equation (5.5).

$$\frac{(x-h)^2}{a^2} + \frac{(y-k)^2}{b^2} = 1 \quad (5.5)$$

Here, h and k are horizontal and vertical offsets of the center of the ellipse, respectively. The major and minor radii of the ellipse are a and b , respectively:

Next, the approximate major diameter of the ellipse, $2a$, is found by determining the left-most and right-most black pixels within the boundary, which are the edges of the droplet. The code calls a non-linear fitting function that fits the outline of the top half of the droplet to the top half an ellipse according to Equation (5.6)

$$y = k - b \sqrt{1 - \frac{(x-h)^2}{a^2}} \quad (5.6)$$

An initial guess for the major radius, a , comes from half the length between the left and right droplet edges. The initial guess for the minor radius, b , originates from the distance between the top of the droplet down to the intersection with the major diameter, $2a$. This intersection point is used as the initial guess for the horizontal and vertical offsets of the center of the droplet, h and k , respectively. The result of the ellipse fitting is shown as a red curve in Figure 5.8 with two small horizontal red lines showing the left-most and right-most edges of the droplet. Additionally, a measure of the goodness-of-fit of the ellipse function to the droplet boundary is given as the ellipse R^2 value.

Now, the only portion of the analysis that is not automated begins. The code displays an image of the droplet on the screen and the user selects a region near the left 3-phase contact point to zoom into. In 3D, this is a 3-phase contact line, but it reduces to a point in the side-view 2D photograph. Then the user clicks the pixel most precisely located at the 3-phase contact point. The user then performs the same for the right 3-phase contact point. These two user-selected 3-phase contact points are shown as yellow “x” marks in Figure 5.8 and are connected by a yellow dashed line. This line serves as the diameter, $2r$, of the base area, A_b (*cf.* Figure 5.9), defined as the circular interfacial area between the water droplet and the substrate, as viewed from above. If the substrate is tilted, the two 3-phase contact points will not be perfectly adjacent to each other. This is quantified as the substrate angle which is simply the slope of the line connecting the two 3-phase contact points. For all measurements taken, the substrate tilt angle was less than 1° and when it was not 0° , it was due only to a ± 2 pixel difference in the vertical direction between the two 3-phase contact points. Finally, the code determines the slope, m , of lines tangent to the ellipse at the points on the ellipse closest to the user-selected 3-phase contact points, which are shown as blue lines in Figure 5.8.

Using the information acquired hitherto, the code now calculates the important droplet parameters of contact angle, θ (degrees), base area, A_b (mm^2), droplet volume, V (μL or mm^3), and droplet surface area A_s (mm^2), defined as the interfacial area between water and air. These values are calculated according to equations (5.7) through (5.13), which are based on an oblate spheroidal cap (*cf.* Figure 5.9).⁵⁹ The cap refers to the fact that the droplets do not form full oblate spheroids because they are cut off at the bottom by the substrate. If the surface exhibits a contact angle $>90^\circ$, then the oblate spheroid is cut off below the major radii, a , that are parallel to the substrate giving a drop height, h_d , such that $b < h_d < 2b$ (*cf.* Figure 5.9). If the surface has a contact angle $<90^\circ$, then the oblate spheroid is cut off above the major radii, a , giving a drop height that is less than the minor radius, $h_d < b$. Thus, the equations for contact angle are slightly different for each scenario and are given by the piece-wise defined function in equation (5.10). The user has to make an educated guess as to whether the contact angle is less than or greater than 90° and use the appropriate code for that particular droplet image.

$$A_b(\text{mm}^2) = \pi r^2 \quad (5.7)$$

$$V(\mu\text{L}) = \frac{\pi a^2 h_d^2}{3b^2} (3b - h_d) \quad (5.8)$$

$$m = -\frac{b\sqrt{b^2 - y_d^2}}{ay_d} \quad (5.9)$$

$$\theta(^{\circ}) = \begin{cases} (\pi - |\tan^{-1} m|) \frac{180}{\pi}, & \text{when } \theta > 90^\circ \\ |\tan^{-1} m| \frac{180}{\pi}, & \text{when } \theta < 90^\circ \end{cases} \quad (5.10)$$

When dealing with the geometry of an ellipse and other conic shapes, a key parameter that defines the shape is called the eccentricity, e . This is a measure of the shape's deviation from circular. A circle has eccentricity $e = 0$. The values of e for an ellipse lie between 0 and 1, with a value of 1 indicating a parabola. The definition of eccentricity in Equation (6.11) is strictly valid for an oblate spheroid where the minor, vertical radius, b , is smaller than the major, equatorial, a , such that $b < a$.⁵⁹

$$\text{eccentricity}, e = \sqrt{\frac{a^2}{b^2} - 1} \geq 0 \quad (5.11)$$

The following term, e_1 , bears no physical significance and is used simply to reduce the amount of terms in Equation (5.12).

$$e_1 = 1 - \frac{h_d}{b} \quad (5.12)$$

The free energy equation for the shape of a droplet on a surface involves a balance of 3 interfacial energies (or tensions) and the effect of gravity. Determination of the exact equilibrium shape of the droplet requires numerical integration of a nonlinear differential equation.⁵⁹ However, by assuming an oblate spheroid shape, which has proven to be a good approximation for 6 μ L water drops,⁵⁹ the surface area, A_s , of the droplet, or interfacial area between liquid and air, can be found by integration to give Equation (5.13).⁵⁹ For more details, refer to the analysis by Lubarda and Talke.⁵⁹

$$A_s(mm^2) = \pi ab \left\{ \frac{a}{b} - e_1 \sqrt{1 + e^2 e_1^2} + \frac{1}{e} [\sinh^{-1}(e) - \sinh^{-1}(e e_1)] \right\} \quad (5.13)$$

Results & Discussion

In this chapter, we present the dynamic water wetting analysis of the Sylgard 184 system with varying Base/Curing Agent (B/C) ratios and the 5 different molecular weights of model Vinyl/TDSS PDMS systems each with various stoichiometric ratios. Samples were studied both before and after Soxhlet extraction, labeled “Pre” and “Post” in the figures that follow, respectively. In the following section, the 28 kDa model PDMS system is displayed as a representative sample of the 5 molecular weight model systems. The data for all other molecular weights are found in the Appendix. This particular model system is compared to Sylgard 184. We take the negative cosine of the contact angle, $-\cos(\theta)$, to indicate positive values with respect to Young’s law when the contact angle is $>90^\circ$. This frame of reference has been used by others.⁶⁰

Droplet Parameters as a Function of Contact Time

Typical data of model PDMS systems and the Sylgard 184 system acquired from the Matlab analysis are shown in Figure 5.10 and Figure 5.11, respectively. Filled symbols represent data pre-extraction while open symbols show data post-extraction. Here, the

negative cosine of the contact angle, $-\cos(\theta)$ (left ordinates), and base area, A_b , are plotted as a function of contact time, t , between the water droplet and the substrate for samples before and after extraction (left and right columns, respectively). The values of contact angle, θ , are given on the right ordinates. The volume, V , and surface area, A_s , of the droplets for the model 28 kDa system and the Sylgard 184 system are shown in Figure A5.12 and Figure A5.25, respectively. The stoichiometric ratios for model systems and B/C ratios for Sylgard 184 change color according to the visible spectrum where red indicates under-crosslinked samples with stoichiometry PDMS is in excess and violet indicates samples with excess crosslinker, where PDMS is the limiting reactant.

The contact angle and base area clearly act inversely to each other as a function of contact time before the samples have undergone Soxhlet extraction as seen in Figure 5.10a and c and Figure 5.11a and c. This means that as the droplet spreads out and A_b increases, the contact angle decreases at a similar rate. Some of these data sets exhibit exponential behavior for very low and very high stoichiometric ratios and B/C ratios. As the r -values and B/C ratios approach an optimal stoichiometry, r_{opt} , and 10:1, respectively, the exponential behavior diminishes and the data become more linear. Relatively long equilibration times occur mostly when non-optimal stoichiometry is used and the data follow a more exponential trend. Such a trend is not observed in the benchmark materials (*cf.* Figure A5.1). This is due to molecular mobility. When the networks are not crosslinked optimally, the molecules have higher

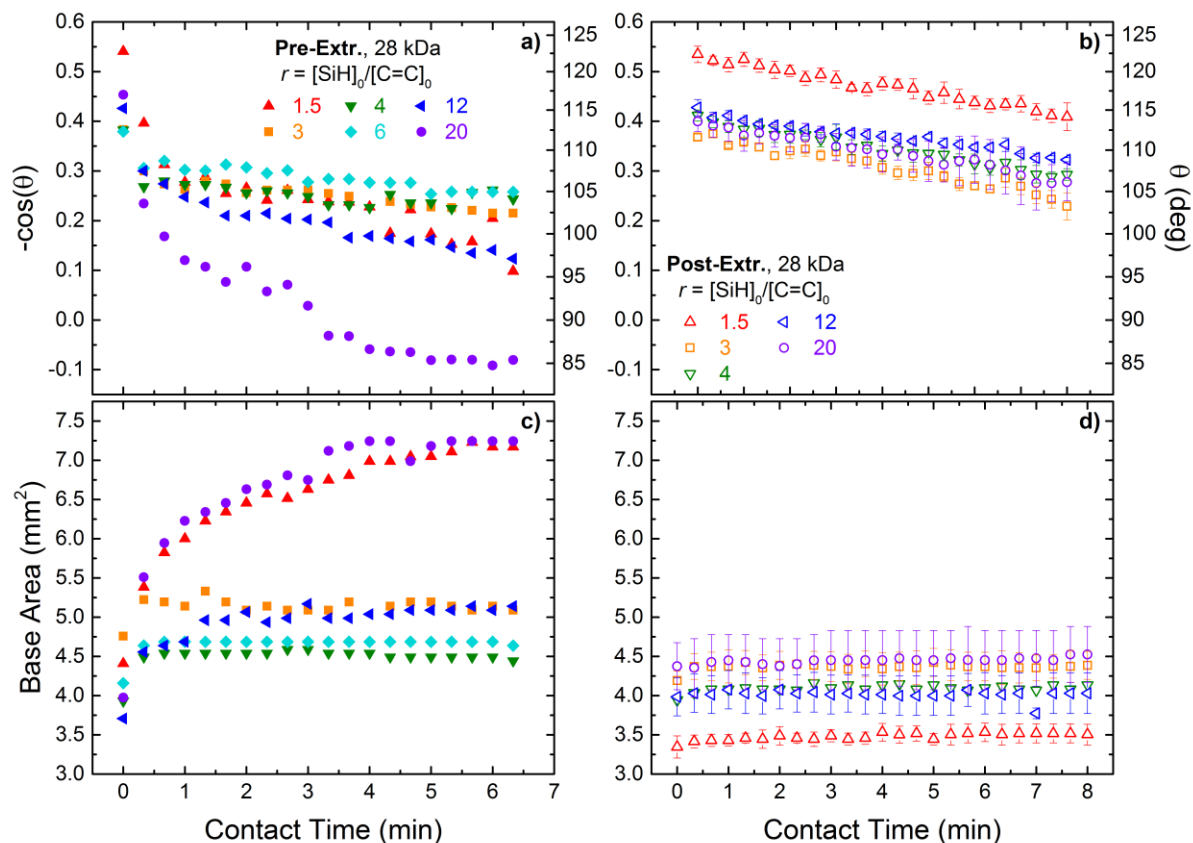


Figure 5.10 – The negative cosine of the contact angle, $-\cos(\theta)$ (left ordinates), and contact angle, θ (right ordinates) are plotted in the top row (a and b) as a function of contact time, t , between water droplet and PDMS substrate pre- (left) and post-extraction (right) for the 28 kDa Vinyl/TDSS system of various stoichiometric ratios, r . The base area, A_b is given in the bottom (c and d).

mobility, which allows for rearrangement and reorientation of surface molecules in an attempt to lower interfacial energy. Additionally, unbound molecules can diffuse to the water/PDMS interface to further lower the interfacial energy. In tightly crosslinked systems, molecular mobility is greatly diminished and there are less unbound molecules due to optimally-crosslinked networks having greater crosslink densities and higher gel fractions, respectively.

We note that equilibration times greater than one minute are required for samples with non-optimal stoichiometry. It is not common practice to wait more than one minute when one measures static contact angles. However, samples at near optimal stoichiometry ($r_{opt} = 3$) in the model system equilibrate more quickly. The Sylgard 184 system seems to be more robust than the model system in that linear behavior and consistent equilibrium contact angle values

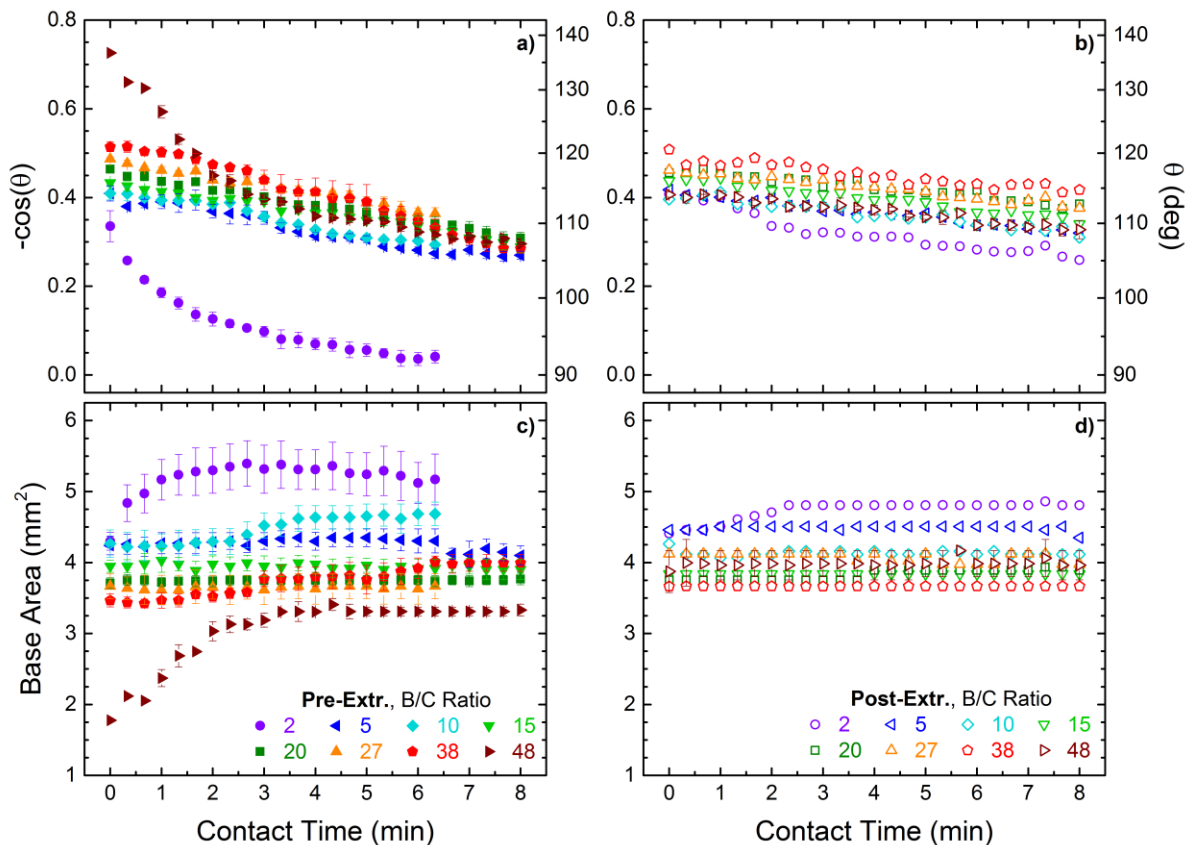


Figure 5.11 – The negative cosine of the contact angle, $-\cos(\theta)$ (left ordinates), and contact angle, θ (right ordinates) are plotted in the top row (a and b) as a function of contact time, t , between water droplet and PDMS substrate pre- (left) and post-extraction (right) for the Sylgard 184 system of various B/C ratios. The base area, A_b is given in the bottom (c and d).

are attained over a wide B/C ratio range. Only when one deviates from the prescribed 10:1 B/C ratio by 5-fold, adding $\sim 5x$ more crosslinker (*i.e.*, $B/C \approx 2$) or $\sim 5x$ less crosslinker (*i.e.*, $B/C \approx 50$) does exponential behavior with large equilibration times emerge. In contrast, the model system possesses a smaller stoichiometric range within which the equilibrium contact angles are consistent and the data behaves linearly. However, caution should be used when making this comparison because the model system is using a molar ratio while Sylgard 184 is using a mass ratio. The two cannot be compared directly. Still, Sylgard 184 exhibits broad linear behavior with respect to its formulation compositions while model PDMS appears to be more sensitive to deviations from optimal stoichiometry.

In addition to the exponential *vs.* linear dynamic behavior of water contact angle and base area as a function of time, the absolute values of contact angle are striking. A large disparity exists between the equilibrium contact angle values for PDMS networks composed of different stoichiometric and B/C ratios before extraction. The cases when $r = 20$ and $B/C = 2$ particularly stand out as quite unusual. PDMS is commonly thought of as a hydrophobic material and has found use in sealants. This means it repels water and is characterized as having a static contact angle $>90^\circ$. It is rather unexpected for PDMS samples to exhibit contact angles $<90^\circ$. This is likely to be due to the chemical composition of the PDMS substrates. A stoichiometric ratio of 20 and B/C ratio of 2 means there is a massive excess of crosslinker. PDMS has predominantly silicon-methyl (Si-CH₃) functional groups, which are known to be very hydrophobic and have even been used to make perfectly hydrophobic surfaces having contact angles of 180° .⁶¹ Recall that the functional groups on the crosslinkers for both model PDMS and Sylgard 184 are silicon-hydride (Si-H). Hydrogen-terminated silicon wafers (Si-H) have been shown to have low water contact angles of 37° and 60° for different crystal lattice structures of Si(111) and Si(001), respectively.⁶² Other researchers⁶³⁻⁶⁶ have found contact angles for hydrogen-terminated silicon wafers to be in the range of 74° – 81° , which although higher, are still less than PDMS is expected to be. It is thus not surprising that the massive excess of Si-H functionality in the networks prior to extraction decreases the contact angle of PDMS networks substantially. In summary, we attribute this lower-than-expected equilibrium contact angle primarily to chemical composition effects rather than network topology or physical properties of the substrate.

In the case where there is a massive excess of polymer instead of crosslinker, the opposite behavior is evident. Where there is not enough crosslinker, such as $r = 1.5$ and $B/C = 48$ in the above figures, higher than expected initial contact angles are observed. The droplets still exhibit exponential behavior in terms of their spreading (*i.e.*, base area) and their contact angle equilibration. However, instead of equilibrating at unusually low values, they equilibrate at the expected values of PDMS. The initially high contact angles are unexpected and are likely due to the excess of free chains in the loosely crosslinked systems.

Until now, we have focused on the samples before extraction and their exponential behavior yielding equilibration times on the order of several minutes. The post-extraction samples exhibit very different behavior (*cf.* Figure 5.10b and d and Figure 5.11b and d). The extraction process, as previously discussed, removes material that is not covalently bound to or trapped in the network. The crosslinkers are small molecules and will readily diffuse out of a PDMS network swollen in toluene. The data post-extraction indicate that the excess crosslinkers have, indeed, been removed for several reasons. First, there is much less evidence of exponential behavior in terms of droplet spreading and water contact angle. Nor is the equilibrium contact angle lower than expected for PDMS. Instead, most samples after extraction have nearly the same contact angles that decrease near linearly with time due to evaporation. According to the base area data, the droplets show no spreading whatsoever, which strongly indicates that free molecules that were allowing for the droplet to slide or spread pre-extraction are no longer present. In summary, post-extraction samples have a less mobile surface on the molecular level compared to pre-extraction samples due to unbound material being removed. This seems to reduce the ease at which droplets spread on the surface. Instead of spreading, the droplets post-extraction appear to be pinned and stay at a fixed base area as a function of time, even though slight evaporation occurs and the contact angle slightly decreases. In other words, there is not much the system can do to lower interfacial energy between the water and substrate, unlike the pre-extraction systems when mobile molecules could migrate and change the interfacial energy.

Post-Extraction vs. Pre-Extraction Contact Angles

In the first section of results, the raw data of how contact angle and base area change as a function of contact time were presented for samples both before and after extraction. Then the fitting functions corresponding to those time-dependent behaviors were analyzed. Now the post-extracted contact angles are plotted as a function of pre-extraction contact angles for all molecular weights in the model PDMS system in Figure 5.12 and for the Sylgard 184 system in Figure 5.13. To view stoichiometric ratios and B/C ratios on an individual basis, see the

Appendix. In these plots, data that fall on the $y = x$ black dashed line means for a given contact time, the post-extraction contact angle is equal to the pre-extraction contact angle.

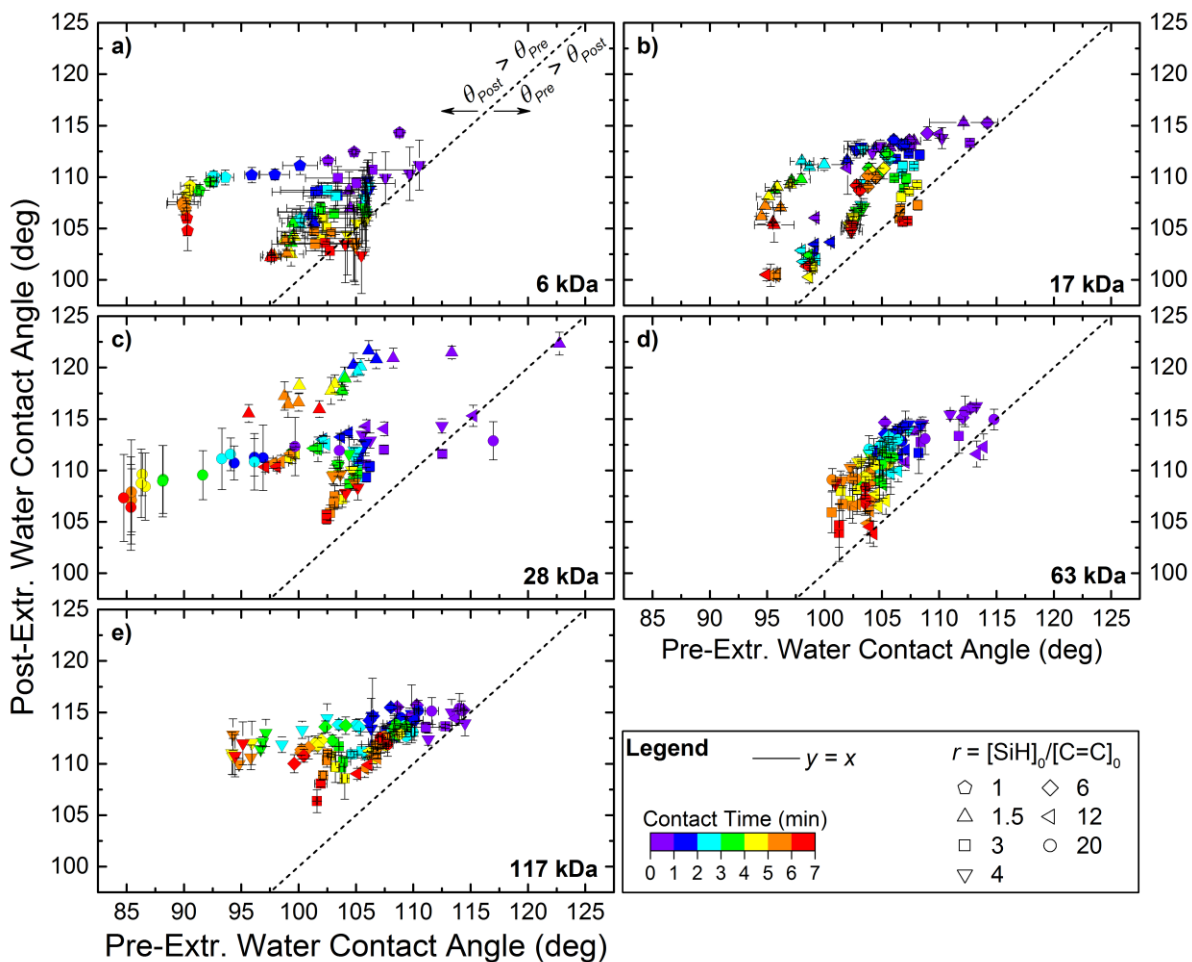


Figure 5.12 – Post-extraction contact angle plotted as a function of pre-extraction contact angle for 6, 17, 28, 63, and 117 kDa model PDMS systems in a) through e), respectively. The diagonal solid black line represents $y = x$. Data to the left the $y = x$ line occur when post-extraction contact angle is greater than pre-extraction contact angle. The opposite occurs for data to the right of the $y = x$ line. Stoichiometric ratio values are given by different shapes according to the legend. The contact time at which each data point was acquired, both pre-extraction and post-extraction is categorized into 7 different colors according to the visible light spectrum. Short times correspond to violet symbols while long times correspond to red symbols.

The data in Figure 5.12 indicate this is a rare occurrence. Instead, most data lie well to the left of the $y = x$ line, meaning the post-extraction values are greater than the pre-extraction values. This could be observed qualitatively in Figure 5.10 but is shown in a quantitative fashion here.

Regardless of stoichiometric ratio or molecular weight, generally the data tends to go from high contact angles at low times (violet) to lower contact angles at high times (red), with a general trend downward and to the left. The farther away from the $y = x$ line, the greater the difference in pre-extraction and post-extraction samples. As molecular weight increases, there appears to be less deviations from the $y = x$ line. While this is true, we note that fewer stoichiometric ratios could be tested with the highest molecular weight of 117 kDa. With increasing molecular weight, non-optimally crosslinked samples became highly “goeey” and soft and difficult to handle. Thus, not all stoichiometric ratios could be tested at higher r -values. If they could be tested, one may still observe large deviations from $y = x$ such as those seen in the 6 kDa system.

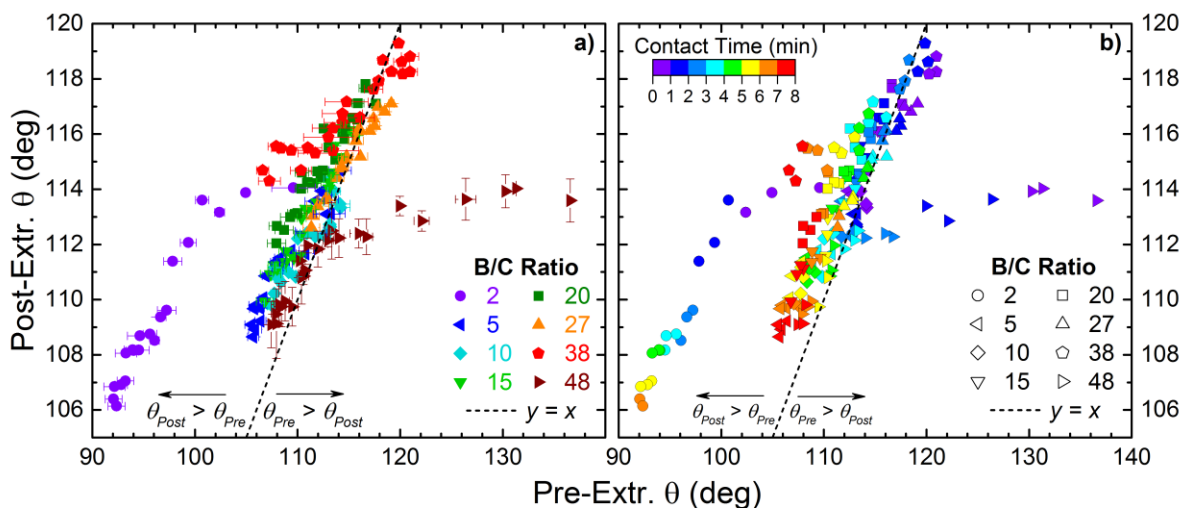


Figure 5.13 – Post-extraction contact angle plotted as a function of pre-extraction contact angle for the Sylgard 184 system. The diagonal solid black dashed line represents $y = x$. Data to the left the $y = x$ line occur when post-extraction contact angle is greater than pre-extraction contact angle. The opposite occurs for data to the right of the $y = x$ line. In plot a), the colors are assigned to B/C ratios while in plot b), the colors change according to the contact time. In b), B/C ratios are given by different shapes according to the legend. The contact time at which each data point was acquired, both pre-extraction and post-extraction is categorized into 8 different colors according to the visible light spectrum. Short times correspond to violet symbols while long times correspond to red symbols.

In Figure 5.13, the same type of analysis is performed where post-extraction contact angle is plotted as a function of pre-extraction contact angle for the Sylgard 184 system. Here

the data seem to be more compact. More data lie closer to the $y = x$ line, indicating very little changes before and after extraction. However, when the data do deviate from $y = x$ behavior, they deviate greatly. The sample sets with massive excess amounts of crosslinker and massive excess of polymer, $B/C = 2$ and 48 , respectively, show very large deviations.

Initial and Final Values

The previous analysis focused on how the droplet parameters change with time. We now turn our attention to studying the differences between initial and final values of droplet parameters, which are plotted in Figure 5.14 and Figure 5.15 for model PDMS of all molecular weights and Sylgard 184, respectively. The pre-extraction data for initial and final contact angle values are blue squares in Figure 5.14. The data for molecular weights equal to and below the critical entanglement molecular weight, M_c , in the left column of Figure 5.14 show some interesting trends. Beginning in plot a with the 6 kDa data, the initial θ values (blue open squares and dashed lines) are fairly independent of the stoichiometric ratio. Yet, the final θ values (blue squares and solid lines) change dramatically with stoichiometric ratio. For both sub-optimal and above-optimal stoichiometric ratios, the contact angle after 6-8 min of equilibration show a maximum value at a stoichiometric ratio of $r = 4$ with significantly lower values when deviating far from $r = 4$. Interestingly, this maximum equilibration contact angle value also corresponds to the smallest difference between initial and final values for pre-extraction data. Towards low and high stoichiometric ratios, the gap between initial and final grows. As the molecular weight prior to crosslinking is increased, looking down the left column of Figure 5.14, this trend of maximum equilibrated θ and smallest difference in θ continues and seems to shift to higher stoichiometric ratios with increasing molecular weight. Furthermore, with higher molecular weights, the pre-extraction initial contact angle starts to increase for low stoichiometric ratios, particularly in plots b), c), and d). As molecular weight continues to increase, the final contact angle data in the right column seem to show less dependence on the stoichiometric ratio. Unfortunately, some small r -value samples were unable to be tested due to their being too soft to handle.

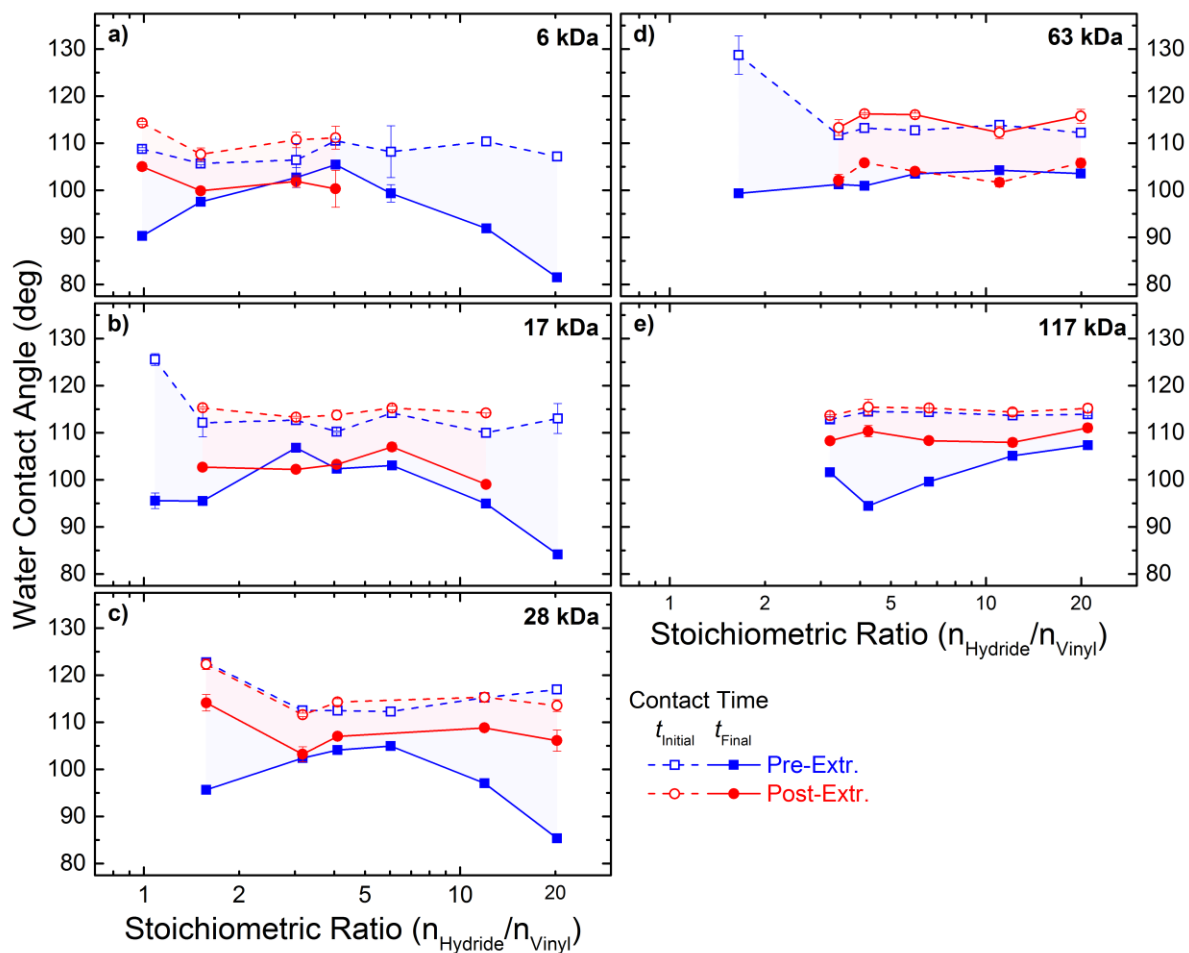


Figure 5.14 – Initial (open symbols, dashed lines) and final (filled symbols, solid lines) water contact angles plotted as a function of stoichiometric ratio for the 6, 17, 28, 63, and 117 kDa model PDMS systems in plots a through e, respectively. Pre-extraction data are blue squares and post-extraction data are red circles. The gaps between initial and final values are shaded blue and red for pre-extraction and post-extraction data, respectively.

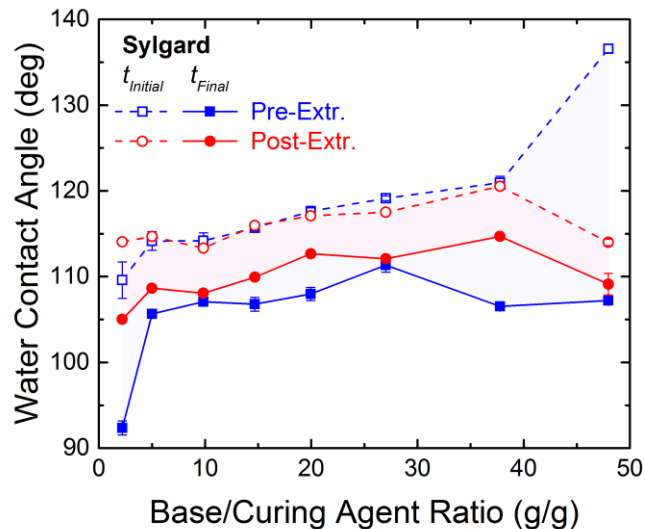


Figure 5.15 – Initial (open symbols, dashed lines) and final (filled symbols, lines) water contact angles plotted as a function of base/curing agent ratio for the Sylgard 184 system. Pre-extraction data are blue squares and post-extraction data are red circles. The gaps between initial and final values are shaded blue and red for pre-extraction and post-extraction, respectively.

The model PDMS networks showed a strong dependence on molecular weight and stoichiometric ratio for pre-extracted initial and final water contact angle data. Sylgard 184 exhibits similar behavior for pre-extracted data, as shown in Figure 5.15. The data are plotted in the same way as those in Figure 5.14 where pre-extraction data are blue squares and post-extraction data are red circles. A large gap occurs between initial and final contact angle values for B/C = 48 and 2. Unlike model PDMS, the final pre-extracted contact angle values are roughly consistent across all B/C ratios except for B/C = 2. Only when the chemical composition of the PDMS substrate is changed substantially with massive excess amounts of crosslinker does the substrate start to exhibit less hydrophobic properties. This is again demonstrating the robustness of the Sylgard 184 formulation, which permits moderate deviations from the 10:1 ratio without significant changes in surface properties. This ability to deviate far from the optimal crosslinking stoichiometry is unique to Sylgard 184 compared to the model PDMS systems examined in this dissertation. Model systems require more precision in crosslinking stoichiometry.

Now consider the post-extraction data shown as red circles in Figure 5.14 and Figure 5.15. The post-extraction samples behave very differently compared to the pre-extraction specimens. These demonstrate an approximately constant difference between initial and final contact angles regardless of molecular weight and stoichiometric ratio. There are very few instances where the post-extraction contact angles are either unexpectedly high or low. Some samples were damaged and broke apart during Soxhlet extraction and, unfortunately, were unable to be tested to acquire post-extraction data. Nevertheless, this reinforces the message that extraction is a very important processing step one should take when investigating surface properties of silicone elastomers. When deviating from optimal stoichiometry, the networks exhibit much more dynamic behavior due to the presence of unbound crosslinkers and polymers that can migrate to the interface and adapt to their environment. The extraction process removes most of them and makes the PDMS network substrate more static, thus producing more consistent water contact angle results regardless of Sylgard 184 formulation and model PDMS molecular weight and stoichiometric ratio.

The preceding two figures showed the initial and final contact angle values, where some were higher and some lower than expected for PDMS. The frequency at which unexpected values of contact angle were observed increased with greater deviation from optimal stoichiometry. In Figure 5.10 and Figure 5.11, we noted that the base area of the droplet (*i.e.*, the interfacial area between water and PDMS) seemed to change with time inversely to $-\cos(\theta)$ and θ . To demonstrate the relationship between contact angle and base area, we now examine the differences between initial and final values (with respect to contact time) of $-\cos(\theta)$ (and θ) and base areas.

In Figure 5.16 and Figure 5.17, we show data for the 28 kDa model PDMS system and the Sylgard 184 system, respectively. Similar plots for all other molecular weight model PDMS systems can be found in the Appendix. In the top row of these figures, the absolute change in the value of $-\cos(\theta)$ (left ordinate, solid lines, filled symbols) and change in contact angle, θ (right ordinate, dashed lines, open symbols) are plotted as a function of the stoichiometric or B/C ratios in the left column and as a function of sol fraction in the right column. Similar data are shown in the bottom row for the change in base area, where absolute

change is given on the left ordinates and the percent change is given on the right ordinates. These figures reinforce the importance of optimal stoichiometry and extraction further.

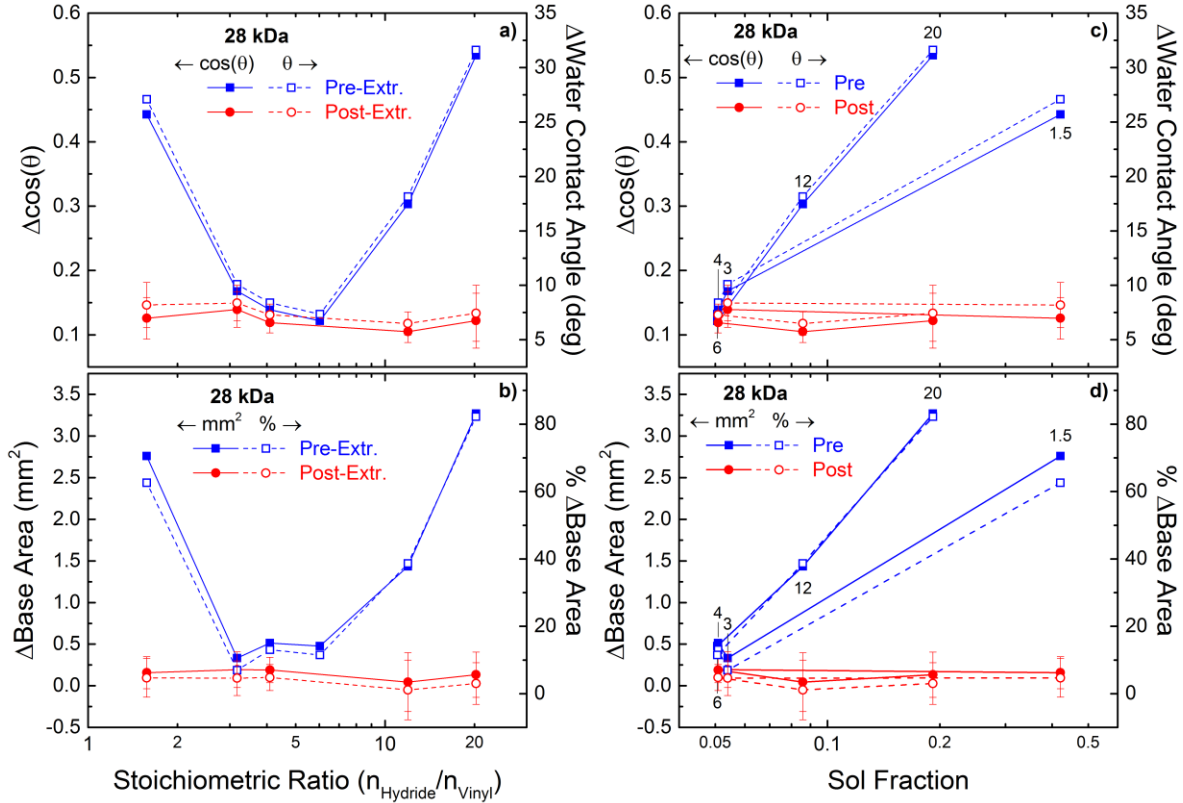


Figure 5.16 – Absolute change (left ordinate, solid lines, filled symbols) and percent change (right ordinate, dashed lines, open symbols) in contact angle (top row) and base area (bottom row) plotted as a function of stoichiometric ratio (left column) and sol fraction (right column) for the 28 kDa model PDMS system. Pre-extraction data are blue squares and post-extraction data are red circles. Numerical labels correspond to stoichiometry ratios.

First, the blue squares represent the pre-extraction data. It is clear that a small range of stoichiometric ratios exists wherein the changes in contact angle and base area are kept to a minimum, as seen in Figure 5.16a and b. In contrast, a wider range of B/C ratios exist that maintain minimal changes in θ and A_b , as shown in Figure 5.17a and Figure 5.17b. Both systems show large differences in $-\cos(\theta)$ (and θ) and A_b when deviating far from the optimal stoichiometry. The base area even changes by more than 80% for largely imbalanced stoichiometry. As discussed in preceding chapters in this dissertation, imbalanced

stoichiometry leads to smaller degrees of gelation. We now observe the effect of degree of crosslinking as measured by sol fraction on the droplet parameters. The trends in Figure 5.16c and d for model PDMS and Figure 5.17c and d for Sylgard 184 systems reveal the differences in water contact angle and base area as a function of sol fraction. Sol fraction is used and plotted on a log scale to extend the region between 0 and 0.1, which corresponds to fairly highly crosslinked materials having gel fractions between 0.9 and 1. This makes the data easier to interpret compared to plotting against gel fraction on a linear scale.

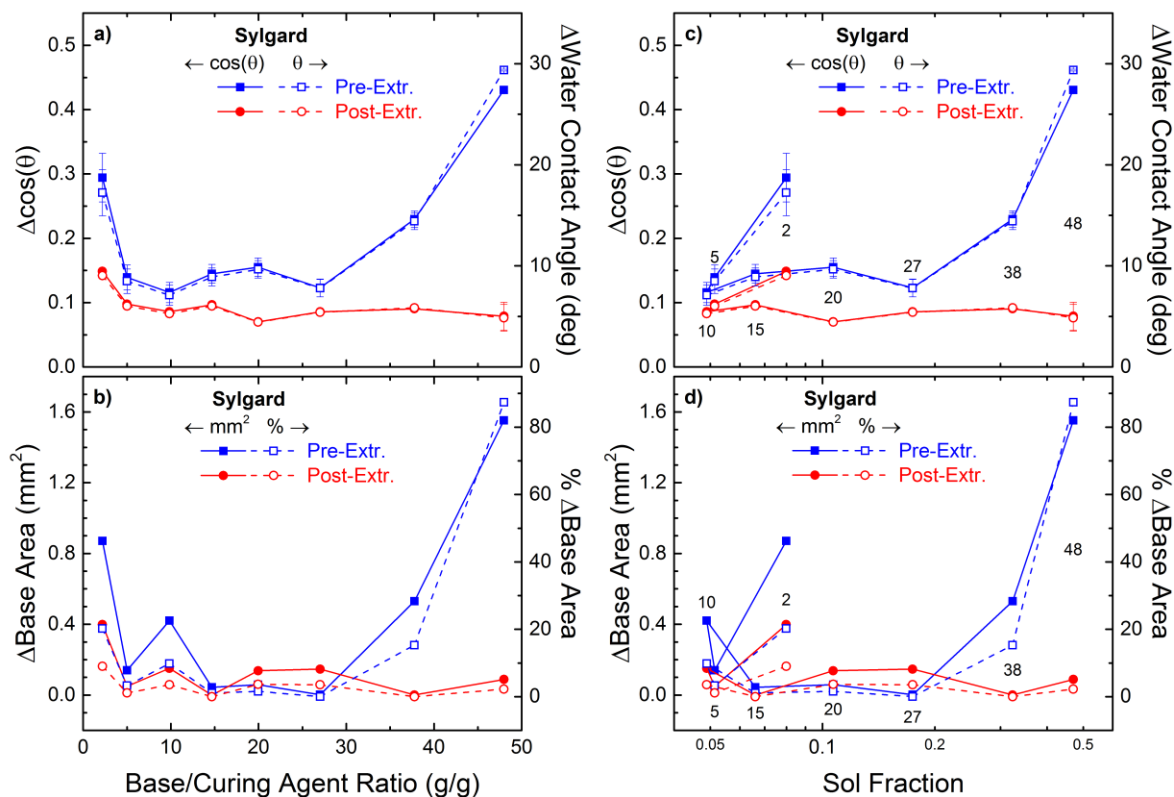


Figure 5.17 – The absolute change in $\cos(\theta)$ (left ordinates) and θ (right ordinates) with respect to contact time are given in plots a) and c). In plots b) and d), the absolute change (left ordinate, solid lines, filled symbols) and percent change (right ordinate, dashed lines, open symbols) in base area are depicted. All variables are plotted as a function of B/C ratio (left column) and sol fraction (right column) for the Sylgard 184 system. Pre-extraction data are blue squares and post-extraction data are red circles. Numerical labels in plots c) and d) correspond to B/C ratios.

When plotted against sol fraction, it becomes apparent how even a small amount of unbound material can cause significant changes to PDMS network surface properties. The 28 kDa model PDMS system shows the smallest changes at r -values of 3, 4, and 6, all of which have gel fractions of ~ 0.95 . (As a side note, this range of optimal stoichiometry may be larger than reported, having r -values of *e.g.*, 1.8-8. Samples prepared from smaller incremental changes in r would elucidate the true range of optimal stoichiometry for minimizing changes in water wettability.) When just a very small amount of material is unbound (*i.e.*, $> \sim 5\%$), for instance at $r = 12$ and sol fraction = 0.08, the change in contact angle and base area is roughly twice as large. However, there does not appear to be a simple one-to-one relationship between sol fraction and changes in contact angle and base area. For instance, in the Sylgard 184 system, the B/C = 27 sample has a sol fraction of about 0.18 and the B/C = 2 sample has a sol fraction of ~ 0.08 . However, there are smaller changes in both contact angle and base area for the B/C = 27 sample instead of the B/C = 2 sample, so the chemical composition of the PDMS network still plays a big role in determining surface properties, in addition to the fraction of unbound material. Additionally, the chemical nature of the unbound material may be the most important factor. In both the 28 kDa model PDMS and the Sylgard 184 systems, it is clear that the extraction process removes what is causing the large changes in contact angle and base area to occur. Regardless of crosslinking stoichiometry and sol fraction, all of the post-extraction data remain flat, indicating no influence of either variable on these changes in droplet parameters.

In the preceding discussions, we have focused on the changes in $\cos(\theta)$ (and θ) and changes in base area with respect to crosslinking stoichiometry and sol fraction. As a result of this analysis, neither of these two droplet parameters is determined to be directly proportional to the stoichiometry and sol fraction. That is, changes in contact angle and base area occur at both high and low ends of the stoichiometry and sol fraction spectra. Now we investigate their dependency on each other. In Figure 5.18, the change in $-\cos(\theta)$ is plotted as a function of change in base area and change in volume for the 28 kDa model PDMS system in a and b, respectively. Blue squares represent pre-extraction data and red circles represent post-

extraction data. The numerical labels correspond to the stoichiometric ratios. The same variables are plotted for the Sylgard 184 system in Figure 5.19.

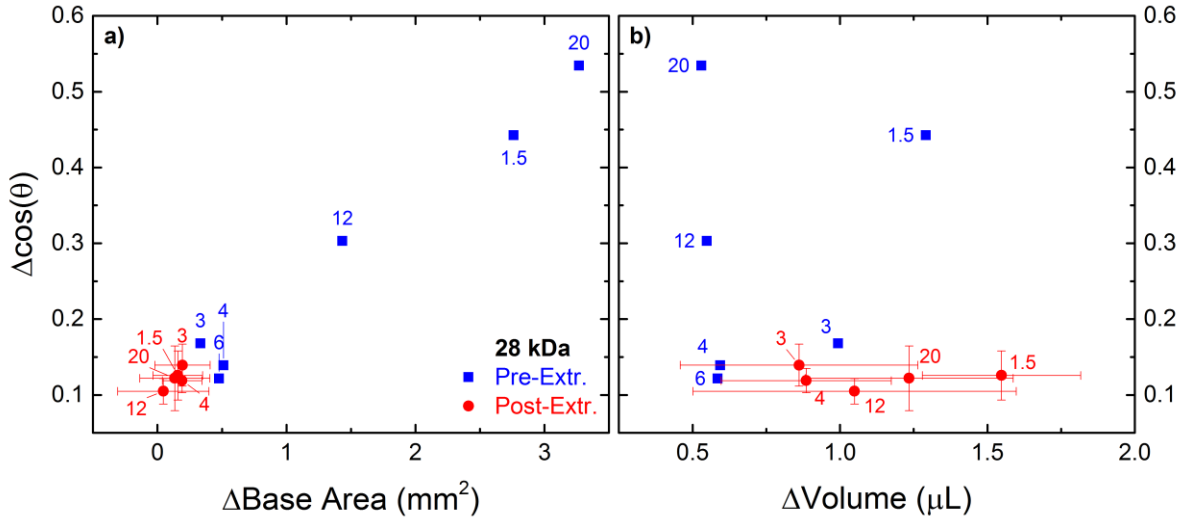


Figure 5.18 – Change in $-\cos(\theta)$ plotted as a function of change in base area in plot a) and change in volume in plot b) for the 28 kDa model PDMS system. Pre-extraction data are blue squares and post-extraction data are red circles. The numerical labels on the data points are the stoichiometric ratio values.

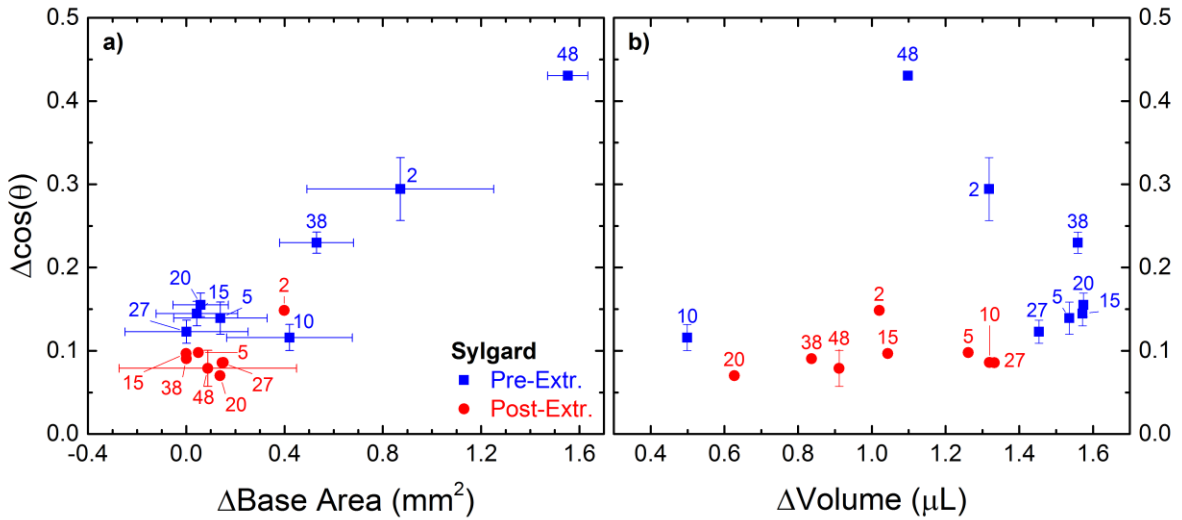


Figure 5.19 – Absolute change in contact angle plotted as a function of absolute change in base area in plot a) and absolute change in volume in plot b) for the Sylgard 184 system. Pre-extraction data are blue squares and post-extraction data are red circles. The numerical labels on the data points are the B/C values.

Here the direct relationship between changes in $-\cos(\theta)$ and changes in base area become apparent. These two parameters do appear to be strongly correlated with each other. Small changes in $-\cos(\theta)$ and A_b occur in both the model PDMS and Sylgard 184 systems for post-extracted data. Larger changes occur when deviating far from optimal stoichiometry in both systems as well, mostly in post-extraction data, but the trends seem to be linear. Importantly, when the change in contact angle is plotted against the change in volume for both systems in Figure 5.18b and Figure 5.19b, no correlation appears to exist. That is, the data are scattered with respect to changes in volume. Sometimes large changes in volume correspond to small changes in contact angle, but other times smaller changes in volume correspond to larger changes in contact angle. There is no consistency with the response of change in $-\cos(\theta)$ with change in volume. This is important because the environment during these wettability experiments was not controlled. Consequently, depending on the temperature and relative humidity in the lab, the water evaporation rates could have differed. These two figures demonstrate, however, that within the ranges of volume changes that did occur during these measurements, they were not significant enough to influence changes in contact angle.

Direct Comparison of Sylgard 184 with Model PDMS

Since Sylgard 184 stoichiometry is based on the Base/Curing Agent mass ratio while model PDMS is based on the stoichiometric ratio, the two types of PDMS networks cannot be directly compared based on chemical composition of the network. However, a measure of gelation is the network gel fraction, so model networks and Sylgard 184 can be compared directly with respect to gel and sol fractions. In Figure 5.20 we plot the change in contact angle (parts a and c) and change in base area (parts b and d) with respect to contact time on the substrate as a function of the sol fraction of the material. Most of the pre-extraction samples exhibit similar behavior in that they all show an increase in $\Delta\theta$ with increases in sol fraction. This indicates strongly that the unbound material present in the PDMS substrate is actively playing a role in the dynamic wetting behavior at the interface. The presence of unbound material enables the droplet to spread out more than it would otherwise and lower the free energy of the system. The data measured post-extraction does not show such a close

relationship to the sol fraction. That is, after the soluble material has been removed, there is no correlation with how much material was removed and how the water droplet behaves on the substrate. The correlation only exists when the unbound material is present and able to participate in the interfacial reorganization. We also note that the magnitude of changes in both water contact angle and base area are much smaller for post-extraction samples compared to pre-extraction samples. This further indicates that the interfacial properties only change significantly in the presence of unbound material.

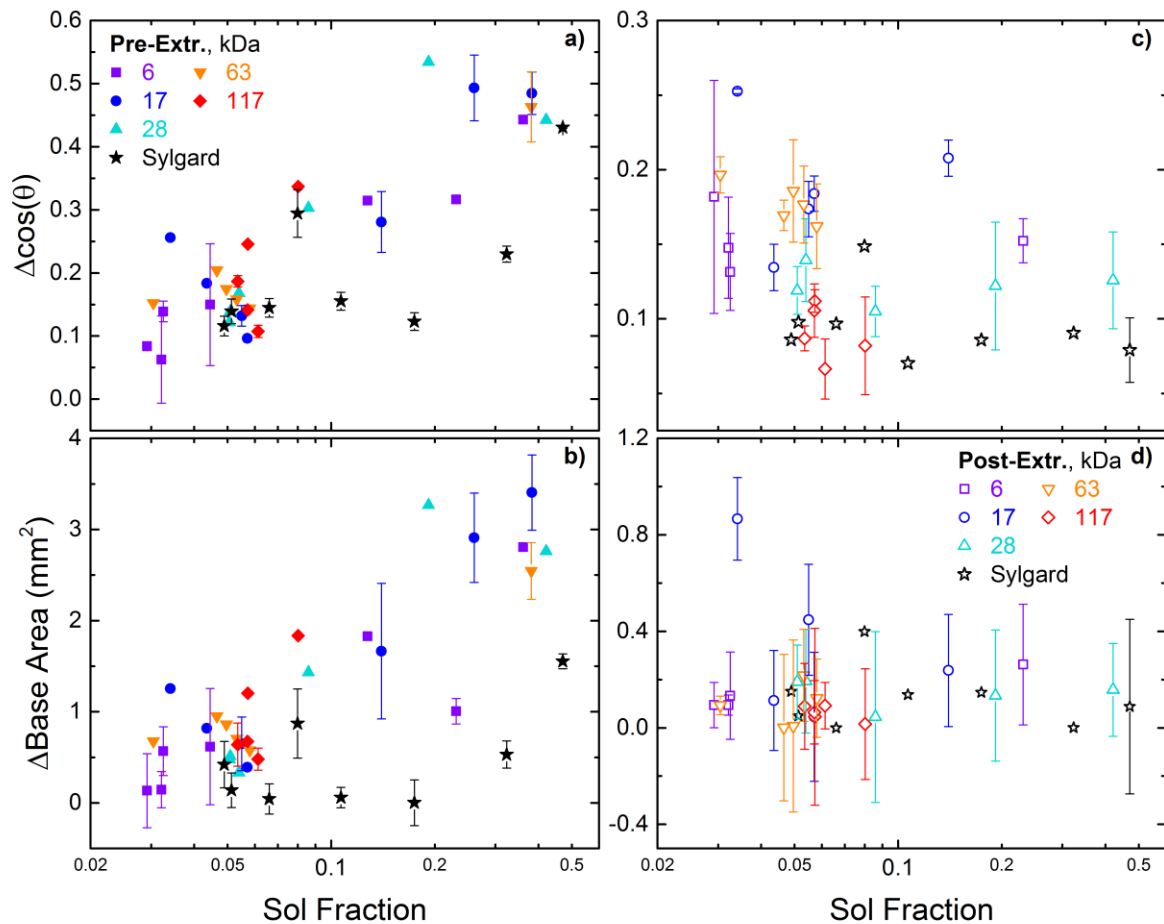


Figure 5.20 – Change in water contact angle ($\theta_{\text{Initial}} - \theta_{\text{Final}}$) and change in base area ($A_{b,\text{Final}} - A_{b,\text{Initial}}$) plotted in the top and bottom rows, respectively, as a function of sol fraction. Left column shows pre-extraction data. Right column shows post-extraction data.

In Figure 5.20a, Sylgard 184 exhibits slightly different behavior than the model PDMS materials. Even when Sylgard 184 has greater sol fractions, the changes in $\cos(\theta)$, contact angle and base area remain small. That is, the Sylgard 184 data (black stars) remain at low values of $\Delta\theta$ and ΔA_b as the sol fraction increases, all the way up to $\sim 20\%$ soluble material. For greater than $\sim 20\%$ soluble material, we then observe an increase in the Δ quantities. This is in contrast to the behavior of model PDMS which begins to show significant increases in $\Delta\theta$ and ΔA_b at sol fractions approximately $>7\%$. This demonstrates the robust nature of Sylgard 184 formulations.

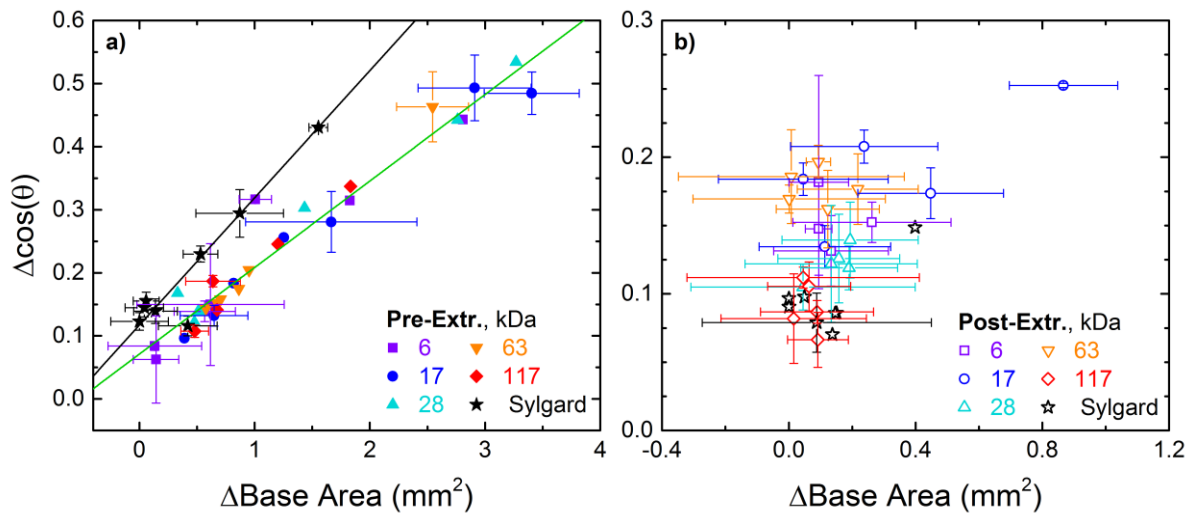


Figure 5.21 – Change in $\cos(\theta)$ as a function of change in base area, with respect to contact time between the water droplet and substrate. Data for pre-extraction samples are given in plot a), and data for post-extraction samples are given in plot b). The straight lines in plot a) are linear best-fit lines. The black line has an equation of $y = 0.202x + 0.117$ with an $R^2 = 0.98$. This is a fit for Sylgard 184 data only. A fit for all model PDMS samples is given by the green line and has the form $y = 0.137x + .071$ with an $R^2 = 0.92$. The post-extraction data do not exhibit a linear trend.

Because changes in both water contact angle and base area demonstrate strong relationships with sol fraction for the pre-extraction samples, in Figure 5.21 we now plot the change in contact angle as a function of change in base area for pre-extraction samples (left) and post-extraction samples (right). Here, the strong relationship between contact angle and base area presents itself. The model PDMS data are fit with a linear trendline (solid black

line) while the Sylgard 184 data is fit with its own trend line (dashed black line). This demonstrates clearly one of the differences between the commercial material and pure PDMS polymer networks. Water droplets on the Sylgard 184 materials tend to spread less than droplets on the model PDMS for the same change in contact area, as evidenced by the steeper slope for Sylgard 184. As before with the preceding figure, there is no trend in post-extraction samples with respect to change in contact angle and change in base area. The data are more compact. Most of the post-extraction data do not show a change in base area throughout the time of the experiment. The drops stay pinned in place for most experiments of most extracted samples.

Real-Time Comparison

The previous figures only demonstrated the dependence on changes between initial and final values of $-\cos(\theta)$ and A_b in the experiment. The following figures elucidate how these two parameters depend on each other at each time interval sampled during the experiments. In Figure 5.22 and Figure 5.23, we plot the $-\cos(\theta)$ as a function of the base area for each time interval over which the data was collected. The downward trend in the data indicates a decrease in the interfacial energy between water and PDMS as a function of both contact time and interfacial area as the system approaches equilibrium. Over time, the interfacial energy decreases due to a variety of factors including mobile unbound material in the network. The migration of these unbound chains to the interface has a surfactant-like effect which lowers the interfacial energy and thus, permits a larger interfacial area. Generally, all data follow the trend of high $-\cos(\theta)$ at initial contact times and decrease to lower $-\cos(\theta)$ and larger A_b for longer contact times. A few B/C ratios exhibit behavior where a maximum A_b is reached and then A_b decreases as $-\cos(\theta)$ continues to decrease. We attribute this to evaporation and de-pinning of the droplet from the substrate as the volume shrinks.

In both Figure 5.22 and Figure 5.23, we see the samples with excess crosslinker (violet) show the lowest values of contact angle and greatest base areas. This indicates the more favorable interactions with water that arise from the slightly more hydrophilic Si-H groups (compared to Si-CH₃ groups). This demonstrates the crosslinking chemistry is very important

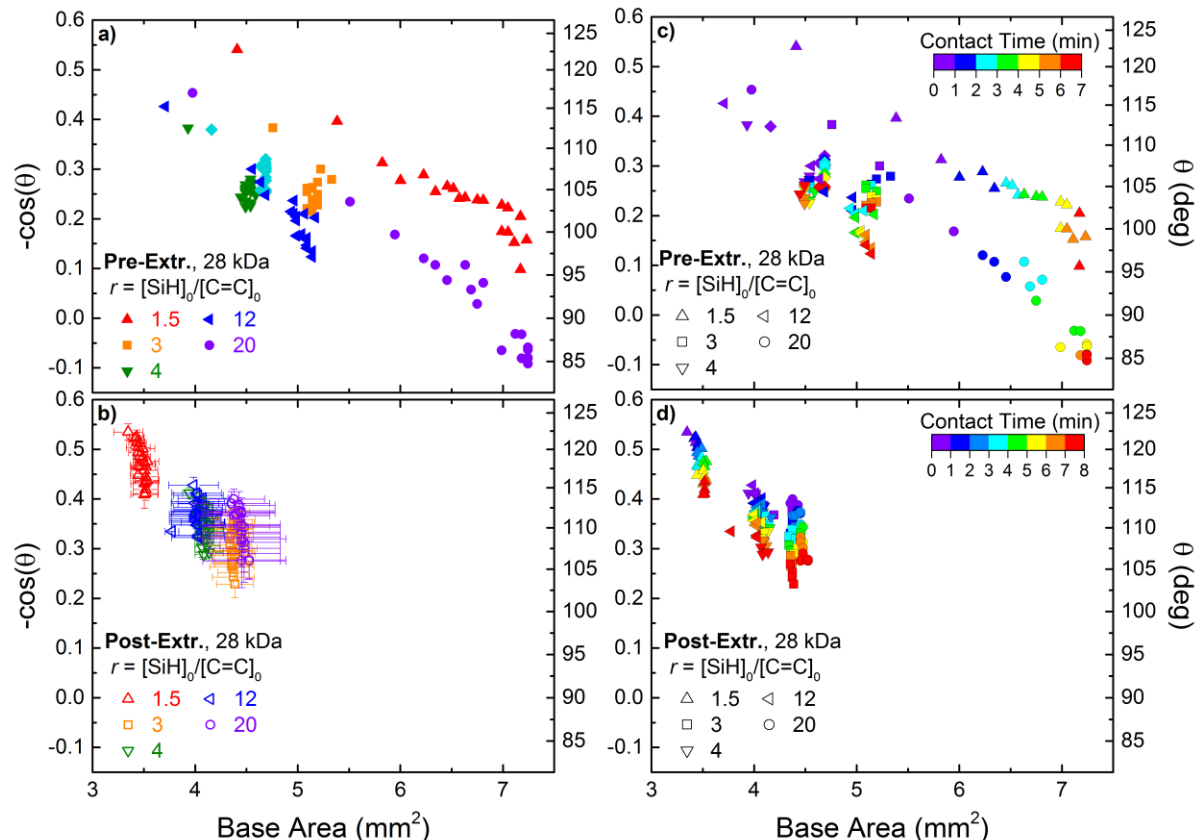


Figure 5.22 – The value of $-\cos(\theta)$ is plotted as a function of the corresponding base area for each stoichiometric ratio at each time interval throughout the course of the experiment for 28 kDa model Vinyl/TDSS PDMS. In plot a), the symbol colors represent different B/C ratios. In plot b), the colors change according to contact time between the droplet and substrate. Plots a) and b) show pre-extracted data and plots c) and d) show post-extracted data. Zoomed in post-extraction data are given in Figure A5.14 in the Appendix.

especially when massive amounts of excess crosslinker are used because doing so changes the chemical composition of PDMS substrates.

The dramatic effect extraction has on the materials is displayed in these two figures. The post-extraction data is much more compact, indicating a system that is much more static and lacks the ability to adapt to the environment of a liquid droplet placed on the surface. This means that after extraction, an equilibrium between water and PDMS substrate is reached rapidly and the only decreases in contact angle observed are due to evaporation, as opposed to lowering of the interfacial energy by uncrosslinked species. A significant difference between model PDMS and Sylgard 184 is apparent in these figures. The under-crosslinked substrates

(dark red data) for Sylgard 184 exhibit unusually high initial contact angles. This behavior is observed to a lesser degree in the model PDMS systems. Under-crosslinked substrates are gooey and sticky. When reinforced with fumed silica particles, this may have the effect of slowing down the equilibration in Sylgard 184 and making the contact angle artificially high initially..

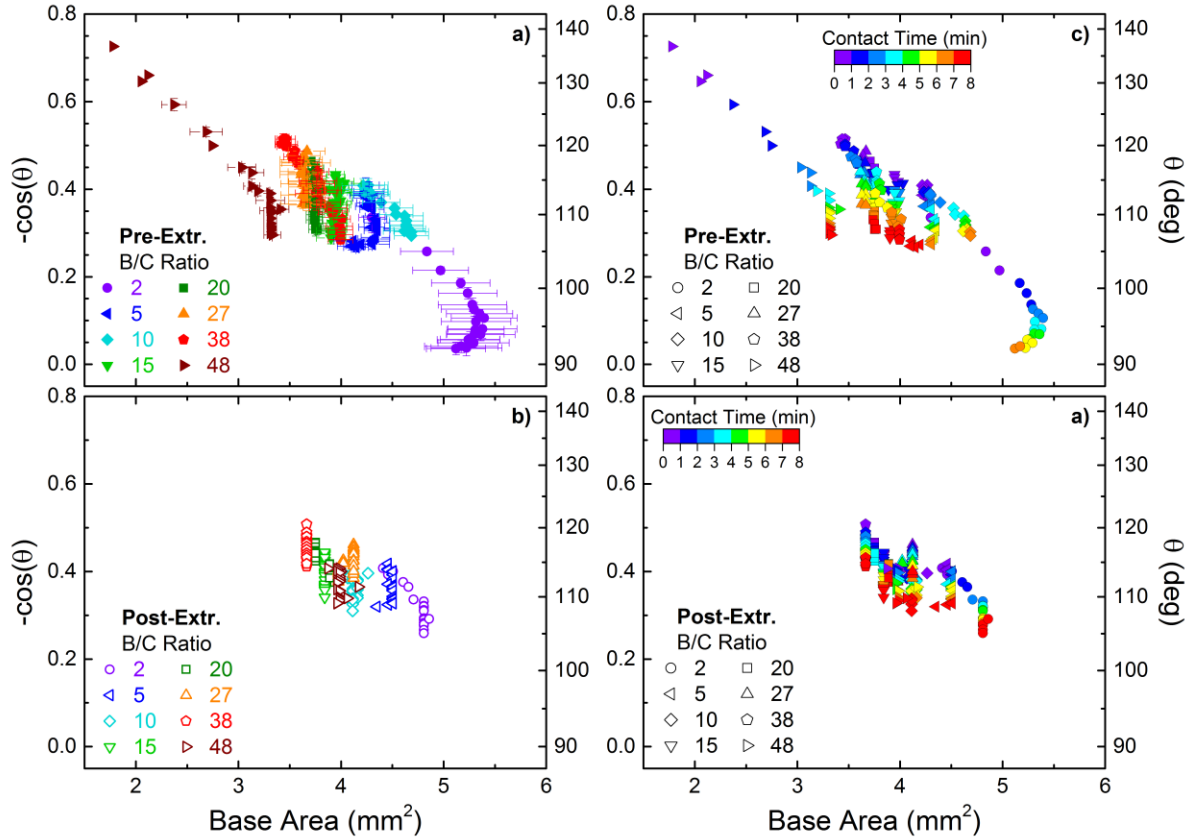


Figure 5.23 – The value of $-\cos(\theta)$ is plotted as a function of the corresponding base area for each B/C ratio at each time interval throughout the course of the experiment for Sylgard 184. In plot a), the symbol colors represent different B/C ratios. In plot b), the colors change according to contact time between the droplet and substrate. Plots a) and b) show pre-extracted data and plots c) and d) show post-extracted data. Zoomed in post-extraction data are given in Figure A5.27 in the Appendix.

PDMS-Water Interfacial Energy

The preceding discussion demonstrated clearly that a relationship exists between $-\cos(\theta)$ and the interfacial area between the water and PDMS (*i.e.*, base area). To investigate this relationship between contact angle and interfacial area between water and PDMS, recall from Equation (6.4) that the cosine of the contact angle between a liquid and a substrate is a measure of the balance of interfacial energies between the two phases in the presence of a third phase or medium (in this case, air). To approximate the relative interfacial energy between water and PDMS over the contact area in which the two phases are interfacing, we take the product of base area and $-\cos(\theta)$ to give a measure of interfacial energy, $-A_b\cos(\theta)$, expressed in terms of the surface tension of the probing liquid, water.

We first plot this parameter of $-A_b\cos(\theta)$ as a function of contact time for all stoichiometric ratios of the 28 kDa system and all B/C ratios of Sylgard 184 and for both pre- and post-extraction samples in Figure 5.24 and Figure 5.25, respectively. The data are fit with a linear best-fit line, although this is clearly not a good fit for a few data sets. Nevertheless, one can see that the slope decreases in magnitude going from pre-extraction data to post-extraction data (*cf.* insets Figure 24 and Figure 25). That is, this measure of interfacial energy in terms of the surface tension of water decreases at a slower rate in post-extraction data compared pre-extraction data. This is due to the substrate's reduced ability to change the interface after the samples have been extracted. There is much less mobile material remaining that can migrate to the interface and act like a surfactant to lower the interfacial energy after the extraction process.

In Figure 5.26 and Figure 5.27, we plot this interfacial energy quantity for post-extracted samples as a function of pre-extraction samples for all stoichiometric and B/C ratios in the 28 kDa system and Sylgard 184 system in plots a) and b). Both of these plots show the same data, but plot a) depicts each stoichiometric ratio or B/C ratio as a different color whereas plot b) demonstrates the change in this quantity as a function of contact time. As with previous graphs, short times are violet and long times are red. Both of these plots show a $y = x$ line, which would indicate the interfacial energy between PDMS and water is the same before and

after extraction. The data are fit fairly well by a linear-best-fit line, which are shown in plot a). We can see that $r=20$ and $B/C = 2$ deviates greatly from the $y = x$ line, indicating that the

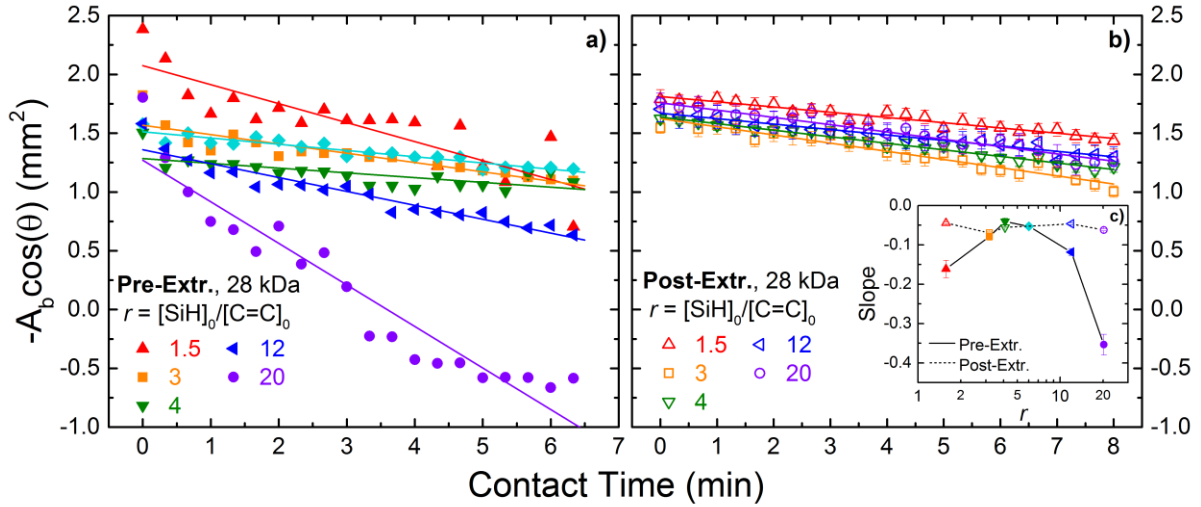


Figure 5.24 – The quantity of base area multiplied by the negative $\cos(\theta)$ is plotted as a function of contact time between the drop and substrate for pre-extraction data and post-extraction data in plots a) and b), respectively for 28 kDa model PDMS samples of various stoichiometric ratios. Data are fit with a linear best-fit line whose slopes are given as a function of the stoichiometric ratio, r , in the inset

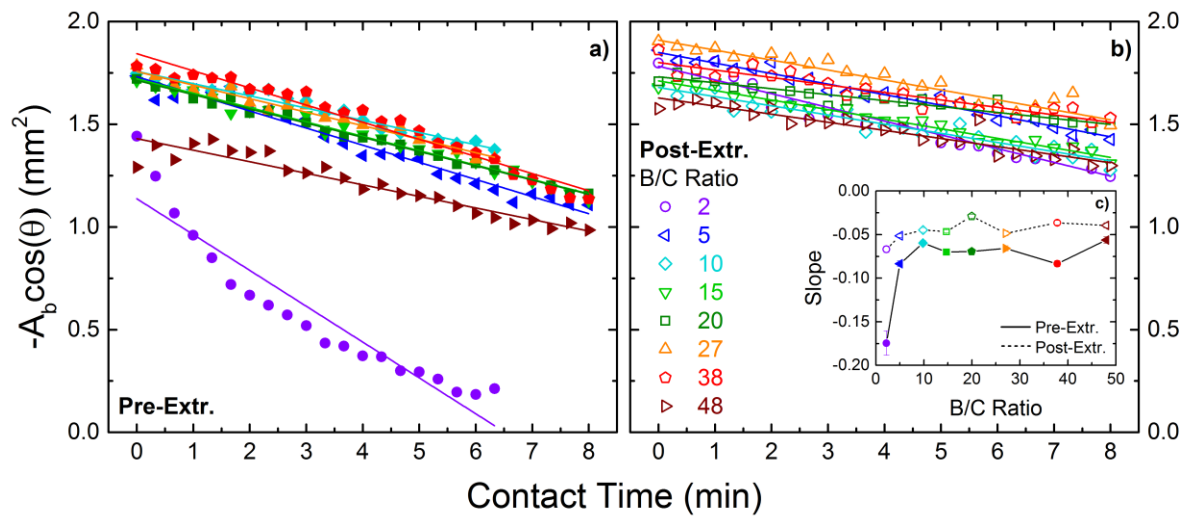


Figure 5.25 – The quantity of base area multiplied by the negative $\cos(\theta)$ is plotted as a function of contact time between the drop and substrate for pre-extraction data and post-extraction data in plots a) and b), respectively for Sylgard 184 samples of various B/C ratios. Data are fit with a linear best-fit line whose slopes are given as a function of B/C ratio in the inset.

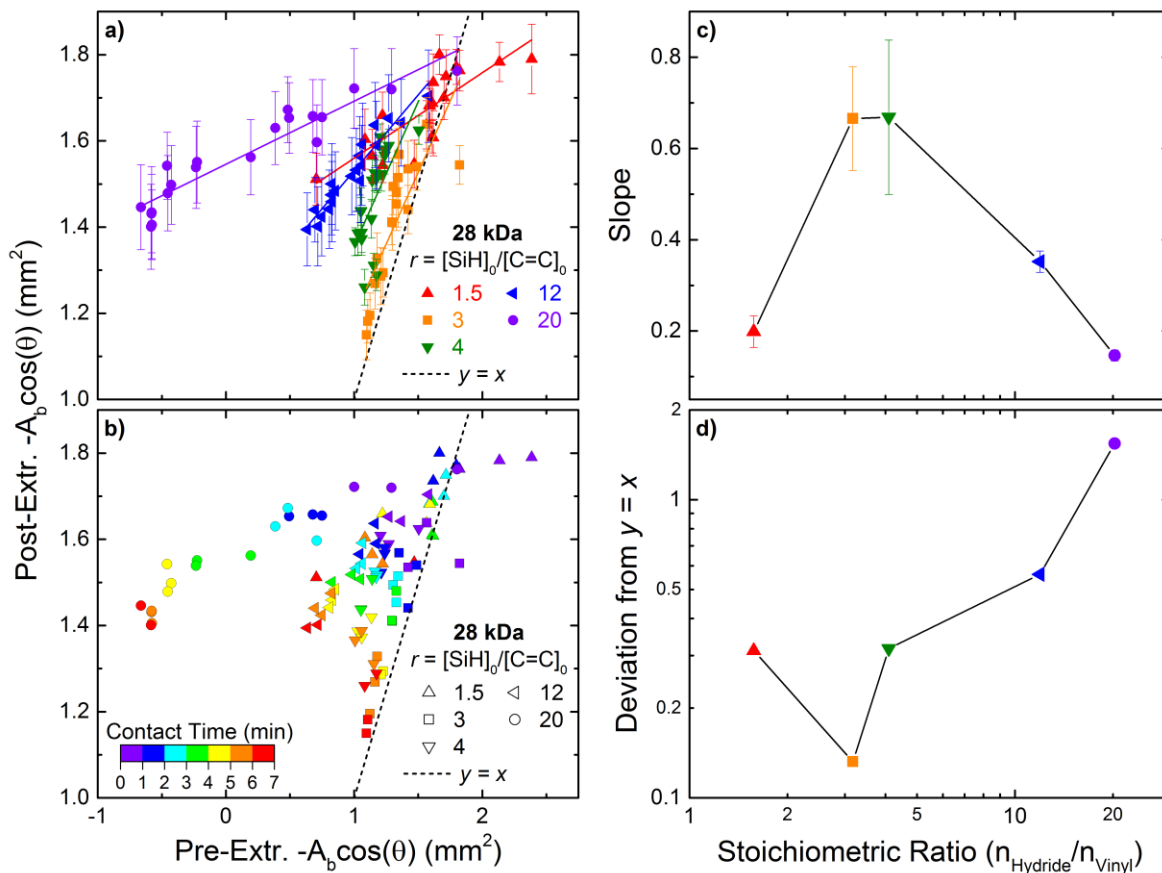


Figure 5.26 – In plots a) and b), the post-extraction value of $-A_b \cos(\theta)$ is plotted as a function of the same value for pre-extraction samples. The colors in plot a) correspond to different stoichiometric ratios. The data are fitted with a linear best-fit line. In plot b), the colors corresponded to the amount of contact time. Generally, the amount of contact time between the water droplet and the substrate increases downward to the left. In plot c), the slope of the data sets in plot a) is given as a function of the stoichiometric ratio. In plot d), a measure of the deviation from the $y = x$, lines in plots a) and b) is given for samples made from each stoichiometric ratio. The equation for deviation from $y = x$ is given in plot d).

extraction process is not only removing material, but that the chemistry of the material removed plays a bigger role in wettability compared to the material removed from other samples. That is, when the sample contains excess crosslinker (*i.e.*, excess Si-H groups) with relatively higher surface energy than the repeat units of PDMS (Si-CH₃ groups), the change in interfacial energy is significant. As we know from previous discussions, the $r = 1.5$ and B/C = 38 and 48 samples have significantly higher sol fractions than B/C = 2 sample, but the majority of the material

removed in those higher ratios is long-chain PDMS, since PDMS is in excess relative to the crosslinker in those samples.

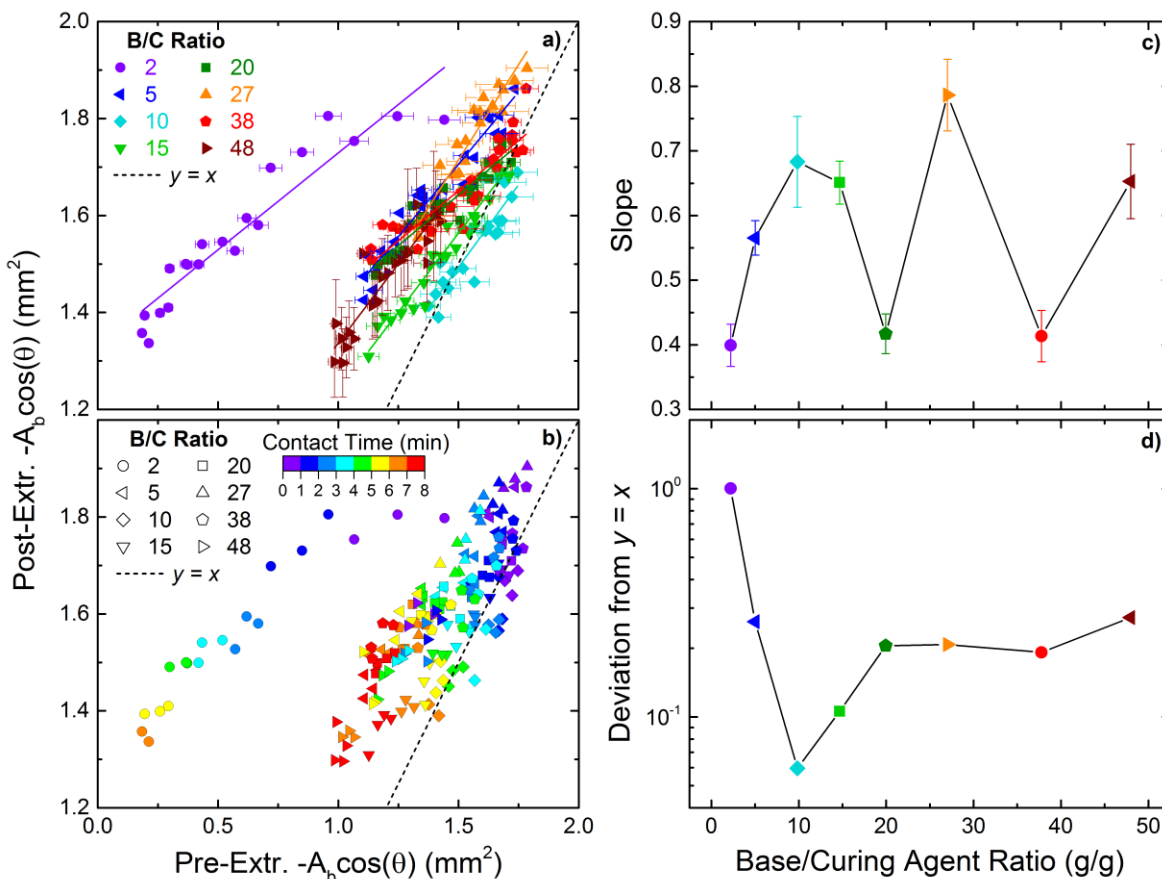


Figure 5.27 – In plots a) and b), the post-extraction value of $-A_b \cos(\theta)$ is plotted as a function of the same value for pre-extraction samples. The colors in plot a) correspond to different B/C ratios. The data are fitted with a linear best-fit line. In plot b), the colors corresponded to the amount of contact time. Generally, the amount of contact time between the water droplet and the substrate increases downward to the left. In plot c), the slope of the data sets in plot a) is given as a function of the B/C ratio. In plot d), a measure of the deviation from the $y = x$, lines in plots a) and b) is given for samples made from each B/C ratio. The equation for deviation from $y = x$ is given in plot d).

The slopes of the best fit lines in Figure 5.26a and Figure 5.27a are given as a function of stoichiometric and B/C ratio in plot c). The slopes are a measure of how quickly the system equilibrates before and after extraction. That is, for a slope of zero, a horizontal line would indicate the post-extraction system rapidly assumed an equilibrium value while it took longer

for the pre-extracted system to do so. This is the ideal case, however, which assumes a constant droplet volume. Unfortunately, the volume was decreasing slightly throughout these experiments, which would decrease the quantity of $-A_b \cos(\theta)$ regardless of the interfacial energy. Regardless, there does not appear to be a trend in the slope as a function of B/C ratio.

Instead of examining the slope (*i.e.*, rate of change post- vs. pre-extraction), we instead consider the deviation from the $y = x$ line. The equation we use for quantifying this deviation is given below where N is the number of data points.

$$\sqrt{\frac{1}{N} \sum_{t=0}^{t=8} \min[(A_b \cos \theta)_{post} - (A_b \cos \theta)_{pre}]^2} \quad (5.14)$$

The $y = x$ line indicates the quantity of interfacial energy is exactly the same at the precise contact time both before and after extraction. Stated differently, the rate of change in interfacial energy is the same both pre- and post-extraction. In such a scenario, the substrate material is likely nearly identical both pre- and post-extraction. This quantity is subtly different from the more commonly used standard deviation, which measures the deviation from the mean of a sample. Instead, here we are determining the deviation of the post-extraction data from the pre-extraction data. In Figure 5.26d and Figure 5.27d, we see that the deviation from $y = x$ is lowest at the optimal stoichiometric ratio of 3 and the prescribed B/C = 10 ratio. This indicates that the optimal crosslinking stoichiometry results in the least amount of change in this term that is a measure of the interfacial energy between water and PDMS that arises due to the extraction process. In other words, at $r = 3$ and B/C = 10, two factors are at play. The *amount* of extracted material is minimized, and the *type* of extracted material is uniform (seemingly equal parts crosslinker and PDMS), which results in the smallest amount of change in interfacial energy for water-PDMS due to extraction. This measure more accurately identifies the minimal change caused by the extraction process as opposed to looking at changes in $-\cos(\theta)$ pre- and post-extraction as a function of sol fraction, which is a measure only of the amount of material removed, not the type of material. We examined this relationship in Figure 5.17 and found that two different Sylgard formulations can exhibit the same sol fraction but dramatically different changes in base area and $-\cos(\theta)$.

Summary of Wetting & Stoichiometry Relationships

In summary, our discussion of PDMS surfaces has not been limited to a mere surface discussion. Instead, we dove deep into the underlying mechanisms at work at a dynamic water-PDMS interface. We have exhaustively investigated the relationships between the dynamic water wettability on PDMS substrates with respect to droplet shape and amount of contact time between water and PDMS. The commercial Sylgard 184 material was compared to the 28 kDa model PDMS system (data for other molecular weights are given in the Appendix). We first demonstrated the inverse relationship between $-\cos(\theta)$ and the interfacial area (*i.e.*, base area) between the water drop and the PDMS substrate in Figure 5.10 and Figure 5.11. The former parameter was found to decrease while the latter increased as a function of contact time. The post-extracted and pre-extracted water contact angles, θ , were then plotted against each other to observe how the extraction process changes the dynamic behavior of water on a PDMS substrate (*cf.* Figure 5.12 and Figure 5.13). In both Sylgard 184 and model PDMS systems, regardless of molecular weight, the smallest deviations between post- and pre-extracted water contact angles occurred at optimal stoichiometry.

Next, we showed that the two parameters of $-\cos(\theta)$ and A_b correlated well when probing the differences between their initial and final values as a function of crosslinking stoichiometry and sol fraction (*cf.* Figure 5.16 and Figure 5.17). The differences were minimized at optimal stoichiometry and for low sol fractions, except in the scenarios where materials were prepared using massive amounts of excess crosslinker. Even with relatively low sol fractions, those samples exhibited significant changes between the initial and final values. We then validated the correlation between these two parameters directly in Figure 5.18 and Figure 5.19. We showed, however, that model PDMS behaves differently than Sylgard 184 with respect to changes in $-\cos(\theta)$ and A_b in Figure 5.20 and Figure 5.21. In addition to initial and final values, we provided the relationship between $-\cos(\theta)$ and A_b at each time-sample interval throughout the experiments in Figure 5.23.

Lastly, we investigated the product of these two parameters, $-A_b\cos(\theta)$, to yield a variable that represents a measure of the total interfacial energy that exists between the base of

the water droplet and the PDMS substrate in terms of the surface tension of water. This variable was shown to decrease faster as a function of contact time in the systems prior to extraction compared to after extraction. This means that post-extraction samples lack the mobile chains and crosslinkers that migrate to the interface and contribute to the decrease in interfacial energy as the system approaches equilibrium. The $r = 3$ and $B/C = 10$ samples had the lowest deviation in this interfacial energy term when comparing pre- and post-extraction samples.

Now, we move on to a different type of analysis and demonstrate a brief example of how we can use this knowledge to design PDMS materials with controlled wetting dynamics. First, we will briefly discuss the relationships between wetting properties and dynamic mechanical properties discussed in Chapter 4 of this dissertation.

Wetting & Mechanical Properties

The previous discussion focused on relating dynamic water wettability to crosslinking chemistry, sol fraction, and the interfacial area between water and PDMS. We demonstrated the significance of how wetting on PDMS materials changes before and after they undergo Soxhlet extraction to remove unbound material. We now turn our attention briefly to the relationships between dynamic mechanical properties and dynamic water wetting on PDMS. In Figure 5.28, the difference in $\cos(\theta)$ for pre-extracted (blue squares) and post-extracted (red circles) samples as a function of contact time (*i.e.*, $\cos(\theta_{\text{Final}}) - \cos(\theta_{\text{Initial}})$), where *Final* and *Initial* refer to the contact time between the water droplet and PDMS substrate, is plotted as a function of the percent change in mechanical properties due to extraction. The percent change in mechanical properties due to extraction is defined as $(M_{\text{Post}} - M_{\text{Pre}})/M_{\text{Pre}}$ where M is a mechanical property. These data are only available for Sylgard 184 materials since mechanical properties on model PDMS were not acquired prior to extraction.

This may seem like a peculiar combination of parameters to plot. The reason for doing so is the following. The $\Delta\cos(\theta_{\text{Pre}})$ term, with respect to contact time for the pre-extraction samples, demonstrates the role uncrosslinked material is playing in the surface wetting dynamics. That is, before extraction, all of the material that is going to be part of the sol

fraction is still present and interacts with the water droplet to minimize the free energy of the system, resulting in lower interfacial energies as a function of contact time compared to post-extraction samples (*cf.* Figure 5.25). Thus, $\Delta\cos(\theta_{\text{Pre}})$ provides a measure of the relative contribution of uncrosslinked material to the dynamic wetting properties. The contribution of

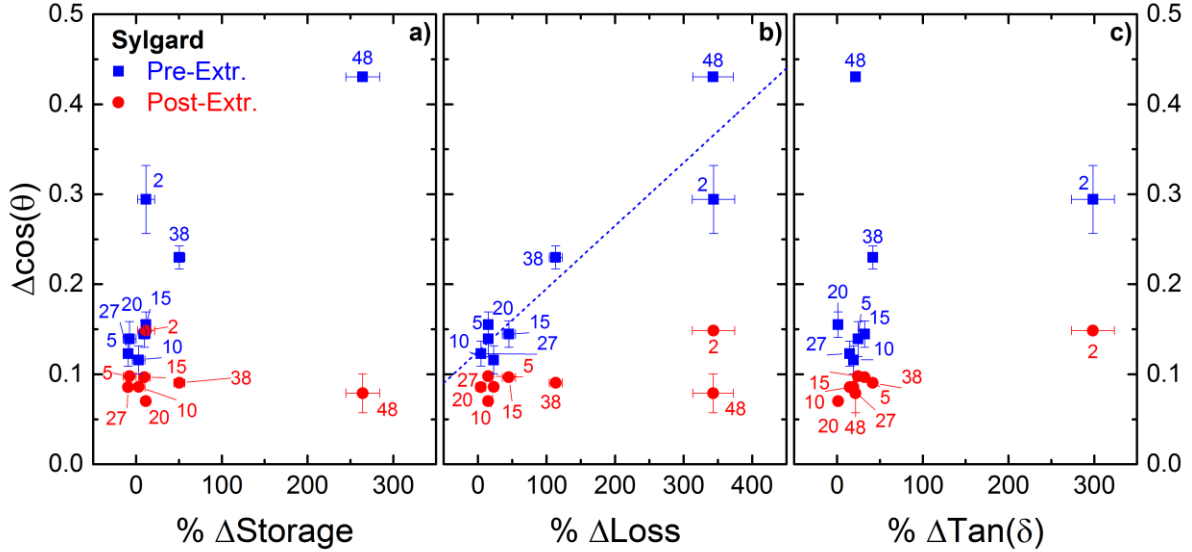


Figure 5.28 – Change in $\cos(\theta)$ for the pre-extracted (blue squares) and post-extracted (red circles) Sylgard 184 data with respect to contact time between water droplet and the substrate ($\cos(\theta_{\text{Initial}}) - \cos(\theta_{\text{Final}})$) is plotted as a function of the percent change in dynamic mechanical properties resulting from the extraction process. The percent change is defined as $(M_{\text{Post}} - M_{\text{Pre}})/M_{\text{Pre}}$, where M is a dynamic mechanical property evaluated at an angular frequency of $\omega = 1$ rad/s. Plot a) shows the change in storage modulus, E' , plot b) gives the change in the loss modulus, E'' and plot c) gives the change in $\tan(\delta)$. The linear best-fit-line has the form $y = 0.07x + 0.125$ with an R^2 value of 0.85. Labels are B/C ratios.

sol material would not be evident using $\Delta\cos(\theta_{\text{Post}})$ because all of the uncrosslinked material has already been removed and hence, cannot interact with the water droplet. As shown in Figure 5.28, the post-extraction data (red circles) demonstrate very little to none dependence on mechanical properties and the quantities themselves are close to zero. This means that the PDMS-water interface changes very little after extraction, and the change in mechanical properties due to extraction does not account for this lack of change.

A similar measure of the contribution of sol material on mechanical properties is given by the % ΔM term. Again, before extraction, the uncrosslinked material is still present and can contribute to the observed mechanical performance of the material, yielding a specific value

of M_{Pre} . After extraction, the sol material is no longer present, and the M_{Post} value reveals how the material behaves without the sol fraction present. To gauge the contribution of sol material, the difference between the two terms is normalized by the term associated with the starting material, revealing the relative contribution of sol material to the mechanical properties.

The pre-extraction $\Delta\cos(\theta)$ values (blue squares) display greater variations than the post-extraction $\Delta\cos(\theta)$ values (red circles) do in Figure 5.28. Additionally, the pre-extraction values do not seem to exhibit any strong dependence on the change in storage modulus or change in $\tan(\delta)$. There seems to be a non-linear relationship to the storage modulus, but the only strong linear relationship that manifests itself is that between the change in $\cos(\theta)$ for pre-extraction samples and the change in the loss modulus, E'' given is $\Delta\cos(\theta_{\text{Pre}})$ vs. $\% \Delta E''$. The linear-best-fit line reveals a fairly strong correlation between the two terms, with an $R^2 = 0.85$. Importantly, the loss modulus is the only mechanical property to show significant changes due to extraction at both high and low B/C ratios as evident by the B/C ratios of 2 and 48 both showing $>300\%$ change in loss modulus due to extraction. This change is similar to the data in Figure 5.17c which showed large changes in $\Delta\cos(\theta)$ for B/C = 2 and 48. The loss modulus being in correlation with the spreading of a liquid droplet on the surface is consistent with the theories of such systems that show energy is dissipated by the substrate as the liquid droplet spreads on the surface until an equilibrium is reached between viscoelastic contributions from the substrate and interfacial energies.¹⁶

Wetting Ridge Height

Although the storage modulus did not exhibit a strong linear correlation with the change in $\cos(\theta)$, it is known to play another role at the PDMS-water interface. As was discussed in the introduction to this chapter, soft substrates can be deformed by the surface tension of a probing droplet. The length scale over which this deformation occurs is proportional to the elastocapillary length, γ/E , where γ is the liquid surface tension (in air) and E is Young's modulus. An approximation for the deformation of the substrate is given in Figure 5.29 where the quantity of approximate wetting ridge height is plotted as a function of storage modulus and $\sin(\theta)$. The value for approximate wetting ridge height, h_{wr} , is taken at the final contact

time where, presumably, the equilibrium contact angle has been reached. The wetting ridge height is plotted as a function of contact time for Sylgard 184 in Figure A5.28. It did not show strong dependency on contact time. The wetting ridge height for Sylgard 184 samples as a function of B/C ratio is given in Figure A5.29.

In Figure 5.29 we observe that the wetting ridge height depends much more strongly on the storage modulus as opposed to the contact angle. Most of the samples were deformed less than 1 micron, which was undetectable using the contact angle goniometer in our lab. However, this analysis illustrates the order of magnitude of surface deformations that can arise when probing the surface wetting behaviors of soft materials.

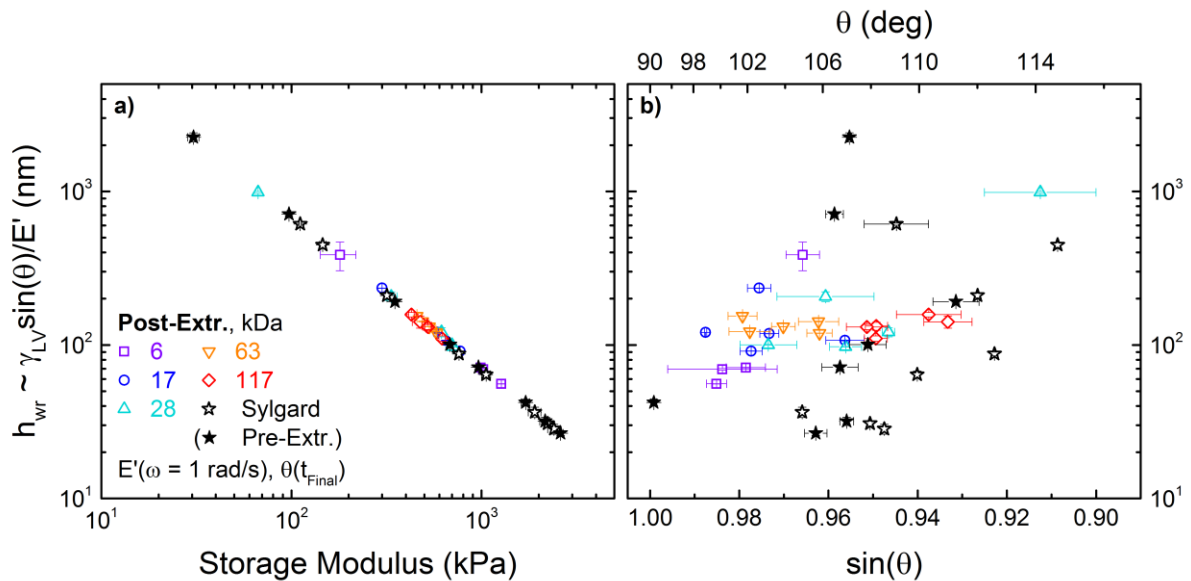


Figure 5.29 – Approximation of the wetting ridge height for pre-extraction (blue squares) and post-extraction (red circles) Sylgard 184 samples.

Silicone Oils Added to Sylgard 184 Networks

Now that we have learned about the sensitivity of the dynamic water wetting behavior on PDMS substrates to both the amount and composition of the sol fraction, we sought to control that dynamic wetting behavior. To do so, we intentionally supplied additional inert

silicone oils to act as the artificial sol fraction in fully crosslinked networks, thereby controlling both the *amount* and *type* of mobile materials present in the sol fraction. We chose 4 different silicone oils (all purchased from Gelest, Inc.) whose properties are given in Table 5.1. The first is a cyclic compound called octamethylcyclotetrasiloxane, commonly referred to as D₄. This is a common impurity in commercial silicones. Additionally, we chose a series of 3 inert linear trimethyl-terminated PDMS oils, which we denote with T_x, where x represents the oil's molecular weight. All oils have the same chemical structure as PDMS for the repeat unit, OSi(CH₃)₂. These oils were mixed in with the base and curing agent of Sylgard 184, which was prepared at the optimal B/C = 10 ratio, and then the silicone-oil infused samples were allowed to crosslink at the same conditions used for all other samples in this dissertation (*i.e.*, 2 h at room temperature followed by 24 h at 70°C). We then probed the resulting samples by dynamic water wetting experiments according to the same procedure discussed in this chapter.

Table 5.1 – Silicone Oils Added to Sylgard 184 Networks

Shorthand Name	Molecular Weight (kDa)	Viscosity (cSt)
D ₄	0.297	2.3
T1	1	10
T6	6	100
T28	28	1000

In Figure 5.30, we demonstrate the effects these oils have on the surface wetting dynamics. The D₄ cyclic, low molecular weight, and low viscosity silicone oil does not seem to cause any change to the substrate compared to pure Sylgard 184, even when up to 10% oils by mass are added. The higher molecular weight linear oils, however, demonstrate interesting surface wetting dynamics. We see that there is a lag time in the decrease in contact angle and this lag time is greater for higher molecular weight oils compared to low molecular weights. We attribute this lag time to chain mobility, which will be slower for higher molecular weight PDMS linear chains. The observed lag time in this system is similar to a recent observation of two different droplet velocities when droplets are placed on vertical slabs of silicone

elastomers. An initial slow falling regime was followed by a fast regime after the droplet had accumulated enough leached silicone oils.⁶⁷ Additional data further exploring the behavior of these oil-infused PDMS materials is provided in the end of the Appendix.

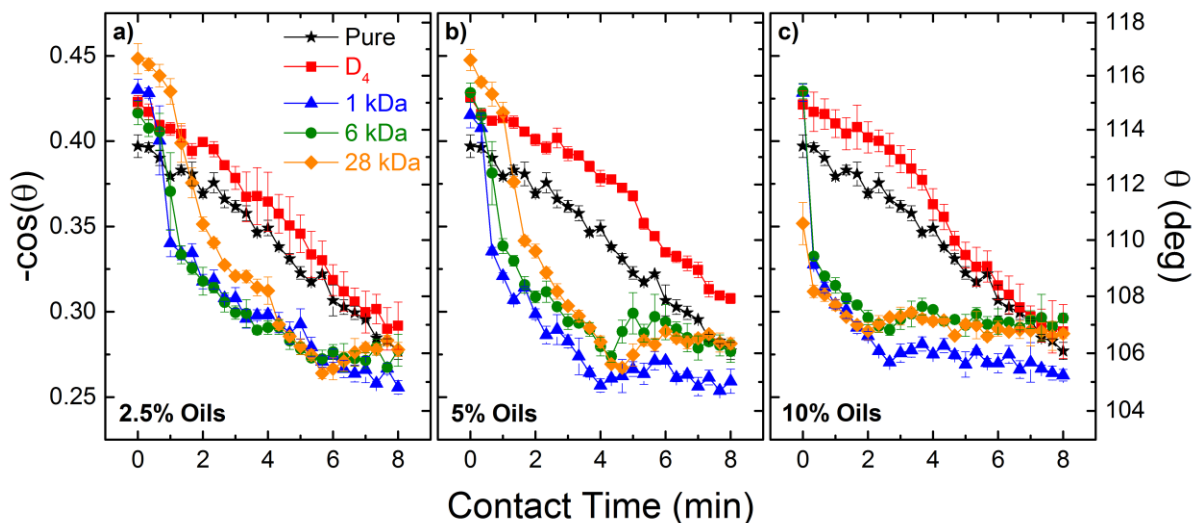


Figure 5.30 – The water contact angle, θ (right ordinates), and $\cos(\theta)$ (left ordinates) are plotted as a function of contact time between the water droplet and the silicone oil-infused Sylgard 184 PDMS substrate for 2.5, 5, and 10% oils in plots a), b), and c), respectively. Pure Sylgard 184 samples at the B/C = 10 ratio with no additional silicone oils are shown as black stars. The D_4 oil is shown as red squares, the 1 kDa oil is shown as blue triangles, the 6 kDa oil is shown as green circles, and the 28 kDa oil is shown as orange diamonds.

Conclusions

In this chapter, we presented a thorough analysis of the dynamic water droplet wetting behavior on PDMS substrates. Model PDMS was compared against the commercial Sylgard 184 material where samples prepared from many different stoichiometric conditions, with respect to the crosslinking reaction, were studied. A brief summary was already reported prior to the discussion of mechanical properties. To continue from there, we demonstrated that the loss modulus is the most significant dynamic mechanical property when it comes to predicting the dynamic wetting behavior of a water droplet on a PDMS substrate. We further demonstrated that the surface wetting dynamics can be tuned based on the properties of the soluble, uncrosslinked materials. Higher molecular weight uncrosslinked materials result in slower wetting dynamics compared to lower molecular weights. However, it seems that a

critically high molecular weight must be present in order to observe any changes in wetting dynamics whatsoever compared to the pure Sylgard 184 system. The fact that the D₄ oils do not change the wetting dynamics until very high loading (*cf.* Figure A5.30) means they are of too low molecular weight. Thus, the region between 300 – 1000 Da should be explored further to determine when this transition occurs. In addition to molecular weight, this may be related to the molecular structure of cyclic *vs.* linear, which will likely have different diffusivities through the PDMS matrix.

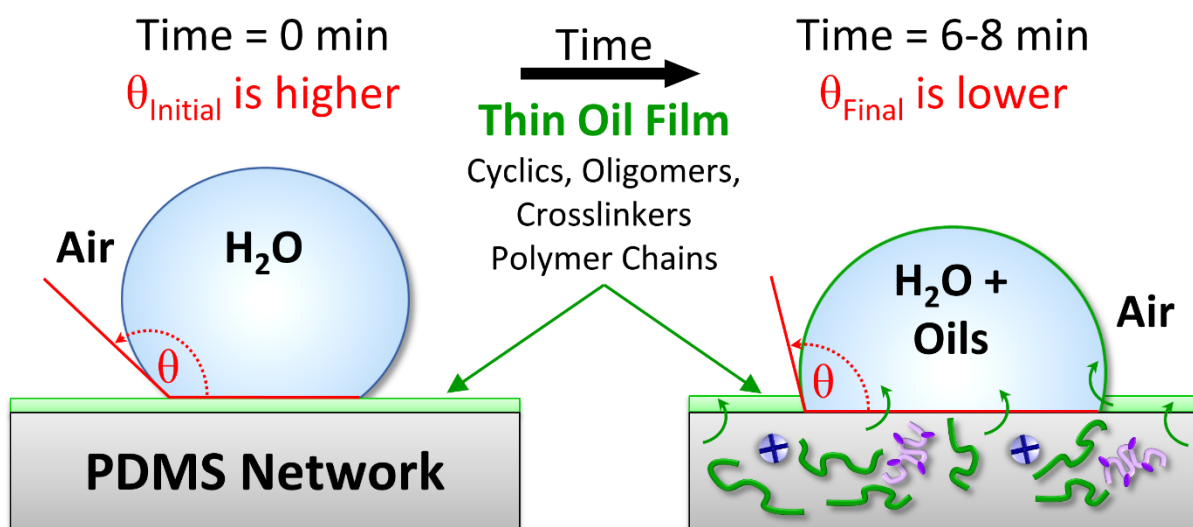


Figure 5.31 – Schematic illustration depicting the dynamic wetting behavior of water on a PDMS substrate. The droplet starts at some initially high contact angle and small base area. Over time, the drop settles into an equilibrium with a lower contact angle and greater base area. Uncrosslinked polymers, oligomers, and crosslinkers present in PDMS materials prior to extraction can migrate to the water-interface and act like a surfactant, lowering the interfacial energy. After extraction, the system approaches equilibrium much more quickly, when most of the uncrosslinked material has been removed.

The primary message of this chapter is that the PDMS-water interface is dynamic, as depicted in Figure 5.31. PDMS substrates do not consist of only perfectly crosslinked polymers. There are small molecules and free polymer chains that have mobility and will migrate to the interface to interact with a water droplet. The system takes several minutes to reach equilibrium prior to extraction, but post-extraction, the water droplet rapidly reaches a stationary base area and does not grow or shrink with time. The crosslinker molecules utilized

in commercial and model PDMS both have silicon-hydride (Si-H) chemical functionality, which is less hydrophobic than silicon-methyl groups (Si-CH₃). This results in observed contact angles lower than typical PDMS materials when excess crosslinker is used to prepare the network. This chemical effect is greater than the influence of the sol fraction alone, which is a measure of only quantity, not type, of unbound material in the network. The crosslinking stoichiometry and the sol fraction both must be taken into account when assessing the wetting behavior of a PDMS surface.

To elucidate the dynamics of the interface, we developed a measure of interfacial energy in the system by taking the product of the base area of the water droplet and the negative cosine of the contact angle. This provided insight as to how the interfacial energy of the system was changing with respect to the surface tension of water. This quantity showed more rapid decreases in the pre-extracted systems compared to the post-extracted systems, indicating that the sol fraction provides surfactant-like properties to the interface, permitting faster equilibration. When the sol fraction has been removed, there are fewer mobile molecules in the system and the interface does not change as rapidly or to the same degree compared to when the sol fraction is still present in the material.

As mentioned in the introduction to this chapter, many researchers have examined the so-called hydrophobic recovery of silicone elastomers after some form of surface treatment. Typical treatments of plasma or UV result in chain scission, making more small molecules available to interact with another phase at the interface. Such treatments are used in the fabrication of microfluidic devices and many biological investigations employ microfluidics as tools for their research. We have demonstrated clearly that the extraction process makes the interface less dynamic by removing many of the uncrosslinked species in the network. We recommend such practices for those working in environments that may be sensitive to leached siloxane molecules, such as biological studies using microfluidics. Although we did not study hydrophobic recovery or plasma treated surfaces, we demonstrated the leaching of siloxanes even without prior chain scission events. Thus, small molecule siloxanes should always be considered when designing experiments with PDMS-based materials.

The majority of the work presented was based on a simple technique using a fairly simple apparatus, *i.e.*, a contact angle goniometer. All one really needs to perform these experiments is a level surface, a syringe, and a camera capable of zooming in close to the droplet. This technique acts as facile, quick test of the static or dynamic nature of a substrate. By observing the contact angle and associated droplet parameters as a function of time in contact with the substrate, one can elucidate qualitatively the presence or lack of uncrosslinked species in the substrate network. Water, an immiscible liquid with PDMS, was able to show the effect of free molecules that have aqueous solubilities on the order of parts per billion (see Table A5.1). Therefore, the probing liquid should not be miscible with the substrate to prevent its dissolution. However, the small amounts of impurities leaching out will make their way to the interface and can be indirectly detected by monitoring the dynamic behavior of droplet on the surface.

Overall, we hope to have provided a broad community of researchers who use PDMS with the knowledge of the dynamic nature of PDMS materials. Our hope is that researchers will consider both the chemical composition, as well as the physical properties (*e.g.*, modulus) when choosing substrates for various applications and be aware of the challenges that come along with the benefits of using PDMS-based materials.

Acknowledgements

The author is grateful to several individuals for their help in producing the results and conclusions presented in this chapter. Dr. Edwin Walker was a collaborator in the beginning of this project and engaged in helpful discussions pertaining to the relationships between water wettability and crosslink density in polymer networks. Steven Zboray provided useful recommendations related to the development of the Matlab Image Analysis code. Dishit Parekh motivated and supported this project through a collaboration in which we attempted to reduce the adhesion of eutectic gallium indium (EGaIn) liquid metal to silicone elastomers. Professors Julie N. L. Albert, Michael Dickey, and Karen Daniels, all provided helpful advice and support related to the data interpretation.

Chapter 5 Appendix

Low Molecular Weight Dimethylsiloxane Oligomers

The high molecular weight (HMW), linear polymeric form of PDMS is prepared primarily by two different growth mechanisms. One is from a ring opening polymerization (ROP) reaction where small cyclic molecules act as the monomer or base unit. These cyclics typically take the form of 3-8 dimethylsiloxane (OSi[CH₃]₂) repeat units per ring molecule and are referred to in shorthand as D_x, where *x* is the number of repeat units in the ring. Thus, the smallest cyclic is D₃. Smaller cyclics have greater ring strain and are more easily polymerized. The ROP reaction can take many forms such as anionic, cationic, acid- or base-catalyzed. Anionic and cationic ROP are sensitive to humidity and must be carried out in a dry inert atmosphere such as nitrogen or argon, but these reactions run quickly at room temperature (~ 30 min) and typically result in rather monodisperse PDMS chains. They are often initiated with moisture-sensitive, pyrophoric organo-lithium species such as n-butyl lithium. On the contrary, acid- or base-catalyzed ROP reactions are insensitive to humidity, require high temperatures (~120°C) and longer durations (>2 h). These reactions use much less dangerous acid or base initiators (*e.g.*, lithium or potassium hydroxide salts, LiOH or KOH, respectively), and yield a greater molecular weight dispersity.

The other form of polymerization reaction that leads to HMW linear PDMS is a condensation reaction of LMW silanol-terminated linear dimethylsiloxane oligomers that have the form HO-[Si(CH₃)₂O]_m-OH where *m* is < 10. This reaction is acid- or base-initiated and is insensitive to moisture. In fact, water is generated during this reaction and must be removed by running at temperatures >100°C. As with typical step-growth polymerizations, high molecular weights are only achieved after very high conversions (*i.e.*, >99%), which means this reaction must be run on the order of >8 h before producing HMW PDMS. Sometimes these linear oligomers used in condensation reactions have trimethyl termini instead of silanol termini. These relatively inert trimethyl-terminated LMW linear oligomers can also be found mixed into HMW PDMS. In shorthand, they take the form of MD_yM, where *y* refers to the number of dimethylsiloxane repeat units between the two trimethylsiloxy end groups, M.

Both cyclic and linear LMW dimethylsiloxane oligomers are present after growing HMW PDMS and they are difficult to separate entirely. They are often found in both commercial silicone elastomers and home-grown PDMS. A summary of the properties of these molecules is given in Table A5.1.

Table A5.1 – Properties of low molecular weight (LMW) dimethylsiloxane oligomers. References for “C” denote cyclics and “L” denote linear.

Oligomer Type	Name	Code	Formula	CAS #	MW (g/mol)	ρ (g/mL) C(25°C) ⁶⁸ L(20°C) ⁶⁹	T _b (°C) ⁷⁰	η (cSt.) at 25°C C ⁶⁸ L ⁷¹	γ (mN/m) C(25°C) ⁶⁸ L(20°C) ⁶⁹	Aqueous Solubility ⁷²
Cyclic	Hexamethyl cyclotrisiloxane	D ₃	C ₆ H ₁₈ O ₃ Si ₃	541-05-9	222.46	1.02	136.45	T _m = 65°C	-	1.56 ± 0.03 ppm
Cyclic	Octamethyl cyclotetrasiloxane	D ₄	C ₈ H ₂₄ O ₄ Si ₄	556-67-2	296.61	0.9497	175.45	2.3	17.37	56.2 ± 2.5 ppb
Cyclic	Decamethyl cyclopentasiloxane	D ₅	C ₁₀ H ₃₀ O ₅ Si ₅	541-02-6	370.77	0.9531	210.95	3.87	17.42	17.0 ± 0.72 ppb
Cyclic	Dodecamethyl cyclohexasiloxane	D ₆	C ₁₂ H ₃₆ O ₆ Si ₆	540-97-6	444.92	0.9613	245.05	6.62	17.61	5.13 ± 0.48 ppb
Cyclic	Tetradecamethyl cycloheptasiloxane	D ₇	C ₁₄ H ₄₂ O ₇ Si ₇	107-50-6	519.07	0.9664	275.55	9.47	18.30	-
Cyclic	Hexadecamethyl cyclooctasiloxane	D ₈	C ₁₆ H ₄₈ O ₈ Si ₈	556-68-3	593.23	1.777 ⁷¹	290 ⁷¹	13.23	-	-
Linear	Hexamethyl disiloxane	MM	C ₆ H ₁₈ O ₂ Si ₂	107-46-0	162.38	0.7636	100.55	0.65	15.7	930.7 ± 33.7 ppb
Linear	Octamethyl trisiloxane	MDM	C ₈ H ₂₄ O ₂ Si ₃	107-51-7	236.53	0.8200	152.55	1.04	16.96	34.49 ± 1 ppb
Linear	Decamethyl tetrasiloxane	MD ₂ M	C ₁₀ H ₃₀ O ₃ Si ₄	141-62-8	310.69	0.8536	194.35	1.53	17.60	6.74 ± 0.8 ppb
Linear	Dodecamethyl pentasiloxane	MD ₃ M	C ₁₂ H ₃₆ O ₄ Si ₅	141-63-9	384.84	0.8755	229.95	2.06	18.10	70.41 ± 8.3 ppt
Linear	Tetradecamethyl hexasiloxane	MD ₄ M	C ₁₄ H ₄₂ O ₅ Si ₆	107-52-8	458.99	0.8910	245 ⁷¹	2.63	18.45	-
Linear	Hexadecamethyl heptasiloxane	MD ₅ M	C ₁₆ H ₄₈ O ₆ Si ₇	541-01-5	533.15	0.911	270 ⁷¹	3.24	18.60	-
Linear	Octadecamethyl octasiloxane	MD ₆ M	C ₁₈ H ₅₄ O ₇ Si ₈	556-69-4	607.03	0.913	290 ⁷¹	3.88	18.82	-
Linear	Eicosamethyl nonasiloxane	MD ₇ M	C ₂₀ H ₆₀ O ₈ Si ₉	2652-13-3	681.46	0.9173	307.5 ⁷¹	4.58	19.24	-
Linear	Hexacosamethyl dodecasiloxane	MD ₁₀ M	C ₂₆ H ₇₈ O ₁₁ Si ₁₂	2471-08-1	903.92	0.9314	-	-	19.56	-
Linear	Hexatriacontamethyl heptadecasiloxane	MD ₁₅ M	C ₃₆ H ₁₀₈ O ₁₆ Si ₁₇	18844-04-7	1274.7	0.9428	-	-	19.87	-

Glassy Benchmark Materials

We tested a variety of polymers that have much higher glass transition temperatures than PDMS. These samples should have dramatically less chain mobility and small molecule impurities. As expected, no non-linear behavior is observed with respect to the change in water contact angle and the droplet spreading. The droplets exhibit similar evaporation rates to those on PDMS samples regardless of the surface exhibiting hydrophobic or hydrophilic behavior. That is, whether the contact angle is greater than or less than 90° does not change the evaporation rate of the system. Therefore, the non-linear behavior we observe in PDMS samples is not due to evaporation.

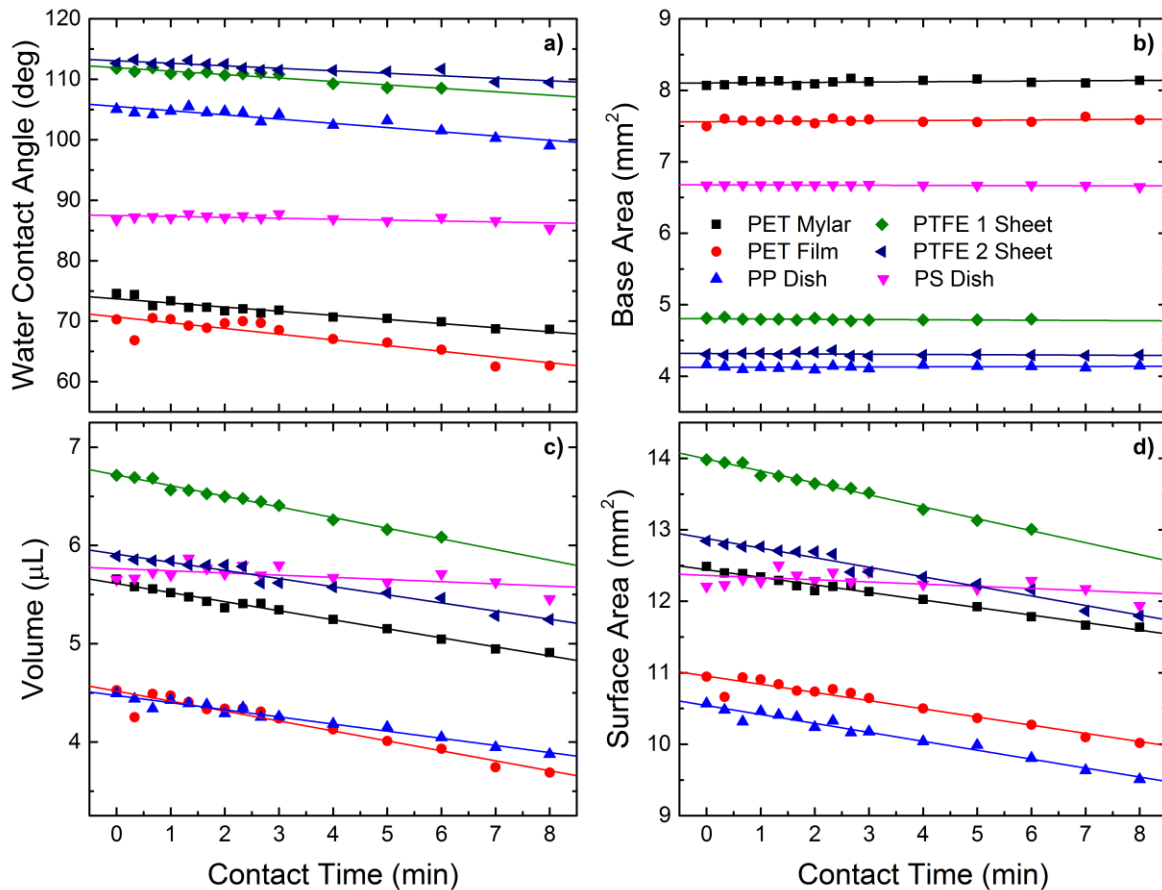


Figure A5.1 – Water contact angle, base area, volume, and surface area of water droplets on glassy polymer substrates are plotted as a function of contact time between the droplet and substrate in parts a), b), c), and d), respectively. All data are fit well with linear best-fit lines.

Model Vinyl/TDSS PDMS Data for All Molecular Weights

We performed the same analyses on all molecular weights used to prepare Vinyl/TDSS model PDMS networks that were shown for the 28 kDa system in the main body of this chapter. The following sections provide the same types of figures for each molecular weight. Overall, similar trends were observed between all molecular weights.

6 kDa Data

The following plots provide data for the 6 kDa model PDMS system.

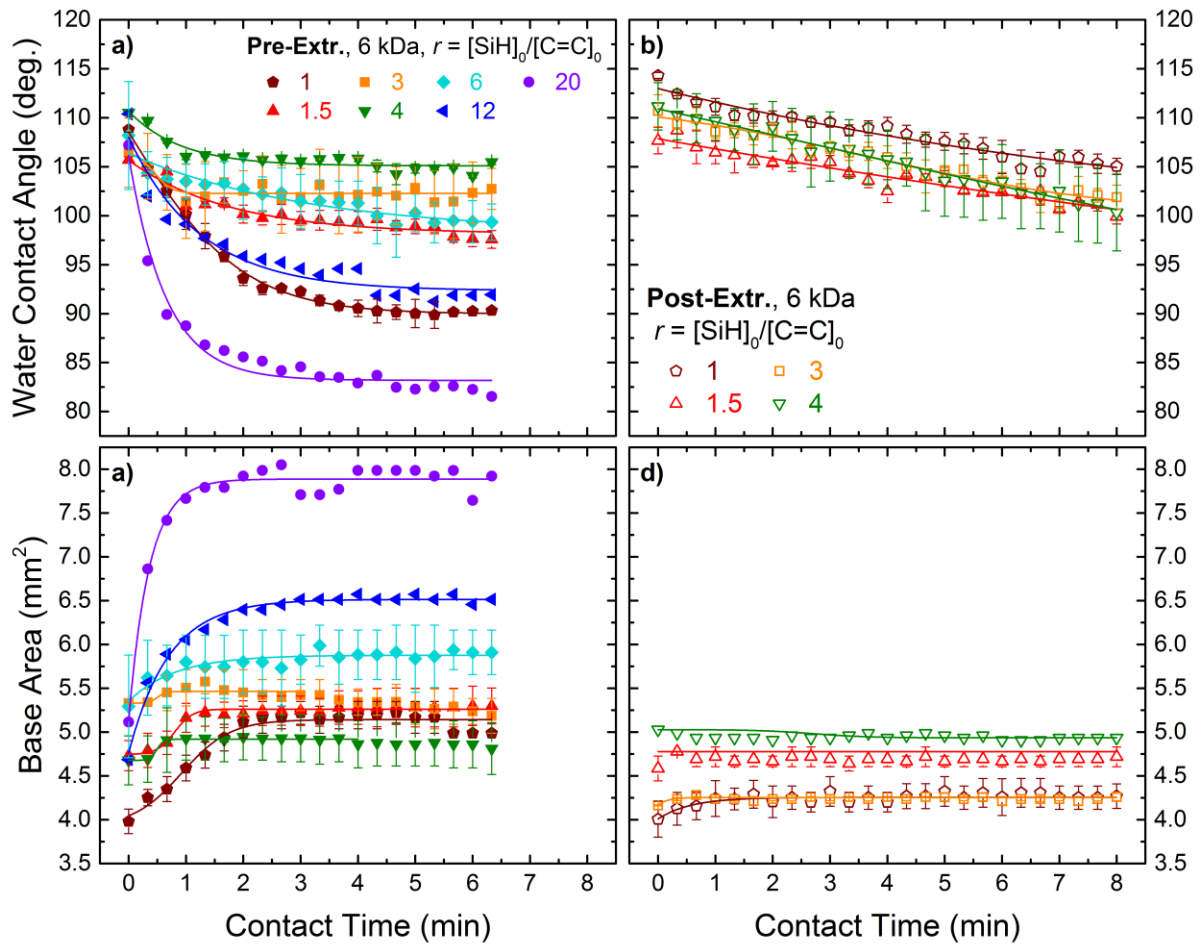


Figure A5.2 – Water contact angle, θ (top), and base area, A_b (bottom), plotted as a function of contact time, t , between water droplet and PDMS substrate pre- (left) and post-extraction (right) for the model vinyl/hydride system of 6 kDa and various stoichiometric ratios. The symbols are data while the lines are fits using the hyperbolic tangent function.

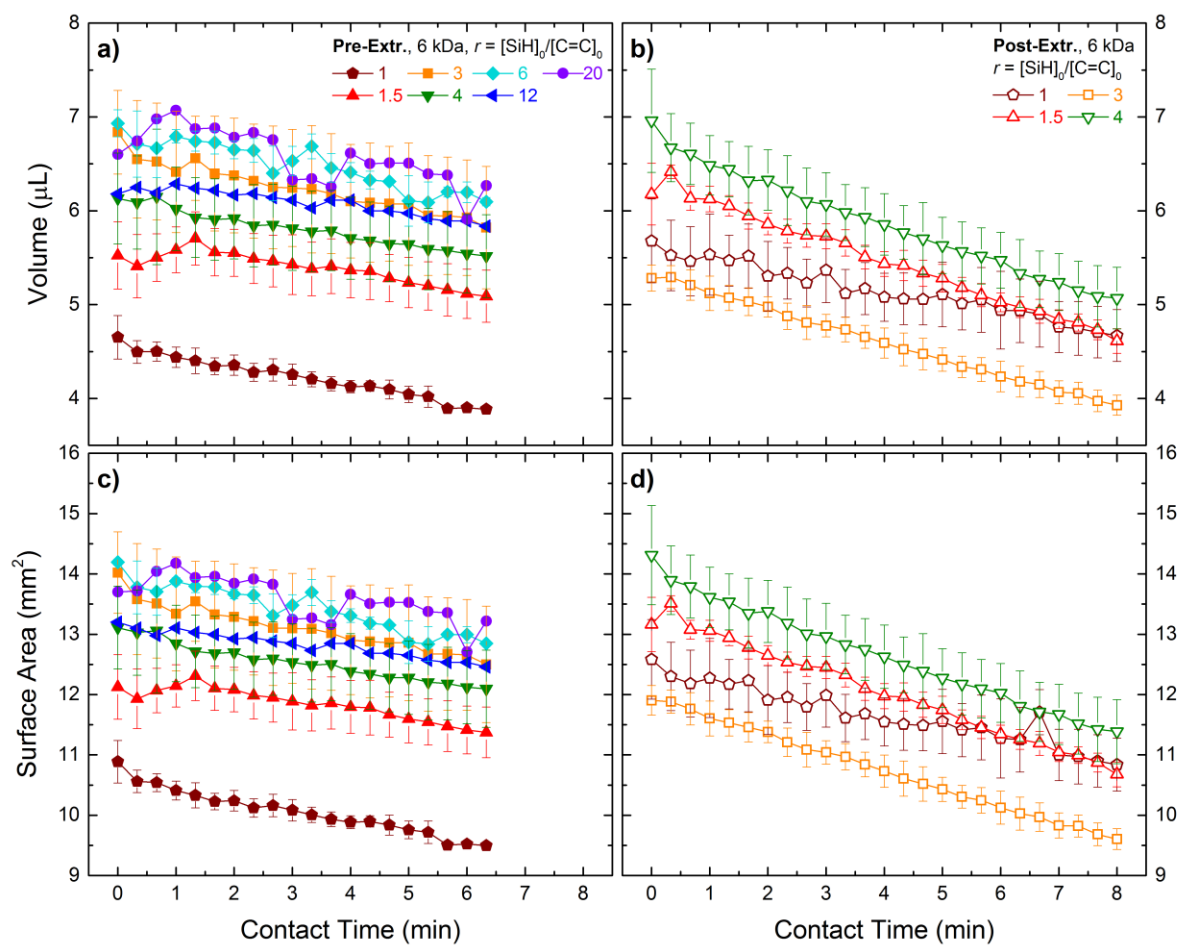


Figure A5.3 – Droplet volume (top) and surface area (bottom) plotted as a function of contact time before (left) and after (right) extraction for the 6 kDa system.

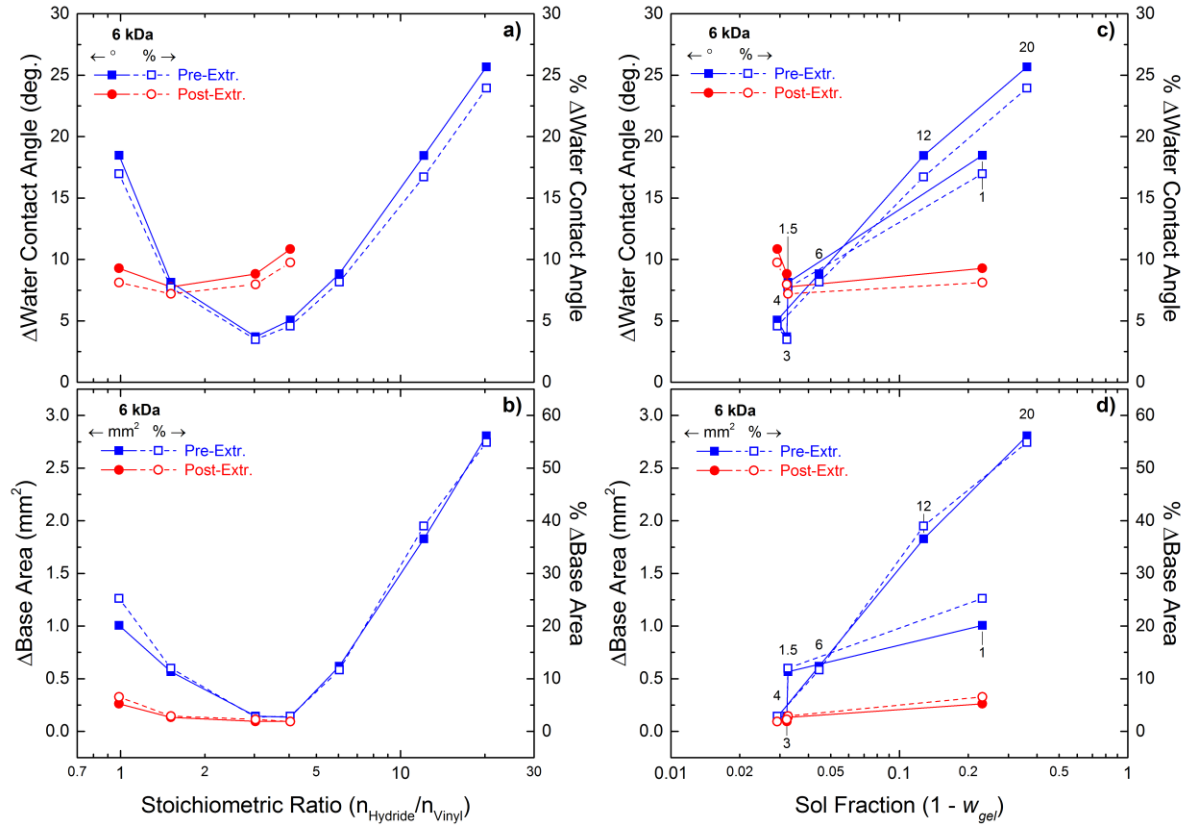


Figure A5.4 – Absolute change (left ordinate, solid lines, filled symbols) and percent change (right ordinate, dashed lines, open symbols) in contact angle (top row) and base area (bottom row) plotted as a function of stoichiometric ratio (left column) and sol fraction (right column) for the 6 kDa model PDMS system. Pre-extraction data are blue squares and post-extraction data are red circles. Numerical labels correspond to stoichiometry ratios.

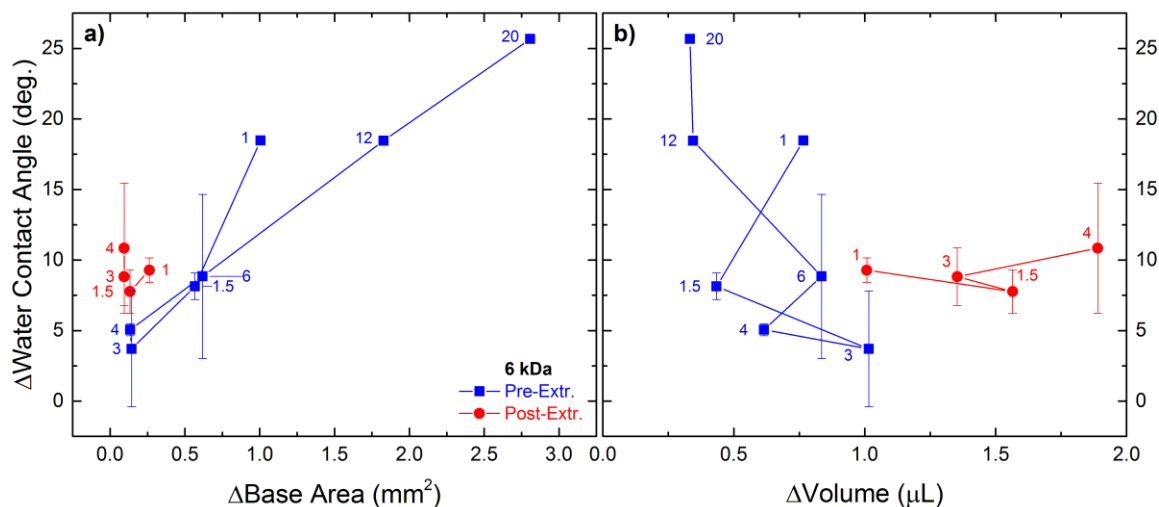


Figure A5.5 – Absolute change in contact angle plotted as a function of absolute change in base area (a) and absolute change in volume (b) for the 6 kDa model PDMS system. Pre-extraction data are blue squares and post-extraction data are red circles. The numerical labels on the data points are the stoichiometric ratio values.

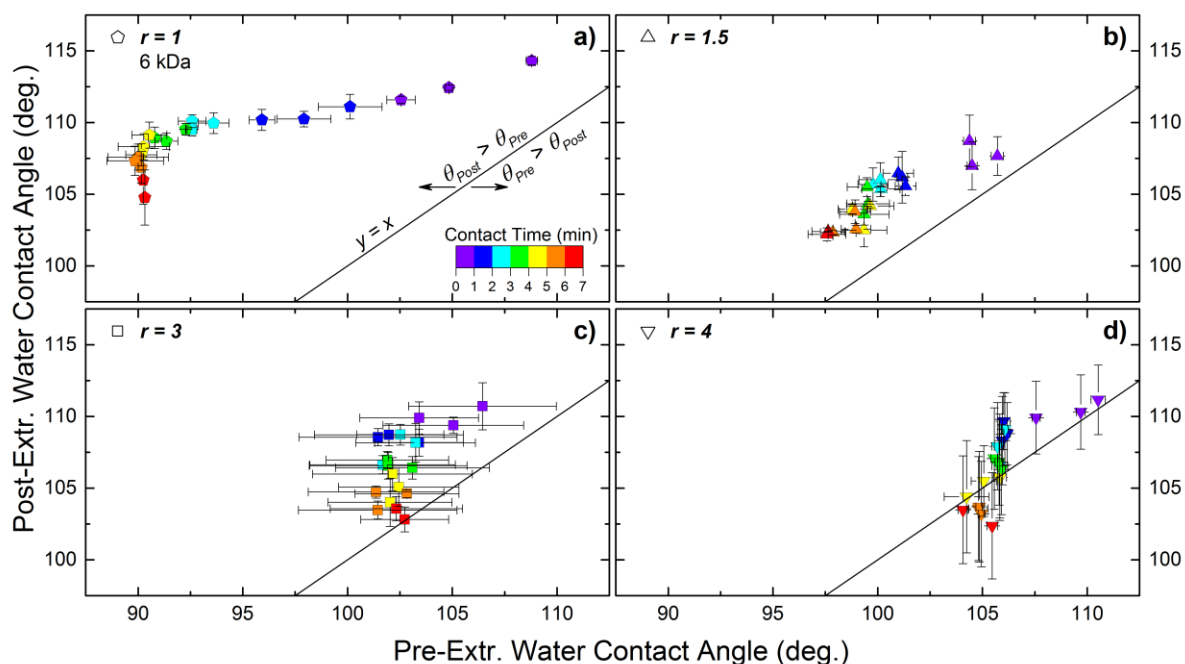


Figure A5.6 – Post-extraction contact angle plotted as a function of pre-extraction contact angle for 6 kDa model PDMS system for stoichiometric ratios of $r = 1, 1.5, 3,$ and 4 in a) through d), respectively. The diagonal solid black line represents $y = x$. Data to the left the $y = x$ line occur when post-extraction contact angle is greater than pre-extraction contact angle. The opposite occurs for data to the right of the $y = x$ line. Stoichiometric ratio values are given by different shapes according to the legend. The contact time at which each data point was acquired, both pre-extr. and post-extr. is categorized into 7 different colors according to the visible light spectrum. Short times correspond to violet symbols while long times correspond to red symbols.

17 kDa Data

The following plots provide data for the 17 kDa model PDMS system.

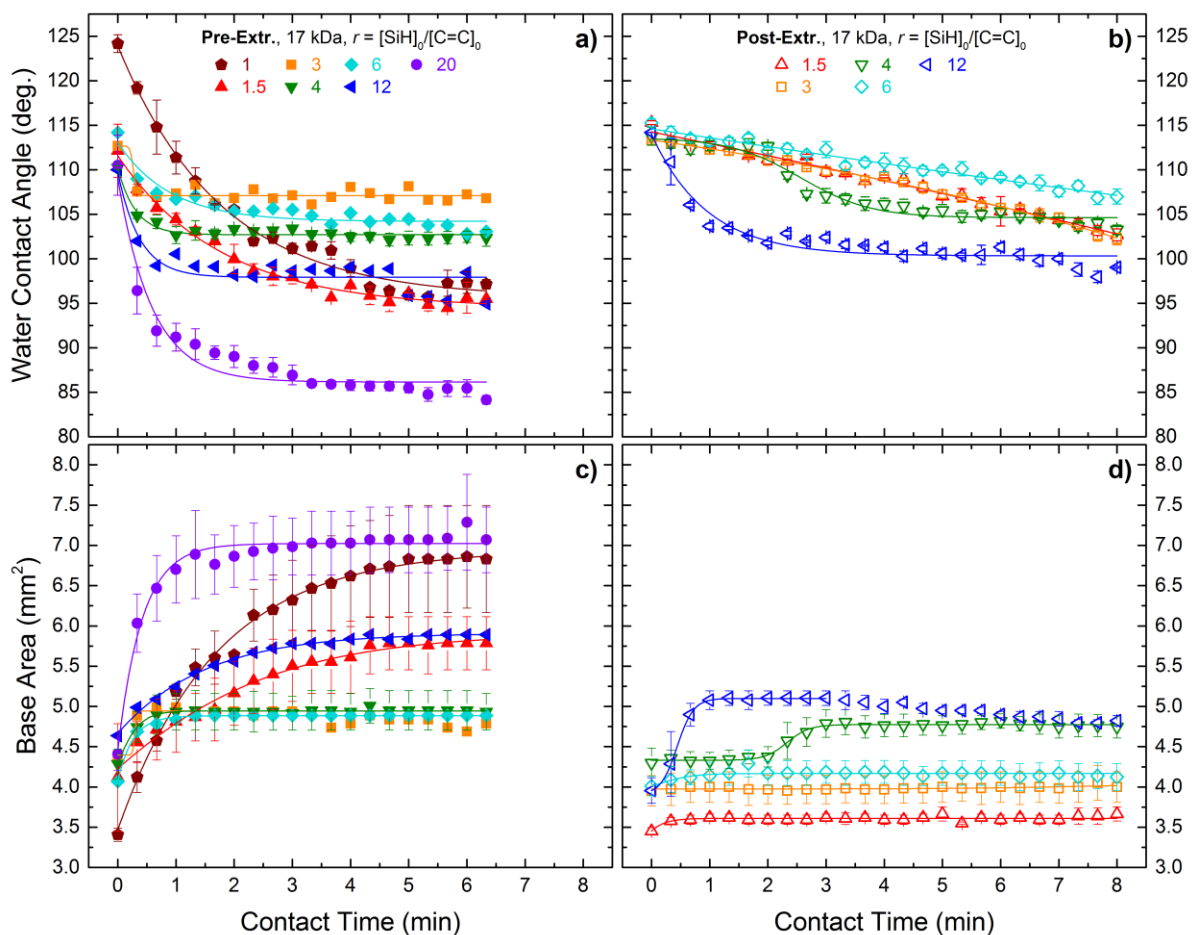


Figure A5.7 – Water contact angle, θ (top), and base area, B (bottom), plotted as a function of contact time, t , between water droplet and PDMS substrate pre- (left) and post-extraction (right) for the model vinyl/hydride system of 17 kDa and various stoichiometric ratios. The symbols are data while the lines are fits using the hyperbolic tangent function.

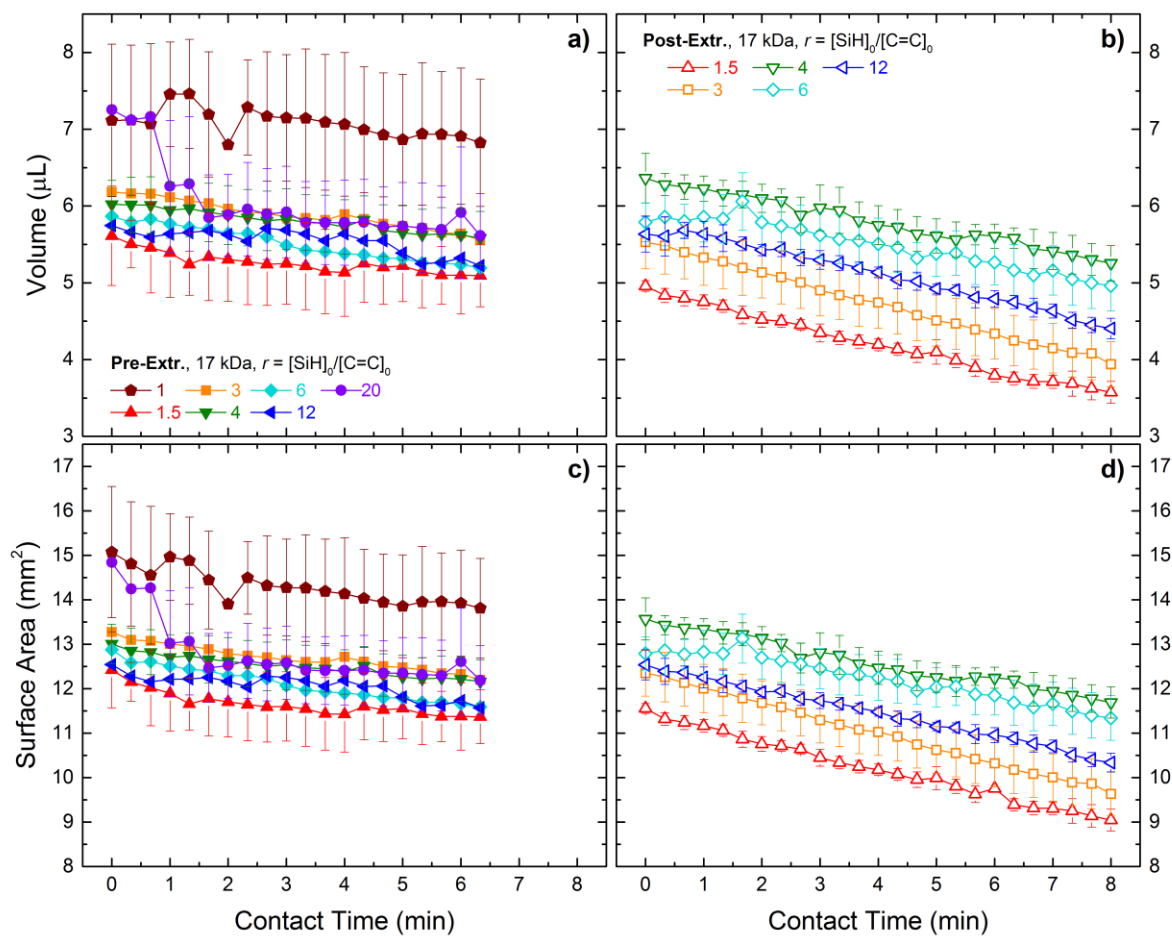


Figure A5.8 – Droplet volume (top) and surface area (bottom) plotted as a function of contact time before (left) and after (right) extraction for the 17 kDa system.

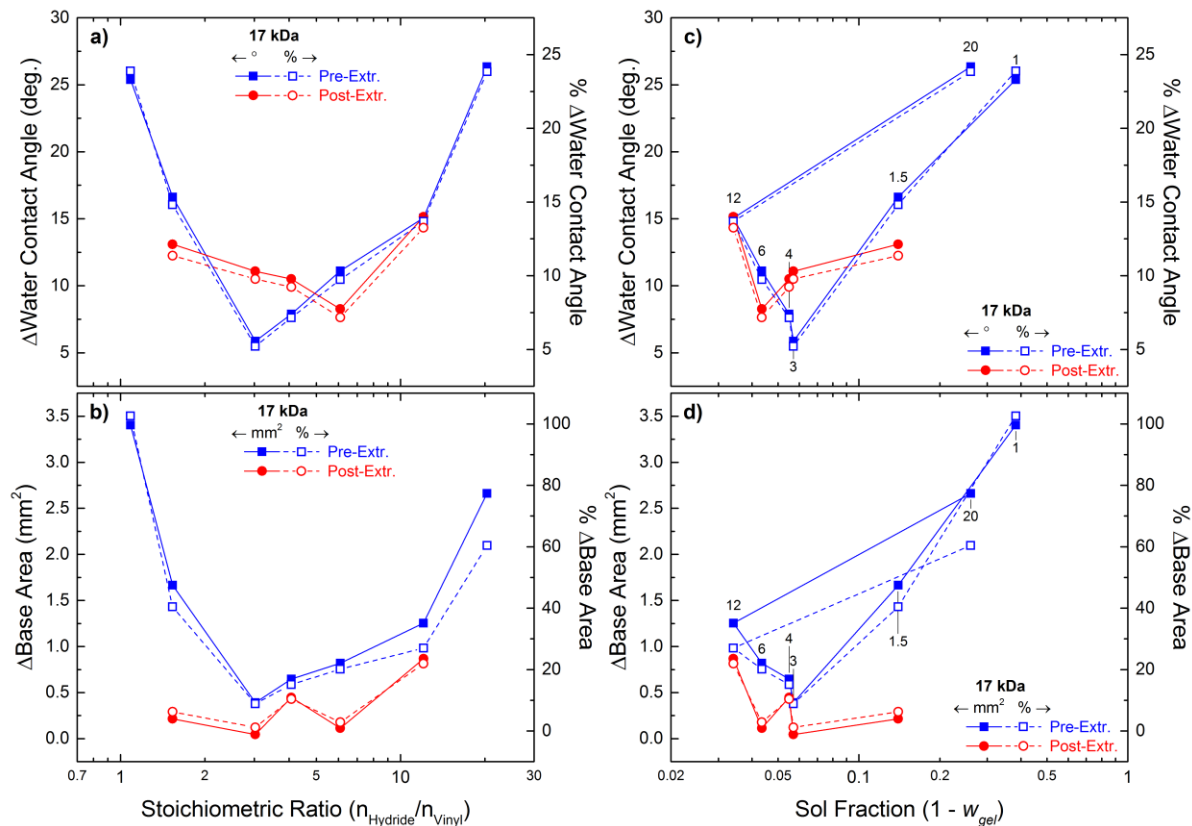


Figure A5.9 – Absolute change (left ordinate, solid lines, filled symbols) and percent change (right ordinate, dashed lines, open symbols) in contact angle (top row) and base area (bottom row) plotted as a function of stoichiometric ratio (left column) and sol fraction (right column) for the 17 kDa model PDMS system. Pre-extraction data are blue squares and post-extraction data are red circles. Numerical labels correspond to stoichiometry ratios.

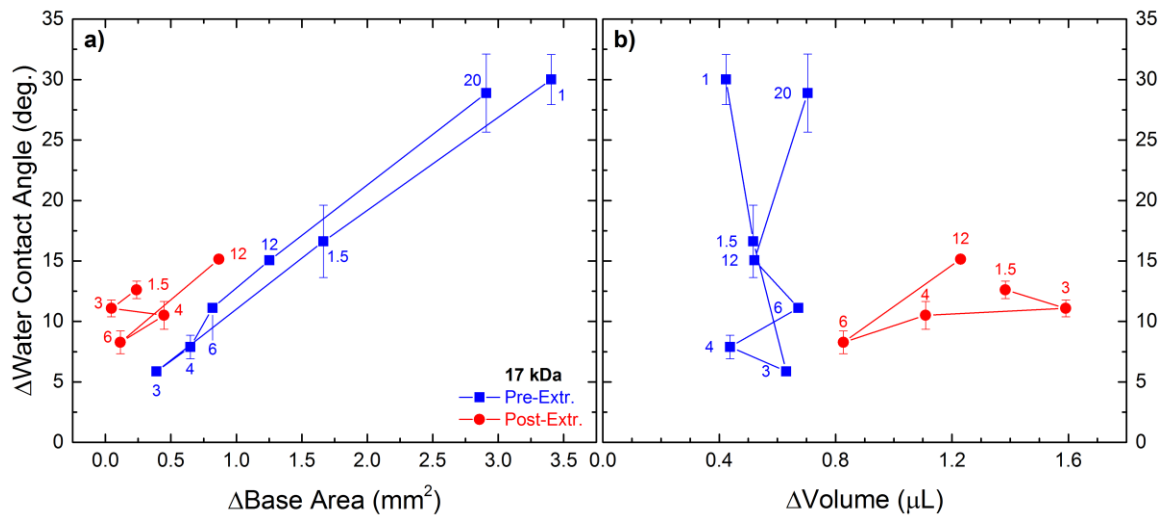


Figure A5.10 – Absolute change in contact angle plotted as a function of absolute change in base area (a) and absolute change in volume (b) for the 17 kDa model PDMS system. Pre-extraction data are blue squares and post-extraction data are red circles. The numerical labels on the data points are the stoichiometric ratio values.

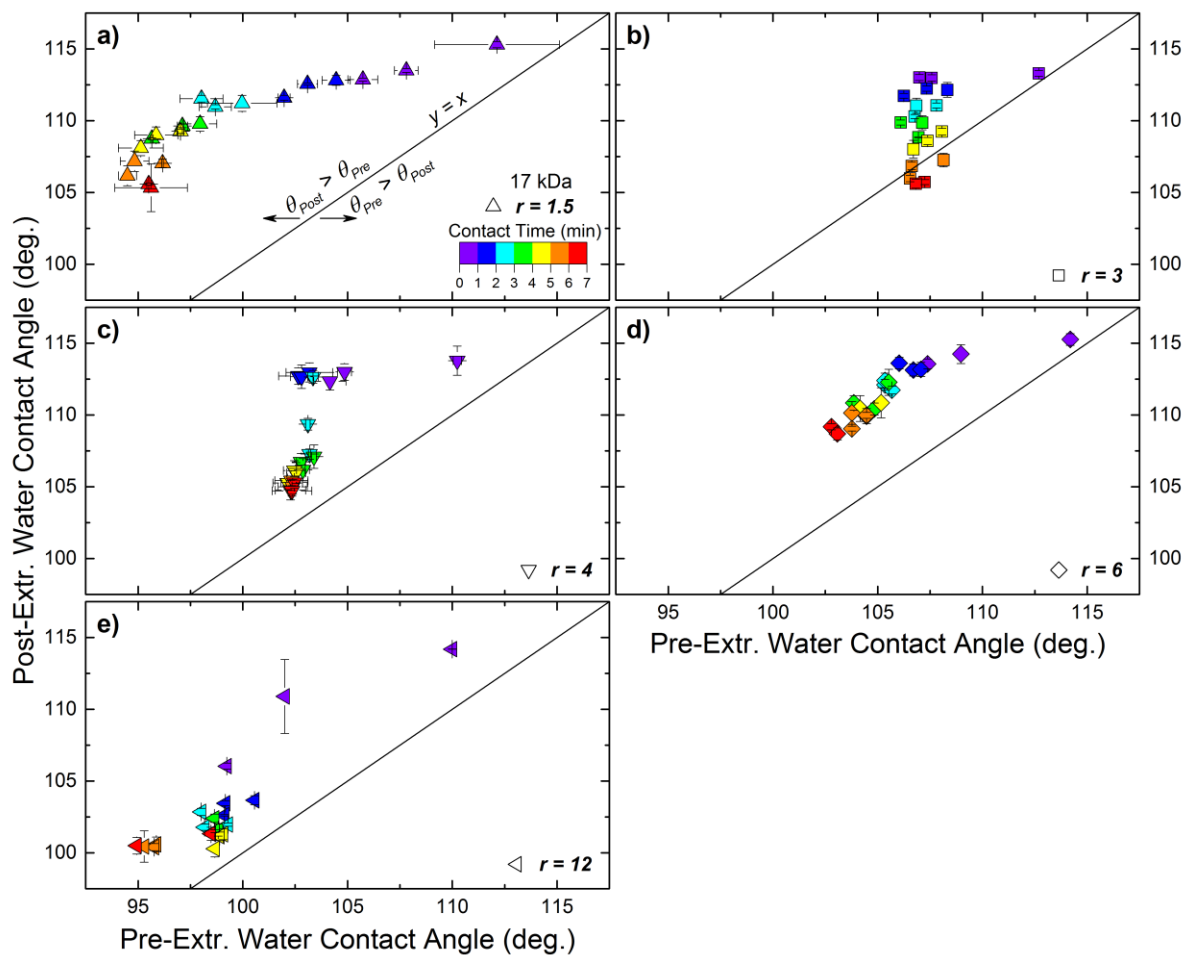


Figure A5.11 – Post-extraction contact angle plotted as a function of pre-extraction contact angle for the 17 kDa model PDMS system for stoichiometric ratios of $r = 1.5, 3, 4, 6,$ and 12 in a) through e), respectively. The diagonal solid black line represents $y = x$. Data to the left the $y = x$ line occur when post-extraction contact angle is greater than pre-extraction contact angle. The opposite occurs for data to the right of the $y = x$ line. Stoichiometric ratio values are given by different shapes according to the legend. The contact time at which each data point was acquired, both pre-extr. and post-extr. is categorized into 7 different colors according to the visible light spectrum. Short times correspond to violet symbols while long times correspond to red symbols.

28 kDa Data

The following plots provide data for the 28 kDa model PDMS system.

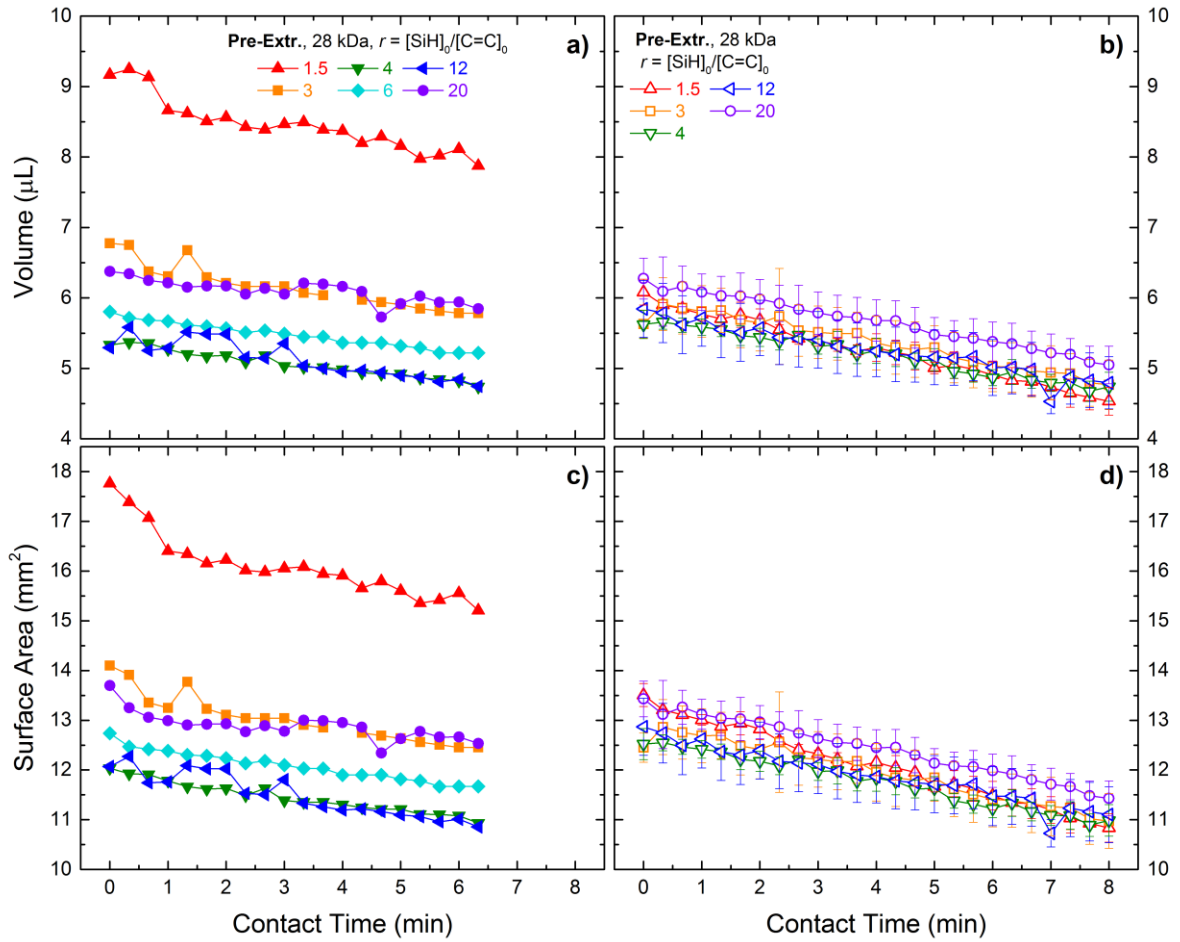


Figure A5.12 – Droplet volume (top) and surface area (bottom) plotted as a function of contact time before (left) and after (right) extraction for the 28 kDa system.

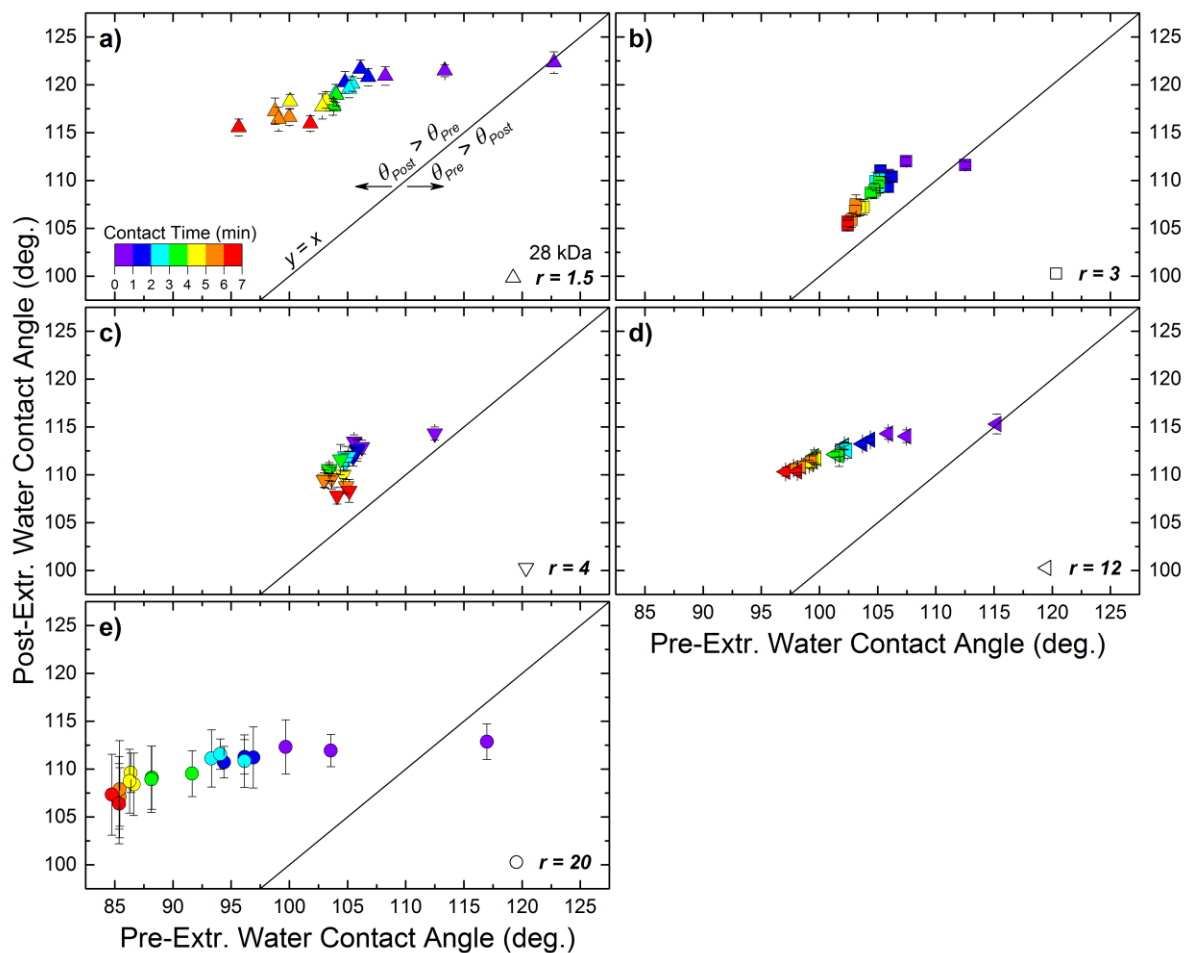


Figure A5.13 – Post-extraction contact angle plotted as a function of pre-extraction contact angle for the 28 kDa model PDMS system for stoichiometric ratios of $r = 1.5, 3, 4, 12,$ and 20 in a) through e), respectively. The diagonal solid black line represents $y = x$. Data to the left the $y = x$ line occur when post-extraction contact angle is greater than pre-extraction contact angle. The opposite occurs for data to the right of the $y = x$ line. Stoichiometric ratio values are given by different shapes according to the legend. The contact time at which each data point was acquired, both pre-extr. and post-extr. is categorized into 7 different colors according to the visible light spectrum. Short times correspond to violet symbols while long times correspond to red symbols.

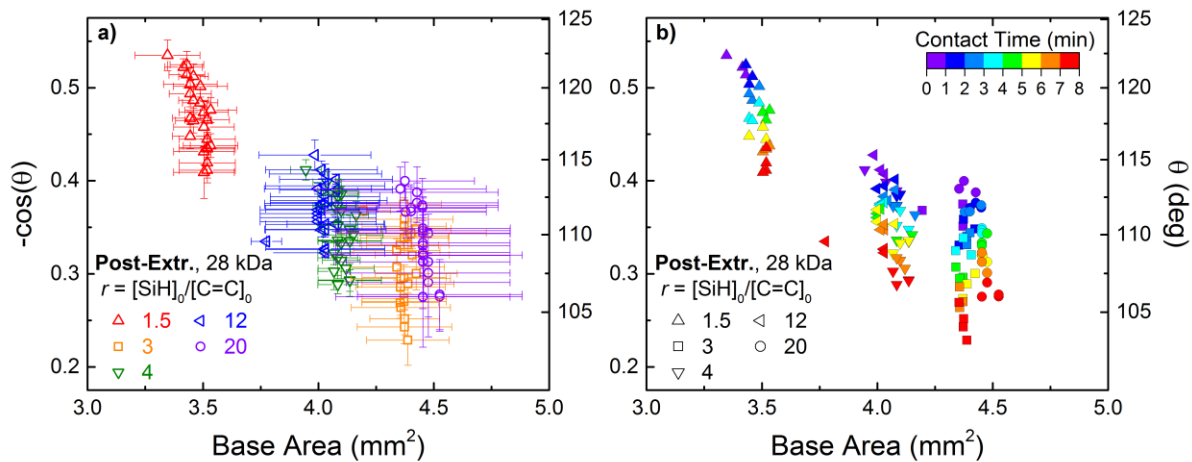


Figure A5.14 – Zoomed in plots from Figure 5.22 provide a more clear picture of the post-extracted $-\cos(\theta)$ data as a function of base area.

63 kDa Data

The following plots provide data for the 63 kDa model PDMS system.

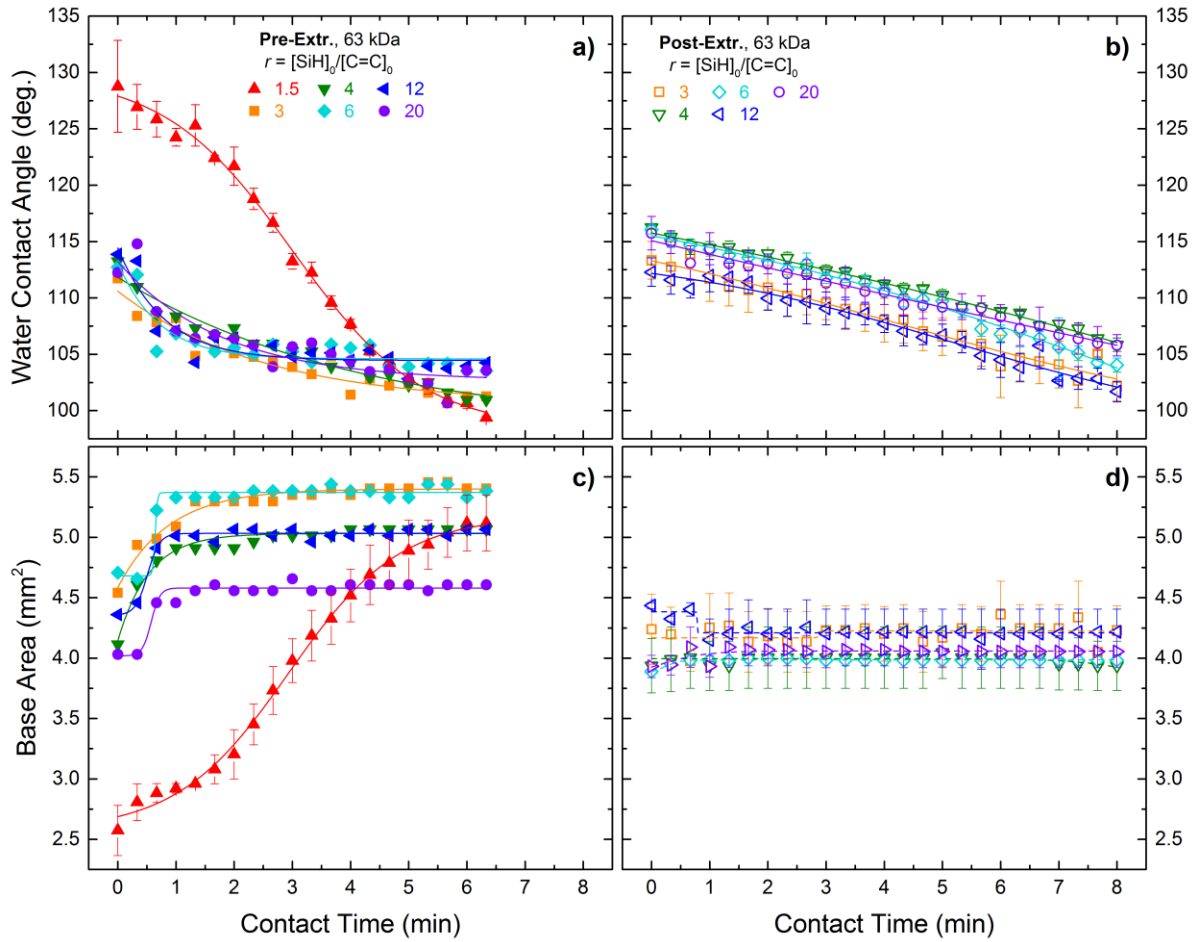


Figure A5.15 – Water contact angle, θ (top), and base area, B (bottom), plotted as a function of contact time, t , between water droplet and PDMS substrate pre- (left) and post-extraction (right) for the model vinyl/hydride system of 63 kDa and various stoichiometric ratios. The symbols are data while the lines are fits using the hyperbolic tangent function.

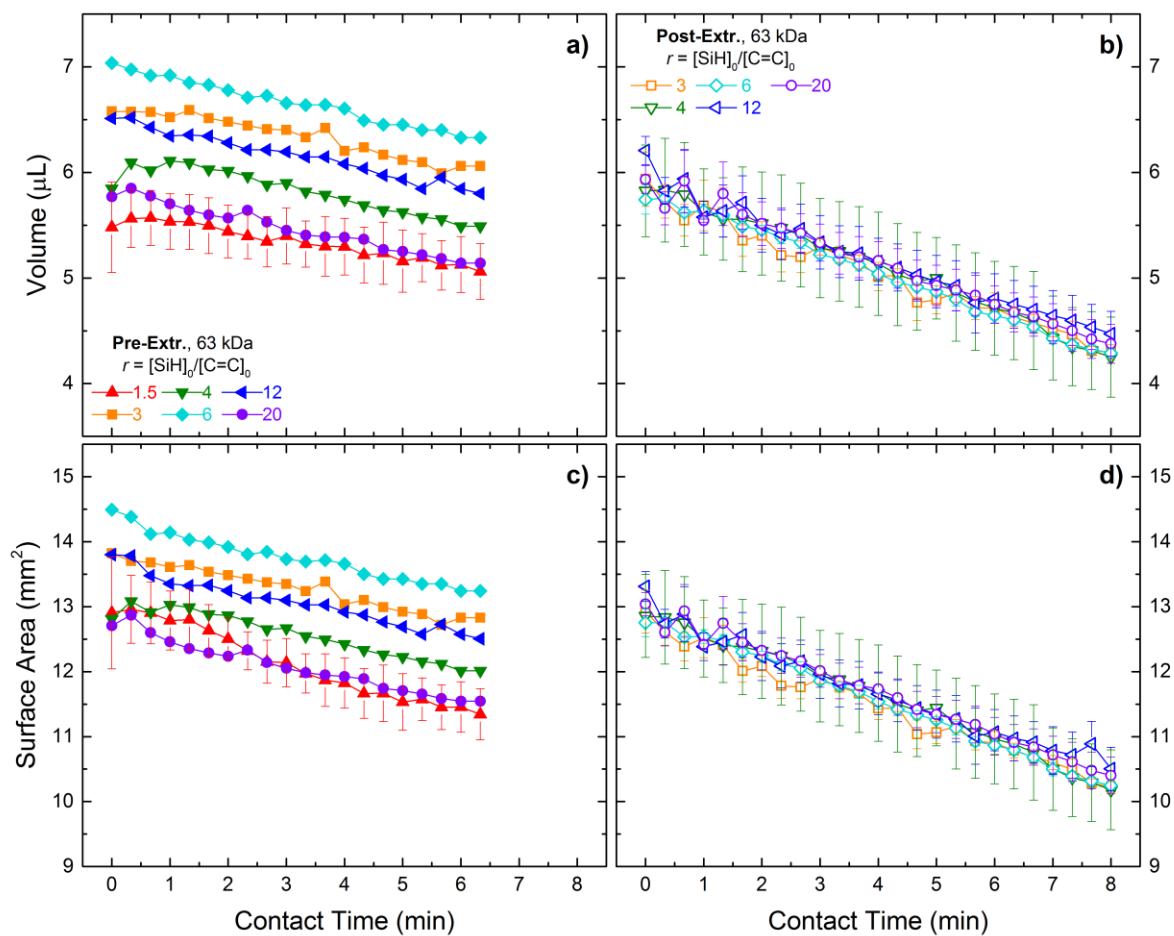


Figure A5.16 – Droplet volume (top) and surface area (bottom) plotted as a function of contact time before (left) and after (right) extraction for the 63 kDa system.

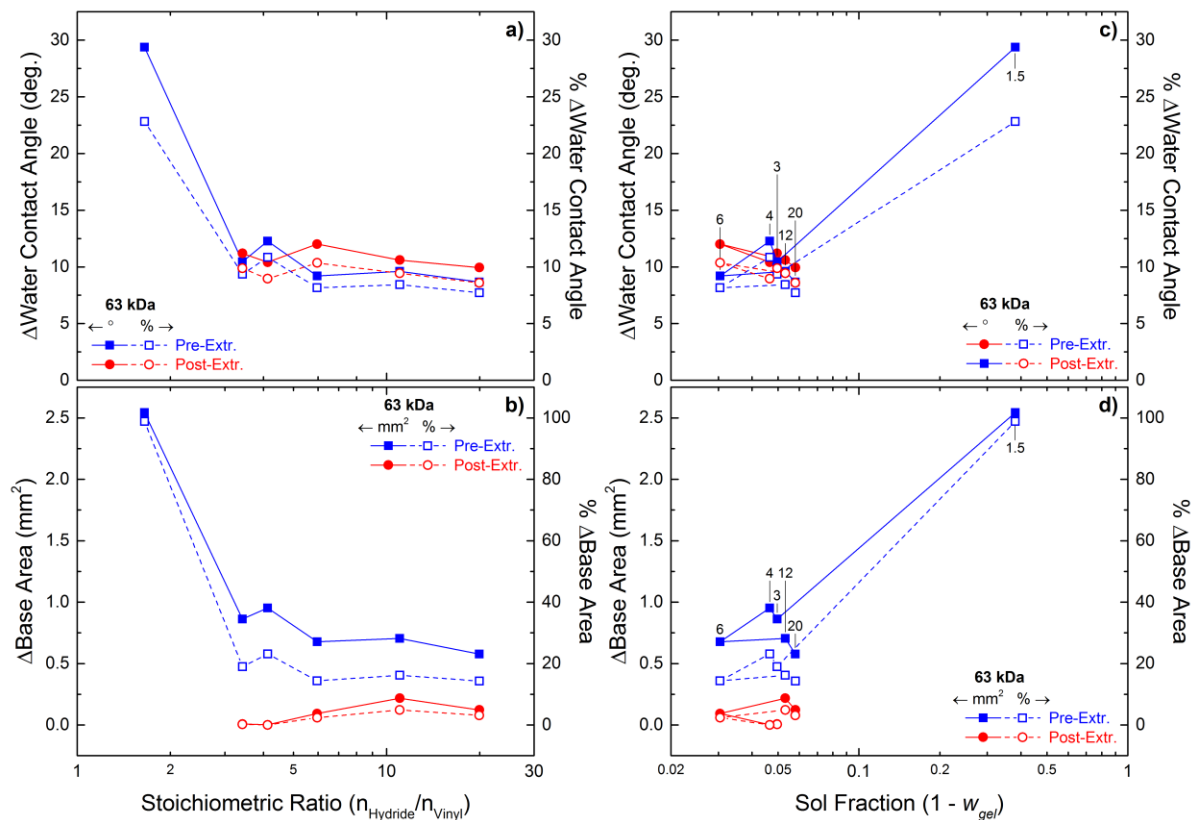


Figure A5.17 – Absolute change (left ordinate, solid lines, filled symbols) and percent change (right ordinate, dashed lines, open symbols) in contact angle (top row) and base area (bottom row) plotted as a function of stoichiometric ratio (left column) and sol fraction (right column) for the 63 kDa model PDMS system. Pre-extraction data are blue squares and post-extraction data are red circles. Numerical labels correspond to stoichiometry ratios.

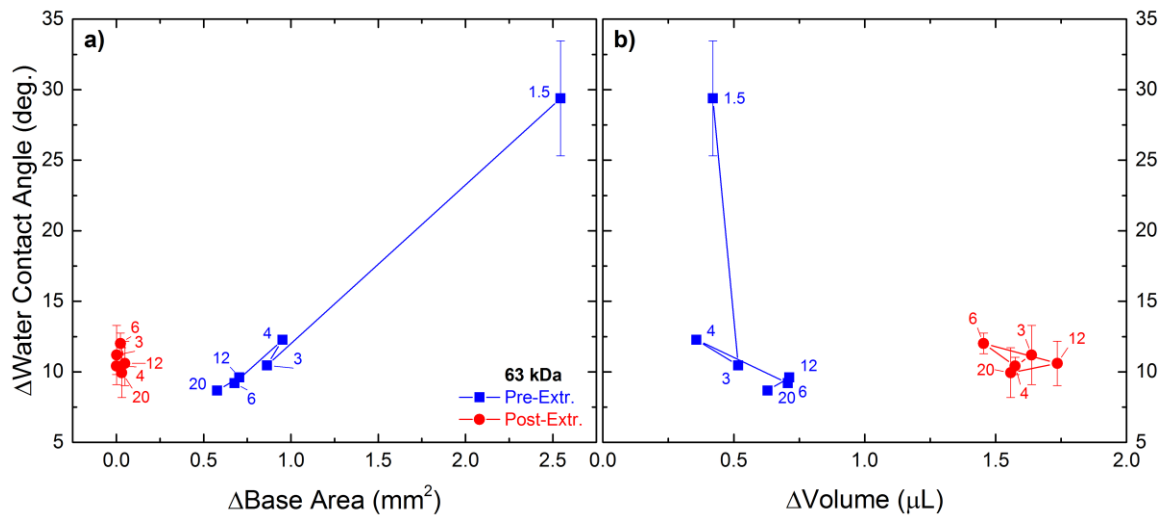


Figure A5.18 – Absolute change in contact angle plotted as a function of absolute change in base area (a) and absolute change in volume (b) for the 63 kDa model PDMS system. Pre-extraction data are blue squares and post-extraction data are red circles. The numerical labels on the data points are the stoichiometric ratio values.

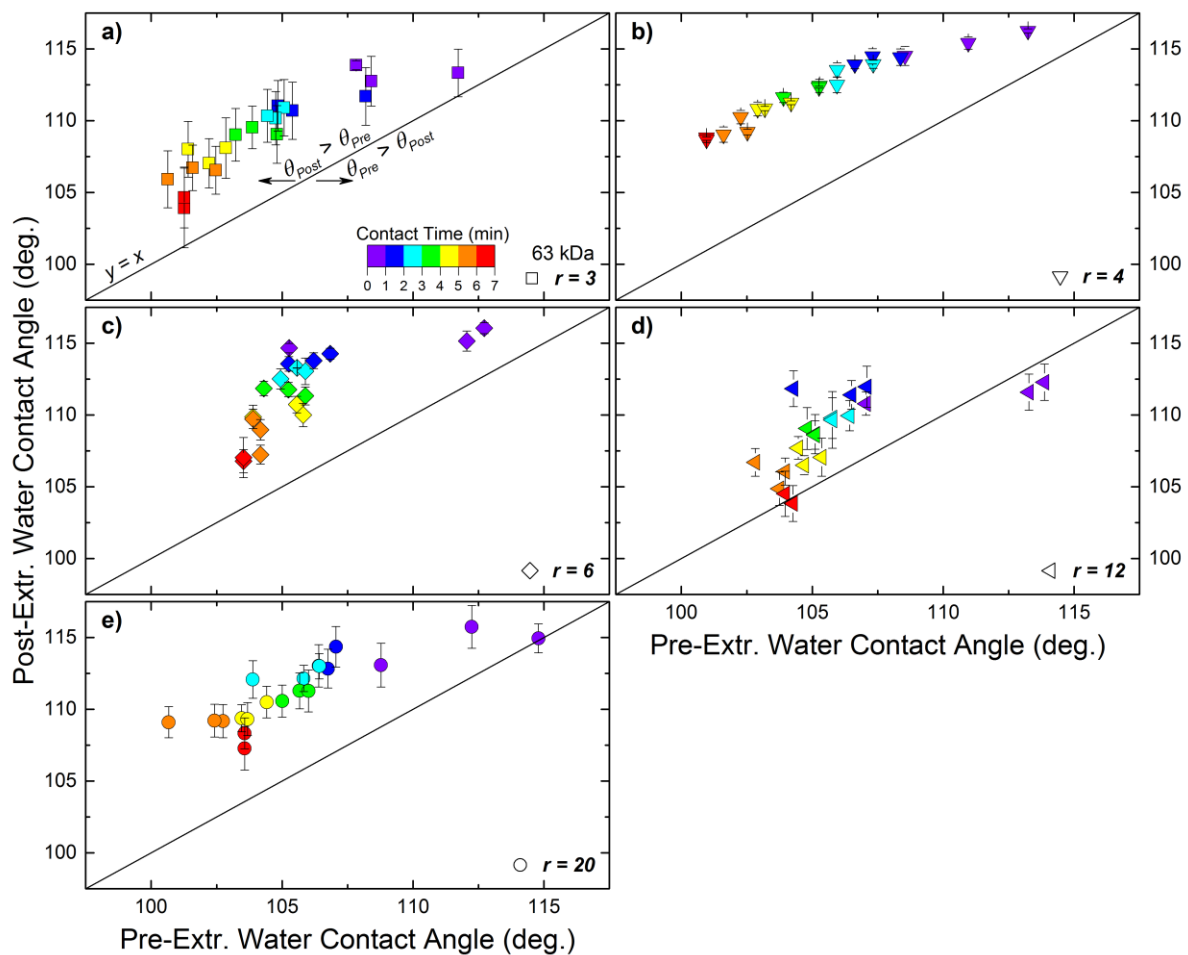


Figure A5.19 – Post-extraction contact angle plotted as a function of pre-extraction contact angle for the 63 kDa model PDMS system for stoichiometric ratios of $r = 3, 4, 6, 12,$ and 20 in a) through e), respectively. The diagonal solid black line represents $y = x$. Data to the left the $y = x$ line occur when post-extraction contact angle is greater than pre-extraction contact angle. The opposite occurs for data to the right of the $y = x$ line. Stoichiometric ratio values are given by different shapes according to the legend. The contact time at which each data point was acquired, both pre-extr. and post-extr. is categorized into 7 different colors according to the visible light spectrum. Short times correspond to violet symbols while long times correspond to red symbols.

117 kDa Data

The following plots provide data for the 117 kDa model PDMS system.

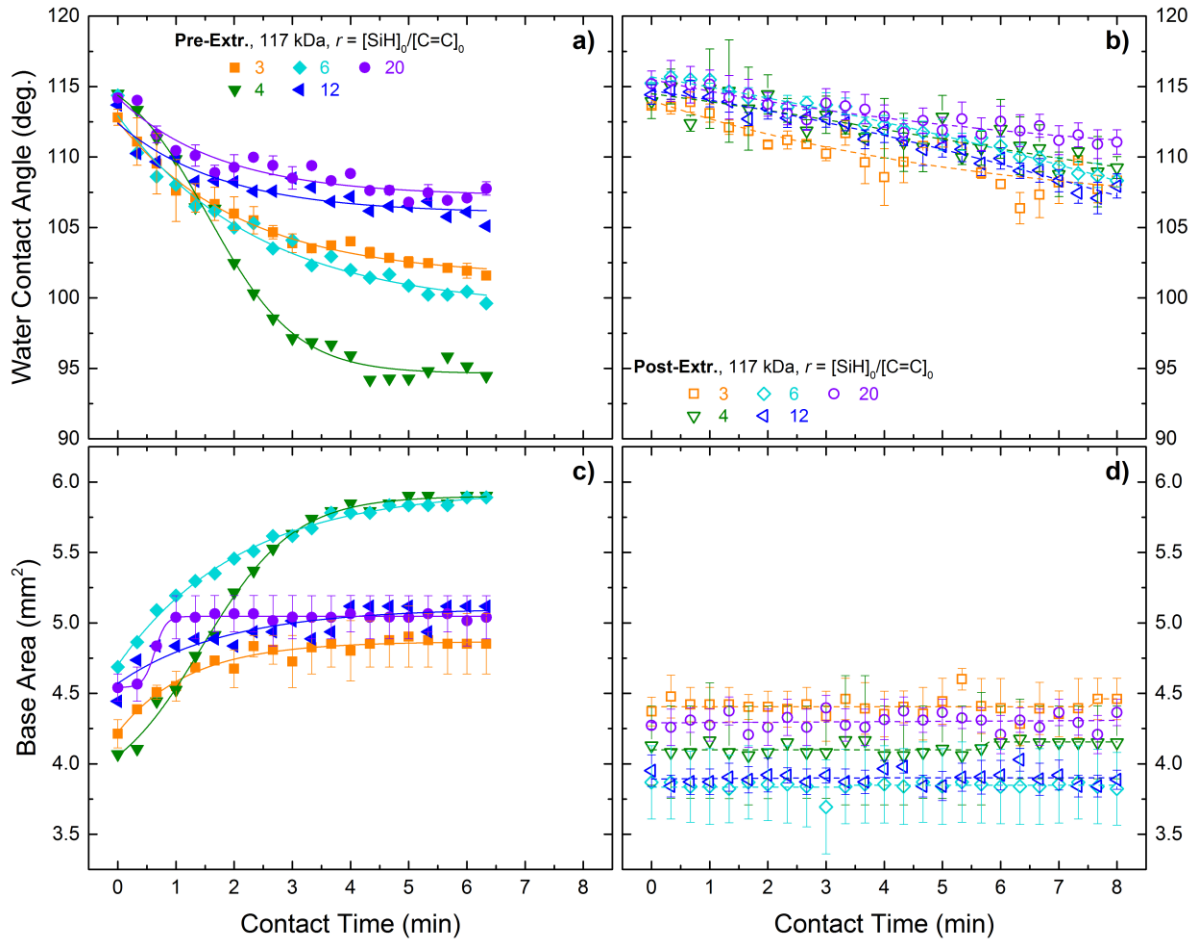


Figure A5.20 – Water contact angle, θ (top), and base area, B (bottom), plotted as a function of contact time, t , between water droplet and PDMS substrate pre- (left) and post-extraction (right) for the model vinyl/hydride system of 117 kDa and various stoichiometric ratios. The symbols are data while the lines are fits using the hyperbolic tangent function.

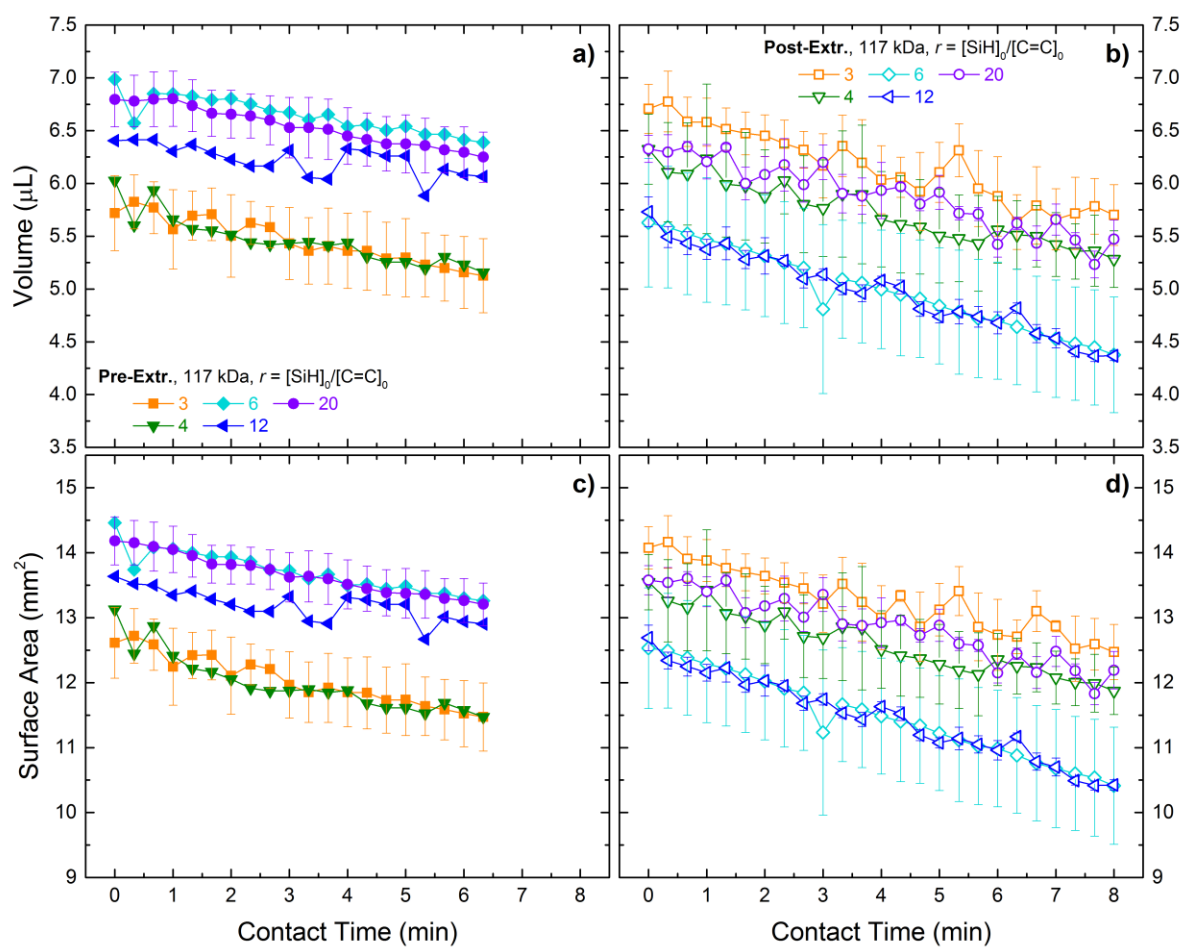


Figure A5.21 – Droplet volume (top) and surface area (bottom) plotted as a function of contact time before (left) and after (right) extraction for the 117 kDa system.

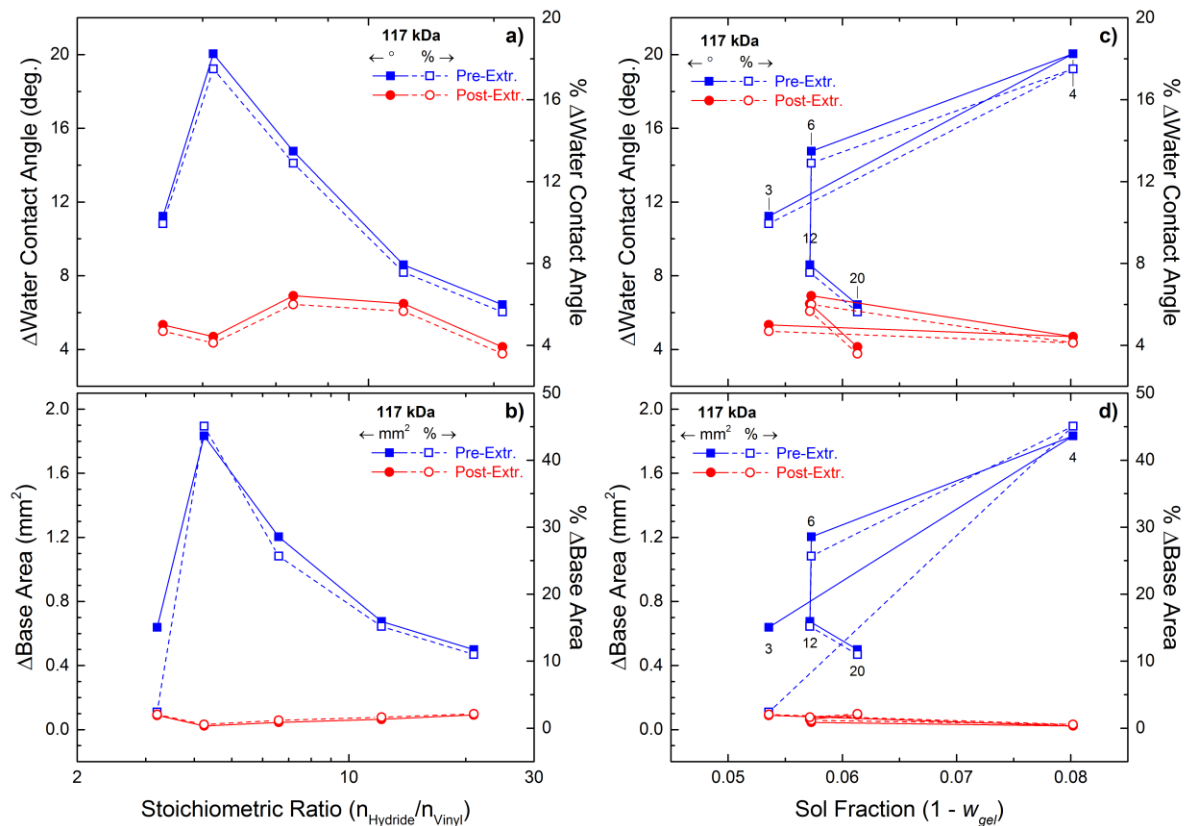


Figure A5.22 – Absolute change (left ordinate, solid lines, filled symbols) and percent change (right ordinate, dashed lines, open symbols) in contact angle (top row) and base area (bottom row) plotted as a function of stoichiometric ratio (left column) and sol fraction (right column) for the 117 kDa model PDMS system. Pre-extraction data are blue squares and post-extraction data are red circles. Numerical labels correspond to stoichiometry ratios.

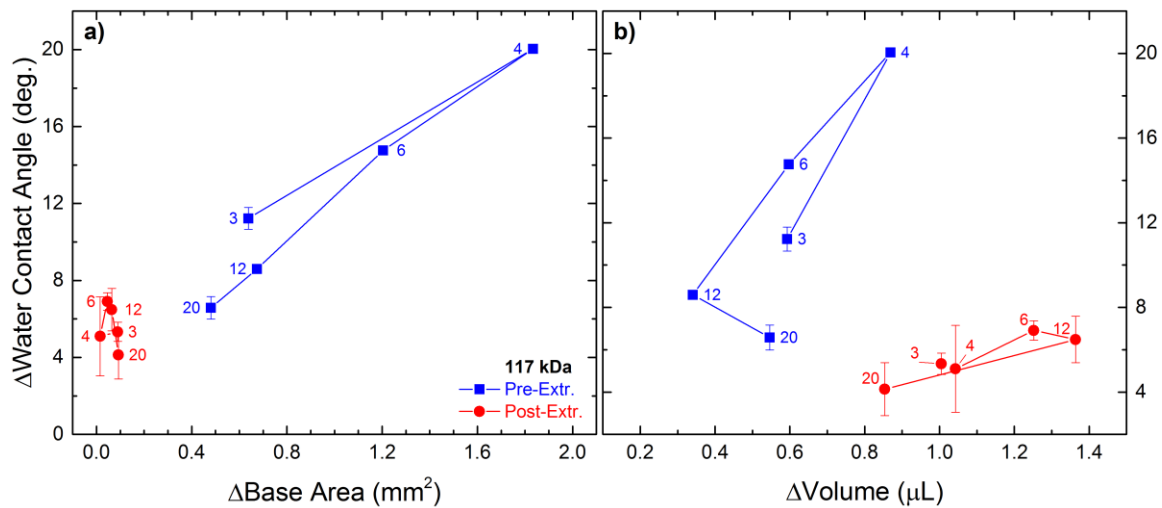


Figure A5.23 – Absolute change in contact angle plotted as a function of absolute change in base area (a) and absolute change in volume (b) for the 117 kDa model PDMS system. Pre-extraction data are blue squares and post-extraction data are red circles. The numerical labels on the data points are the stoichiometric ratio values.

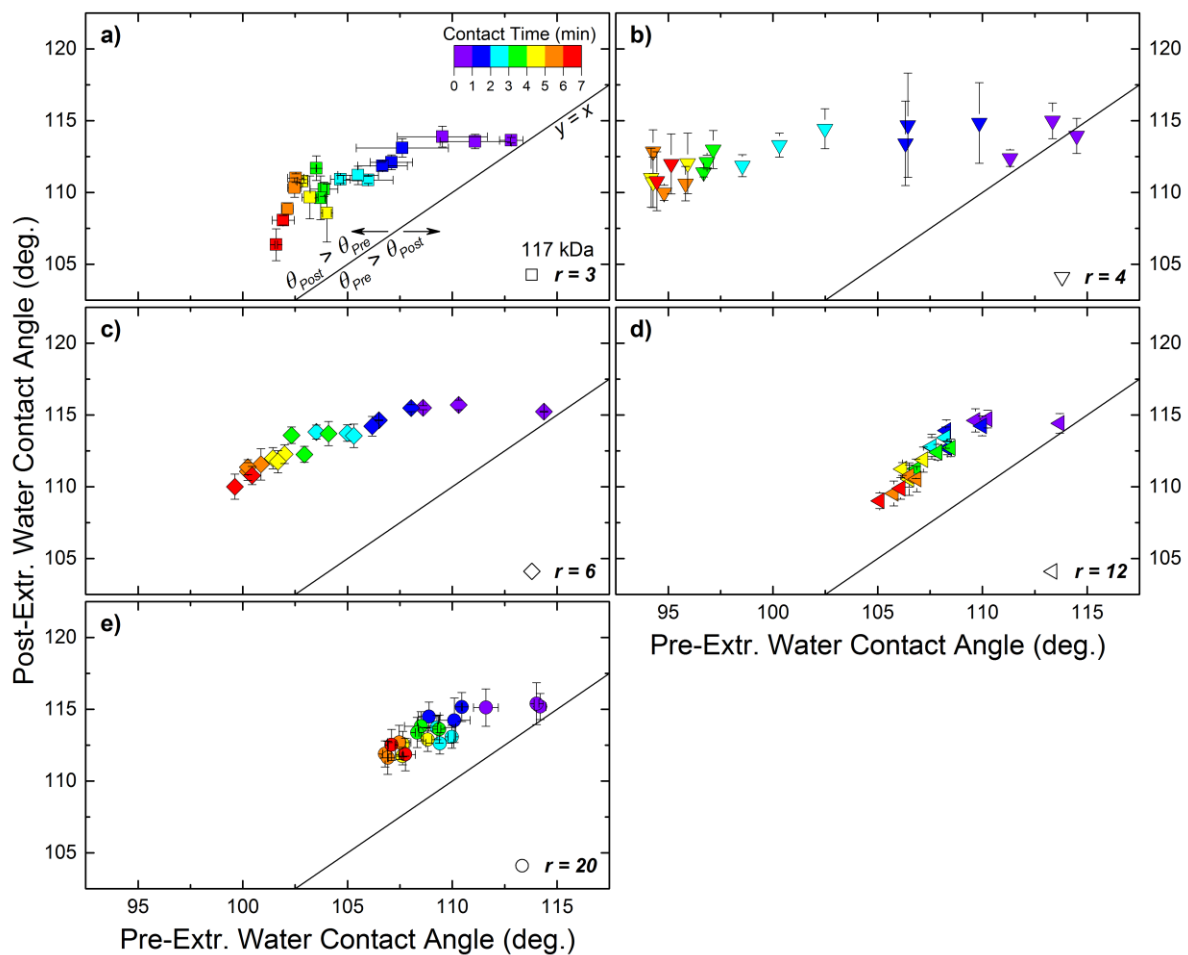


Figure A5.24 – Post-extraction contact angle plotted as a function of pre-extraction contact angle for the 117 kDa model PDMS system for stoichiometric ratios of $r = 3, 4, 6, 12,$ and 20 in a) through e), respectively. The diagonal solid black line represents $y = x$. Data to the left the $y = x$ line occur when post-extraction contact angle is greater than pre-extraction contact angle. The opposite occurs for data to the right of the $y = x$ line. Stoichiometric ratio values are given by different shapes according to the legend. The contact time at which each data point was acquired, both pre-extr. and post-extr. is categorized into 7 different colors according to the visible light spectrum. Short times correspond to violet symbols while long times correspond to red symbols.

Pure Sylgard 184 Data

The following plots provide data for the Sylgard 184 PDMS system.

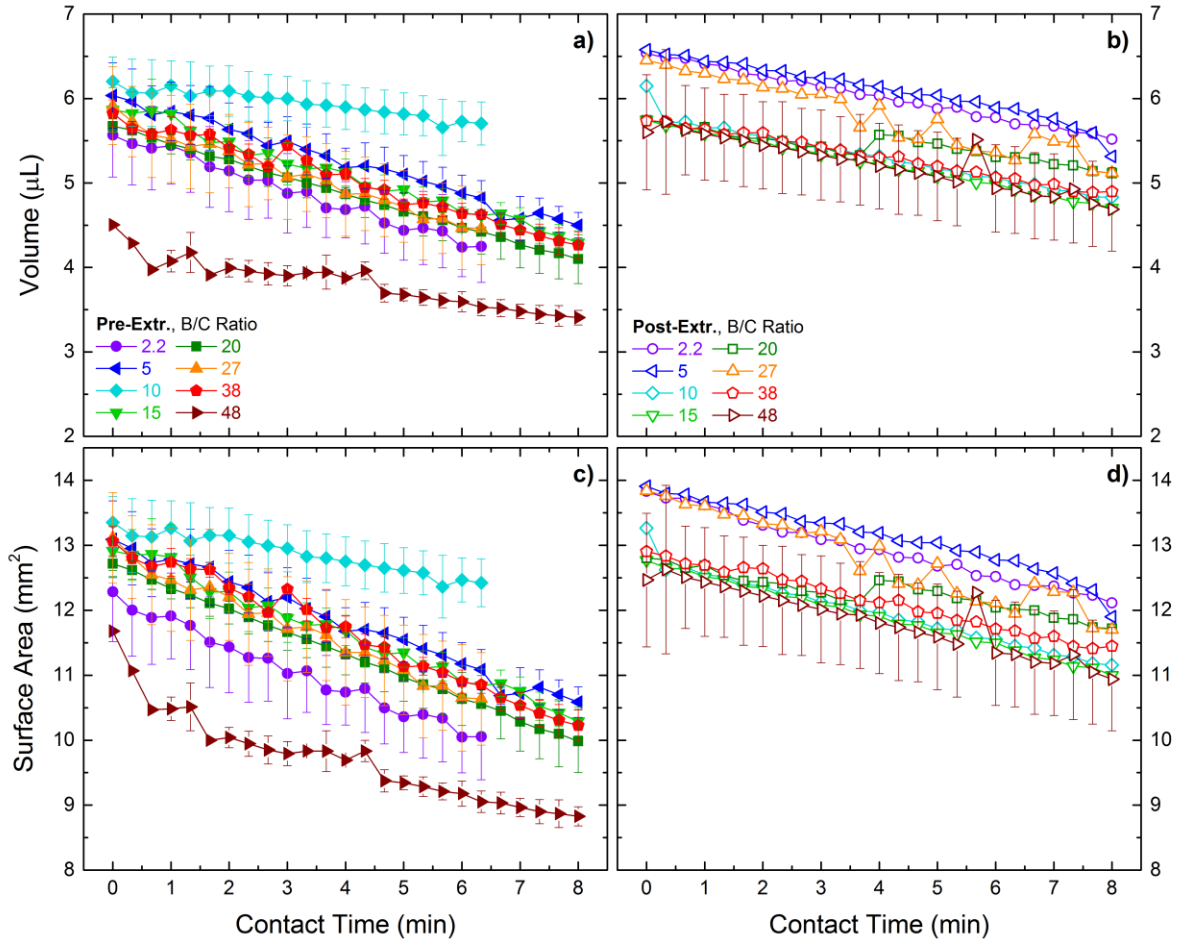


Figure A5.25 – Droplet volume (top) and surface area (bottom) plotted as a function of contact time before (left) and after (right) extraction for the Sylgard 184 system.

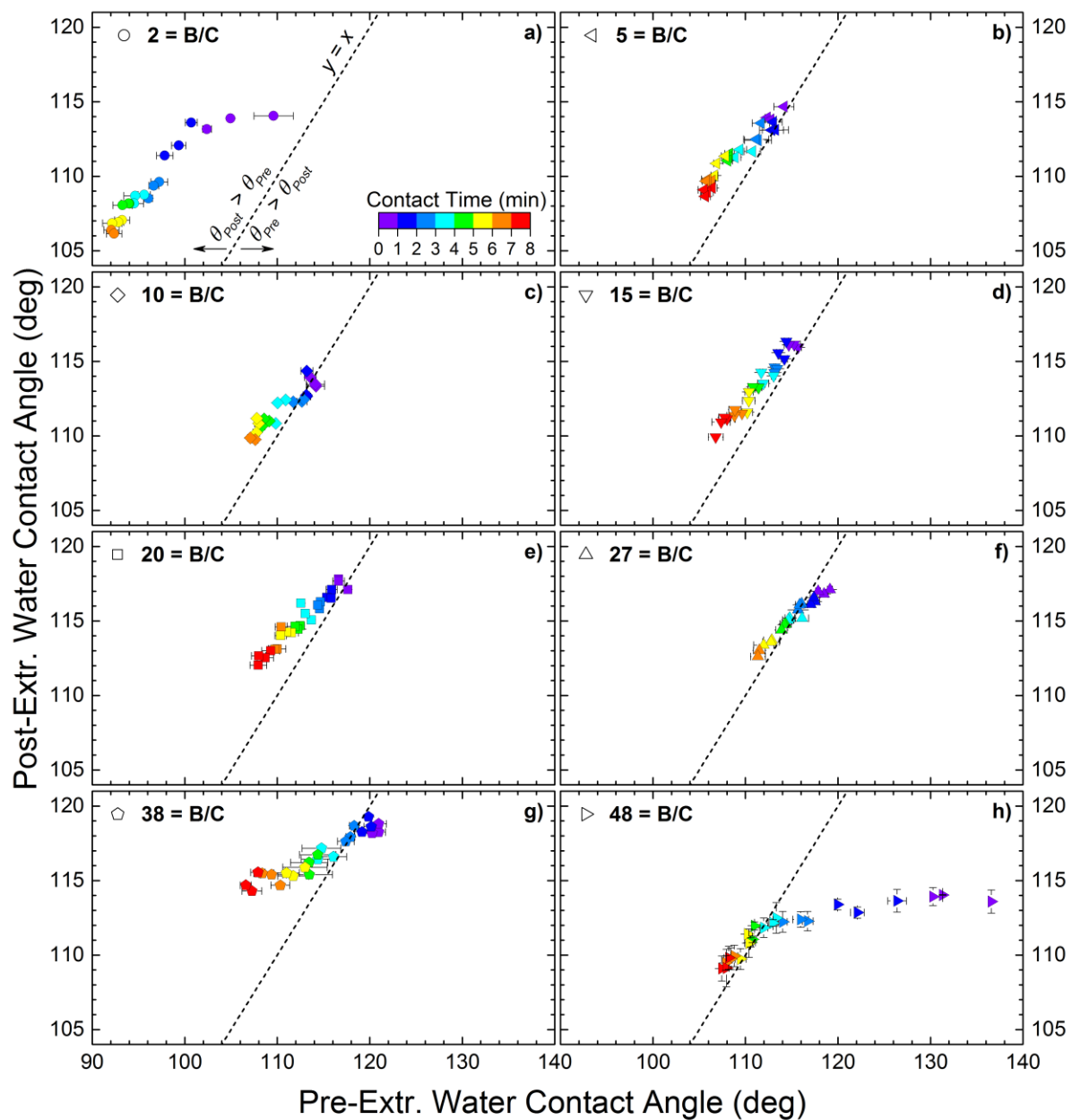


Figure A5.26 – Post-extraction contact angle plotted as a function of pre-extraction contact angle for the Sylgard system for Base/Curing Agent ratios of $B/C = 2, 5, 10, 15, 20, 27, 38,$ and 48 in a) through h), respectively. The diagonal solid black line represents $y = x$. Data to the left the $y = x$ line occur when post-extraction contact angle is greater than pre-extraction contact angle. The opposite occurs for data to the right of the $y = x$ line. Stoichiometric ratio values are given by different shapes according to the legend. The contact time at which each data point was acquired, both pre-extr. and post-extr. is categorized into 8 different colors according to the visible light spectrum. Short times correspond to violet symbols while long times correspond to red symbols.

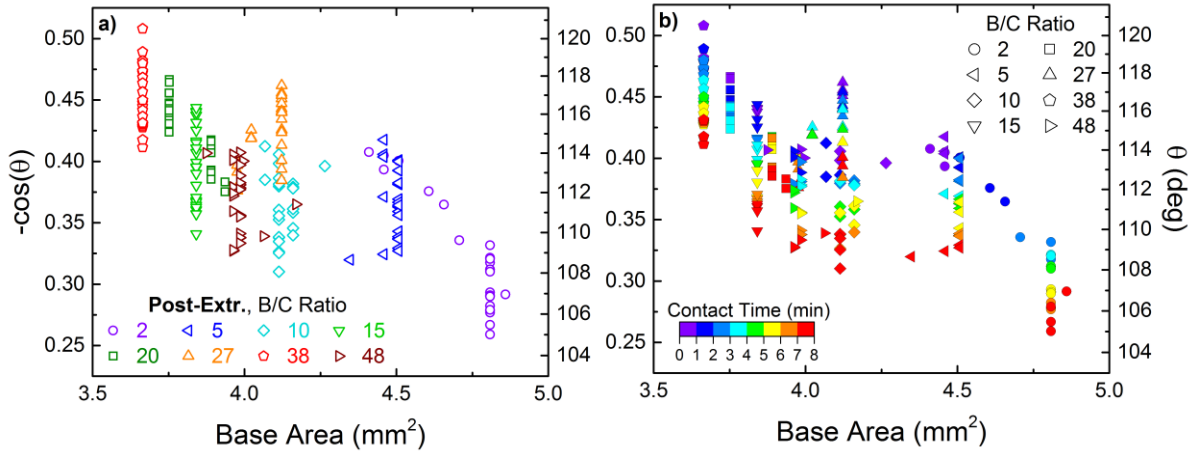


Figure A5.27 – Zoomed in plots from Figure 5.23 provide a more clear picture of the post-extracted $-\cos(\theta)$ data as a function of base area.

Wetting Ridge Height

The wetting ridge height is plotted as a function of contact time for pre- and post-extraction Sylgard 184 samples at various B/C ratios. This parameter is more strongly influenced by storage modulus than contact angle, given that the values are approximately constant as a function of contact time.

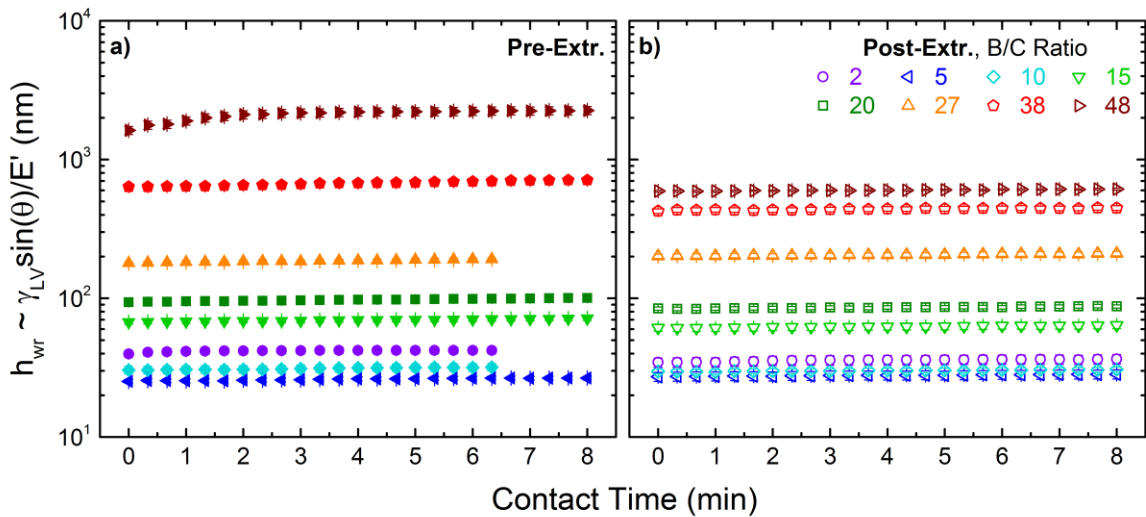


Figure A5.28 – Approximate height of the wetting ridge resulting from the vertical component of surface tension of the water droplet at the 3-phase contact line.

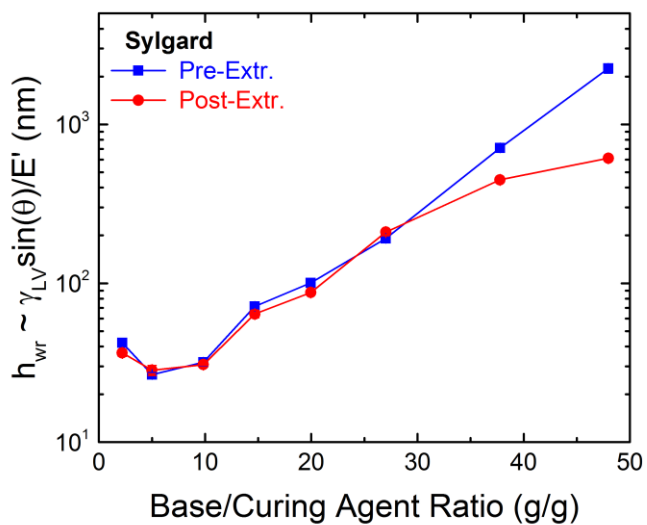


Figure A5.29 – Approximate wetting ridge height of Sylgard 184 samples at the final contact time for pre- and post-extracted samples in blue and red, respectively.

Silicone Oils Added to Sylgard 184 Networks Data

The data presented for these materials is only for pre-extraction samples. No data is provided for post-extraction samples. In Figure A5.30, we plot the water contact angle (left column) and base area (right column) as a function of contact time.

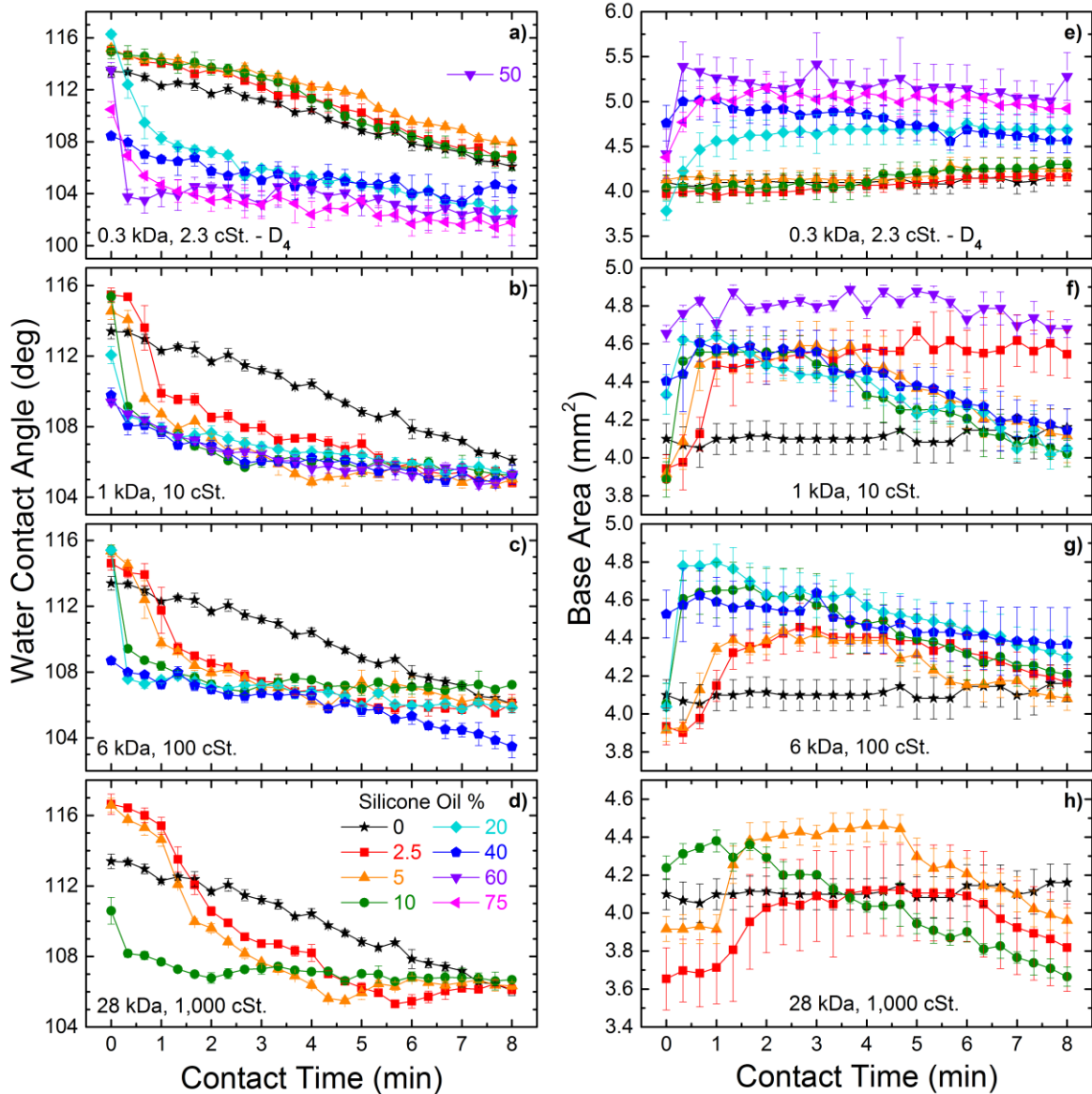


Figure A5.30 – Water contact angle (left column) and base area (right column) plotted as a function of contact time between water droplet and the substrate. Substrates are B/C = 10 Sylgard 184 samples with various mass fractions of silicone oils of various molecular weights. Plots a) and e) are for the cyclic siloxane oligomer, D₄. Plots b) and f) show data for samples filled with a linear trimethyl-terminated PDMS silicone oil of molecular weight 1 kDa and viscosity of 10 cSt. Plots c) and g) show data for a 6 kDa and 100 cSt. silicone oil. Plots d) and h) show data for 28 kDa and 1000 cSt. silicone oil.

As we look down the left column, higher viscosity oils result in a greater “lag-time” before dramatic decrease in contact angle. I believe there is some mixing effect going on or some

diffusion limitation. After this delay passes, the water droplet is allowed to slide. WE also see that higher concentrations of smaller molecule oils can persist before the onset of rapid decreasing behavior. It takes 20% oils of D4 to cause the dramatic decrease, whereas this occurs with only 2.5% oils for 1 kDa linear silicone oil. The delays correspond will with the delays in spreading base area. However, unlike pure systems without oils, the base area shows a decrease at long times. I believe the droplets get pinned without oils and just shrink as evaporation occurs. With a slippery surface, however, the droplet shrinks as it evaporates.

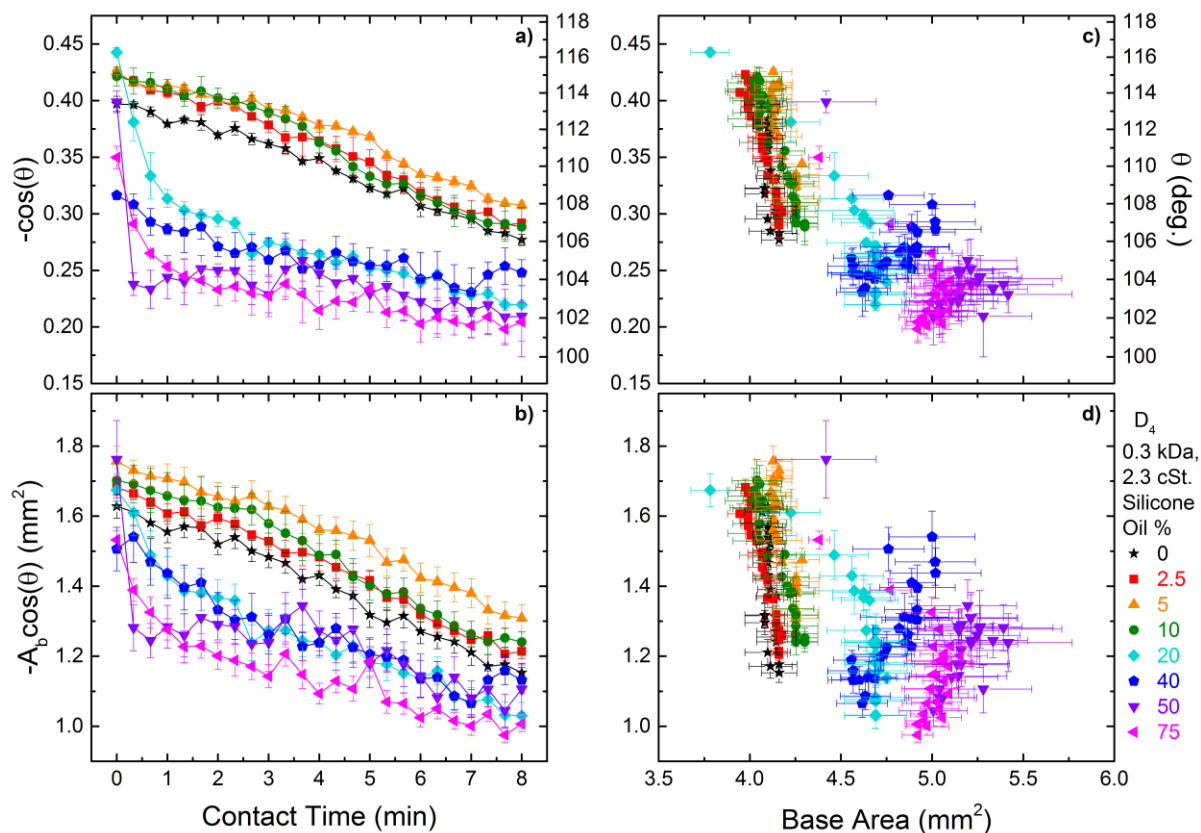


Figure A5.31 - Changes in interfacial energy between water droplet and silicone-oil-infused PDMS substrates as a function of contact time (left columns). The oil is a cyclic, D₄, with ~0.3 kDa and 2.3 cst. Various mass fractions of oils are shown. The interfacial energy terms are plotted as a function of base area in the right columns.

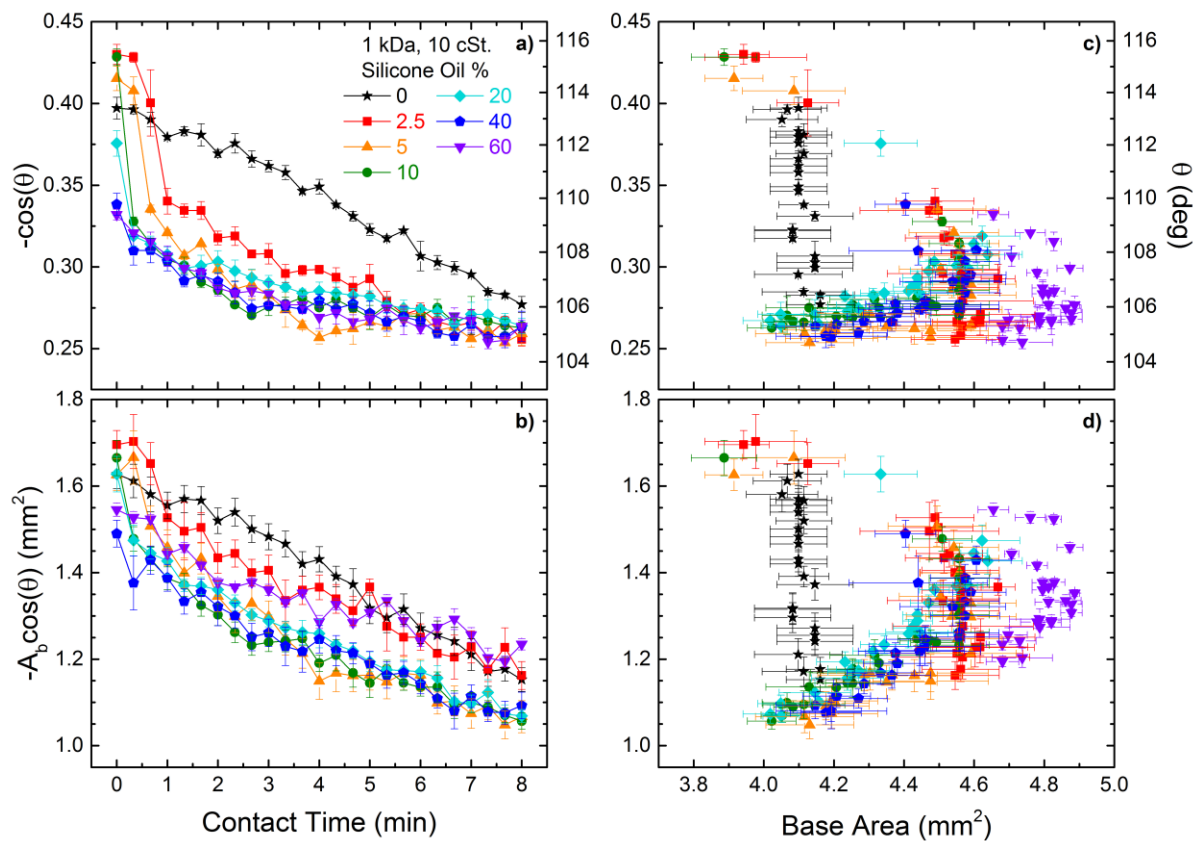


Figure A5.32 - Changes in interfacial energy between water droplet and silicone-oil-infused PDMS substrates as a function of contact time (left columns). The oil is 1 kDa and 10 cst. Various mass fractions of oils are shown. The interfacial energy terms are plotted as a function of base area in the right columns.

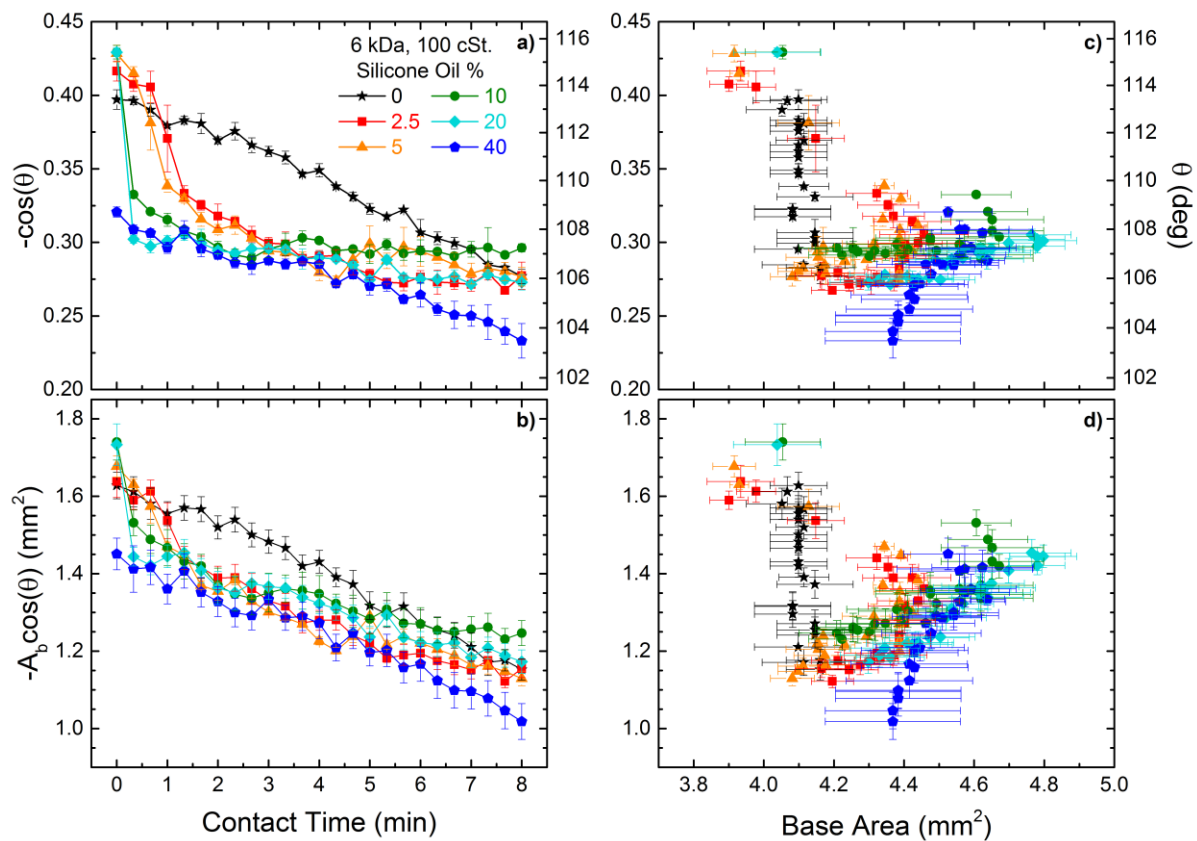


Figure A5.33 – Changes in interfacial energy between water droplet and silicone-oil-infused PDMS substrates as a function of contact time (left columns). The oil is 6 kDa and 100 cst. Various mass fractions of oils are shown. The interfacial energy terms are plotted as a function of base area in the right columns.

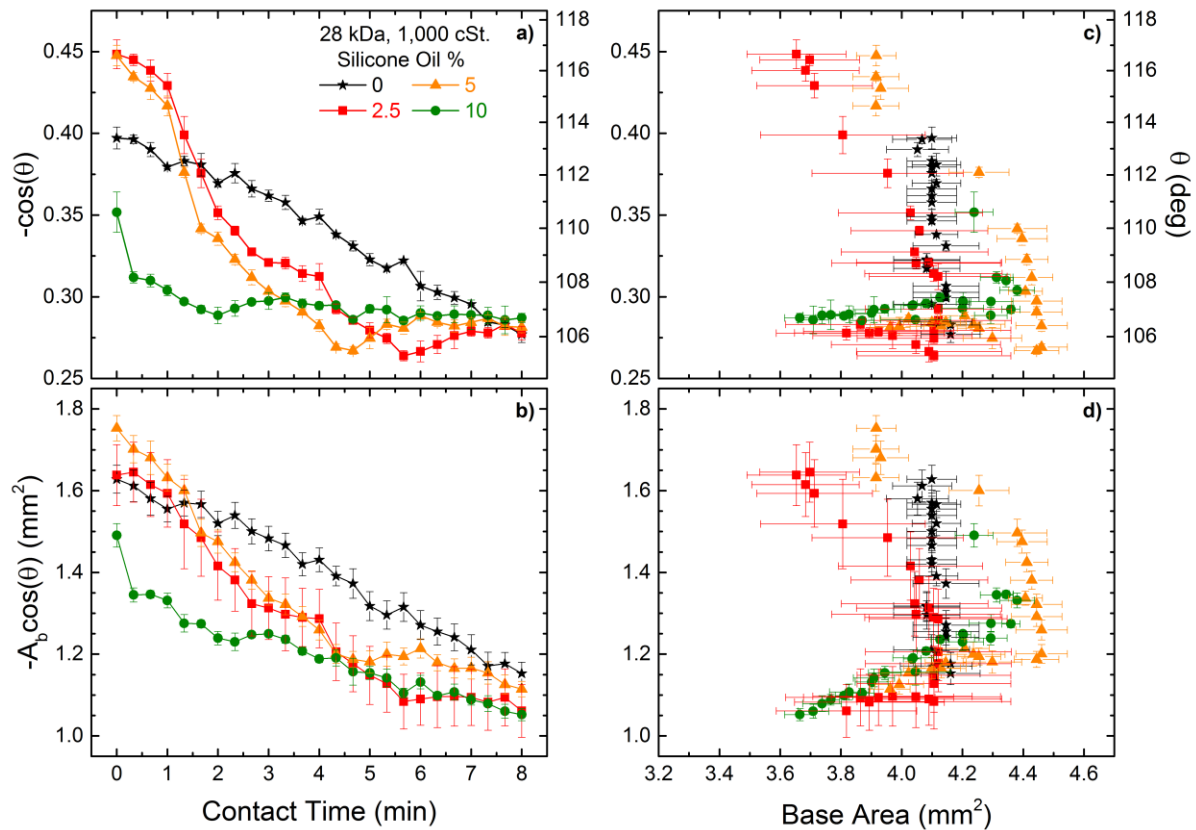


Figure A5.34 – Changes in interfacial energy between water droplet and silicone-oil-infused PDMS substrates as a function of contact time (left columns). The oil is 28 kDa and 1000 cst. Various mass fractions of oils are shown. The interfacial energy terms are plotted as a function of base area in the right columns.

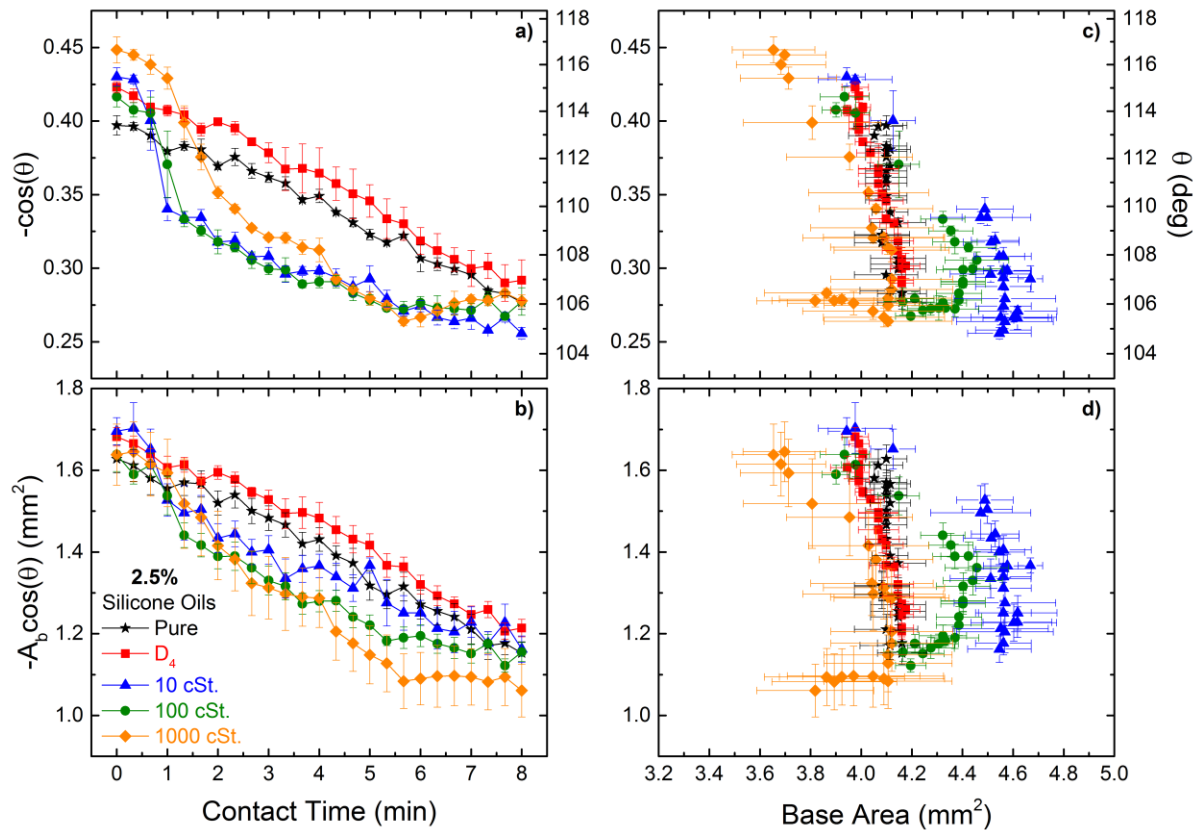


Figure A5.35 – Changes in interfacial energy between water droplet and silicone-oil-infused PDMS substrates as a function of contact time (left columns). The mass fraction of oil is constant at 2.5% and the oils change according to the legend. The interfacial energy terms are plotted as a function of base area in the right columns.

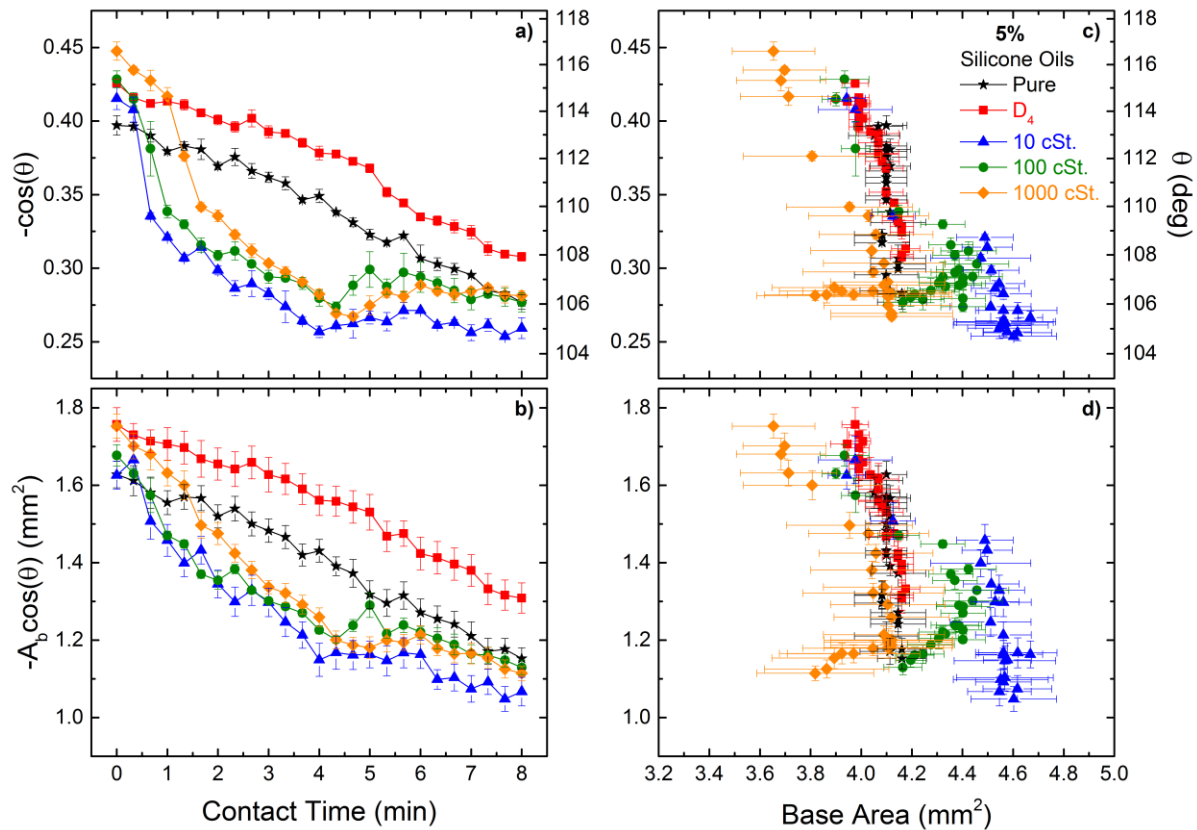


Figure A5.36 – Changes in interfacial energy between water droplet and silicone-oil-infused PDMS substrates as a function of contact time (left columns). The mass fraction of oil is constant at 5% and the oils change according to the legend. The interfacial energy terms are plotted as a function of base area in the right columns.

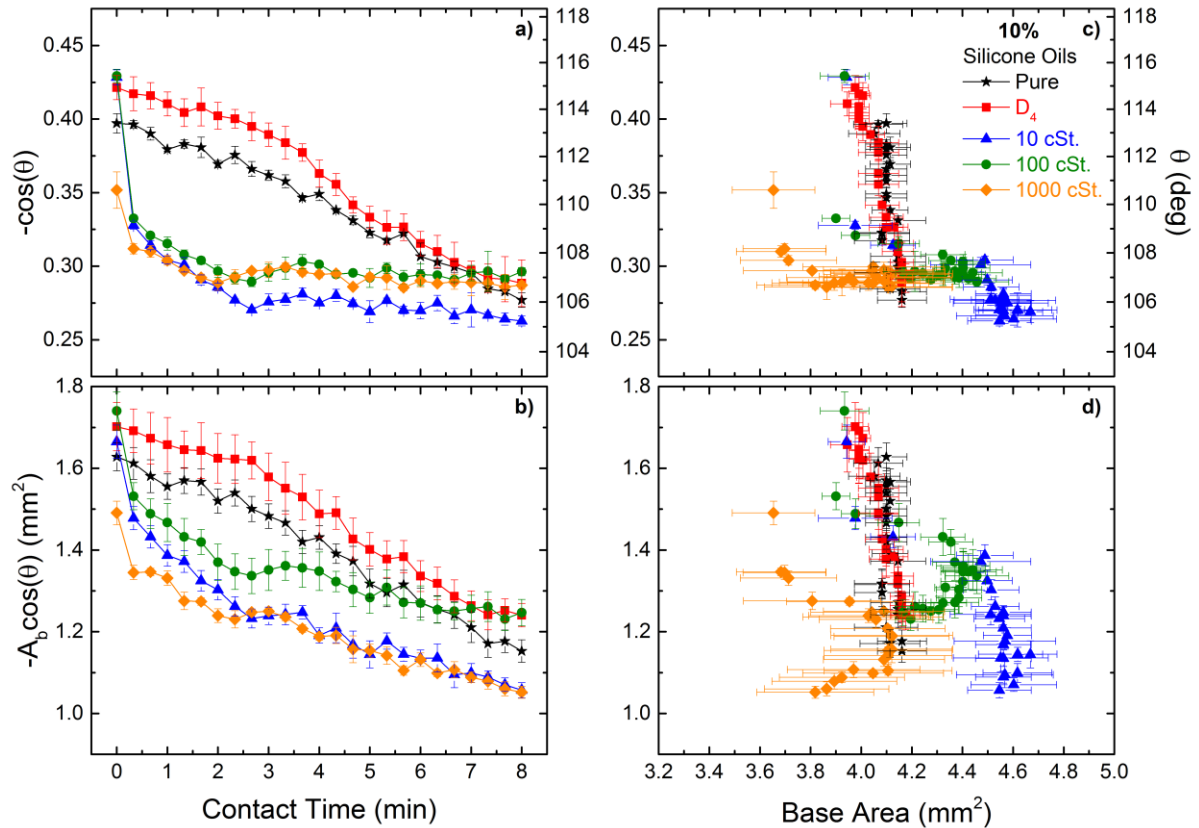


Figure A5.37 – Changes in interfacial energy between water droplet and silicone-oil-infused PDMS substrates as a function of contact time (left columns). The mass fraction of oil is constant at 10% and the oils change according to the legend. The interfacial energy terms are plotted as a function of base area in the right columns.

Matlab Image Analysis Code

Code for Contact Angles >90°

```

%*****
% This file will determine drop parameters and contact angles for multiple
% images in a directory with user-defined 3-phase contact points
% (i.e., where the base of the droplet interfaces with the substrate.
% This only works for hydrophobic droplets, i.e., contact angle > 90
% degrees and TIFF (.tif) files.

% Written By Matthew Melillo
% North Carolina State University
% Updated February 1, 2017

clc

```

```

clear all
close all

%***** Read Image Files From Current Directory

files = dir('*.tif'); %Reads in all tif files in directory
numfids = length(files); %Determines number of files
filenames = cell(numfids,1); %Copies all of the names into a vector
Results = cell(numfids+1,19); %Creates an empty cell to store results
Results(1,:) = {'Filename', 'Time(sec)', 'Time(min)', 'Pixels/mm', 'Major radius (mm)',
'Minor radius (mm)', 'Drop Height (mm)', 'Contact Line length (mm)', 'Contact Angle (deg)',
'Drop Base Area (mm^2)', 'Drop Volume (mm^3)', 'Drop Surface Area (mm^2)', 'Substrate Angle
(deg)', 'Ellipse R2', 'Root MSE', 'Major Radius Bounds', 'Minor Radius Bounds', 'Contact Angle
Bounds', 'Drop Volume Bounds'};
mkdir('Fitted_Images'); %Creates a directory to save the fitted images
cd('Fitted_Images');
fpath = pwd; %Gets path of newly created directy
cd ../; %Moves back up to current directory

%***** Begin Loop that Performs Operations on Every Image in Directory

for j=1:numfids
    filenames{j}=files(j).name; %Adds filename to variable 'filenames'
    Current_filename = filenames{j};
    [pathstr,name,ext] = fileparts(Current_filename);
    %Find the index at the beginnig of the word "Spot" of "spot" in filename
    spot = strfind(Current_filename,'Spot');
    if isempty(spot) == 1;
        spot = strfind(Current_filename,'spot');
    end

    %Find time (sec) from filename
    time_sec(j) = str2double(Current_filename(end-6:end-4)); %Stores time in sec
    if isnan(time_sec(j)) == 1;
        time_sec(j) = str2double(Current_filename(end-5:end-4));
    end
    if isnan(time_sec(j)) == 1;
        time_sec(j) = str2double(Current_filename(end-4:end-4));
    end
    time_min(j) = time_sec(j)/60; % Stores time in min

    new_name = strcat('Fit_',name);

    % ***** Performs Operations on Image
    I = imread(filenames{j});
    % Sharpen Image
    Isharp = imsharpen(I, 'radius',2,'amount',1.5);
    % Convert to black and white binary
    %***** use 2nd input for values between 0 and 1 for thresholding)
    % Lower number means higher gray values in each pixel are needed to be

```

```

% turned to black. Higher number means pixels closer to white (light
% gray) will still be turned to black
BW = im2bw(Isharp, 0.1);
% Convert such that droplet is white and background is black
WB = imcomplement(BW);
% Fill in holes
WB2 = imfill(WB, 'holes');

% ***** Set Scale bar based on needle width *****
scaleIndex = find(WB2(50,:)); %Finds needle width 50 pixels from top
needlewidth = scaleIndex(end)+1/2-(scaleIndex(1)-1/2);
Scale_barX = [scaleIndex(1)-1/2 scaleIndex(end)+1/2];
pixel_mm = needlewidth/0.72; % length of needle in pixels/0.72 mm

%Find top of droplet by searching for next black pixel below middle of
%needle
needle_center = round((scaleIndex(1)+scaleIndex(end))/2);
center_rows = find(WB2(:,needle_center)); %Finds all rows below center of needle
change = center_rows(diff(center_rows)~=1); %Looks for the difference between row n and
(n-1) to be not equal to 1
drop_top = [needle_center,center_rows(change(1)+1)]; %Drop top is the first row where the
change isn't equal to 1

%Skips images that are distorted due to camera/stage shake
if (250 - drop_top(2)) > 100
    continue
end

% ***** Finds boundaries in the image *****
[height,width] = size(I);
boundary = bwboundaries(WB2, 'noholes'); %Finds the boundary of the outer white edge of
the drop shape and all other white features in image
voids = cellfun('size',boundary,1); %Finds the number of data points in each array in
boundary

%Search through all arrays within "boundary" cell to find one that
%matches the outline for the top of the droplet
for m=1:length(boundary)
    for n=1:length(boundary{m,1})
        if drop_top(2) == boundary{m,1}(n,1) && drop_top(1) == boundary{m,1}(n,2)
            droplet_index = m;
        end
    end
end

outline = boundary{droplet_index,1}; %Returns boundary coordinates of the first image
feature (only 1 for WCA images)
x = outline(:,2); %defines x values of the outline from the 2nd column of the boundary
y = outline(:,1); %defines y values of the outline from the 1st column of the boundary

```

```

totalHeight = max(y)-min(y); %Height of top of edge to bottom, including reflection in
pixels

% ***** User-defined three-phase contact points (vertices) *****
figure(j)
imshow(Isharp)
fig = figure(j);
set (fig, 'Units', 'normalized', 'Position', [0,0,1,1]);
%User zooms into LEFT contact point region, clicks enter, then clicks on left contact
points, then clicks "enter"
zoom on
pause;
%datacursormode on %Allows for seeing the exact pixel coordinates
%pause;
[x_coord(1), y_coord(1), Pixel_value] = impixel;
close
zoom off
%datacursormode off

figure(j)
imshow(Isharp)
fig = figure(j);
set (fig, 'Units', 'normalized', 'Position', [0,0,1,1]);
%User zooms into RIGHT contact point region, clicks enter, then clicks on left contact
points, then clicks "enter"
hold on
plot([1,600],[y_coord(1),y_coord(1)],'r--');
zoom on
pause;
[x_coord(2), y_coord(2), Pixel_value] = impixel;
close
zoom off

%Calculate the substrate angle in degrees
substrate_angle = atan((y_coord(2)-y_coord(1))/(x_coord(2)-x_coord(1)))*180/pi();

xvertexLeft = x_coord(1);
xvertexRight = x_coord(2);
yvertexLeft = y_coord(1);
yvertexRight = y_coord(2);
CL_length = sqrt((x_coord(2)-x_coord(1))^2+(y_coord(2)-y_coord(1))^2); %Length in pixels
of contact line
CL_height = (yvertexLeft + yvertexRight)/2; %Height in pixels of contact line

% ***** Identifying Droplet Shape Parameters *****
%Find coordinates of top of droplet
yTop = min(y); % Top of drop, y-coordinate, in pixels
xTopFirstIndex = find(y == min(y), 1, 'first'); %left-most x index for ytop
xTopFirst = x(xTopFirstIndex); %value of left-most ytop x pixel
xTopLastIndex = find(y == min(y), 1, 'last'); %right-most x index for ytop

```

```

xTopLast = x(xTopLastIndex);% value of right-most ytop x pixel
xTopCenter = (xTopFirst + xTopLast)/2;% center of top of droplet, x coordinate

%Find the left and right edges of the droplet, looking at y values not at
%the top or the bottom of the green outline.

%Finds all the indices with non-zero values droplet top and
%above intersection line

LeftRightEdgeIndex = find(y >= min(y) & y <= (CL_height) & x >= (x_coord(1)-20) & x <=
(x_coord(2)+20));
x_drop = x(LeftRightEdgeIndex);
y_drop = y(LeftRightEdgeIndex);

% Find coordinates of left droplet edge
xLeft = min(x_drop); %Left-most x point, edge
LeftIndex = find(x_drop == xLeft); %Index of left-most x point
%Finds left most y index, averaged to center in height
yLeftIndex = round(length(LeftIndex)/2);
yLeftCenter = y_drop(LeftIndex(yLeftIndex)); %y value in pixels for left edge

% Find coordinates of right droplet edge
xRight = max(x_drop); %highest number in x pixels, i.e., farthest right edge
RightIndex = find(x_drop == xRight); %index of right edge of drop x pixels
%Finds right most y index, averaged to center in height
yRightIndex = round(length(RightIndex)/2);
yRightCenter = y_drop(RightIndex(yRightIndex));
%yRightCenter = yLeftCenter; % Major axis should be horizontal

%Take average y-value of left and right edges of droplet
yMajor = (yLeftCenter + yRightCenter)/2;

%Find the outline only for the top half of the drop
drop_top_index = find(y_drop < (yMajor) & x_drop > (xLeft) & x_drop < (xRight));
x_drop_top = x_drop(drop_top_index);
y_drop_top = y_drop(drop_top_index);

%If white circle in center of drop meets bottom of substrate, the
%outline may connect the drop edge to the center of drop. Use the "final" drop top
%variables in the optimization function

if length(x_drop_top) > 285
    changes = diff(x_drop_top); %Takes the difference between row n and n-1
    final_index = find(abs(changes) > 1); %Looks for the difference between row n and (n-
1) to be > 1 (correspondign from jump from edge of droplet to center white spot)
    if final_index < 100
        x_drop_top_final = x_drop_top(final_index+1:end);
        y_drop_top_final = y_drop_top(final_index+1:end);
    else
        x_drop_top_final = x_drop_top(1:final_index); %Drop top is the first row where

```

```

the change isn't equal to 1
    y_drop_top_final = y_drop_top(1:final_index);
end

end

%Perform fitting of top half of ellipse to outline

%Initial guess of fitting parameters
param0(1) = abs(xLeft - xRight)/2; %major radius, half the distance between user-selected
3-phase points
param0(2) = abs(yTop - yMajor); %minor radius, diffence between top of drop and 3-phase
contact line
param0(3) = yMajor; %vertical offset, height of 3-phase contact points
param0(4) = xTopCenter; %Horizontal offset

%Function to minimize sum of square differences between outline and
%function for top half of drop,  $y = k - b\sqrt{1 - ((x-h)^2/a^2)}$ 
yPosFun = @(param,xdata)param(3)-param(2)*sqrt(1-((xdata-param(4)).^2/param(1)^2));

if length(x_drop_top) > 285
    [param,resnorm,residual,exitflag,output,lambda,jacobian] =
lsqcurvefit(yPosFun,param0,x_drop_top_final,y_drop_top_final);
else
    [param,resnorm,residual,exitflag,output,lambda,jacobian] =
lsqcurvefit(yPosFun,param0,x_drop_top, y_drop_top);
end

%Ignoring imaginary parts of parameters
a = real(param(1)); %major radius
b = real(param(2)); %minor radius
k = real(param(3)); %vertical offset
h = real(param(4)); %horizontal offset

%Ignoring imaginary parts of parameters
real_param = real(param);
real_res = real(residual);
real_jac = real(jacobian);

%Determine 95% confidence intervals on 4 parameters, a, b, h, k (rows
%1-4). Lower bounds are column 1, upper bounds are column 2
conf = nlparci(real_param,real_res,'jacobian',real_jac);
a_upper = conf(1,2);
a_lower = conf(1,1);
a_bounds = ((a_upper - a) + (a - a_lower))/2;
b_upper = conf(2,2);
b_lower = conf(2,1);
b_bounds = ((b_upper - b) + (b - b_lower))/2;

```

```

% Define boundaries of ellipse in x-direction
x_e11 = x_coord(1)-15:1:x_coord(2)+15;
%x_e11 = x_drop_top;

%Define x-values and y-values for fitting
yPos = zeros(length(x_e11),1);
yNeg = zeros(length(x_e11),1);

% Fill vectors for top and bottom half of ellipse
for i=1:length(x_e11);
    yPos(i) = k - b*sqrt((1-(x_e11(i)-h).^2/a^2));
    yNeg(i) = k + b*sqrt((1-(x_e11(i)-h).^2/a^2));
end

%Measure of Goodness-of-fit for ellipse to droplet
r2 = real(1 - resnorm/sum((yPos-mean(yPos)).^2)); %Should be close to 1

if length(x_drop_top) > 285
    RootMSE = sqrt(resnorm/(length(y_drop_top_final)-4)); %Should be close to 0
else
    RootMSE = sqrt(resnorm/(length(y_drop_top)-4));
end

%Define major and minor radii of ellipse, in mm
amm = a/pixel_mm;
bmm = b/pixel_mm;

amm_bounds = a_bounds/pixel_mm;
bmm_bounds = b_bounds/pixel_mm;

% ***** Contact Angle and Drop Parameters Calculations *****
% Determine contact angle based on slope of tangent line to ellipse at
% intersection of base contact line and ellipse

ydist = k - CL_height; % Distance from contact line to height of major axis
Drop_Height = CL_height - yTop; % Height of drop, in pixels

slope = -b*sqrt((b^2)-(ydist^2))/(a*ydist);

%Bounds of slope, 95% confidence from fitting ellipse
slope_high = -b_upper*sqrt((b_upper^2)-(ydist^2))/(a_lower*ydist);
slope_low = -b_lower*sqrt((b_lower^2)-(ydist^2))/(a_upper*ydist);

%Bounds of contact angle, CA, 95% confidence from fitting ellipse
CA_upper = (pi()-abs(atan(slope_low)))/(pi()/180);
CA_lower = (pi()-abs(atan(slope_high)))/(pi()/180);

%Tangent lines
LeftTan = [20/slope+x_coord(1) y_coord(1)+20; -75/slope+x_coord(1) y_coord(1)-75];
%LeftTan = [x_coord(1) y_coord(1); -75/slope+x_coord(1) y_coord(1)-75];

```

```

RightTan = [-20/slope+x_coord(2) y_coord(2)+20; 75/slope+x_coord(2) y_coord(2)-75];
%RightTan = [x_coord(2) y_coord(2); 75/slope+x_coord(2) y_coord(2)-75];

% Drop Parameters, Hydrophobic, > 90 deg.
CA = (pi()-abs(atan(slope)))/(pi()/180); %Hydrophobic, > 90 deg.
CA_bounds = ((CA_upper - CA) + (CA - CA_lower))/2;

DBA = pi()*(CL_length/pxel_mm)^2/4; %Drop Base Area, in mm

DV = ((pi()*a^2)/(3*b^2)*Drop_Height^2*(3*b-Drop_Height))/((pxel_mm)^3); %Drop volume in
mm^3
DV_upper = ((pi()*a_upper^2)/(3*b_upper^2)*Drop_Height^2*(3*b_upper-
Drop_Height))/((pxel_mm)^3); %Max drop volume
DV_lower = ((pi()*a_lower^2)/(3*b_lower^2)*Drop_Height^2*(3*b_lower-
Drop_Height))/((pxel_mm)^3); %Min drop volume
DV_bounds = abs((DV_upper - DV) + (DV - DV_lower))/2);

e11 = sqrt((a^2)/(b^2)-1); %Ellipticity = sqrt(a^2/b^2-1)
e112 = 1-Drop_Height/b; % ellipticity_2 = 1 - drop height/minor axis
DSA = pi()*amm*bmm*(amm/bmm-e112*sqrt(1+e11.^2*e112.^2)+1/e11*(asinh(e11)-
asinh(e11*e112)));

% write results to a matrix cell
Results(j+1,:) = {filenames{j}, time_sec(j), time_min(j), pxel_mm, amm, bmm,
Drop_Height/pxel_mm, CL_length/pxel_mm, CA, DBA, DV, DSA, substrate_angle, r2, RootMSE,
amm_bounds, bmm_bounds, CA_bounds, DV_bounds};

% Visualize results
figure(j)
imshow(I)
axis ij
axis equal
axis on
hold on
set(gca,'TickDir','in')
title(Current_filename(1:spot+5),'interpreter','none')

% Plot scalebar
plot(Scale_barX,[50 50],'g-','Linewidth',0.5)

%Plot outline of ellipse itself
plot(x_e11,yPos,'r','Linewidth',0.5)
plot(x_e11,yNeg,'r','Linewidth',0.5)

%Plot boundary determined from Matlab function
plot(x,y, 'g:', 'Linewidth', 1)
%plot(x_drop,y_drop, 'g:', 'Linewidth', 1)

%Plot tangent lines
plot(LeftTan(:,1),LeftTan(:,2), 'b','Linewidth',0.5)

```

```

plot(RightTan(:,1),RightTan(:,2), 'b','Linewidth',0.5)

%Plot user-defined 3-phase contact line points
plot(x_coord,y_coord,'y--','Linewidth',0.5)
plot(x_coord,y_coord,'yx', 'Markersize', 3,'Linewidth',0.5)

%Output drop parameters to image and PDF file
str = sprintf('Contact Time = %.2f min \nContact Angle = %.2f +/- %.2f\circ \nDrop
Volume = %.2f +/- %.2f \muL \nDrop Base Area = %.2f mm^2 \nDrop Surface Area %.2f mm^2
\nSubstrate Angle = %.2f\circ \nEllipse R^2 =
%.4f',time_min(j),CA,CA_bounds,DV,DV_bounds,DBA,DSA,substrate_angle,r2);
text(20,75,str)
str2 = sprintf('%.2f pixels/mm',pixel_mm);
text(Scale_barX(2)+15,50,str2)
print(gcf,fullfile(fpath,new_name),'-dpdf');
print(gcf,fullfile(fpath,new_name),'-dtiff');
close
end
xlswrite(new_name(1:end-3),Results);

```

[Published with MATLAB® R2015a](#)

Code for Contact Angles < 90°

```

%*****
% This file will determine drop parameters and contact angles for multiple
% images in a directory with user-defined vertex points (i.e., where the
% base of the droplet interfaces with the substrate. This only works for
% hydrophilic droplets, i.e., contact angle < 90 degrees and TIFF (.tif)
% files)

% Written By Matthew Melillo
% North Carolina State University
% Updated February 1, 2017

clc
clear all
close all

%***** Read Image Files From Current Directory

files = dir('*.tif'); %Reads in all tif files in directory
numfids = length(files); %Determines number of files
filenames = cell(numfids,1); %Copies all of the names into a vector
Results = cell(numfids+1,19); %Creates an empty cell to store results
Results(1,:) = {'Filename', 'Time(sec)', 'Time(min)', 'Pixels/mm', 'Major radius (mm)',
'Minor radius (mm)', 'Drop Height (mm)', 'Contact Line length (mm)', 'Contact Angle (deg)',
'Drop Base Area (mm^2)', 'Drop Volume (mm^3)', 'Drop Surface Area (mm^2)', 'Substrate Angle
(deg)', 'Ellipse R^2', 'Root MSE', 'Major Radius Bounds', 'Minor Radius Bounds', 'Contact Angle

```

```

Bounds', 'Drop Volume Bounds'});
mkdir('Fitted_Images'); %Creates a directory to save the fitted images
cd('Fitted_Images');
fpath = pwd; %Gets path of newly created directy
cd ../; %Moves back up to current directory

%***** Begin Loop that Performs Operations on Every Image in Directory

for j=1:numfids
    filenames{j}=files(j).name; %Adds filename to variable 'filenames'
    Current_filename = filenames{j};
    [pathstr,name,ext] = fileparts(Current_filename);
    %Find the index at the beginnig of the word "Spot" of "spot" in filename
    spot = strfind(Current_filename,'Spot');
    if isempty(spot) == 1;
        spot = strfind(Current_filename,'spot');
    end

    %Find time (sec) from filename
    time_sec(j) = str2double(Current_filename(end-6:end-4)); %Stores time in sec
    if isnan(time_sec(j)) == 1;
        time_sec(j) = str2double(Current_filename(end-5:end-4));
    end
    if isnan(time_sec(j)) == 1;
        time_sec(j) = str2double(Current_filename(end-4:end-4));
    end
    time_min(j) = time_sec(j)/60; % Stores time in min

    new_name = strcat('Fit_',name);

    % ***** Performs Operations on Image
    I = imread(filenames{j});
    % Sharpen Image
    Isharp = imsharpen(I, 'radius',2,'amount',1.5);
    % Convert to black and white binary
    %***** use 2nd input for values between 0 and 1 for thresholding)
    % Lower number means higher gray values in each pixel are needed to be
    % turned to black. Higher number means pixels closer to white (light
    % gray) will still be turned to black
    BW = im2bw(Isharp, 0.4);
    % Convert such that droplet is white and background is black
    WB = imcomplement(BW);
    % Fill in holes
    WB2 = imfill(WB,'holes');

    % ***** Set Scale bar based on needle width *****
    scaleIndex = find(WB2(50,:)); %Finds needle width 50 pixels from top
    needlewidth = scaleIndex(end)+1/2-(scaleIndex(1)-1/2);
    Scale_barX = [scaleIndex(1)-1/2 scaleIndex(end)+1/2];
    pixel_mm = needlewidth/0.72; % length of needle in pixels/0.72 mm

```

```

%Find top of droplet by searching for next black pixel below middle of
%needle
needle_center = round((scaleIndex(1)+scaleIndex(end))/2);
rows = find(WB2(:,needle_center));
change = rows(diff(rows)~=1);
drop_top = rows(change(1)+1);

%Skips images that are distorted due to camera/stage shake
if (250 - drop_top) > 100
    continue
end

% ***** Finds boundaries in the image *****
[height,width] = size(I);
boundary = bwboundaries(WB2, 'noholes'); %Finds the boundary of the outer white edge of
the drop shape and all other white features in image
voids = cellfun('size',boundary,1); %Finds the number of data points in each array in
boundary

%Search through all arrays within "boundary" cell to find one that
%matches the outline for hte top of the droplet
for m=1:length(boundary)
    for n=1:length(boundary{m,1})
        if drop_top == boundary{m,1}(n,1)
            droplet_index = m;
        end
    end
end

outline = boundary{droplet_index,1}; %Returns boundary coordinates of the first image
feature (only 1 for WCA images)
x = outline(:,2); %defines x values of the outline from the 2nd column of the boundary
y = outline(:,1); %defines y values of the outline from the 1st column of the boundary

totalHeight = max(y)-min(y); %Height of top of edge to bottom, including reflection in
pixels

% ***** User-defined three-phase contact points (vertices) *****
figure(j)
imshow(Isharp)
fig = figure(j);
set (fig, 'Units', 'normalized', 'Position', [0,0,1,1]);
%User zooms into LEFT contact point region, clicks enter, then clicks on left contact
points, then clicks "enter"
zoom on
pause;
%datacursormode on
%pause;
[x_coord(1), y_coord(1), Pixel_value] = impixel;

```

```

close
zoom off
%datacursormode off

figure(j)
imshow(Isharp)
fig = figure(j);
set (fig, 'Units', 'normalized', 'Position', [0,0,1,1]);
%User zooms into RIGHT contact point region, clicks enter, then clicks on left contact
points, then clicks "enter"
hold on
plot([1,600],[y_coord(1),y_coord(1)],'r--');
zoom on
pause;
[x_coord(2), y_coord(2), Pixel_value] = impixel;
close
zoom off

%Calculate the substrate angle in degrees
substrate_angle = atan((y_coord(2)-y_coord(1))/(x_coord(2)-x_coord(1)))*180/pi();

xvertexLeft = x_coord(1);
xvertexRight = x_coord(2);
yvertexLeft = y_coord(1);
yvertexRight = y_coord(2);
CL_length = sqrt((x_coord(2)-x_coord(1))^2+(y_coord(2)-y_coord(1))^2); %Length in pixels
of contact line
CL_height = (yvertexLeft + yvertexRight)/2; %Height in pixels of contact line

% ***** Identifying Droplet Shape Parameters *****
%Find coordinates of top of droplet
yTop = min(y); % Top of drop, y-coordinate, in pixels
xTopFirstIndex = find(y == min(y), 1, 'first'); %left-most x index for ytop
xTopFirst = x(xTopFirstIndex); %value of left-most ytop x pixel
xTopLastIndex = find(y == min(y), 1, 'last'); %right-most x index for ytop
xTopLast = x(xTopLastIndex); % value of right-most ytop x pixel
xTopCenter = (xTopFirst + xTopLast)/2;% center of top of droplet, x coordinate

%Find the left and right edges of the droplet, looking at y values not at
%the top or the bottom of the green outline.

%Finds all the indices with non-zero values droplet top and
%above intersection line

LeftRightEdgeIndex = find(y >= min(y) & y < CL_height & x >= x_coord(1) & x <=
x_coord(2));
x_drop = x(LeftRightEdgeIndex);
y_drop = y(LeftRightEdgeIndex);

%Perform fitting of top half of ellipse to outline

```

```

%Initial guess of fitting parameters
param0(1) = (x_coord(2)-x_coord(1))/2; %major radius, half the distance between user-
selected 3-phase points
param0(2) = y_coord(1)-yTop; %minor radius, diffence between top of drop and 3-phase
contact line
param0(3) = y_coord(2); %vertical offset, height of 3-phase contact points
param0(4) = xTopCenter; %Horizontal offset

%Function to minimize sum of square differences between outline and
%function

%Top half of ellipse: yPos = k - b*sqrt(1-(x-h)^2/a^2)
yPosFun = @(param,xdata)param(3)-param(2)*sqrt(1-((xdata-param(4)).^2/param(1)^2));

[param,resnorm,residual,exitflag,output,lambda,jacobian] =
lsqcurvefit(yPosFun,param0,x_drop,y_drop);

%Ignoring imaginary parts of parameters
a = real(param(1)); %major radius
b = real(param(2)); %minor radius
k = real(param(3)); %vertical offset
h = real(param(4)); %horizontal offset

%Ignoring imaginary parts of parameters
real_param = real(param);
real_res = real(residual);
real_jac = real(jacobian);

%Determine 95% confidence intervals on 4 parameters, a, b, h, k (rows
%1-4). Lower bounds are column 1, upper bounds are column 2
conf = nlparci(real_param,real_res,'jacobian',real_jac);
a_upper = conf(1,2);
a_lower = conf(1,1);
a_bounds = ((a_upper - a) + (a - a_lower))/2;
b_upper = conf(2,2);
b_lower = conf(2,1);
b_bounds = ((b_upper - b) + (b - b_lower))/2;

% Define x-values (in pixels) that will be used to fit ellipse
x_e11 = zeros(length(x_drop)+50,1);
yPos = zeros(length(x_e11),1);
yNeg = zeros(length(x_e11),1);

for i=1:1:25
    x_e11(i) = x_drop(1)-(25-i);
end

for i=26:1:length(x_drop)+25
    x_e11(i) = x_drop(i-25);

```

```

end
n=1;
for i=length(x_drop)+25:1:length(x_drop)+50;
    x_ell(i) = x_drop(end)+n;
    n=n+1;
end

% Fill vectors for top and bottom half of ellipse
for i=1:length(x_ell);
    yPos(i) = k - b*sqrt((1-(x_ell(i)-h).^2/a^2));
    yNeg(i) = k + b*sqrt((1-(x_ell(i)-h).^2/a^2));
end

%Measure of Goodness-of-fit for ellipse to droplet
r2 = real(1 - resnorm/sum((yPos-mean(yPos)).^2)); %Should be close to 1
RootMSE = sqrt(resnorm/(length(y_drop)-4));

%   if length(x_drop) > 275
%       RootMSE = sqrt(resnorm/(length(y_drop_top_final)-4)); %Should be close to 0
%   else
%       RootMSE = sqrt(resnorm/(length(y_drop_top)-4));
%   end

%Define major and minor radii of ellipse, in mm
amm = a/pixel_mm;
bmm = b/pixel_mm;

amm_bounds = a_bounds/pixel_mm;
bmm_bounds = b_bounds/pixel_mm;

% ***** Contact Angle and Drop Parameters Calculations *****
% Determine contact angle based on slope of tangent line to ellipse at
% intersection of base contact line and ellipse

ydist = k - CL_height; % Distance from contact line to height of major axis
Drop_Height = CL_height - yTop; % Height of drop, in pixels

slope = -b*sqrt((b^2)-(ydist^2))/(a*ydist);

%Bounds of slope, 95% confidence from fitting ellipse
slope_high = -b_upper*sqrt((b_upper^2)-(ydist^2))/(a_lower*ydist);
slope_low = -b_lower*sqrt((b_lower^2)-(ydist^2))/(a_upper*ydist);

%Bounds of contact angle, CA, 95% confidence from fitting ellipse
CA_upper = abs(atan(slope_low))/(pi()/180);
CA_lower = abs(atan(slope_high))/(pi()/180);

%Tangent lines
LeftTan = [20/slope+x_coord(1) y_coord(1)+20; -75/slope+x_coord(1) y_coord(1)-75];

```

```

%LeftTan = [x_coord(1) y_coord(1); -75/slope+x_coord(1) y_coord(1)-75];
RightTan = [-20/slope+x_coord(2) y_coord(2)+20; 75/slope+x_coord(2) y_coord(2)-75];
%RightTan = [x_coord(2) y_coord(2); 75/slope+x_coord(2) y_coord(2)-75];

% Drop Parameters, Hydrophilic, < 90 deg.
CA = abs(atan(slope))/(pi()/180); %Hydrophilic, <90 deg.
CA_bounds = ((CA_upper - CA) + (CA - CA_lower))/2;

DBA = pi()*(CL_length/pixel_mm)^2/4; %Drop Base Area

DV = ((pi()*a^2)/(3*b^2)*Drop_Height^2*(3*b-Drop_Height))/((pixel_mm)^3); %Drop volume
DV_upper = ((pi()*a_upper^2)/(3*b_upper^2)*Drop_Height^2*(3*b_upper-
Drop_Height))/((pixel_mm)^3); %Max drop volume
DV_lower = ((pi()*a_lower^2)/(3*b_lower^2)*Drop_Height^2*(3*b_lower-
Drop_Height))/((pixel_mm)^3); %Min drop volume
DV_bounds = abs((DV_upper - DV) + (DV - DV_lower))/2;

e11 = sqrt((a^2)/(b^2)-1); %Ellipticity = sqrt(a^2/b^2-1)
e112 = 1-Drop_Height/b; % ellipticity_2 = 1 - drop height/minor axis
DSA = pi()*amm*bmm*(amm/bmm-e112*sqrt(1+e11.^2*e112.^2)+1/e11*(asinh(e11)-
asinh(e11*e112)));

% write results to a matrix cell
Results(j+1,:) = {filenames{j}, time_sec(j), time_min(j), pixel_mm, amm, bmm,
Drop_Height/pixel_mm, CL_length/pixel_mm, CA, DBA, DV, DSA, substrate_angle, r2, RootMSE,
amm_bounds, bmm_bounds, CA_bounds, DV_bounds};

% Visualize results
figure(j)
imshow(I)
axis ij
axis equal
axis on
hold on
set(gca,'TickDir','in')
title(Current_filename(1:spot+5),'interpreter','none')

% Plot scalebar
plot(Scale_barX,[50 50],'r-','Linewidth',0.5)

%Plot outline of ellipse itself
plot(x_e11,yPos,'r','Linewidth',0.5)
plot(x_e11,yNeg,'r','Linewidth',0.5)

%Plot boundary determined from Matlab function
plot(x,y, 'g:', 'Linewidth', 0.5)
%plot(x_drop,y_drop, 'g:', 'Linewidth', 1)

%Plot tangent lines

```

```

plot(LeftTan(:,1),LeftTan(:,2), 'b','Linewidth',0.5)
plot(RightTan(:,1),RightTan(:,2), 'b','Linewidth',0.5)

%Plot user-defined 3-phase contact line points
plot(x_coord,y_coord,'y--','Linewidth',0.5)
plot(x_coord,y_coord,'yx', 'Markersize', 3,'Linewidth',0.5)

%Output drop parameters to image and PDF file
str = sprintf('Contact Time = %.2f min \nContact Angle = %.2f +/- %.2f\\circ \nDrop
Volume = %.2f +/- %.2f \\muL \nDrop Base Area = %.2f mm^2 \nDrop Surface Area %.2f mm^2
\nSubstrate Angle = %.2f\\circ \nEllipse R^2 =
%.4f',time_min(j),CA,CA_bounds,DV,DV_bounds,DBA,DSA,substrate_angle,r2);
text(20,75,str)
str2 = sprintf('%.2f pixels/mm',pixel_mm);
text(Scale_barX(2)+15,50,str2)
print(gcf,fullfile(fpath,name),'-dpdf');
print(gcf,fullfile(fpath,name),'-dtiff');
close
end
xlswrite(name(1:end-3),Results);

```

[Published with MATLAB® R2015a](#)

References

1. Brantley, S. L., White, A. F. & Hodson, M. E. in *Growth, Dissolution and Pattern Formation in Geosystems* (eds. Jamtveit, B. & Meakin, P.) 291–326 (Springer Netherlands, 1999). doi:10.1007/978-94-015-9179-9_14
2. Israelachvili, J. N. in *Intermolecular and Surface Forces* 415–467 (Academic Press, 2011). doi:10.1016/B978-0-12-375182-9.10017-X
3. Surface Tension. *Wikipedia* at <https://en.wikipedia.org/wiki/Surface_tension>
4. Legrand, D. G. & Gaines, G. L. The molecular weight dependence of polymer surface tension. *J. Colloid Interface Sci.* **31**, 162–167 (1969).
5. Kobayashi, H. & Owen, M. J. Surface Tension of liquid polysiloxanes having fluorinated alkyl side-chains. *Die Makromol. Chemie* **194**, 1785–1792 (1993).
6. Berry, J. D., Neeson, M. J., Dagastine, R. R., Chan, D. Y. C. & Tabor, R. F. Measurement of surface and interfacial tension using pendant drop tensiometry. *J. Colloid Interface Sci.* **454**, 226–237 (2015).
7. du Nouy, P. L. A NEW APPARATUS FOR MEASURING SURFACE TENSION. *J. Gen. Physiol.* **1**, 521–524 (1919).
8. du Nouy, P. L. AN INTERFACIAL TENSIO METER FOR UNIVERSAL USE. *J. Gen. Physiol.* **7**, 625–631 (1925).
9. Jalbert, C., Koberstein, J. T., Yilgor, I., Gallagher, P. & Krukonis, V. Molecular weight dependence and end-group effects on the surface tension of poly(dimethylsiloxane). *Macromolecules* **26**, 3069–3074 (1993).
10. Chaudhury, M. K. & Whitesides, G. M. Direct measurement of interfacial interactions between semispherical lenses and flat sheets of poly(dimethylsiloxane) and their chemical derivatives. *Langmuir* **7**, 1013–1025 (1991).
11. Genzer, J. & Efimenko, K. Recent developments in superhydrophobic surfaces and their relevance to marine fouling: a review. *Biofouling* **22**, 339–360 (2006).
12. Young, T. An Essay on the Cohesion of Fluids. *Philos. Trans. R. Soc. London* **95**, 65–87 (1805).
13. Wenzel, R. N. RESISTANCE OF SOLID SURFACES TO WETTING BY WATER. *Ind. Eng. Chem.* **28**, 988–994 (1936).
14. Cassie, A. B. D. & Baxter, S. Wettability of porous surfaces. *Trans. Faraday Soc.* **40**,

546 (1944).

15. Simpson, J. T., Hunter, S. R. & Aytug, T. Superhydrophobic materials and coatings: a review. *Reports Prog. Phys.* **78**, 86501 (2015).
16. Shanahan, M. & Carre, A. Viscoelastic dissipation in wetting and adhesion phenomena. *Langmuir* 1396–1402 (1995). at <<http://pubs.acs.org/doi/abs/10.1021/la00004a055>>
17. Shanahan, M. & Carré, A. Spreading and dynamics of liquid drops involving nanometric deformations on soft substrates. *Colloids Surfaces A Physicochem. ...* **206**, 115–123 (2002).
18. Cao, Z. & Dobrynin, A. V. Polymeric Droplets on Soft Surfaces: From Neumann's Triangle to Young's Law. *Macromolecules* **48**, 443–451 (2015).
19. Park, S. J. *et al.* Visualization of asymmetric wetting ridges on soft solids with X-ray microscopy. *Nat. Commun.* **5**, 4369 (2014).
20. Lester, G. . Contact angles of liquids at deformable solid surfaces. *J. Colloid Sci.* **16**, 315–326 (1961).
21. Shanahan, M. E. R. The spreading dynamics of a liquid drop on a viscoelastic solid. *J. Phys. D. Appl. Phys.* **21**, 981–985 (1988).
22. Shanahan, M. E. R. Anomalous Spreading. 1647–1649 (1994).
23. Carre, A. & Shanahan, M. E. R. Direct Evidence for Viscosity-Independent Spreading on a Soft Solid. *Langmuir* **11**, 24–26 (1995).
24. Carré, A., Gastel, J. & Shanahan, M. Viscoelastic effects in the spreading of liquids. *Nature* **379**, 432–434 (1996).
25. Long, D., Ajdari, A. & Leibler, L. Static and dynamic wetting properties of thin rubber films. *Langmuir* **12**, 5221–5230 (1996).
26. Carré, A. & Shanahan, M. Effect of cross-linking on the dewetting of an elastomeric surface. *J. Colloid Interface Sci.* **191**, 141–145 (1997).
27. Style, R. W. & Dufresne, E. R. Static wetting on deformable substrates, from liquids to soft solids. *Soft Matter* **8**, 7177 (2012).
28. Style, R. W. *et al.* Universal deformation of soft substrates near a contact line and the direct measurement of solid surface stresses. *Phys. Rev. Lett.* **110**, 1–5 (2013).
29. Style, R. W., Hyland, C., Boltyanskiy, R., Wettlaufer, J. S. & Dufresne, E. R. Surface

- tension and contact with soft elastic solids. *Nat. Commun.* **4**, 2728 (2013).
30. Style, R. W. *et al.* Patterning droplets with durotaxis. *Proc. Natl. Acad. Sci. U. S. A.* **110**, 12541–4 (2013).
 31. Jensen, K. E. *et al.* Wetting and phase separation in soft adhesion. *Proc. Natl. Acad. Sci.* **112**, 14490–14494 (2015).
 32. Style, R. W., Jagota, A., Hui, C.-Y. & Dufresne, E. R. Elastocapillarity: Surface Tension and the Mechanics of Soft Solids. *Soft Condens. Matter* 1–20 (2016). doi:10.1073/pnas.1607893113
 33. Genzer, J. & Efimenko, K. Creating Long-Lived Superhydrophobic Polymer Surfaces Through Mechanically Assembled Monolayers. *Science (80-.)*. **290**, 2130–2133 (2000).
 34. Cao, M. *et al.* Water-Repellent Properties of Superhydrophobic and Lubricant-Infused ‘Slippery’ Surfaces: A Brief Study on the Functions and Applications. *ACS Appl. Mater. Interfaces* 151008094034001 (2015). doi:10.1021/acsami.5b07881
 35. Grozea, C. M. & Walker, G. C. Approaches in designing non-toxic polymer surfaces to deter marine biofouling. *Soft Matter* **5**, 4088 (2009).
 36. Banerjee, I., Pangule, R. C. & Kane, R. S. Antifouling coatings: Recent developments in the design of surfaces that prevent fouling by proteins, bacteria, and marine organisms. *Adv. Mater.* **23**, 690–718 (2011).
 37. Zhang, H. & Chiao, M. Anti-fouling coatings of poly(dimethylsiloxane) devices for biological and biomedical applications. *J. Med. Biol. Eng.* **35**, 143–155 (2015).
 38. Magennis, E. P., Hook, A. L., Williams, P. & Alexander, M. R. Making Silicone Rubber Highly Resistant to Bacterial Attachment Using Thiol-ene Grafting. *ACS Appl. Mater. Interfaces* **8**, 30780–30787 (2016).
 39. Galhenage, T. P. *et al.* Fouling-Release Performance of Silicone Oil-Modified Siloxane-Polyurethane Coatings. *ACS Appl. Mater. Interfaces* **8**, 29025–29036 (2016).
 40. Lejars, M., Margailan, A. & Bressy, C. Fouling release coatings: A nontoxic alternative to biocidal antifouling coatings. *Chem. Rev.* **112**, 4347–4390 (2012).
 41. Xia, Y. & Whitesides, G. M. SOFT LITHOGRAPHY. *Annu. Rev. Mater. Sci.* **28**, 153–184 (1998).
 42. Duffy, D. C., McDonald, J. C., Schueller, O. J. A. & Whitesides, G. M. Rapid prototyping of microfluidic systems in poly(dimethylsiloxane). *Anal. Chem.* **70**, 4974–4984 (1998).

43. McDonald, J. C. *et al.* Fabrication of microfluidic systems in poly(dimethylsiloxane). *Electrophoresis* **21**, 27–40 (2000).
44. Whitesides, G. M., Ostuni, E., Takayama, S., Jiang, X. & Ingber, D. E. Soft Lithography in Biology and Biochemistry. *Annu. Rev. Biomed. Eng.* **3**, 335–373 (2001).
45. McDonald, J. C. & Whitesides, G. M. Poly(dimethylsiloxane) as a material for fabricating microfluidic devices. *Acc. Chem. Res.* **35**, 491–499 (2002).
46. Sia, S. K. & Whitesides, G. M. Microfluidic devices fabricated in Poly(dimethylsiloxane) for biological studies. *Electrophoresis* **24**, 3563–3576 (2003).
47. Efimenko, K., Wallace, W. E. & Genzer, J. Surface Modification of Sylgard-184 Poly(dimethyl siloxane) Networks by Ultraviolet and Ultraviolet/Ozone Treatment. *J. Colloid Interface Sci.* **254**, 306–315 (2002).
48. Hillborg, H. & Gedde, U. W. Hydrophobicity recovery of polydimethylsiloxane after exposure to corona discharges. *Polymer* **39**, 1991–1998 (1998).
49. Hillborg, H. & Gedde, U. W. Hydrophobicity changes in silicone rubbers. *IEEE Trans. Dielectr. Electr. Insul.* **6**, 703–717 (1999).
50. Hillborg, H., Tomczak, N., Oláh, A., Schönherr, H. & Vancso, G. J. Nanoscale hydrophobic recovery: A chemical force microscopy study of UV/ozone-treated cross-linked poly(dimethylsiloxane). *Langmuir* **20**, 785–794 (2004).
51. Oláh, A., Hillborg, H. & Vancso, G. J. Hydrophobic recovery of UV/ozone treated poly(dimethylsiloxane): adhesion studies by contact mechanics and mechanism of surface modification. *Appl. Surf. Sci.* **239**, 410–423 (2005).
52. Kim, J., Chaudhury, M. K. & Owen, M. J. Hydrophobic Recovery of Polydimethylsiloxane Elastomer Exposed to Partial Electrical Discharge. *J. Colloid Interface Sci.* **226**, 231–236 (2000).
53. Hassler, C., Boretius, T. & Stieglitz, T. Polymers for neural implants. *J. Polym. Sci. Part B Polym. Phys.* **49**, 18–33 (2011).
54. Halldorsson, S., Lucumi, E., Gómez-Sjöberg, R. & Fleming, R. M. T. Advantages and challenges of microfluidic cell culture in polydimethylsiloxane devices. *Biosens. Bioelectron.* **63**, 218–231 (2015).
55. Brindley, G. S. The first 500 sacral anterior root stimulators: implant failures and their repair. *Paraplegia* **33**, 5–9 (1995).
56. Regehr, K. J. *et al.* Biological implications of polydimethylsiloxane-based microfluidic

- cell culture. *Lab Chip* **9**, 2132 (2009).
57. Farasani, A. & Darbre, P. D. Exposure to cyclic volatile methylsiloxanes (cVMS) causes anchorage-independent growth and reduction of BRCA1 in non-transformed human breast epithelial cells. *J. Appl. Toxicol.* 454–461 (2016). doi:10.1002/jat.3378
 58. Lee, J. N., Park, C. & Whitesides, G. M. Solvent Compatibility of Poly(dimethylsiloxane)-Based Microfluidic Devices. *Anal. Chem.* **75**, 6544–6554 (2003).
 59. Lubarda, V. A. & Talke, K. A. Analysis of the Equilibrium Droplet Shape Based on an Ellipsoidal Droplet Model. *Langmuir* **27**, 10705–10713 (2011).
 60. Efimenko, K. & Genzer, J. How to prepare tunable planar molecular chemical gradients. *Adv. Mater.* **13**, 1560–1563 (2001).
 61. Gao, L. & McCarthy, T. J. A Perfectly Hydrophobic Surface ($\theta_A / \theta_R = 180^\circ / 180^\circ$). *J. Am. Chem. Soc.* **128**, 9052–9053 (2006).
 62. Miyagi, T., Sasahara, A. & Tomitori, M. Water wettability of Si(111) and (001) surfaces prepared to be reconstructed, atomic-hydrogen terminated and thinly oxidized in an ultrahigh vacuum chamber. *Appl. Surf. Sci.* **349**, 904–910 (2015).
 63. Cao, L., Hu, H. A. & Gao, D. Design and fabrication of micro-textures for inducing a superhydrophobic behavior on hydrophilic materials. *Langmuir* **23**, 4310–4314 (2007).
 64. Cao, L., Price, T. P., Weiss, M. & Gao, D. Super Water- and Oil-Repellent Surfaces on Intrinsically Hydrophilic and Oleophilic Porous Silicon Films. *Langmuir* **24**, 1640–1643 (2008).
 65. Miramond, C. & Vuillaume, D. 1-Octadecene monolayers on Si(111) hydrogen-terminated surfaces: Effect of substrate doping. *J. Appl. Phys.* **96**, 1529–1536 (2004).
 66. Thissen, P. *et al.* Activation of surface hydroxyl groups by modification of H-terminated Si(111) surfaces. *J. Am. Chem. Soc.* **134**, 8869–8874 (2012).
 67. Hourlier-Fargette, A., Antkowiak, A., Chateauminois, A. & Neukirch, S. Role of uncrosslinked chains in droplets dynamics on silicone elastomers. *Soft Matter* **13**, 3484–3491 (2017).
 68. Hunter, M. J., Hyde, J. F., Warrick, E. L. & Fletcher, H. J. Organo-Silicon Polymers. The Cyclic Dimethyl Siloxanes *. *J. Am. Chem. Soc.* **68**, 667–672 (1946).
 69. Fox, H., Taylor, P. & Zisman, W. Polyorganosiloxanes...Surface Active Properties. *Ind. Eng. Chem.* **39**, 1401–1409 (1947).

70. Flaningam, O. L. Vapor pressures of poly(dimethylsiloxane) oligomers. *J. Chem. Eng. Data* **31**, 266–272 (1986).
71. Butts, M. *et al.* in *Kirk-Othmer Encyclopedia of Chemical Technology* (John Wiley & Sons, Inc., 2002). doi:10.1002/0471238961.1909120918090308.a01.pub2
72. Varaprath, S., Frye, C. L. & Hamelink, J. Aqueous Solubility of Permethylsiloxanes (Silicones). *Environ. Toxicol. Chem.* **15**, 1263–1265 (1996).

CHAPTER 6: Summary & Outlook

Summary

Chapter 1

In chapter 1 we introduced PDMS and demonstrated examples of its many advantages over purely hydrocarbon and alkane-backbone based polymers. The expanding use of a commercial silicone elastomer, Sylgard 184, in numerous research communities was brought to light. The challenges that arise from using commercial materials, such as imprecise knowledge of chemical composition and, likely, non-ideal network topology were mentioned. We also noted that a direct comparison between two common forms of model PDMS, vinyl/TDSS and silanol/TEOS, has not been published to the best of our knowledge. The overarching goal of this Ph.D. dissertation has been to provide molecular level structure to macroscopic property relationships by systematically investigating the performance of PDMS materials made from two different model crosslinking reactions and a commercial product.

Chapter 2

We began our analysis in chapter 2 of this dissertation by providing the preparation details for making silicone elastomers that were studied throughout the remainder of the dissertation. Two model systems, vinyl/TDSS and silanol/TEOS, and one commercial product were prepared from silicones with a variety of different molecular weights and crosslinking stoichiometric ratios while maintaining the same curing conditions (temperature and time) and relative amounts of catalyst (see chapters 2-5 for details). The gel fractions of the networks were calculated by measuring the mass of samples before and after Soxhlet extraction in toluene, which allowed molecules that were not covalently attached to or permanently trapped in the network to diffuse out of the gel and into the pure toluene solvent, thus lowering the sample mass. The influence of stoichiometric ratio on gel fraction was examined. We found that a rapid increase in gel fraction occurs with minimal increases in crosslinker loading for all systems up to an optimal level of crosslinker loading. From there, the gel fraction plateaued

with increasing crosslinker loading. For the vinyl/TDSS and Sylgard systems, we observed a decrease in gel fraction at large excesses of crosslinker, but not for the silanol/TEOS system. This is due to the TEOS molecule being able to react with itself, but TDSS (and all silicone hydride, Si-H, functional groups) being unable to react with itself. When a massive excess of TEOS was added, the crosslinker molecules clustered together and formed aggregates, which were verified by SEM. In contrast, when a massive excess of TDSS was present, these crosslinker molecules reacted individually with each polymer chain end, but with no other unique polymer chains, thus creating an “end-capping” effect that causes those chains to become inert and part of the sol fraction.

Chapter 3

Next, in chapter 3, we used the knowledge of precise chemical composition and the extent of the gelation reactions as inputs to a polymer network theory called the Miller-Macosko model.^{1,2} This powerful model, which has been verified experimentally,³ provided a plethora of information pertaining to the network topology, such as the fractions of elastic and pendant material, the molecular weight between chemical crosslinks, and the average effective functionality of the crosslinker molecule, which, did not fully react. Significant differences for networks formed from polymers below and above the critical molecular weight of entanglement were noted. Specifically, samples prepared from the lowest molecular weight achieved the highest average crosslinker functionality and highest elastic fraction. We infer that this behavior has to do with reactive groups being present in lower concentrations for high molecular weight systems and reduced chain mobility for samples above the entanglement molecular weight, which limits the extent of the gelation reaction. The derivations of the model and the final equations used to determine such parameters are not trivial, but taking the time to understand them and apply them is worth the effort based on the vast topological network knowledge gained.

Chapter 4

The findings from the Miller-Macosko model revealed information about network topology and have ramifications specifically on the dynamic mechanical properties of silicone elastomers. Hence, in chapter 4, we investigated those properties. We performed dynamic mechanical analyses on both vinyl/TDSS and silanol/TEOS model systems as well as Sylgard 184 to elucidate both the viscous and elastic responses of these materials. We found that the silanol/TEOS system demonstrated a broader range of possible mechanical properties, depending on the material composition. That is, the mechanical properties depended more strongly on molecular weight and crosslinking stoichiometry in this system compared to the vinyl/TDSS system. Overall, the possibilities of purely polymeric materials were limited in that only strong and brittle or soft and flexible materials could be made, as opposed to both strong and flexible materials with particles. The samples with massive excess in TEOS loading formed aggregates and exhibited similar mechanical properties to Sylgard 184, which is known to contain up to 50% of fumed silica particles added. The addition of particles to polymer networks adds both strength and flexibility by creating a secondary network of filler particles and creates additional surfaces wherein polymer-filler and filler-filler interactions provide for dissipation mechanisms. We showed that the dynamic mechanical properties of storage modulus, loss modulus, and $\tan(\delta)$ together demonstrate the advantages of Sylgard 184 and filled polymer composite materials over purely polymer materials.

The topological network parameters obtained from the Miller-Macosko model were compared to the dynamic mechanical properties in the vinyl/TDSS system. We found that the storage modulus correlated well with the elastic fraction (*i.e.*, the fraction of material that is elastically effective) and the stoichiometric ratio that yielded the highest storage modulus also coincided with the highest average effective crosslinker functionality. Additionally, $\tan(\delta)$, a measure of the material's ability to dissipate forces and energy, correlated with a maximum in pendant fraction (*i.e.*, the fraction of material that is not elastically effective). By independently measuring network gel fraction and mechanical properties, and comparing them to outputs from the model, we demonstrated the strength of all three techniques to fully characterize the PDMS materials. This analysis elucidated how and why materials act the way

they do under macroscopic deformations. Their behavior was related back to molecular level topology.

We also demonstrated the importance of the Soxhlet extraction technique in this chapter by comparing the mechanical properties of Sylgard 184 before and after extraction. The loss modulus was shown to change dramatically for Sylgard 184 materials prepared at sub- and super-optimal stoichiometry, particularly when deviating 5-fold in either direction from the prescribed 10:1 base to curing agent ratio. This reveals the role that material in the sol fraction plays, such as acting like plasticizers to make materials softer. Finally, we performed classical stress-strain experiments on Sylgard 184 samples of different formulations and revealed how the extent of crosslinking changed the material's ultimate performance. Samples that were under-crosslinked could be stretched to large strains with very little applied stress, while the opposite was true for optimally crosslinked materials. Overall, the systematic investigation of mechanical properties enabled us to present a cookbook of recipes for making model PDMS materials over a wide range of mechanical properties.

Chapter 5

Lastly, in chapter 5, we investigated the dynamic behavior of water droplets wetting PDMS substrates. We observed non-linear wetting behaviors that were markedly different from linear behaviors seen on glassy polymer substrates. The water contact angle, θ , and $\cos(\theta)$ both decreased exponentially and the interfacial area between the water droplet and the substrate, *i.e.*, the base area, increased exponentially with contact time until both leveled off reaching some equilibrium value. The dynamic wetting behavior on model vinyl PDMS was compared to Sylgard 184 on samples both before and after the extraction process. The non-linear behavior was only observed prior to extraction, while after extraction, both systems demonstrated behavior similar to glassy polymers. That is, the post-extraction samples rapidly reached equilibrium because the water droplets were encountering a largely static substrate, as opposed to pre-extraction samples that contained uncrosslinked materials that were mobile and could migrate to the interface. This reveals the dramatic role small amounts of uncrosslinked materials play in the surface wetting dynamics of PDMS materials.

We demonstrated the dynamic nature of the interfacial energy between water and PDMS further by taking the product of the interfacial area and the negative cosine of the contact angle, which elucidates the changes in interfacial energy with respect to the probing liquid, water. After that, we briefly compared the wetting behavior to mechanical properties for Sylgard 184 materials. Here, we found that the percent change in loss modulus as a result of the extraction process correlated most with the change in $\cos(\theta)$ with respect to contact time prior to extraction. There was also a nonlinear correlation between storage modulus and change in $\cos(\theta)$. Lastly, we revealed the ability to tune the dynamic wetting behavior by incorporating extra inert silicone oils into otherwise fully crosslinked materials, thereby controlling both the amount and type of material that is present in the soluble fraction and able to migrate to the water-PDMS interface. We found a lag time in the decrease in contact angle as a function of time. This lag time was shorter for lower molecular weight oils and longer for higher molecular weight oils, indicating the mobility of the sol material is crucial in wetting dynamics.

Conclusions

Overall, we hope we have demonstrated that through careful formulation and preparation of PDMS materials, compared to simply mixing two formulations present in Sylgard 184, one can apply polymer network models to glean useful information about network topology, and that the benefits of doing so outweigh the costs. We stress the importance of performing Soxhlet extraction to remove substantial amounts of unreacted components from PDMS materials, even when using optimal stoichiometry. These mobile molecules that remain after crosslinking can alter significantly wetting behavior and readily leach into liquid environments. However, it is equally important to stress that Soxhlet extraction will not remove all unreacted material. Some will always remain in PDMS systems, especially if the materials have been physically treated in such a way as to cause chain scission, which is often the practice in preparing microfluidic devices. Lastly, while Sylgard 184 is very well suited for some applications, we believe that the results presented in this dissertation demonstrate to researchers that the material does have its limitations and that other options are available.

Outlook

The parameter space for preparing silicone materials is vast and only a small fraction was explored in this dissertation. We emphasized the importance of molecular architecture and its relationship to macroscopic properties as well as the importance of the sol fraction in dynamic wetting properties. However, the architectures we studied were limited to tetrafunctional crosslinkers connected by chains of varying but unimodal molecular weight distributions. In one system, the crosslinker could react with itself, and in the other, it could not. The molecular architecture can be changed in many more ways than those we studied. Now that the fundamentals of polymer network topology have been elucidated with tetrafunctional end-linking PDMS systems, this knowledge can be used to design materials of more complicated architectures. Some examples of opportunities for interesting and useful architectures are outlined in the following section.

Mechanical Properties

While our dynamic mechanical analysis of model PDMS materials was thorough, more opportunities exist to study the stress-strain behavior these materials to elucidate their ultimate properties. Beyond the model PDMS systems we studied, ample opportunities exist for enhancing the mechanical properties of silicone materials by further investigations of network architecture. Below we outline some proposed areas of research.

Composite Materials

We demonstrated clearly in chapter 4 of this dissertation that composite materials that contain both polymers and particles exhibit superior dynamic mechanical properties. The samples we prepared that had TEOS aggregates performed similarly to Sylgard 184. Fumed silica particles are common fillers in PDMS materials, but a variety of fillers exist that can provide additional functionality such as electrical conductivity or magnetic responses in addition to simply enhancing mechanical properties.^{4,5} With the use of magnetic nanoparticles, one can impart anisotropy into the materials by aligning particles prior to crosslinking, then locking them in place by curing. Such work has been explored in various polymers⁶ and in

PDMS materials.⁷ Opportunities for further research involve a systematic study of TEOS aggregation as a function of TEOS loading, molecular weight of polymer chains, catalyst type and amount, and reaction conditions. Some work in this area has been done by Mark and co-workers who studied excess TEOS during crosslinking,⁸ similar to the work done in this dissertation, and studied swelling PDMS in TEOS after curing and precipitating aggregates into the network.⁹ Only stress-strain rather than dynamic mechanical properties were investigated in these systems, however. It would be advantageous to determine if *in situ* or mechanically blended particles produce better mechanical properties. The *in situ* method has the advantage of reducing the uncertainty of blending into the preparation of the materials. Processing and blending conditions can alter mechanical properties significantly if, for instance, particles are dispersed well enough.

High Crosslinker Functionality

In regard to preparing model networks, we only studied tetrafunctional crosslinkers. Sylgard 184 uses a higher functionality crosslinker in the form a copolymer chain. This material demonstrated a robustness in its ability to maintain similar wetting properties over a wide range of B/C ratios whereas the model PDMS prepared showed a more narrow range of constant wetting properties with respect to stoichiometric ratio. Thus, higher functionality crosslinker molecules are a good area to explore in model networks. When switching to copolymers, however, as the crosslinking copolymer gets large, the system resembles less end-linking and more side-chain crosslinking, where the molecular weight between chemical crosslinks is less uniform. The stress-strain behavior of higher functionality crosslinks was investigated by Meyers *et al.* who found the Young's modulus increased until about a functionality equal to 20, after which the modulus plateaued for further increases.¹⁰ Similar results were found by Llorente and Mark.¹¹ Such systems would be interesting to study using dynamic mechanical properties in addition to stress-strain experiments to determine how the loss modulus and $\tan(\delta)$ change with increasing functionality.

Multi-Modal Chain Length Distributions

In this dissertation, we studied PDMS with a variety of molecular weights in preparing silicone elastomers. They all had unimodal chain length distributions. Making materials of bimodal or multi-modal chain length distributions has been shown to enhance mechanical properties. For example, double network hydrogels prepared with a short chain, stiff network and a secondary high molecular weight flexible network exhibited enhanced toughness over either of the unimodal networks used to make them.^{12,13} Additionally, PDMS materials, that are simultaneously crosslinked with a combination of ~ 90 mol% short chains and the remainder long chains, thus forming a single network with a bimodal chain length distribution, have been shown to increase ultimate stress and strain of materials significantly.^{14,15} Even trimodal chain length distributions have been explored,¹⁶ although the parameter space in such systems is immense. Overall, heterogeneity in the network structure may actually be key to enhancing mechanical properties, as opposed to uniform chain length distributions.

Chain Extension Elastomers

In chapter 3 of this dissertation, we demonstrated that the Miller-Macosko model identified many instances of chain extension in our model systems. The model also showed that the highest elastic fraction and highest crosslinker functionality was achieved with the lowest molecular weight system, 6 kDa, which was well below the entanglement molecular weight. Even at optimal crosslinking stoichiometry, the model predicted a molecular weight between chemical crosslinks of ~ 10 kDa for this system, indicating chain extension was still occurring. Recently, Goff *et al.* demonstrated that PDMS materials made of solely chain extension reactions exhibit remarkably high extensions before rupture and can be deformed to very high strains and return back to their original shape.¹⁷ They synthesized PDMS materials with one end hydride functional and the other end vinyl functional, then added a platinum hydrosilylation catalyst. Thus, we propose investigating systems formed by chain extension with short, commercially available PDMS precursors. This has the potential dual advantage of creating highly stretchable materials while achieving high extents of reaction.

We have done some preliminary work in this area by combining hydride-terminated and vinyl-terminated PDMS materials with different molecular weights and amounts and types of catalysts. The reaction scheme and mechanical properties are given in Figure 6.1 a) and b), respectively. Networks seem to form only under certain conditions with only low molecular weight initial polymers. When they do form, gelation occurs rapidly at room temperature in a matter of minutes. Gelation may not be occurring for high molecular weights due to reaction-diffusion limitations in high molecular weight polymers. The resulting materials are incredibly soft but can still be measured in tension for dynamic mechanical properties. The parallel storage and loss moduli indicate a network-like structure, albeit the system is scarcely crosslinked since the storage modulus does not exhibit frequency-independent behavior. Nevertheless, these elastomers provide an exciting and interesting system to explore for fabricating soft materials.

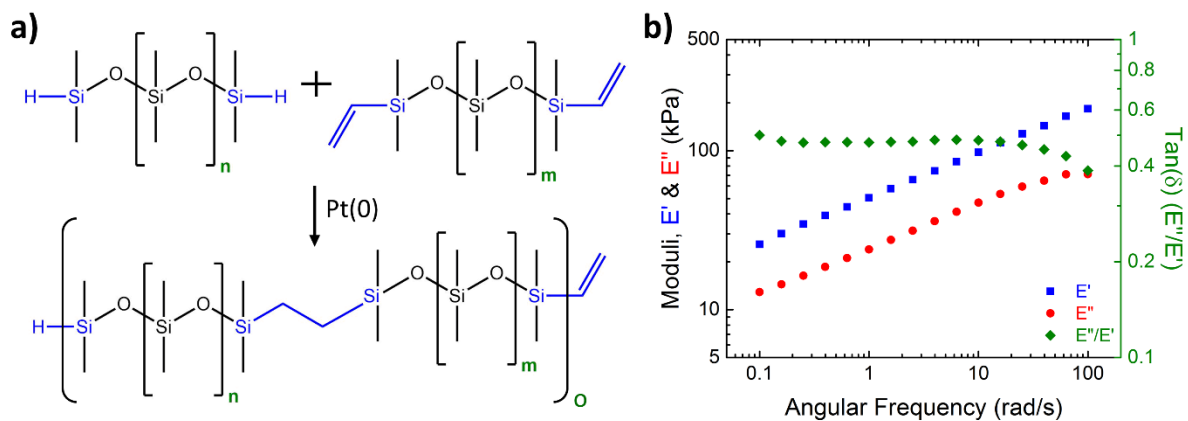


Figure 6.1 – Elastomers formed solely by chain extension through the combination of hydride- and vinyl-terminated PDMS with a Pt catalyst (a) and corresponding dynamic mechanical properties (b).

Bottlebrush Polymers

Other architectures to explore in creating soft materials involve so-called “bottlebrush” polymers. These are classified as graft-copolymers where side-chain polymers are chemically grafted to a polymer backbone. With high grafting density, the polymer exhibits local

increases in stiffness due to steric hindrance of the side-chain polymers, which has the effect of reducing entanglements. Thus, this serves as a way to achieve materials softer than the plateau modulus caused by entanglements. PDMS materials of this architecture have been synthesized and characterized¹⁸ and the results of their work are given in Figure 6.2. However, work remains to be done by exploring more parameters such as side-chain length vs. backbone length and grafting density along the backbone. Additionally, one can conceive of a more controlled end-group crosslinking mechanism as opposed to side-chain crosslinking employed in their work to have better control over network architecture.

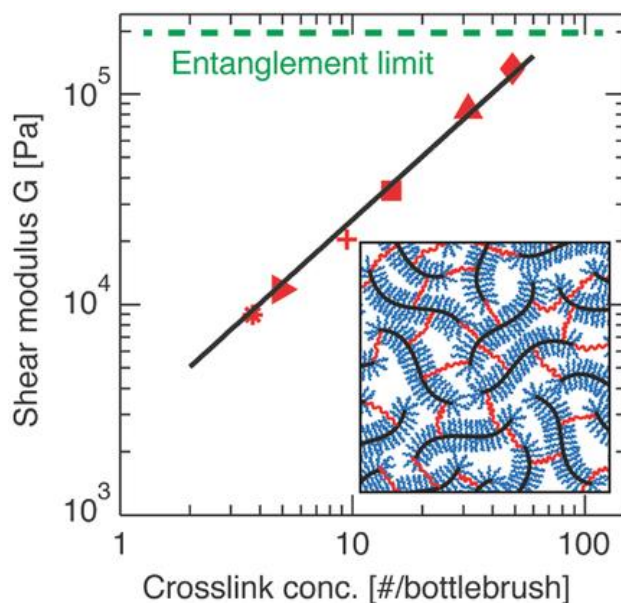


Figure 6.2 – Reproduced from Cai *et al.*¹⁸ Soft PDMS bottle-brush polymers yielding storage modulus values below the entanglement plateau.

Combining Techniques

Given the propositions for controlling the mechanical properties beyond simply changing molecular weight and crosslinker previously described, one has to ponder what kind of properties such a material would exhibit if all of the different architectures were combined into a single material. For instance, a bimodal chain length distribution of bottle brush

polymers crosslinked in solution through functional end-groups at high-functionality crosslink junctions combined with chain extenders and precipitated TEOS aggregates would potentially be a super soft yet super tough and perhaps highly extendable material. Such materials are incredibly enticing to bring to fruition.

Wetting Dynamics

In addition to changing the architecture to enhance mechanical properties, further work remains to probe the wettability of PDMS materials. In fact, as we showed, the bulk dynamic mechanical and dynamic surface wetting properties are related, so this upcoming discussion serves as a compliment to the preceding one. As discussed extensively in chapter 5 of this dissertation, the components of the sol fraction of PDMS substrates influence greatly the dynamic water wetting behavior. Thus, it is advantageous to develop materials of desired mechanical properties with known chemical compositions but also, crucially, very low sol fractions. Some of the proposals outlined above may prove useful in making such materials.

Soft Materials

We mentioned in chapter 5 that soft materials resist water droplet spreading due to viscous dissipations of energy (recall relationship of wetting to loss modulus). The sol fraction, however, seemed to have a stronger influence on dynamic wetting phenomenon than mechanical properties due to the chemical composition and quantity of sol material. Bottlebrush materials serve as excellent candidate materials to study the effects of substrate deformations by probing liquids. They have the potential to be extremely soft where the wetting ridge height may be on the order of tens of microns. Such a wetting ridge would allow easier observation and examination compared to nanometer scale ridges. This could be achieved with a material that contains a low sol fraction so the influence of leached siloxanes is minimized, leaving only the physical forces to determine equilibrium.

Additionally, the chain extension elastomers can also serve as candidate soft materials for wetting investigations. We performed some preliminary wetting experiments on the same material whose mechanical properties are given in Figure 6.1 and were pleased to observe the

wetting ridge height visible to the naked eye. The ridge remained visible for up to 3.5 min after the droplet was removed, as seen in Figure 6.3. This particular sample did show a significant sol fraction on the order of 20%. However, since no small molecule crosslinker with silicon-hydride (more hydrophilic) groups was used, the only material in the sol could possibly be other PDMS macromolecules (and any short chain impurities), which should have similar surface tensions to the network-like material.

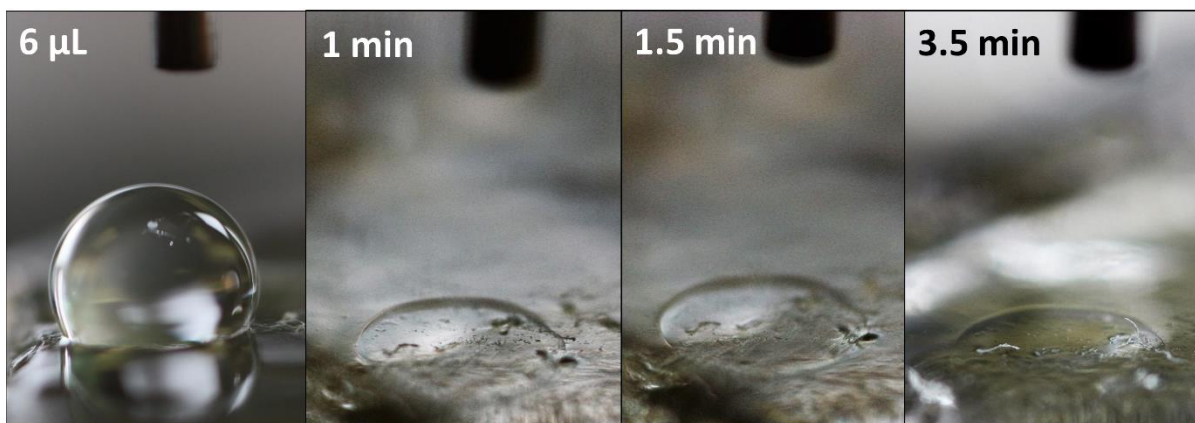


Figure 6.3 – Wetting ridge observed on same sample corresponding to mechanical properties given in Figure 6.1. A 6 µL water droplet was placed on the substrate and allowed to equilibrate for ~ 8 min. Times in upper left correspond to time after droplet removal. It was then removed and the wetting ridge remained visible for up to 3.5 min after droplet removal. The needle in the background has an outer diameter of 0.72 mm.

Surface Roughness

Surface roughness is readily imparted on materials to achieve superhydrophobic coatings with water contact angles $>170^\circ$. This property was not investigated in this dissertation, but would certainly provide a ripe area for examination. Preliminary atomic force microscopy (AFM) measurements on some of our softest samples that exhibited the highest initial contact angles showed roughness on the order of <10 nm, indicating that surface roughness was not a major factor in our studies, although this property was not thoroughly investigated.

Wetting Experiments

Besides changing the materials and investigating the surface roughness, the experiments themselves could be modified to yield more consistent results. To remove the effect of evaporation, a chamber with controlled atmosphere could be used to conduct the dynamic wetting experiments. Another option is to use mixtures of ethylene glycol and water, which have lower vapor pressure than pure water and have been used by others.^{19,20}

Functional Siloxane Polymers and Copolymers

While PDMS has many beneficial attributes, it is certainly not the only polysiloxane. Other polymers such as poly(vinylmethylsiloxane) (PVMS) and poly(hydromethylsiloxane) (PHMS) and their corresponding copolymers with PDMS provide opportunities for chemical functionalization of siloxanes.

Chemical Modification

It is desirable to have orthogonal chemical functionalities on both the end-groups and side-chains of polysiloxanes. This type of molecular architecture provides end-groups for crosslinking and side-chains for chemical functionalization. Such materials, such as silanol-terminated PVMS exist and have been studied in several instances, notably by Genzer, Efimenko, and co-workers.²¹⁻²⁴ Importantly, PVMS maintains many of the favorable attributes of PDMS, such as high flexibility and low glass transition temperature despite having an extra carbon atom on every repeat group, making it slightly more bulky. A systematic investigation of the network structure-property relationships based on different molecular weights and crosslinker loadings similar to the one carried out on PDMS in this dissertation is recommended for PVMS to help share the usefulness of this functional material.

Self-Healing Materials

Self-healing materials have received great attention lately due to their ability to provide mechanical integrity to materials over longer time-scales than traditional materials. PDMS has been shown to function as a self-healing material by using metal-ligand complexes as crosslink

junctions, which permitted facile reversible “bonding,” albeit not quite covalent bonding.²⁵ Still, these materials were able to fully recover over repeated deformation cycles of up to 1,500% strain.²⁵

Our proposal for self-healing PDMS based materials involves using disulfide bonds, which are weaker than C-C bonds but are reversible at room temperature.²⁶ An interesting system to study would be silanol-terminated PDMS with sporadic thiol groups throughout the length of the molecule. This could be achieved using the same tin catalyst for crosslinking with TEOS but instead using it for chain extension with mercaptopropyl dimethoxy methylsilane, depicted in Figure 6.4a. After that, as indicated in portions b) and c) of the same figure, permanent crosslinks could be formed with TEOS (red circles) and reversible crosslinks could be formed by disulfide linkages (blue S-S links). If first crosslinked with low TEOS loading, this would provide a loosely crosslinked permanent network structure and a more tightly crosslinked reversible network structure through the disulfide bonds, as shown in Figure 6.4. Additionally, one could add thiol-terminated PDMS chain extenders to make longer chain lengths between disulfide bonds, as shown in portion c).

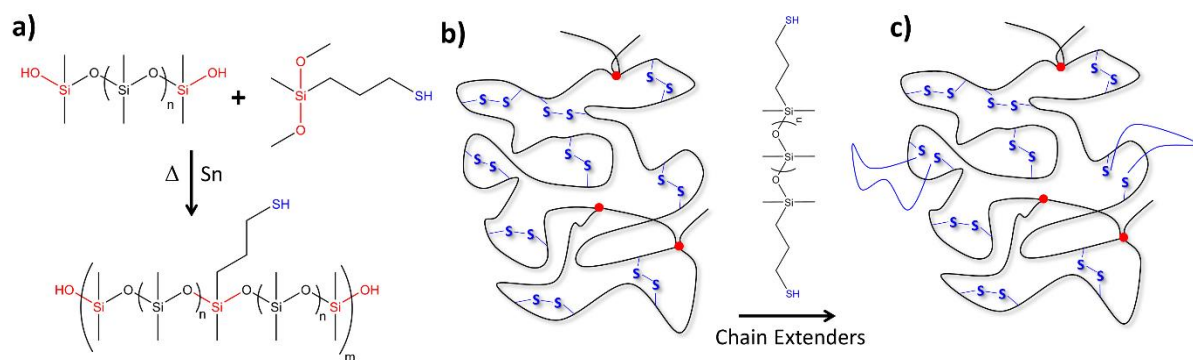


Figure 6.4 – Scheme for endowing silanol-terminated PDMS with functional thiol side-chains at sporadic intervals along the linear chain through chain extension reactions. A primary permanently network could be formed by crosslinking with TEOS (red circles) and a secondary reversible network could be formed by disulfide bonds along the side-chains (blue S-S linkages).

This self-healing scheme could be taken one step farther by either adding fumed silica particles or high TEOS doses. Both would have the effect of incorporating silanol-functional particles into the PDMS matrix, which could react with the silanol-functional PDMS end

groups. Additionally, mercaptopropyl trimethoxysilane could be added to create thiol functional and silanol functional particles to provide both permanent and reversible covalent attachments of the polymer chain to the particles. This scheme is depicted in Figure 6.5. Perhaps such a system would exhibit stronger self-healing behaviors than one without particles.

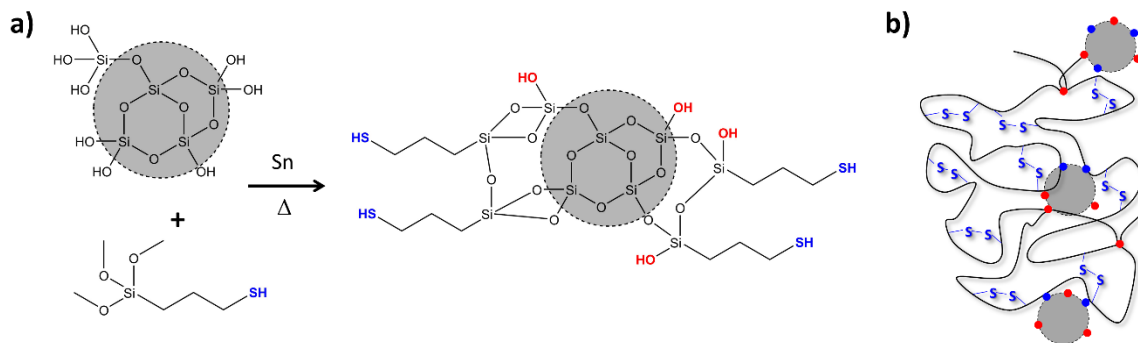


Figure 6.5 – Thiol-functional (blue circles) and silanol functional (red circles) silica particles for both reversible and permanent covalent attachment to PDMS chains.

Overall, there are many more polymer architectures to explore for numerous applications. The results in this dissertation serve as the foundation upon which others can use to build materials of desired topological, mechanical, and surface properties.

References

1. Macosko, C. W. & Miller, D. R. A New Derivation of Average Molecular Weights of Nonlinear Polymers. *Macromolecules* **9**, 199–206 (1976).
2. Miller, D. R. & Macosko, C. W. A New Derivation of Post Gel Properties of Network Polymers. *Macromolecules* **9**, 206–211 (1976).
3. Chassé, W., Lang, M., Sommer, J.-U. & Saalwächter, K. Cross-Link Density Estimation of PDMS Networks with Precise Consideration of Networks Defects. *Macromolecules* **45**, 899–912 (2011).
4. Paul, D. R. & Mark, J. E. Fillers for polysiloxane ('silicone') elastomers. *Prog. Polym. Sci.* **35**, 893–901 (2010).
5. Kumar, S. K., Benicewicz, B. C., Vaia, R. A. & Winey, K. I. 50th Anniversary Perspective: Are Polymer Nanocomposites Practical for Applications? *Macromolecules* **50**, 714–731 (2017).
6. Krommenhoek, P. J. & Tracy, J. B. Magnetic Field-Directed Self-Assembly of Magnetic Nanoparticle Chains in Bulk Polymers. *Part. Part. Syst. Charact.* **30**, 759–763 (2013).
7. Cabal-Velarde, J. G. *et al.* Shape-Anisotropic Nickel-PDMS Composites with Uniaxial Magnetic Anisotropy Obtained by Emulsification Under Magnetic Field. *J. Supercond. Nov. Magn.* 6–11 (2017). doi:10.1007/s10948-017-3996-6
8. Mark, J. E., Jiang, C. & Tang, M. Simultaneous curing and filling of elastomers. *Macromolecules* **17**, 2613–2616 (1984).
9. Yuan, Q. W. & Mark, J. E. Reinforcement of poly(dimethylsiloxane) networks by blended and in-situ generated silica fillers having various sizes, size distributions, and modified surfaces. *Macromol. Chem. Phys.* **200**, 206–220 (1999).
10. Meyers, K. O., Bye, M. L. & Merrill, E. W. Model Silicone Elastomer Networks of High Junction Functionality: Synthesis, Tensile Behavior, Swelling Behavior, and Comparison with Molecular Theories of Rubber Elasticity. *Macromolecules* **13**, 1045–1053 (1980).
11. Llorente, M. A. & Mark, J. E. Model Networks of End-Linked Poly(dimethylsiloxane) Chains. 8. Networks Having Cross-Links of Very High Functionality. *Macromolecules* **13**, 681–685 (1980).
12. Gong, J. P. Why are double network hydrogels so tough? *Soft Matter* **6**, 2583 (2010).
13. Haque, M. A., Kurokawa, T. & Gong, J. P. Super tough double network hydrogels and their application as biomaterials. *Polymer* **53**, 1805–1822 (2012).
14. Llorente, M. a., Andradý, a. L. & Mark, J. E. Model networks of end-linked polydimethylsiloxane chains. XI. Use of very short network chains to improve ultimate properties. *J. Polym. Sci. Polym. Phys. Ed.* **19**, 621–630 (1981).

15. Genesky, G. D., Aguilera-Mercado, B. M., Bhawe, D. M., Escobedo, F. A. & Cohen, C. Experiments and simulations: Enhanced mechanical Properties of end-linked bimodal elastomers. *Macromolecules* **41**, 8231–8241 (2008).
16. Genesky, G. D. & Cohen, C. Toughness and fracture energy of PDMS bimodal and trimodal networks with widely separated precursor molar masses. *Polymer* **51**, 4152–4159 (2010).
17. Goff, J., Sulaiman, S., Arkles, B. & Lewicki, J. P. Soft Materials with Recoverable Shape Factors from Extreme Distortion States. *Adv. Mater.* **28**, 2393–2398 (2016).
18. Cai, L.-H. *et al.* Soft Poly(dimethylsiloxane) Elastomers from Architecture-Driven Entanglement Free Design. *Adv. Mater.* n/a-n/a (2015). doi:10.1002/adma.201502771
19. Hourlier-Fargette, A., Antkowiak, A., Chateauminois, A. & Neukirch, S. Role of uncrosslinked chains in droplets dynamics on silicone elastomers. *Soft Matter* **13**, 3484–3491 (2017).
20. Park, S. J. *et al.* Visualization of asymmetric wetting ridges on soft solids with X-ray microscopy. *Nat. Commun.* **5**, 4369 (2014).
21. Ahmed, S. *et al.* Poly(vinylmethylsiloxane) elastomer networks as functional materials for cell adhesion and migration studies. *Biomacromolecules* **12**, 1265–71 (2011).
22. Efimenko, K. *et al.* Rapid formation of soft hydrophilic silicone elastomer surfaces. *Polymer* **46**, 9329–9341 (2005).
23. Crowe, J. A. & Genzer, J. Creating responsive surfaces with tailored wettability switching kinetics and reconstruction reversibility. *J. Am. Chem. Soc.* **127**, 17610–1 (2005).
24. Crowe-Willoughby, J. a., Weiger, K. L., Özçam, A. E. & Genzer, J. Formation of silicone elastomer networks films with gradients in modulus. *Polymer* **51**, 763–773 (2010).
25. Li, C.-H. *et al.* A highly stretchable autonomous self-healing elastomer. *Nat. Chem.* **8**, 618–624 (2016).
26. Yang, Y., Ding, X. & Urban, M. W. Chemical and physical aspects of self-healing materials. *Prog. Polym. Sci.* **49–50**, 34–59 (2015).